The Instability of Geophysical Flows: Two-layer Frontal Instabilities and Continuously Stratified Inertial Instabilities

by

Matthew William Harris

A thesis
presented to the University of Waterloo
in fulfillment of the
thesis requirement for the degree of
Doctor of Philosophy
in
Applied Mathematics

Waterloo, Ontario, Canada, 2020

Examining Committee Membership

The following served on the Examining Committee for this thesis. The decision of the Examining Committee is by majority vote.

Supervisor:	Francis Poulin Professor, Dept. of Applied Mathematics, University of Waterloo
Supervisor:	Kevin Lamb Professor, Dept. of Applied Mathematics, University of Waterloo
External Examiner:	Vladimir Zeitlin Professor, Sorbonne University and Ecole Normale Superieure
Internal Member:	Marek Stastna Professor, Dept. of Applied Mathematics, University of Waterloo
Internal Member:	Sander Rhebergen Professor, Dept. of Applied Mathematics, University of Waterloo
Internal-External Member:	Fue-Sang Lien Professor, Dept. Mechanical and Mechatronics Engineering University of Waterloo

Author's Declaration

I hereby declare that I am the sole author of this thesis. This is a true copy of the thesis, including any required final revisions, as accepted by my examiners.

I understand that my thesis may be made electronically available to the public.

Abstract

This thesis examines the instabilities of idealized two layer fronts with vertically curved interfaces as well as the inertial instabilities of barotropic and baroclinic jets with background linear stratification.

We begin with our investigation of frontal instabilities in the context of a two-layer shallow water model with both linear and vertically curved interfaces. First, we generalize the model previously established to allow for vertically curved interfaces. Second, we revisit the linear interface case but with higher spatial resolution and study the impact of no-normal flow or radiation boundary conditions. The results show that the former prevents a baroclinic mode from occurring. Third, we investigate the novel problem of vertically curved interfaces and deduce that it does not have a significant impact on a baroclinic instability, however, it does alter the regions of Kelvin-Helmholtz and Rossby-Kelvin instabilities. Furthermore it introduces a new type of baroclinic instability that we refer to as the curved-interface baroclinic instability.

We then investigate the stability of inertially unstable barotropic and baroclinic jets within the context of a forced Navier-Stokes model under the Boussinesq and f-plane approximations. First, we derive two eigenvalue problems for the linear stability analysis of each jet. The eigenvalue problem for barotropic jets includes viscous terms that were neglected in previous studies and the eigenvalue problem for baroclinic jets is entirely novel. We then develop numerical methods to solve each eigenvalue problem. The stability details of three particular baroclinic and barotropic jets are then examined by using our code for the eigenvalue problems alongside fully nonlinear simulations. Despite having different modal structures in the vertical direction, it is shown that the barotropic and baroclinic jets have similar growth rates in some parameter regimes. Finally to compare the growth rates of the unstable modes for the two jets, we perform five parameter studies for each jet. We find that for sufficiently large Reynolds numbers, the growth rates for both jets are similar but for $\mathrm{Re} \lesssim 10^7$ the growth rates for the barotropic jet can be up to twice as large as those for the baroclinic jet.

Acknowledgements

This work is the culmination of 5 years of my mom asking "How's the thesis coming?" while having no idea what the thesis is about.

Thank you Francis and Kevin for your guidance throughout my time at Waterloo. You have both taught me a lot, were always close by, gave me amazing feedback and criticism when needed and helped to keep me funded in my last year. I greatly appreciate everything you have done for me.

Ben and David, thank you both for taking the time to setup my computing environment on Graham. Your scripts to setup and post process SPINS runs have served me well and Ben asking "What did you do?" always made me laugh.

Dedication

This thesis is dedicated to my father who would be "tickled to death" to see this page.

Table of Contents

List of Figures

List of Tables

Chapter 1

Introduction

The dynamics of the Earth's atmosphere, oceans and lakes strongly impact all life on our planet. While at first glance the flows in the atmosphere and oceans may appear to be primarily composed of large slowly evolving jets and vortices that are dominated by rotation and stratification, small scale flows that cascade energy to both smaller and larger scales are crucial to the overall behaviour of these systems. Instabilities are a mechanism that allows for the transfer of energy between large and small scales and can produce small scale flows. Thus, knowledge of how instabilities develop and interact with large scale flows is crucial for understanding geophysical flows. While the saturation of perturbations and the interactions between perturbations with the geophysical flows that generate them is fundamentally a nonlinear process, the initial onset of instability can be analyzed by linearized versions of the equations of motion. This is because perturbations are initially of very small amplitude compared to the background flow, Linear stability analysis is a tool that has been commonly used to analyze the initial onset of instability.

The basic algorithm for the temporal linear stability analysis of a time independent flow is as follows. First one adds small perturbations to the background flow, substitutes the sum into the governing equations and then linearizes the resulting system with respect to the perturbations. If one can solve this system of linear equations, then the stability of the background state to temporal modes will be fully understood at least until the perturbations are sufficiently large so that their nonlinear interactions can no longer be neglected. To simplify solving the linear equations, it is common to assume that the perturbations admit an appropriate Fourier decomposition in both space and time. Under this assumption, the linearized equations become an eigenvalue problem whose spectrum completely characterizes the linear stability of the system. By solving this eigenvalue

problem for the fastest growing mode(s), one can determine the stability of the flow and in the case of unstable flows, the structure and growth rate of the fastest growing mode(s).

Historically linear stability analysis has been extensively used to find various stability criteria for simple geophysical flows. In 1871, Kelvin [41] applied linear stability theory to a simple two layer shear flow with uniform constant density to quantify an instability now referred to as Kelvin-Helmholtz instability. He found that as long as there is a difference in the velocities in the two layers, the flow is unconditionally unstable. Rayleigh-Taylor instability, a type of gravitational instability where a higher density fluid is above a less dense fluid, was characterized in 1883 by Rayleigh and Strutt [72]. The stability of viscous parallel shear flows was examined in the early 1900's by Orr [59, 60] and Sommerfield [80]. The eigenvalue problem for the linear stability of such flows is known as the Orr-Sommerfeld equation. The centrifugal instability of Couette flow was analyzed by Rayleigh [70, 71] and Taylor [85]. In the early 1960's, Charney and Stern [12] along with Pedlosky [62] found the Charney-Stern-Pedlosky necessary conditions for barotropic and baroclinic instabilities. The results, analysis and derivations of the above classical works are all important and have been reproduced in many modern fluid dynamics textbooks such as those by Cushman-Roisin and Beckers [15], Drazin and Reid [17], Kundu [48], Pedlosky [63] and Vallis [91].

Fronts, flows where the properties of some scaler field (e.g. temperature, salinity, etc.) dramatically change over a short distance, and geostrophically balanced barotropic/baroclinic jets are two examples of geophysical flows that are both prevalent in Earth's oceans and atmosphere and susceptible to linear instabilities. Mesoscale oceanic fronts play an important role in the energy budgets of the oceans both because of how they form, a process called frontogenesis, and how they destabilize [6, 7, 8, 32, 55, 98]. This destabilization can give rise to smaller scale coherent structures, such as vortices, and these inherently nonlinear features then contribute to the transfer of energy between different length scales [32]. Similarly, geostrophically balanced barotropic and baroclinic jets can be destabilized by various linear instabilities to give rise to small scale features that transfer energy to smaller length scales. Inertial instability (II) for example can transfer energy from large scale geostrophically balanced fronts and barotropic/baroclinic jets into the smaller scales where mixing can occur [16, 18, 28, 33, 46, 53, 56, 69, 73]. II is of particular interest to the oceanic energy budget because of its high mixing efficiency [16, 37, 69]. In addition to its mixing efficiency, II like all instabilities has the potential to cause secondary instabilities [9, 16] which can further mix the water column. Observations of the ocean as well as numerical models have shown that the conditions for II can be met by many geophysical flows [16, 20, 27, 77]. In particular recent studies argue that II has been observed in the California Undercurrent [16], the Kuroshio Current [40], and the Gulf Stream [87]. One

mechanism for the generation of inertially unstable jets is the interaction of surface or subsurface jets with topography [27]. We now briefly summarize some of the relevant research that has been conducted on two layer fronts and on inertial instabilities of barotropic and baroclinic jets.

1.1 Review of the Instabilities of Fronts

Studying fronts in a primitive equation ocean model is computationally expensive since it is necessary to resolve the motions in three-dimensions. As an alternative, many have considered idealized layered models that are essentially two-dimensional [11]. While layered models cannot account for all aspects of stratification, they can yield insights to some aspects of the motion, and these can then be further explored in more complex models [76].

Many studies of fronts [26, 34, 66, 47, 58, 75] have assumed that the interface has constant slope and considered one of two lateral boundary conditions: 1) radiation boundary conditions [34, 47, 58]; and 2) no-normal flow boundary conditions [26, 66, 75]. Examples of the domains these studies considered are shown in Figures 1.1a and 1.1b. Each of these boundary conditions is associated with a different physical assumption however they often yield similar stability characteristics. One notable difference is that for large Richardson numbers, the radiating boundary conditions admit unstable modes with large wavelengths that are not present in a finite domain.

Orlanski [58] examined the instabilities of a two-layer shallow water (SW) front with a linear interface, a rigid lid and a flat bottom, and an unbounded domain in the horizontal (see Figure 1.1a). The linear stability model was formulated in terms of a Richardson number, Ri, and a wavenumber scaled by the Rossby number, Ro_k. Analytic solutions were obtained in three different regimes: the limit of a vertical front with no density jump across it; the long wave limit ($Ro_k \ll 1$); and the limit of no growth and zero phase speed. A numerical method was used to explore the stability problem outside of these three regimes. Orlanski [58] classified the various instabilities into five distinct types: (i) Rayleigh shear instability, R; (ii) Kelvin-Helmholtz instability, H; (iii) baroclinic instability, E; (iv) an unclassified geostrophic instability, B; and (v) an unknown instability. Orlanski incorrectly concluded that instabilities existed for all (Ro_k,Ri) values and misclassified parts of the H region [34].

Sakai [75] also used a two-layer SW model to explore the instabilities of a front with a linear interface. The major differences are that no-normal flow boundary conditions

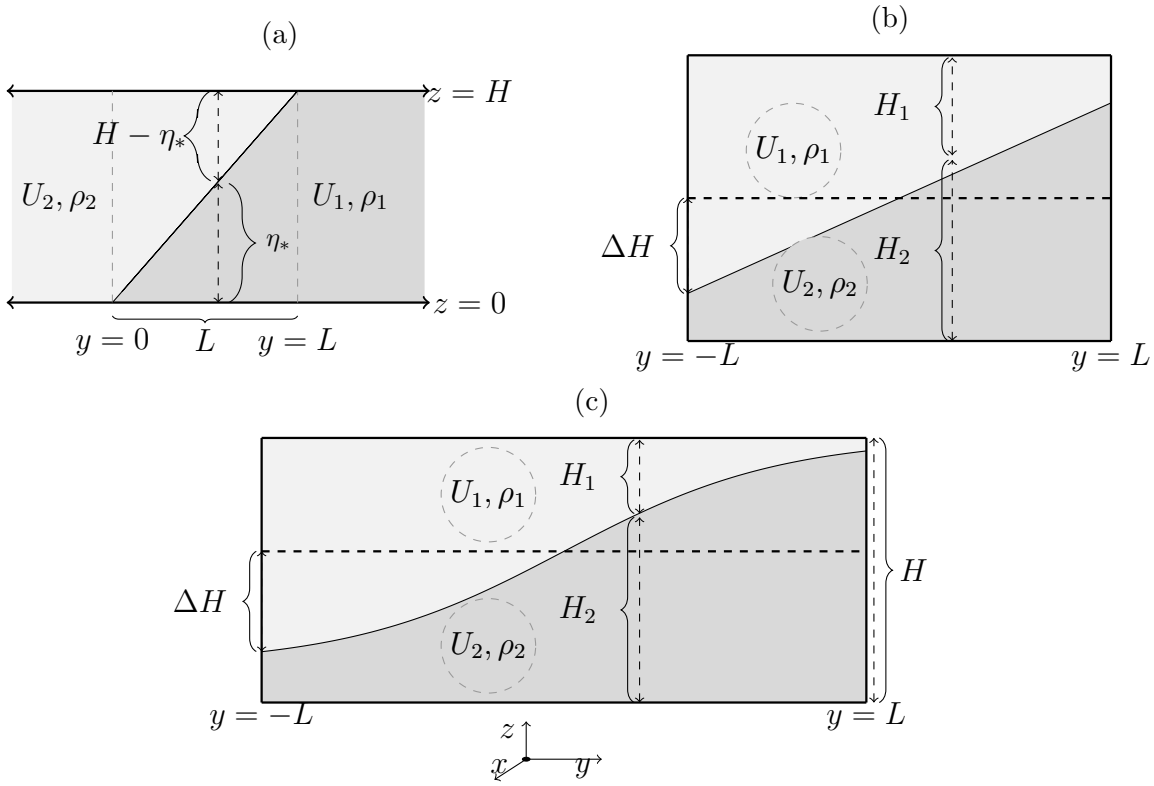

Figure 1.1: Schematics showing (a) the front that is investigated in Orlanski [58] and Iga [34] (b) the front that is investigated in Sakai [75] and GPZ and (c) the more general front we consider. We allow for an arbitrary rigid lid pressure along with a vertically curved interface between the fluids.

were assumed and the fluid depths did not vanish (see Figure 1.1b). Sakai described the instabilities by examining the resonant interactions between waves in each layer and classified the instabilities as either ageostrophic baroclinic, Rossby-Kelvin or Kelvin-Helmholtz instabilities.

Iga [34] revisited the results of Orlanski [58] but used the methodology and framework of Sakai [75]. It is well known in the literature that there are three types of waves that can exist in a single layer: Rossby waves (where the potential vorticity gradient is due to the background flow), Poincaré waves or gravity waves (due to rotation and gravity) and Rossby-Poincaré waves (similar to Yanai waves at the equator) [50]. It was concluded that the so called Rayleigh instabilities (R mode) are caused by the resonance of two mixed Rossby-Poincaré waves, the baroclinic instabilities (E mode) are caused by the resonance of a mixed Rossby-Poincaré wave with a Rossby wave, that the so called Kelvin-Helmholtz instabilities (H mode) are caused by the resonance of a Poincaré wave with either a Rossby wave or a mixed Rossby-Poincaré wave, and the unclassified geostrophically balanced instability (B mode) is a geostrophic baroclinic instability that is caused by the resonance between a mixed Rossby-Poincaré wave and a Rossby wave. Finally, Iga [34] showed that there are parameters where the front is stable and that the unknown instability in Orlanski's work does not exist.

Gula et al. [26] (henceforth GPZ) generalized the work of Sakai [75] by relaxing the symmetry about the center of the domain that arises by imposing $H_1(0) = H_2(0)$. With no-normal flow boundary conditions they determined that the mixed Rossby-Poincaré waves that exist in an unbounded horizontal domain are eliminated by the presence of lateral boundaries and are replaced with Kelvin waves which are trapped by the boundary. Furthermore, it was determined that the region of Rossby-Kelvin instability, a type of ageostrophic instability, found by Sakai [75] contains two instabilities that grow at the same rate: one with a Rossby wave in the top layer and a Kelvin wave in the bottom layer and another one with the waves swapped. The three-dimensional hydrodynamic model WRF [78] was used to verify that the results of the two layer system still hold in a continuously stratified system and to explore the nonlinear evolution of the instabilities. They found analogues of the Rossby-Kelvin instabilities predicted by the two layer model and showed that the growth rates of these modes depend on the thickness of the frontal zone. Physically, this is not unexpected as the Rossby-Kelvin instabilities exist because of the background shear and a thickening of the interface should lead to slower propagating waves. The existence of the Rossby-Kelvin instability in the continuously stratified model confirms that the two layer model provides useful information that can help us to interpret the results of more complicated models.

Bouchut et al. [4] studied the inertial, barotropic and baroclinic instabilities of a Bickley

jet within a two layer SW model. The geometry they use is similar to what was considered by GPZ but they used a hyperbolic tangent interface. At sufficiently large Rossby numbers, the vertical curvature of their interface causes the EPV fields within each SW layer to become negative which in turn allows inertial instabilities to exist. Bouchut et al. [4] found that the barotropic instability was the most unstable mode for a Rossby number of 0.5, that barotropic and baroclinic instabilities have comparable growth rates for order 2 Rossby numbers and that II dominates when the Rossby number is 5.

The last work we summarize here is the work by Wang et al. [92] on the ageostrophic instabilities of shear flows within a single-layer SW model on a f-plane. Due to their lack of stratification, Raleigh-Tayler, Kelvin-Helmholtz and inertial instabilities are not present in their model. This allowed then to focus on ageostrophic instabilities. They examined four different shear profiles: a Bickley jet, cyclonic and anticyclonic double jet, and a triple jet. They found that each jet was unstable to barotropic instabilities caused by the resonance of two balanced shear waves, as well as two types of ageostrophic instabilities caused by the resonance of a balanced shear wave with a gravity wave and the resonance of two gravity waves respectfully.

1.2 Previous Studies on Inertial Instabilities

While two-layer fronts can be subject to II when the EPV is negative in one of the layers but such models cannot capture the full complexity of II since they do lack continuous background stratification. On the other hand using the complex stratifications found in real world flows can make it difficult to ascertain the basic physics of II and how the mechanism manifests itself differently based on the non-dimensional parameters. Using a continuously stratified model with a simple linear background stratification as opposed to the more complex stratification profiles as observed in the world's oceans is one idealization that is common in the literature, which we adopt. Another common idealization is to use background flows that can be described by a simple analytic function. We now summarize a small subset of the many idealized studies of II.

Dunkerton [19] examined II on an equatorial β-plane with a focus on nonsymmetric II, that is to say inertial instabilities that have a nonuniform structure in the along flow direction. Dunkerton focused on nonsymmetric inertial instabilities in part because the growth rates of the symmetric inertial instability (SI), those being inertial instabilities that have a uniform structure in the along flow direction [14, 82], were already known analytically. In the inviscid case, Dunkerton found that the SI mode has the largest growth rate and undergoes an ultraviolet catastrophe with the most unstable mode having a vertical wavenumber

tending to infinity. The addition of viscosity arrests this ultraviolet catastrophe and can allow the nonsymmetric inertial modes to have comparable and sometimes larger growth rates than the SI mode [19]. In terms of the vertical spatial structure of the nonsymmetric modes, Dunkerton found that nonsymmetric modes with large growth rates tended to have similar structures to their SI counterparts.

Griffiths [25] examined the II of inviscid steady barotropic parallel shear flows in a rotating fluid with a background linear stratification. Griffiths [25] used his general solution to examine the details of a hyperbolic tangent velocity profile on an f-plane as well as a uniform shear flow on an equatorial β-plane. Griffiths points out that the historic difficulty of finding analytic solutions for the nonsymmetric II reflects the fact that for nonzero horizontal wavenumbers there are a range of possible instabilities ranging from barotropic/baroclinic instabilities to inertial instabilities and classifying the various modes can be problematic [84]. Nevertheless, he found asymptotic series solutions for the nonsymmetric II modes by using Rayleigh-Schrödinger perturbation analysis and analytic solutions for the SI modes. This asymptotic series solution for the nonsymmetric II modes agrees with the SI modes in the limit as the horizontal and vertical wave numbers of the instability approach zero and infinity respectfully. This agreement suggest that the asymptotic series solutions are indeed nonsymmetric II rather than some other instability. Using his analytical solution, Griffiths was able to show that the eigenvalue, ω, of the most unstable II mode satisfies $\omega^2 \to \min(fQ)$ as $|m| \to \infty$ where f is the Coriolis parameter and Q is the PV of the flow. This describes the ultraviolet catastrophe for the flows considered by Griffiths and shows that the growth rates in the small vertical scale limit are bounded. Griffiths then compared the results of his asymptotic series solutions to numerical solutions in the cases of a hyperbolic tangent velocity profile on an f-plane and a uniform shear flow on a beta plane. Like Dunkerton [19], Griffiths found that without viscosity to arrest the ultraviolet catastrophe, the SI mode was the most unstable mode.

Plougonven and Zeitlin [67] studied the SI of barotropic Bickley jets on an f-plane within a stratified viscous 2D model. They first found analytic solutions to the linear stability problem in terms of hypergeometric functions [3, Chapter 15]. Using their analytic solutions, they confirmed the ultraviolet catastrophe in the inviscid limit and quantified the effects that vertical dissipation has on the growth rates. They then turned their attention to the results of numerical simulations using the WRF model. Even though their analytic solution assumes the Boussinesq approximation and WRF models a compressible atmosphere, they found that their analytic solution and WRF predict comparable growth rates across a range of Ekman and Rossby numbers. They then examined the spatial structure of the most unstable II mode as predicted by their analytical solution and the most unstable mode as predicted by WRF with good agreement. Finally, they examined the

nonlinear saturation of II for two different parameter sets. They found that the vertical length scales of the convective cells that form during the nonlinear saturation of the II decrease with the viscosity.

Carnevale et al. [9] studied the II of an unstratified Gaussian barotropic jet. Their analysis was split into two phases: the initial onset of II to an equilibrated current and the subsequent barotropic instabilities of said equilibrated current. Due to the simplicity of their background current, Carnevale et al. [9] were able to produce analytic approximations for the width of the initial inertial mode along with approximations for the shape of the jet upon the nonlinear saturation of said mode. Their analytic work was validated against numerical simulation with good agreement. They then presented an analysis of the most unstable vertical wavenumber as a function of the Rossby and Reynolds number finding that for their jet the vertical wavenumber scales like $\log_{10}(\mathrm{Re})$ and has a small dependence on the Rossby number. They further demonstrated that the growth rates are not significantly affected by the Reynolds number but have a strong non-monotonic dependence on the Rossby number. Turning their focus to the secondary instability, they performed linear stability analysis on the equilibrated current to find the growth rates and wave numbers of the barotropic instability. The resulting modal structure matched with nonlinear simulations.

Wang et al. [93] examined the instabilities of vertical shear flows within a stably stratified rotating Boussinesq model. For the three profiles they considered, they found that classic baroclinic instability dominates in the quasigeostrophic regime. As the Rossby number increases anticyclonic ageostrophic instability (AAI), II (which they refer to as centrifugal instability) and finally Kelvin-Helmholtz instability dominate. They differentiated between the geostrophic baroclinic modes, the AAI modes, and the Kelvin-Helmholtz modes by their energetics and the degree to which the background state is geostrophically balanced. The problem of separating AAI from II was addressed by appealing to the necessary condition for II that $f \cdot \mathrm{EPV} < 0$ where f is the Coriolis parameter and EPV is the Ertel potential vorticity associated with the background flow [15]. When this necessary condition is met, they conclude that II is the most unstable mode. As the Rossby number increases, it was found that there is a continuous transformation from the growth rate of the most unstable geostrophic baroclinic modes to the AAI modes and finally to the II modes. In addition to the aforementioned instabilities, Wang et al. [93] found two slower growing secondary types of AAI that are associated with inertia critical layers. These slower growing AAI modes were classified by the waves that resonate to cause them.

Ribstein et al. [73] examined the II of a baroclinic Bickley jet with background linear stratification. They started by examining the linear stability of the barotropic version of their Bickley jet but unlike Carnevale et al. [9], they included a background linear stratifi-

cation. In their linear analysis they included viscosity in the vertical direction in order to arrest the ultraviolet catastrophe that is commonly found when studying inertially unstable jets [9, 24, 42, 43]. Without the inclusion of viscosity the growth rate is a monotonically increasing function of the wavenumber that saturates to some supremum [9, 24, 43]. Ribstein et al. [73] then presented results for the fastest growing modes as a function of the horizontal and vertical wavenumbers for a few different nondimensional parameters. Following this study of the growth rates, Ribstein et al. [73] showed the spatial structures for several of the modes. They then used the numerical model WRF to examine the 3D dynamics of the baroclinic jet. While viscosity has an effect on the most unstable II mode, Ribstein et al. [73] did not specify an exact viscosity in their numerical model but instead relied on the numerical dissipation to arrest the ultraviolet catastrophe. Their numerical results showed that the jet was inertially unstable and they were able to capture the process of the nonlinear saturation of the instability.

Tort et al. [89] examined the SI and nonsymmetric II of a barotropic Bickley jet within both a 2-layer SW model and a continuously stratified viscous model. In their study they examined the effects of both the traditional and non-traditional (NT) f-planes. For the 2-layer SW model, they found that at large Rossby numbers there is only one SI mode which has a barotropic structure. They then examined how the growth rate of the SI mode is effected by the Burger number, the Rossby number, the ratio of densities, and the ratio of layer depths. For all of the parameters they considered, the growth rates were larger under the NT approximation than the traditional one. As the stratification increased the difference in the growth rates decreased. In terms of the nonsymmetric II modes, Tort et al. [89] found that the nonsymmetric modes were more unstable than the SI modes but the horizontal wavenumber of the most unstable mode decreased with the Rossby number. In their examination of the stratified case they found that in the inviscid case the ultraviolet catastrophe was present and the addition of viscosity arrests the ultraviolet catastrophe. As with the 2-layer SW model, the NT f-plane produces larger growth rates than the traditional f-plane and the difference in the growth rates for the two approximations decreases for stronger stratifications. They also found that depending on the parameters the most unstable mode could be SI of a nonsymmetric II.

Yim et al. [98] studied centrifugal instability, the anticyclone analog of inertial instability, in three types of anticyclones: a columnar anticyclone, an anticyclone with a Gaussian structure in both the horizontal and vertical directions and an anticyclone with a Gaussian structure in the horizontal direction but an exponential structure in the vertical direction. This work is an extension of Yim et al. [97] where only Gaussian-Gaussian anticyclones were considered. They developed a finite element method to numerically solve the eigenvalue problem for the linear stability of the anticyclones. Their solver was then used to

perform a parameter test for a restricted but interesting range of nondimensional parameters. The results of these tests show how the growth rates of the instabilities for each of the anticyclones depend on the non-dimensional parameters of the flow.

The last work we wish to discuss here is the study of the II of jets with a Gaussian structure in both the horizontal and vertical directions with the addition of background linear stratification by Radko and Lorfeld [69]. Similar to Yim et al. [97] and Yim et al. [98], Radko and Lorfeld [69] solved the linear stability problem for their jet via numerical integration. Unlike the previous studies, Radko and Lorfeld [69] focused on II for O(100) Rossby numbers. Their focus was on exploring the relative dominance of II and barotropic instability. They found that even in this large Rossby number regime, II can be relevant. This was demonstrated by a brief parameter study exploring the relative growth rates of inertial and barotropic instability followed by the detailed analysis of a numerical simulation of a inertially unstable jet. They showed that the II quite efficiently mixed the fluid.

In this thesis we study the temporal instabilities of two layer fronts, and the inertial instabilities of barotropic and baroclinic jets. Our study of fronts is presented in Chapter 2 where we consider the instabilities of two layer shallow water fronts with vertically curved interfaces. Here we apply the methods of linear stability analysis to study how the shape of the interface between the two fluid layers modifies the resulting frontal instabilities. We show that while many of the results of previous works on fronts are still valid, some fronts have been destabilized by a new type of baroclinic instability that is caused by the interaction of Rossby waves that have been modified by the now non-constant EPV field. In Chapters 3-5, we turn our attention to inertial instabilities of continuously stratified barotropic and baroclinic jets within the incompressible Navier-Stokes equations under the Boussinesq approximation. After presenting the relevant background and methodologies in Chapters 3 and 4, we use linear stability analysis to study the onset of inertial instability and nonlinear simulations to explore the nonlinear saturation of the instabilities in Chapter 5.

Chapter 2

Two Layer Instabilities of Vertically Curved Fronts

In this chapter, we extend the works of Sakai [75] and GPZ to allow for vertically curved interfaces as well as arbitrary surface pressures at the rigid lid. Physically, this could account for variable pressures at the surface of the ocean. We choose to use the framework of Sakai [75] and GPZ and thus use no-normal flow boundary conditions. In Section 2.1, we present our generalization of the instability problem considered by Sakai [75] and GPZ. In Section 2.2, we give a comparison of the results of the models studied in Orlanski [58], Iga [34] and GPZ. This comparison shows that even though the frameworks are different, the model results agree quite well and thus the gap between these two frameworks is closed. In Section 2.3, we explore how curved interfaces affect the linear stability characteristics of the instabilities by examining two families of fronts. We find that in addition to the instabilities found previously, the flow is sometimes potentially unstable to inertial instabilities and there is also a new baroclinic mode that we refer to as the vertically curved-interface baroclinic instability. The cause of the new instability is the interaction of Rossby waves that are modified by the vertically curved interface. Finally in Section 2.4, we summarize our results and discuss areas for future study.

2.1 Linear Stability of Vertically Curved Fronts

We generalize the model of Sakai [75] and GPZ to include both an arbitrary rigid lid pressure and an arbitrarily shaped smooth interface and derive a generalized eigenvalue problem that determines the linear stability characteristics of the system.

2.1.1 Derivation of an eigenvalue problem

The geometry of the physical system we consider is shown in Figure 1.1c. Here, we consider two SW layers that are bounded above and below by flat rigid surfaces at $z_* = 0,\ H$ and with vertical walls at $y_* = \pm L$ (here the asterisks indicate dimensional values). The domain is unbounded in the x-direction. In each layer, we have a background velocity $U_{*1,2}(y_*)$ and a constant density $\rho_{1,2}$. The interface is located at $z = H_2(y_*) = \overline{H_2} + \eta_*(y_*)$ where $\eta_*(y_*)$ is a smooth function, with the restriction that $\overline{H_2} + \eta_*(y_*) \in (0, H)$ for $y_* \in (-L, L)$ and $\overline{H_2}$ is the average depth of the lower layer. Note that our restrictions on $\eta_*(y_*)$ force the interface to span the entire width of the domain. Similarly, the depth of the top layer is $H_1(y_*) = \overline{H_1} - \eta_*(y_*)$ where $\overline{H_1} = H - \overline{H}_2$ is the average depth of the top layer. We also allow the rigid lid and bottom pressures to be given by some sufficiently smooth functions $p_{*2}(y_*)$ and $p_{*1}(y_*)$, respectively. Our physical setup is a direct generalization of the system considered by Sakai [75] and GPZ and when the layer depths vanish at the walls (i.e. $\eta_*(-L) = -\overline{H}_2$ and $\eta_*(L) = \overline{H}_1$) it is a "generalization" (albeit with different boundary conditions) of the system considered by Orlanski [58] and Iga [34]. Note that our model allows for both outcropping and incropping in the corners of the domain and since we consider vertically curved interfaces, our fronts are potentially unstable to inertial instabilities for sufficiently large Rossby numbers.

GPZ used the following nondimensional parameters: $\lambda = \Delta H / H_2(0)$ and $\delta = H_1(0)/H_2(0)$, where $\Delta H = H_2(0) - H_2(-L) \geq 0$. With a linear interface, $\lambda \in [0, 1]$ represents the relative change of the interface height with respect to the total depth of the bottom layer and $\delta \in (0, \infty)$ represents the location of the mid-depth. In our more general case, we instead define the nondimensional parameters

$$\lambda = \frac{\max\{|\eta_*(y_*)|\}}{\overline{H_2}} \qquad \text{and} \qquad \delta = \frac{\overline{H_1}}{\overline{H_2}}.$$

Note that λ is the ratio of the maximum deviation of the interface with the average depth of the bottom layer and δ is the ratio of the average fluid depths in each layer. In the case of a linear interface, our generalization reduces to that of GPZ.

The two-layer SW equations are

$$\frac{D\boldsymbol{v}_{*j}}{Dt_*} + f\ \boldsymbol{k} \times \boldsymbol{v}_{*j} = -\frac{1}{\rho_j}\nabla_* p_{*j} \tag{2.1}$$

$$p_{*2} - p_{*1} = \Delta\rho g \eta_* + \rho_1 g H \tag{2.2}$$

$$\frac{\partial \eta_*}{\partial t_*} = -\nabla_* \cdot ([\overline{H_2} + \eta_*]\boldsymbol{v}_{*2}) = -\nabla_* \cdot ([\overline{H_1} - \eta_*]\boldsymbol{v}_{*1}) \tag{2.3}$$

where the asterisks represent dimensional quantities, $j = 1, 2$, ∇_* is the horizontal gradient operator, $\boldsymbol{k}$ is the vertical unit vector, D/Dt_* is the material derivative, $\boldsymbol{v}_{*j} = (u_{*j}, v_{*j})$ is a vector of the x and y directional velocities in the j^{th} layer, f is the constant Coriolis parameter given by the f-plane approximation, g is the constant gravitational acceleration, and $\Delta\rho = \rho_2 - \rho_1$ is the positive density difference between the two fluids.

The basic state is in geostrophic balance with interface $\eta_{*I}(y)$, surface pressure $P_{*1}(y)$ and channel velocities $U_{*j}(y)$. We thus limit our examination to background states that satisfy the following,

$$\begin{aligned} U_{*j} = -\frac{1}{f\rho_j}\frac{\partial P_{*j}}{\partial y_*}, \qquad & V_{*j} = 0, \\ P_{*1} = P_{*1}(y_*), \qquad & P_{*2} = P_{*1} + \Delta\rho g\eta_{*I} + \rho_2 gH, \\ \text{and} \qquad & \eta_{*I} = \eta_{*I}(y_*). \end{aligned} \tag{2.4}$$

Our background state simplifies to the case considered by GPZ when the interface is given by the linear function $\eta_{*I} = \frac{\rho f(U_{*1}-U_{*2})}{\Delta\rho g} y_*$ where $\rho = 0.5(\rho_1 + \rho_2)$, the surface pressure is given by the linear profile $P_{1*} = -\rho_1 f U_{*1} y_* + P_{c*}$, where U_{*i} are constant velocities for each layer, and P_{c*} is the surface pressure at $y_* = 0$. We will derive the eigenvalue problem for the most general case but focus our analysis on the non-linear pressure and non-linear interface cases where the rigid lid pressure is proportional to the interface.

We non-dimensionalize our equations with,

$$\begin{aligned} (x_*, y_*) = R_d\ (x, y), \qquad & (u_{*j}, v_{*j}) = U\ (u_j, v_j), \\ t_* = \frac{1}{f}t, \qquad \eta_* = \overline{H_2}\eta, \qquad & p_{*j} = \rho_i U f R_d p_j, \end{aligned} \tag{2.5}$$

where $R_d = (g'\overline{H_2}/2)^{1/2}/f$ is the external Rossby radius of deformation with $g' = 2\Delta\rho g/(\rho_1 + \rho_2)$ being the reduced gravity, and U is the maximum velocity in each layer.

With this non-dimensionalization, the linearized equations about the geostrophic background state (2.4) are

$$\frac{\partial u_j}{\partial t} + FU_j\frac{\partial u_j}{\partial x} + F\frac{\partial U_j}{\partial y}v_j - v_j = -\frac{\partial p_j}{\partial x}, \tag{2.6}$$

$$\frac{\partial v_j}{\partial t} + FU_j\frac{\partial v_j}{\partial x} + u_j = -\frac{\partial p_j}{\partial y}, \tag{2.7}$$

$$p_2 - p_1 = \frac{2}{F}\eta, \tag{2.8}$$

$$\frac{\partial \eta}{\partial t} + FU_j\frac{\partial \eta}{\partial x} = (-1)^{j+1}F\left(H_j\frac{\partial u_j}{\partial x} + \frac{\partial (H_j v_j)}{\partial y}\right), \tag{2.9}$$

where $F = U/(fR_d)$ is the Froude number, $U_j(y)$ is the background velocity, u_j and v_j are the velocity perturbations, p_j is the pressure perturbation, η is the interface perturbation, and $H_1 = \delta - F\eta_I(y)$ and $H_2 = 1 + F\eta_I(y)$ are layer thicknesses. All of these terms are non-dimensional. Note that the top boundary is now at $z = H/\overline{H}_2$

This system has three nondimensional parameters, the ratio of average layer depths δ, the Froude number F, and a Burger number $Bu = (R_d/(2L))^2$. In the previous works of Orlanski [58], Hoskins [32], Sakai [75], Iga [34], and Perret et al. [65], both δ and Bu were eliminated from discussion by considering symmetric configurations (*i.e.* $\delta = 1$) and examining the so called frontal regime by setting $F = \sqrt{Bu}$. The restriction that $F = \sqrt{Bu}$ places these works into the so called semi-geostrophic (SG) regime [32]. For consistency with previous works, we eliminate the Burger number by requiring that $\lambda = F/(2\sqrt{Bu})$ is constant. Sakai [75] and GPZ examined the case with $\lambda = 0.5$ whereas Orlanski [58] and Iga [34] considered $\lambda = 1$. In our work on vertically curved fronts we consider $\lambda = 0.5$ but when examining the differences between the models used by GPZ and Iga [34] we use $\lambda = 1$. In terms of the current system, this restriction is realized by imposing

$$\lambda = F\max\{|\eta_I(y)|\}.$$

In the case of a linear interface $\eta_I(y) = y$, the above restriction implies that the computational domain is $[-y_m, y_m]$ where $y_m = \lambda/F$. GPZ used this domain in their numerical simulations. In our generalization, imposing this restriction is more complicated since changing the domain length also changes the width of the nonlinear interface. We address this issue by decomposing the interface as

$$\eta_I(y) = y + 2y_m\tilde{\eta}_I\left(\frac{y}{2y_m}\right) + S$$

where y is defined on $[-y_m, y_m]$, S is a constant used to ensure that the nondimensional average depth of the bottom layer is 1, $\tilde{\eta}_I$ is the nonlinear part of the interface and the scaling factor $2y_m$ ensures that the nondimensional interface is consistent with our nondimensionalizations. Note that since $\tilde{\eta}_I$ is a function of $y/(2y_m)$, it is defined on the interval $[-0.5, 0, 5]$ regardless of the value of y_m. Furthermore, the results of Orlanski [58], Iga [34] and GPZ are obtained in the case where $\tilde{\eta}_I(y) = 0$ and $S = 0$. We present an algorithm for computing y_m and the constant S for curved interfaces in Appendix A.

We decompose the perturbation into normal modes in the channel direction and time

$$\langle u_j, v_j, p_j, \eta\rangle = e^{i(kx-\omega t)}\langle \hat{u}_j(y), i\hat{v}_j(y), \hat{p}_j(y), \hat{\eta}(y)\rangle,$$

where k is the non-dimensional wavenumber, ω is the frequency, $Re(\omega)/k$ is the phase speed and $\mathrm{Im}(\omega)$ is the growth rate. We drop the hats and use primes to represent the y derivative to obtain the following equations

$$-\omega u_j + kFU_j u_j + F(U_j' - 1)v_j = -kp_j, \tag{2.10}$$

$$-\omega v_j + kFU_j v_j + u_j = -p_j', \tag{2.11}$$

$$p_2 - p_1 = \frac{2}{F}\eta, \tag{2.12}$$

$$-\omega\eta + kFU_1\eta = kF(\delta - F\eta_I)u_1 + F(\delta - F\eta_I)v_1' - F^2\eta_I' v_1, \tag{2.13}$$

$$-\omega\eta + kFU_2\eta = -kF(1 + F\eta_I)u_2 - F(1 + F\eta_I)v_2' + F^2\eta_I' v_2, \tag{2.14}$$

where U_1, U_2 and η_I are the background velocities and interface given in (2.4). Equations (2.10)-(2.14) have two non-dimensional parameters, F and δ, a nondimensional wavenumber k, and we recall that the basic state is specified by the interface profile and surface pressure. This system reduces to that of GPZ when $\eta_I = y$ and $P_1 = -y/2$.

We now use the work of Iga [34] as motivation for transforming system (2.10)-(2.14) into a generalized eigenvalue problem. To simplify the system of equations, we compute the curl of the momentum equations (*i.e.* $\frac{d}{dy}(2.9) - k(2.10)$) and simplify the result to

$$\begin{aligned}\omega(u_j' + kv_j) = (FkU_j' - k)u_j + kFU_j u_j' \\ + (k^2 FU_j + FU_j'')v_j + (FU_j' - 1)v_j'.\end{aligned} \tag{2.15}$$

Next, the pressure terms are eliminated from the dynamic boundary condition, equation (2.12), via the x-momentum equations (2.10) to obtain

$$\begin{aligned}\omega(Fu_1 - Fu_2) = kF^2U_1u_1 - kF^2U_2u_2 + (F^2U_1' - F)v_1 \\ - (F^2U_2' - F)v_2 - 2k\eta.\end{aligned} \tag{2.16}$$

The generalized eigenvalue problem for $u_1,\ u_2,\ v_1,\ v_2$ is composed of the two vorticity equations (2.15), the continuity equations, (2.13) and (2.14), and the dynamic boundary condition (2.16). These can be written in matrix form as

$$\omega\mathbf{A}\begin{bmatrix} u_1 \\ u_2 \\ v_1 \\ v_2 \\ \eta \end{bmatrix} = \mathbf{B}\begin{bmatrix} u_1 \\ u_2 \\ v_1 \\ v_2 \\ \eta \end{bmatrix}, \tag{2.17}$$

where

$$\mathbf{A} = \begin{bmatrix} \frac{d}{dy} & 0 & k & 0 & 0 \\ 0 & \frac{d}{dy} & 0 & k & 0 \\ 0 & 0 & 0 & 0 & 1 \\ 0 & 0 & 0 & 0 & 1 \\ F & -F & 0 & 0 & 0 \end{bmatrix},$$

and

$$\mathbf{B} = \begin{bmatrix} k[(FU_1' - 1) + FU_1\frac{d}{dy}] & 0 & F(k^2U_1 + U_1'') + (FU_1' - 1)\frac{d}{dy} & 0 & 0 \\ 0 & k[(FU_2' - 1) + FU_2\frac{d}{dy}] & 0 & F(k^2U_2 + U_2'') + (FU_2' - 1)\frac{d}{dy} & 0 \\ kF(F\eta_I - \delta) & 0 & F(F\eta_I - \delta)\frac{d}{dy} + F^2\eta_I' & 0 & kFU_1 \\ 0 & kF(F\eta_I + 1) & 0 & F(F\eta_I + 1)\frac{d}{dy} + F^2\eta_I' & -kFU_2 \\ kF^2U_1 & -kF^2U_2 & (F^2U_1' - F) & -(F^2U_2' - F) & -2k \end{bmatrix}.$$

To fully specify the problem, boundary conditions must be enforced at the channel walls. When one fluid layer vanishes, imposing radiation conditions at the point where the fluid depth goes to zero is trivial as seen in the works of Orlanski [58] and Iga [34] but when the fluid layer does not vanish, imposing such conditions becomes problematic. No-normal flow conditions at the walls give

$$v_1(1) = 0 \qquad \text{and} \qquad v_2(0) = 0.$$

This choice was also used in the works of Phillips [66], Sakai [75], Gula et al. [26]. Imposing these boundary conditions eliminates waves that decay away from the boundary and modifies the dispersion relations for some waves. As we will show, no-normal flow conditions eliminates the baroclinic instability (E mode) that was present in the works of Orlanski [58] and Iga [34]. This is further discussed in Section 2.3. One example where no-normal flow boundary conditions are a good approximation for a front is the Antarctic Circumpolar Current flowing through the Drake Passage [95]. This type of boundary condition is also appropriate in describing circular flow in an annulus [22, 23].

To numerically solve (2.17), we discretize the generalized eigenvalue problem on a staggered grid and then use a direct eigenvalue solver. The details of our algorithm are presented in Appendix A. We do not explicitly examine the potential for critical layer instabilities which exist when a mode has the same velocity as the background velocity at some point in the domain [35]. In the case of curved fronts, the velocities in each layer range continuously between the maximum and minimum values. Obviously, this potentially allows for more critical layer instabilities to exist. Nevertheless, throughout our investigation our numerical method to solve system (2.17) has produced well resolved results and we have not seen any evidence of singularities.

2.2 Linear Interfaces: revisited and compared

In this section, we bridge the gap between previous works on the stability of linear fronts. In particular, we examine how the choice of boundary condition effects the stability properties of fronts with vanishing layer depths, summarize the different instability classifications of Iga [34] and GPZ and then examine the dispersion relations of the unstable modes with no-flow and radiation boundary conditions. To produce our numerical results, we use the numerical methods outlined in Iga [34] and GPZ respectively and our implementation of these methods were validated by comparing with the results in the respective papers. It should be noted that we use much higher spatial resolutions than those used in Orlanski [58] and Iga [34], examine the effects of changing the boundary conditions of the models used in Orlanski [58] and Iga [34] and also apply the GPZ model to a linear front with vanishing layer depths (i.e $\lambda = \delta = 1$).

2.2.1 Most unstable modes

Before we examine the most unstable modes within each framework, we recall that Orlanski [58] and Iga [34] presented their results in terms of (Ri, Ro_k) whereas GPZ used (F, k) and these quantities are related by

$$k = Ro_k\sqrt{Ri} \qquad \text{and} \qquad F = \frac{1}{\sqrt{Ri}}. \tag{2.18}$$

Figure 2.1a shows the results of using the method outlined in Iga [34] with radiation boundary conditions. The boxed region shows the region of our parameter space that overlaps with the parameter space considered by Iga [34] who also included larger Froude numbers. We restrict our focus on $F \leq 1$ in order to compare to the work of GPZ. We plot the 10^{-6} contour level of the nondimensional inverse wavenumber normalized growth rate with a thick black line, and then plot the 0.1 contour and further contours at an interval of 0.2. We also separate the parameter space into labeled regions for the various types of modes Iga [34] found by using the resonance of single layer modes to classify the instabilities. The E mode is a baroclinic mode and exists for large wavelengths and small Froude numbers, the B mode is a geostrophic baroclinic mode and exists for wavenumbers up to O(1), and the R and H modes are the Rayleigh shear and Rossby-gravity/Kelvin-Helmholtz modes respectively and do not exist for $F \lesssim 1/3$. In Section 2.2.2 we discuss the details of which waves resonate to produce each type of instability. Even though the spatial resolution used by Iga [34] is sufficient for convergence for $F \gtrsim 0.6$, we need four times the spatial resolution in order to get convergence for smaller values of F. Finally,

the non-normalized growth rate of the most unstable modes are 0.22 for the E region, 0.35 for the B region, 0.92 for the R region and 2.12 for the H region. Thus even though the E modes were a key focus of the studies of Orlanski [58] and Iga [34], they grow more slowly than some of the other modes.

We now explore the stability properties of the model used in Iga [34] except with no-normal flow boundary conditions. The results of previous works[29, 75, 26] suggests that the E mode should not be present within this model and should be replaced by a B mode. This is indeed observed in Figure 2.1b. Qualitatively, the B region is quite different and it now has local maxima at $(k, F) \approx (0, 0.59)$ and $(0, 0.31)$ as well as much smaller normalized growth rates. The H region is left relatively unchanged with only slightly smaller normalized growth rates and a smaller area of instability. The contours within the R region now intersect the $k = 0$ axis and the largest values are smaller than in the case of radiation boundary conditions. The non-normalized growth rates of the most unstable modes are 0.10 for the B region, 0.45 for the R region and 0.48 for the H region, which are between 22-48% of their respective maximum values in the case of radiation boundary conditions. Therefore, we conclude that the effect of channel walls is to eliminate the E mode and to reduce the growth rates.

Finally, to confirm that the model of GPZ agrees with the model used by Iga [34] when considering the same front, we examine the normalized growth rates computed by the model used in GPZ within the same frontal region that Iga [34] considered. This is done by simply imposing $\lambda = 1 = \delta$ in the framework used by GPZ. Figure 2.2 shows the largest normalized growth rates along with lines separating the regions found by Iga [34]. Here we labeled the instabilities with the nomenclature used by GPZ. The (a) mode is a baroclinic instability, the (b) mode is the Kelvin-Helmholtz instability and the (c) and (d) modes are two different instances of Rossby-Kelvin instabilities. Note that some of the names of the modes conflict with the names that Iga [34] used. We address this difference in nomenclature in Section 2.2.2. The curve separating the baroclinic modes from the Rossby-Kelvin modes was provided in the work of GPZ. Although the normalized growth rates should be virtually identical, the (a) modes slightly differ from what the Iga [34] model predicted. The differences are most apparent for small values of F and are likely the result of numerical error when applying Iga's framework due to its inclusion of the unbounded coefficients $1/(2F)$.

2.2.2 Nomenclature and causes of instabilities

Sakai [75] demonstrated that unstable modes in a two layer system can be classified by which waves resonate to produce them. Iga [34] showed that the waves that can exist

(a)

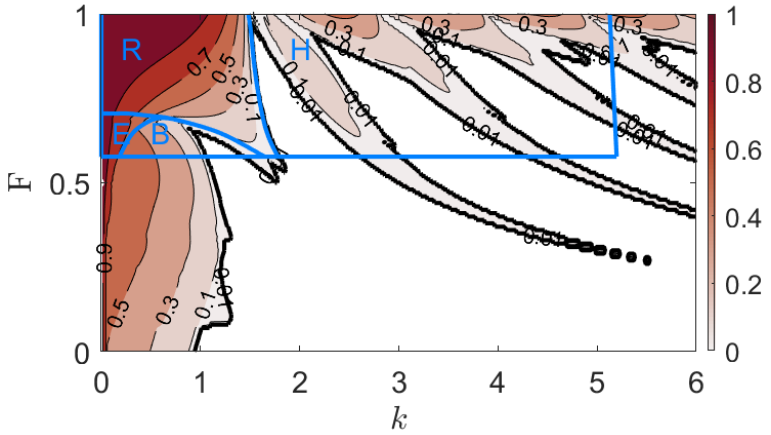

(b)

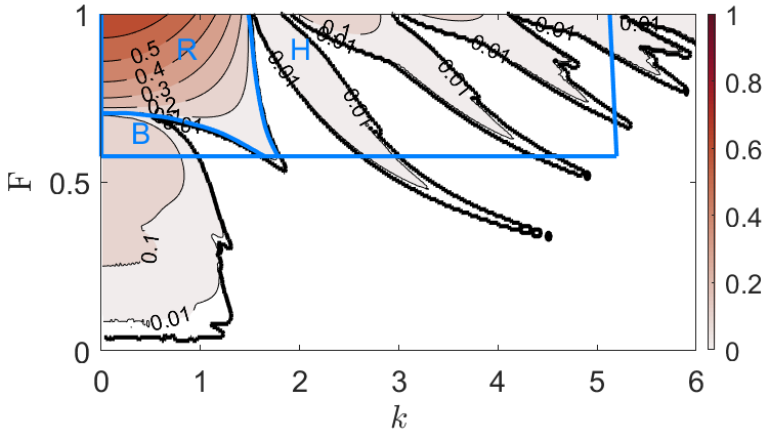

Figure 2.1: The largest inverse wavenumber normalized growth rates as computed by the method given in Iga [34] with radiating boundary conditions (a) and wall boundary conditions (b). The boxed in region is the original parameter region studied by Orlanski [58] and Iga [34] and the labeled subregions split the domain by the instability types found in their works. The regions are R (Rayleigh shear), H (Kelvin-Helmholtz), B (geostrophic baroclinic) and E (baroclinic). Note that this front has both incroppings and outcroppings. White represents an inverse wavenumber normalized growth rate of less than 0.01 and we use thick black lines to show the 10^{-6} contour. The colormap used was developed in Thyng et al. [88].

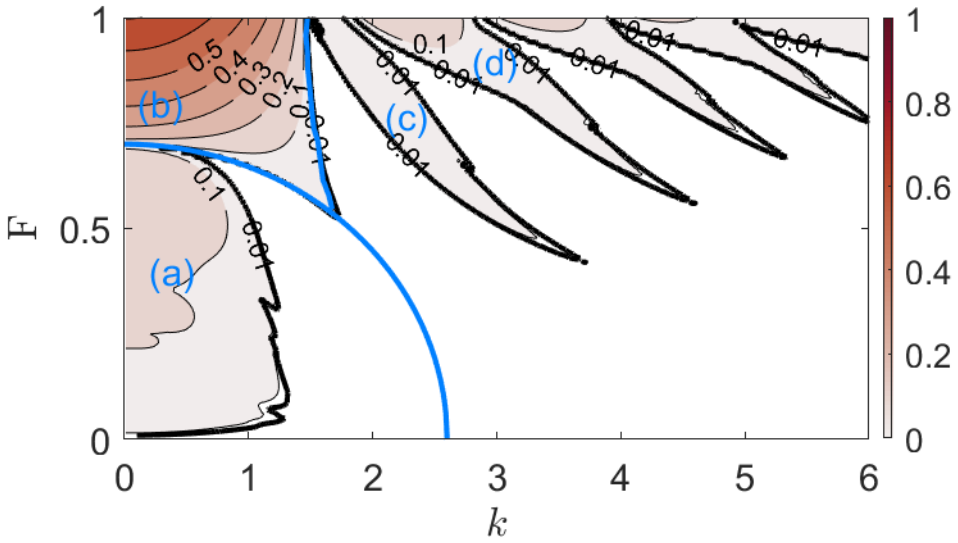

Figure 2.2: The largest inverse wavenumber normalized growth rates as computed by the method given in GPZ with $\lambda = \delta = 1$. Here we separate the instabilities into regions labeled (a), (b) and (c)-(d) for baroclinic, Kelvin-Helmholtz and Rossby-Kelvin modes respectively. These regions correspond to the types of instabilities given in the work of Orlanski [58] and Iga [34] as well as those given in the works of [75] and GPZ. We use thick black lines to mark the 10^{-6} contour.

Fig 2.1	Fig 2.2	Resonance (Iga)	Resonance (Sakai)
B	(a)	geostrophic baroclinic (MR-R)	baroclinic (R-R)
E	N/A	baroclinic (MR-MR)	N/A
R	(b)	Rayleigh shear (MG-MG or MR-MR)	Kevin-Helmholtz (K-K)
H	(c)-(d)	Rossby-gravity or Kelvin-Helmholtz (R-G or MG-G)	Rossby-Kelvin (R-K or R-G)

Table 2.1: A summary of the nomenclature and proposed cause of the various instabilities for two layer fronts. The first column is the region in Figure 2 where the instability exists, the second column is the region in Figure 3 where the instability exists and the last two columns are the name and proposed cause that Iga [34] and Sakai [75] gave to the instabilities respectively.

in a SW model with radiation boundary conditions are Rossby waves, Poincaré waves, and mixed Rossby-Poincaré waves (Yanai waves at the equator), which for $Ro_k > 1$ are Poincaré like and for $Ro_k < 1$ are Rossby like. In the presence of walls, Sakai [75] and GPZ showed that mixed Rossby-Poincaré waves are replaced by Kelvin waves. The difference in waves that exist with either boundary condition yields different resonances and therefore the different classifications of the instabilities.

Table 2.1 lists the regions of instability shown in Figures 2.1 and 2.2, the nomenclature used by previous studies as well as the previously proposed causes of instability. Here we denote the types of single layer waves by R for Rossby waves, G for Poincaré waves, K for Kelvin waves, MR for a mixed wave acting like a Rossby wave and MG for a mixed wave acting like a Poincaré wave. Both Sakai [75] and Iga [34] agree that all of these modes are shear instabilities, the R mode is completely unbalanced, the H mode is balanced in one layer but not in the other and the B and E modes tend to be balanced. The largest differences between the two frameworks is the lack of what Iga [34] calls the baroclinic mode in the model considered by Sakai [75]. The rest of the differences are due to the nomenclature used in the two different approaches.

2.2.3 Dispersion relationships

To examine the differences between these two choices of boundary conditions, we turn our attention to the dispersion relations for both one-layer and two-layer models. First, we compare the dispersion relations of the single layer problems with no-normal flow and radiation boundary conditions. Then, we examine the dispersion relations for the Iga [34] model with and without walls along with the dispersion relations as computed by the GPZ model with $\lambda = 1 = \delta$.

The governing equations for the perturbations in the one-layer problem of GPZ with $\lambda = \delta = 1$ are

$$kF\ (\omega - U)u = -v + 2\frac{k}{F}\eta, \tag{2.19}$$

$$kF\ (\omega - U)v = -u - 2\frac{d}{dy}\eta, \tag{2.20}$$

$$kF\ (\omega - U)\eta = kFyu + \frac{F^2}{2}\frac{d}{dy}(yv), \tag{2.21}$$

which agrees with the corresponding model in Iga [34].

The real parts of the frequency, ω, for $F = 1/\sqrt{3}$ with both wall and radiating boundary conditions are shown in Figure 2.3. These correspond to a slice taken along the bottom of the rectangles in Figures 2.1a and 2.1b and was used by Iga [34], likely because it shows all four types of instabilities. The case with radiation boundary conditions agree with the results of Iga [34]. The main effects of no normal flow boundary conditions is to a) flatten the dispersion relation curves of both the Rossby waves (R) and the mode zero mixed Rossby-Poincaré wave (M_0) for small Ro_k, b) change the mode zero leftward propagating Poincaré wave (G_0^-) to a leftward propagating mixed wave (M_0), and c) cause the leftward propagating mode N Poincaré wave (G_N^-) to act like the leftward propagating N-1 mode Poincaré wave (G_{N-1}^-) for sufficiently small k. The fastest Rossby modes are affected more than the slower modes. Physically this means that walls lead to a decrease in the phase speeds of both the long mixed modes and the long Rossby modes. Since the M_0 and R waves for small k are affected by walls and these are precisely the waves that resonate to form the E mode, we conclude that the flattening of the one-layer dispersion relations is what prevents these modes from resonating to produce an instability. The change in the dispersion curve for the M_0 mode for small wavenumbers causes this mode to act like a Kelvin wave and is the reason for the different classifications of this mode by Iga [34] and GPZ.

We now examine the dispersion relations for the two-layer model as considered by Iga [34] as well as the dispersion relations predicted by the models of Iga [34] and GPZ with no-normal flow and vanishing layer depths respectively. Figures 2.4a-2.4c show the dispersion relations for the parameters $F = 1, 1/\sqrt{2.1}$ and $1/\sqrt{3}$ respectively. In each of the top plots, we show the inverse wavenumber normalized growth rates for all three models and the bottom plots show the dispersion relations. In the plots of the dispersion relations, growing modes are marked with asterisks. Since the dispersion relations are symmetric about $\omega_r = 0$ we restrict our focus to $\omega_r \geq 0$. For simplicity of nomenclature, we use the nomenclature of Iga [34] to label the instabilities.

Generally speaking, we see that the no-normal flow conditions has a minor effect on all B modes and the H and R modes for wavenumbers $k \gtrsim 0.5$. The change to no-normal flow conditions replaces the E mode with a pair of leftward/rightward propagating B modes. Aside from the loss of the E mode, all of the other changes we see are explained by changes to the critical flow parameters for the various instabilities. In particular outside of small shifts to the critical wavelengths, there is little difference between Iga's model with walls and the model of GPZ with $\delta = \lambda = 1$. We thus conclude that the models used in Orlanski [58] and Iga [34] with the addition of wall boundaries agree at least qualitatively with the limiting case of the models used by Sakai [75] and GPZ.

2.3 Vertically Curved Interfaces

In this section, we first analyze the linear symmetric fronts with $\lambda = 0.5$ and $\delta = 1$ shown in Figure 1.1b and considered by Sakai [75] and GPZ. We then examine the stability properties of two distinct classes of curved interfaces. Unlike in Section 2.2 the interface no longer has outcroppings/incroppings in the upper right/lower left corners.

2.3.1 Base linear case

Figure 2.5 shows the largest growth rates for the base case of the linear front with non-vanishing layer depths and equal layer volumes (i.e. $\lambda = 0.5$ and $\delta = 1$) shown in Figure 1.1b. We choose to plot the largest growth rates instead of this quantity normalized by the inverse wavenumber because the lack of the E mode means we no longer need to differentiate the E mode from the B mode. There are four regions of instabilities: (a) baroclinic instability, (b) Kelvin-Helmholtz instability and (c), (d) instances of the Rossby-Kelvin instability caused by two distinct resonances. This is not a new result[26] but is presented here to help to show that new features arise as a result of a curved interface.

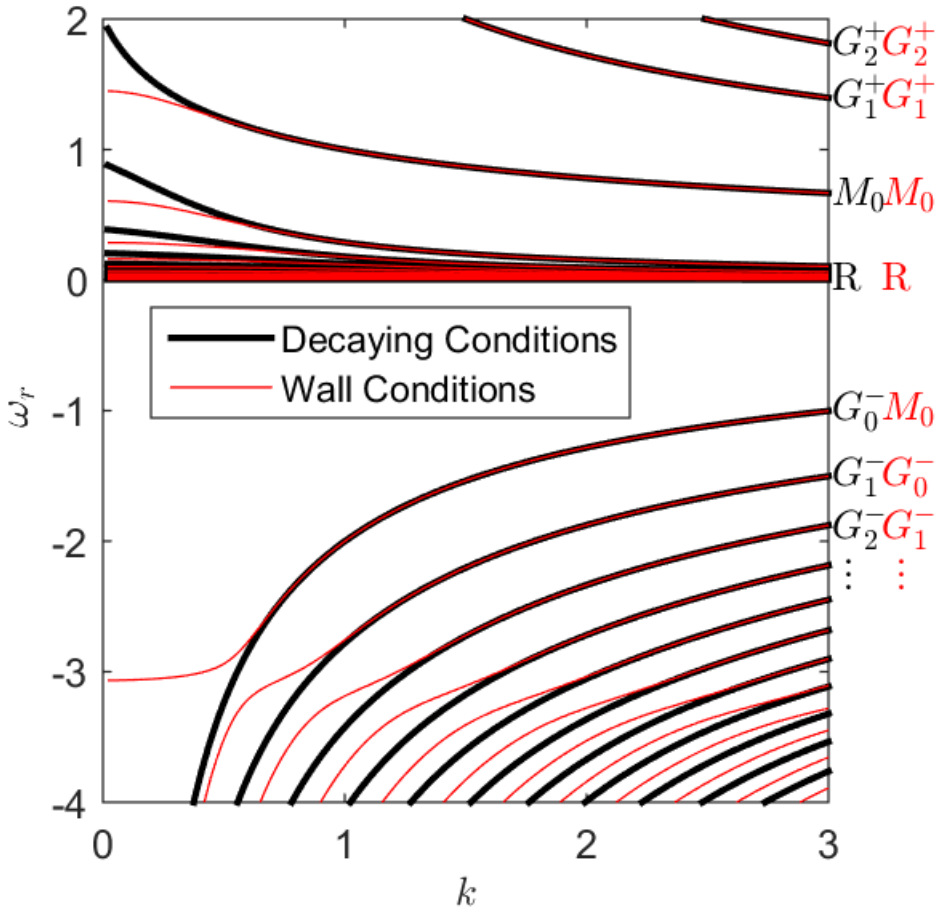

Figure 2.3: The dispersion relation for the single layer problem with linear interface and rigid lid pressure for both wall boundary conditions and radiating boundary conditions for $F = 1/\sqrt{3}$ and various values of k. The types of single layer waves are labeled on the right. Here R denotes the Rossby waves, $G_i^{\pm}$ are the ith Poincaré wave traveling in the $\pm$ direction, M_0 is the 0th mixed mode.

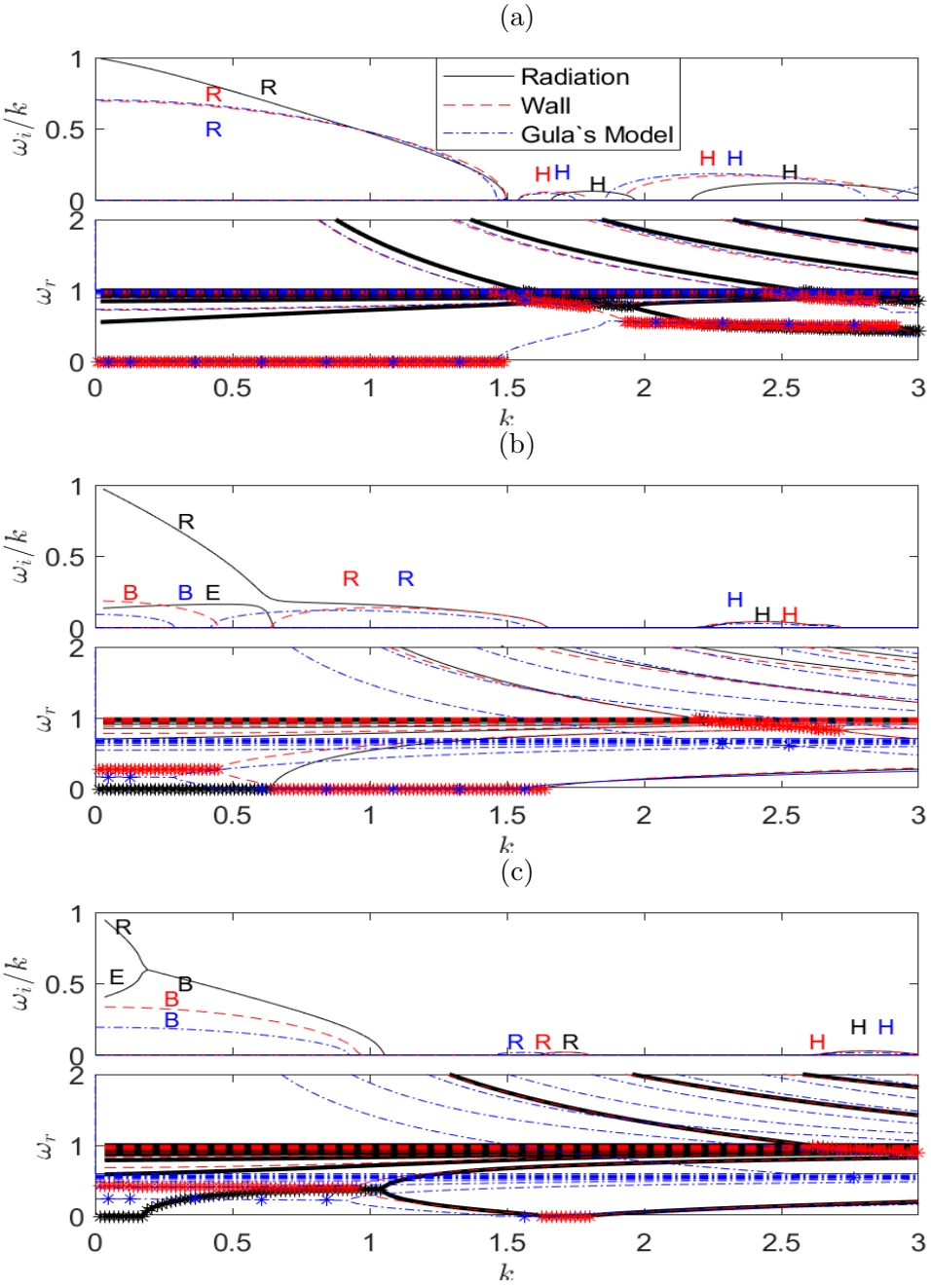

Figure 2.4: Inverse wavenumber normalized growth rates and phase speeds for the three models used in this work. (a), (b) and (c) show the cases for $F = 1.0$, $F = 1/\sqrt{2.1}$ and $F = 1/\sqrt{3}$ respectively. In each ω_r plot we mark modes with an inverse wavenumber normalized growth rate larger than 0.01 by asterisks. The mode names correspond to those given in Table 2.1.

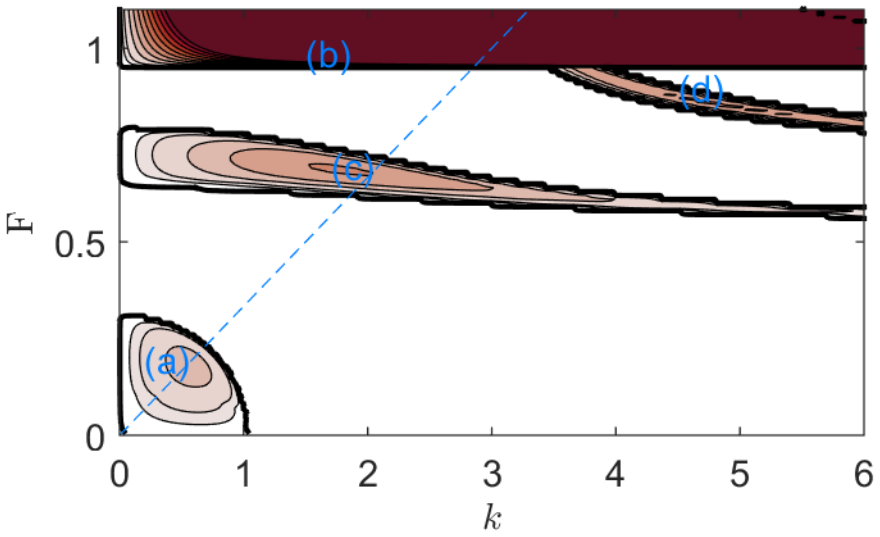

Figure 2.5: The largest growth rates for the base case of a linear interface with $\lambda = 0.5$ and $\delta = 1$. Here contours are at 10^{-6} (thick black line), 0.01, 0.02 with further contours at 0.02 intervals up to 0.1 with more contours at 0.1 intervals. This is the main case considered by Sakai [75] and GPZ. Here we separate the instabilities into regions labeled (a) for the baroclinic instability, (b) for the Kelvin-Helmholtz instability and (c), (d) for two different instances of the Rossby-Kelvin instability caused by two different Poincaré waves. Unlike previous growth rate plots, this front does not have incroppings or outcroppings.

In Figure 2.6 we present the growth rates and frequencies for the various instabilities along the line $F = k/3$. In the bottom panel, we see that: the baroclinic instabilities, region (a), are present in the region where the Rossby waves in each layer can interact: the Rossby-Kelvin instability, region (c), occurs when Kelvin waves interact with Rossby waves; and the Kelvin-Helmholtz instability, region (b), is present when Kelvin waves interact with each other. The resonance that caused the (d) region of Rossby-Kelvin instability is not shown in Figure 2.6 but this mode is caused by gravity waves resonating with Rossby waves.

The necessary condition for baroclinic instability for uniform flow in the Quasi-Geostrophic (QG) model[63] applied to our model is

$$k^2 + \left(\frac{\pi F}{2\lambda}\right)^2 < \frac{1}{\sqrt{\delta}}. \tag{2.22}$$

Since the QG model is a simplified subset of the SW model that is valid for geostrophically balanced flows, this criterion should still be relevant to our study of the stability of a front. The case of a curved interface corresponds to non-constant shear in each layer, and therefore the above equation no longer holds, however, this criterion could be useful in assessing whether the shear flow is unstable or not.

In discussing Rossby-Kelvin instabilities, GPZ used the estimate $\omega_k \approx kF$ for the Rossby wave propagation speed and used the constant layer depth Kelvin wave velocity to estimate the Kelvin wave propagation speed as $\omega_k \approx k\sqrt{g'H}$. By taking the extreme values of the layer depth to get bounds for H, GPZ found the interaction condition

$$\frac{\sqrt{2\ \min_y(H_j(y))}}{2} < F < \frac{\sqrt{2\ \max_y(H_j(y))}}{2} \tag{2.23}$$

where H_j are the nondimensional layer depths in each layer. We expect to see Rossby-Kelvin instability whenever this inequality holds for either $j = 1$ or 2. In the case of the linear interface, this provides a good estimate for the F parameters where the Rossby-Kelvin instabilities exist. Because this condition depends on the largest values of the layer depths, a curved interface could effect the regime that is unstable to Rossby-Kelvin instabilities. The symmetry about $\omega_r = 0$ in the dispersion relation plot in Figure 2.6 shows that the region (c) is composed of two instances of Rossby-Kelvin instability, one leftward propagating and one rightward propagation. When $\delta = 1$ these two Rossby-Kelvin instabilities have the same growth rate. GPZ showed that when $\delta \neq 1$ the symmetry in the dispersion relations about $\omega_r = 0$ disappears and the (c) region splits into two instances of Rossby-Kelvin instability. One can thus expect vertically curved fronts to also lack symmetry in the critical thresholds or growth rates of the two Rossby-Kelvin modes.

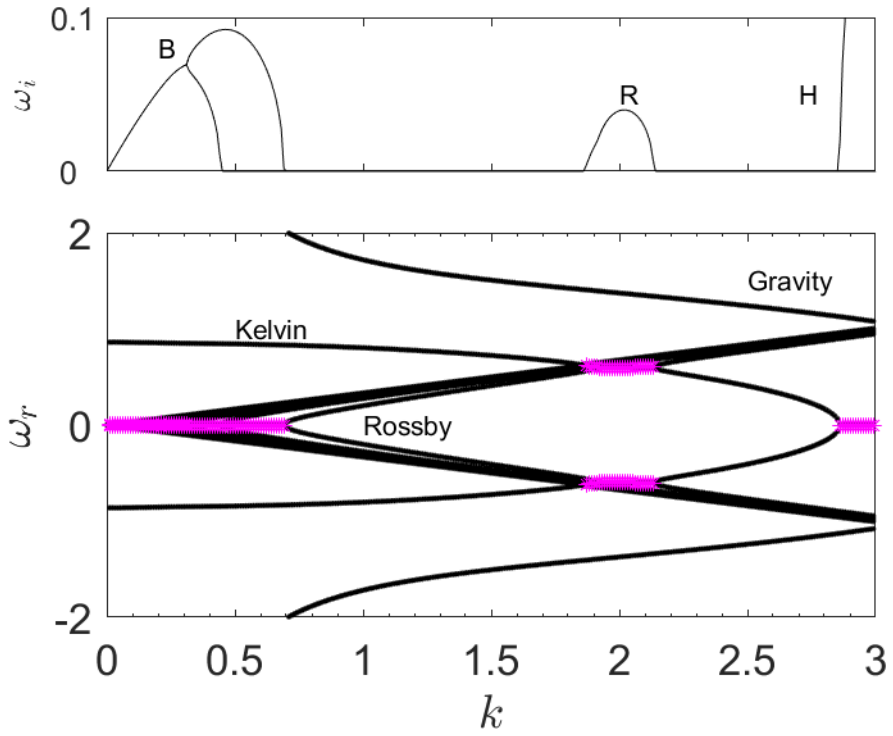

Figure 2.6: Growth rates and dispersion curves for the base case of a symmetric linear front with $\lambda = 0.5$ and $\delta = 1$. Here we plot the values along the dashed line given in Figure 2.5. The labels (B), (H) and (R) correspond to the baroclinic, Kelvin-Helmholtz and Rossby-Kelvin instabilities respectively. We mark unstable modes by asterisks.

Finally, since the Kelvin-Helmholtz instability is caused by the resonance of two Kelvin waves, the parameters for which this instability occurs should be influenced by Doppler shifting of the Kelvin waves in each layer [26]. GPZ found that in the $\delta = 0.7$ case the Froude number critical threshhold for Kelvin-Helmholtz instability was lowered. Thus in our exploration of vertically curved fronts, Doppler shifting of the Kelvin waves could result in changes to the critical Froude number for Kelvin-Helmholtz instability.

2.3.2 Vertically curved fronts

To consider a curved interface, we introduced the decomposition

$$\eta_I(y) = y + 2y_m\tilde{\eta}_I\left(\frac{y}{2y_m}\right) + S. \tag{2.24}$$

In our analysis of curved interfaces, we consider the two interfaces denoted by

$$\tilde{\eta}_S(y; v, N) = \frac{v}{2\pi N}\sin\left(2N\pi y\right), \tag{2.25}$$

and

$$\tilde{\eta}_T(y; v, a) = \frac{v}{a}\tanh\left(ay\right), \tag{2.26}$$

with the surface pressures proportional to the interface. In both profiles, v is the maximal velocity deviation and a or N set the length scale. Because of the forms of the deviations of the interface, we refer to the two profiles as the sinusoidal and hyperbolic tangent profiles respectively even though the interfaces themselves are not sinusoidal and hyperbolic tangent profiles. Sample interfaces are shown in Figure 2.7.

These profiles are chosen because they are simple, give rise to curved interfaces and are qualitatively different. The sinusoidal profiles contains oscillations and the hyperbolic tangent profile can be used to produce a geostrophically balanced Bickley jet[68]. Before we present our new results, we briefly note that we have validated our methodologies for curved fronts by reproducing the results of Bouchut et al. [4] in the case of a purely hyperbolic tangent profile (i.e. $\tilde{\eta}_I(y, v, a) = -y + v\tanh(ay)$).

2.3.3 The hyperbolic tangent profile

For this profile we examined interfaces with values of a ranging from 1 to 15 and velocity deviations, v ranging from -0.5 to 0.5 but for brevity we only present the results for 9 interfaces with $a = 5$, $a = 10$ or $a = 15$ and maximal velocity deviations of -10%, 10% or 30%. These velocity profiles are shown in Figure 2.8. The results we present are representative of those for the other hyperbolic tangent profile we examined.

Figure 2.9 presents contour plots for the most unstable growth rates for nine different hyperbolic tangent profiles. For consistency, we use the same contour intervals and colorbar used in the linear case to allow for direct comparisons with the linear interface results shown

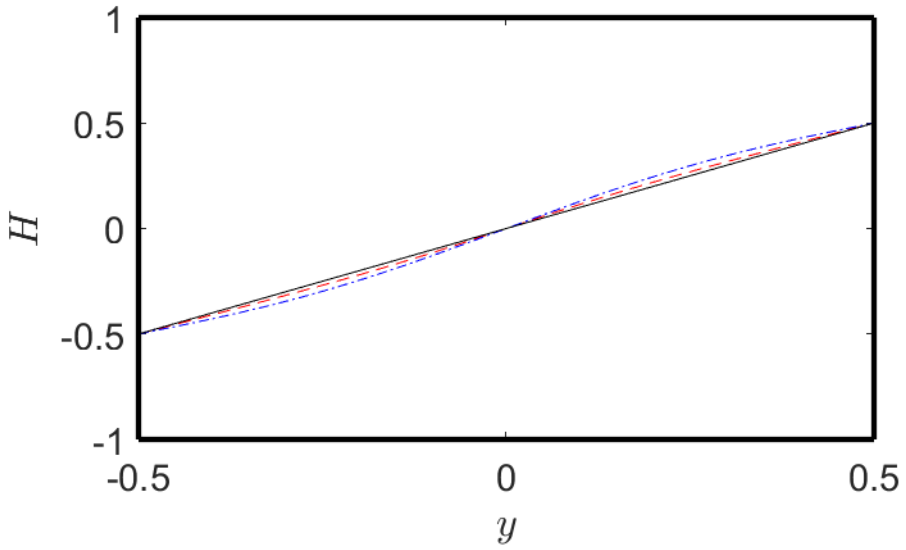

Figure 2.7: The interfaces with the largest deviations from a linear interface we consider in this work. Here we plot the interface for $\tilde{\eta}_T(y; 0.3, 5)$ (red dashed line), $\tilde{\eta}_S(y; 0.3, 1)$ (blue dotted line), and the linear interface (black solid line) for reference. The boundaries are shown by thick black lines. The boundaries are shown by thick black lines. Both of these interface plots have a maximum velocity deviation of 30%.

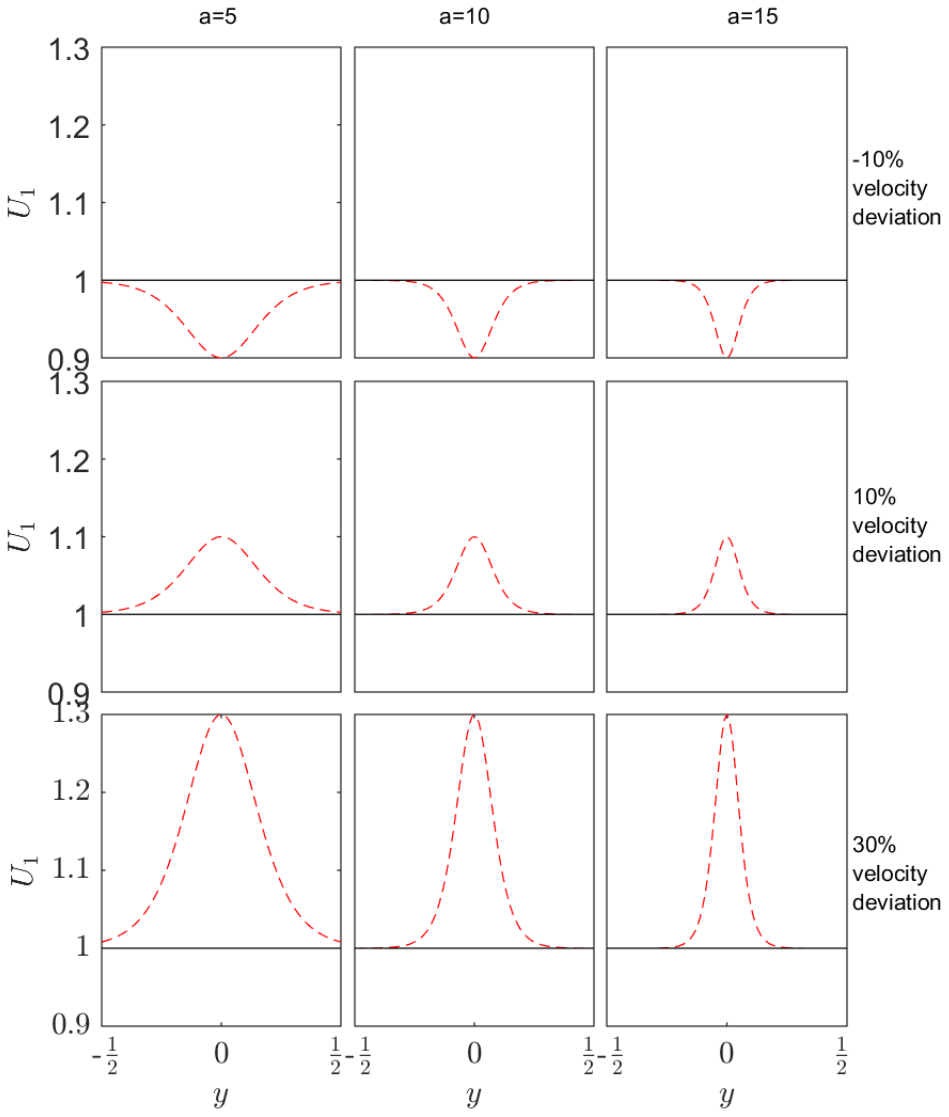

Figure 2.8: The background jets that correspond to the hyperbolic tangent interfaces we examine in Section 2.3.3. Here the parameters for the background jets are listed on the top and right of the figures.

in Figure 2.5. In the bottom left plot we label regions (a)-(d) for the instabilities that were previously seen in linear fronts but we also label a new type of instability by (e). The details of this new instability will be provided when we examine the dispersion relations along the two blue dashed lines in Figure 2.9. The green lines in the bottom middle and bottom left plots indicate the critical threshold for the necessary condition for inertial instability. Above the lines, the fronts could be unstable to inertial instabilities but below the lines the fronts are stable to such instabilities. All other fronts were stable to inertial instabilities for the values of F we examined.

Focusing on the baroclinic instability region, (a), in each plot in Figure 2.9 we see that this instability is not strongly affected by changes to the interface. By comparing the contours in Figures 2.5 and 2.9 we see that there is virtually no change to the critical (F, k) values for baroclinic instability and that the growth rates are similar in magnitude. Further, we see that changing a has little effect on the size of the largest contour in the (a) region but the maximal growth rate tends to increase with v.

Like the baroclinic instability, the Kelvin-Helmholtz instability, (b), is not strongly impacted by changes to v or a. This is clearly seen by the minimal changes to the critical Froude numbers for each of the parameter we present.

The Rossby-Kelvin instability, (c)-(d), on the other hand changes considerably in some cases. We first focus on the (c) region of this instability which is caused by the resonance of a Rossby wave with a Kelvin wave. Here, the critical Froude numbers depend on both a and v. For a fixed value of a, as v increases the range of critical Froude numbers widens and the maximal growth rate in the (c) region increases. This must be due to the fact that the maximum depth increases with v in conjunction with Equation (2.23). With $v > 0$ the maximal growth rate in the (c) region tends to increase as a decreases but the opposite is true for $v < 0$. This is an interesting property that we have not yet been able to explain. We now examine the (d) region of Rossby-Kelvin instability which is caused by the resonance of a Rossby wave with a gravity wave. This mode intensifies as v increases. For $v < 0$ there is no clear (d) region and for all values of v it becomes more difficult to separate the (d) region from the new (e) region as a increases. As the changes to the (c)-(d) modes are caused by modifications to the dispersion relations of the Rossby waves, Kelvin waves and gravity waves, an examination of the dispersion curves within this region will make it more clear how to distinguish the (e) region from the (c) and (d) regions.

We now examine the (e) region which in this preliminary analysis we take to be any unstable region that is not located in Figure 2.5. New regions of instability appear to form across a large range of parameter values as either the width of the jet or $|v|$ increase. This instability thus can dramatically change the Froude numbers for which the front is stable.

To this point, in several of the nine examples we provide here, the flow is unstable for all values of F. Generally, as a increases the front becomes more localized, and the (e) region exists for larger ranges of parameters. This new region of instability is thus likely to be of physical importance.

To rule out the possibility that the new (e) region of instability is caused by an inertial instability, we first note that the necessary condition for inertial instability is only satisfied in two of the hyperbolic tangent fronts considered. Finally, in their work Bouchut et al. [4] found that inertial instability was not the most dominate instability for a Rossby number of 2. In our work a Rossby number of 2 corresponds to $F = 1$ and thus we do not expect any of the most unstable modes to be inertial instabilities. Even though their interface differs from the one we use, the behaviour of the largest growth rate and the structures of the most unstable modes are good indications that the unstable modes we see are not likely the result of inertial instability.

We now examine the dispersion relations along the blue dashed lines given by $F = k/3$ in Figure 2.9, to see what resonating waves cause the various regions of instabilities. The profiles we examine in detail are $\tilde{\eta}_T(y; -0.1, 10)$ and $\tilde{\eta}_T(y; 0.3, 10)$. In the top plots of Figure 2.10, we plot the growth rate and label the types of modes by B, R, H and B2 for the baroclinic, Rossby-Kelvin, Kelvin-Helmholtz and the instability in the (e) region respectively. The bottom plots show the dispersion curves with growing modes marked in green for baroclinic, Rossby-Kelvin or Kelvin-Helmholtz and magenta for modes that cannot be caused by any of the previously proposed resonances. Note that the symmetry of the Rossby-Kelvin modes we saw in the case of a linear interface is no longer present.

We first focus on the baroclinic, Kelvin-Helmholtz and Rossby-Kelvin instabilities. In Figure 2.10, the baroclinic instabilities are present when Rossby waves from each layer interact. The Rossby-Kelvin instabilities only exist when the Rossby waves can interact with either a Kelvin or Poincaré wave and thus have the same underlying mechanisms that they do for a linear interface. The symmetry that was previously present for the Rossby-Kelvin instabilities is no longer present. Note that the leftward propagating Rossby-Kelvin instabilities generally have smaller growth rates than the rightward propagating ones. More importantly, both the leftward and rightward propagating instabilities have smaller growth rates than the new B2 instability. This explains why the Rossby-Kelvin instability region is difficult to identify in Figure 2.9. Finally, the Kelvin-Helmholtz instability is seen only when Kelvin waves interact with each other and has the largest growth rate of all of the instability types. The above analysis shows that the underlying causes of the three instabilities are not modified by curved interfaces while the parameters for which they exist have been changed due to the modifications in the dispersion relations of the waves that resonate to cause the instability.

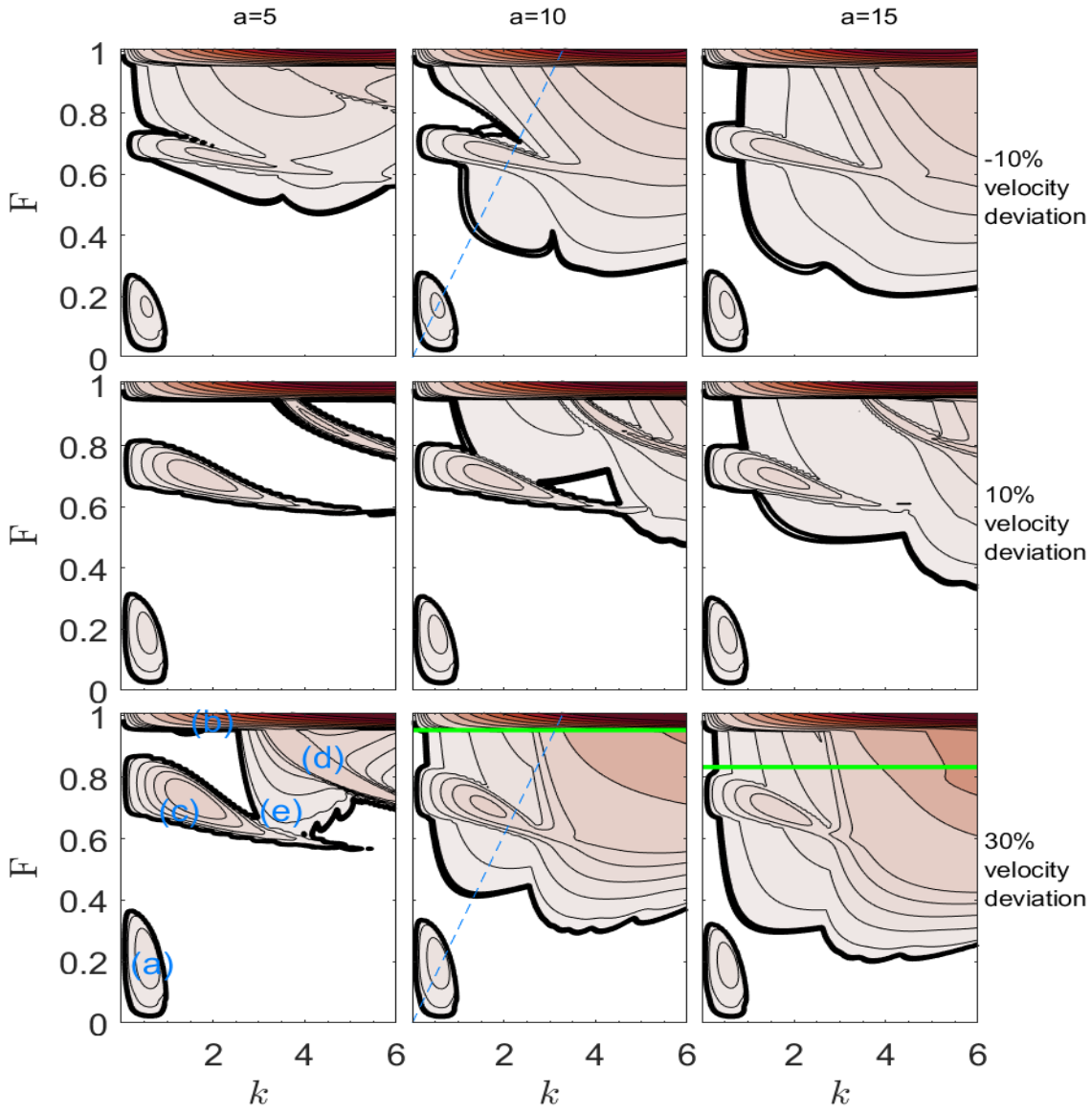

Figure 2.9: Growth rate contour plots for various hyperbolic tangent profiles. From left to right the width factor increases from $a = 5$ to $a = 15$ and from top to bottom the v parameter is -10%, 10% and 30%. Here the contours and colorbars are the same as those in Figure 2.5. The growth rates and dispersion relations along the blue lines are examined in detail. The labels (a)-(d) correspond to the regions in Figure 2.5. The green lines show the minimum Froude numbers for which the fronts could potentially be unstable to inertial instabilities.

This leaves the new B2 instability. The magenta asterisks marking the new instability in Figure 2.10 are located in regions where there are only Rossby waves. This eliminates the possibility that the B2 instability is one of the previously studied instabilities and shows that it thus must be caused by Rossby waves traveling in the same direction resonating with each other. Jones [38, 39] showed that in the presence of a non-constant ambient background vorticity, Rossby waves are modified in such a way that they resonant either with each other or with traditional Rossby waves to produce instabilities [38, 39]. The curvature of our fronts produce a non-constant ambient background vorticity fields and thus are capable of producing modified Rossby waves. We will refer to these waves as vertically curved-interface Rossby waves since they are caused by the curvature of the interface. We propose that these vertically curved-interface Rossby waves resonate either with other vertically curved-interface Rossby waves or traditional Rossby waves to produce the B2 instability which we will call the vertically curved-interface baroclinic instability. Since there are no other possible resonating wave pairs, this must be the case. Finally, we note that because the vertically curved-interface baroclinic instability occurs for relatively large Froude numbers, they are unbalanced and can thus be classified as an ageostrophic baroclinic instability.

2.3.4 The sinusoidal profile

We now examine the effects of adding sinusoidal variations to a linear interface. The results are similar to those with the hyperbolic profile but there are some differences that are of interest. For this profile, we examined interfaces with values of N ranging from 1 to 3 and velocity deviations ranging from -50% to 50% but for brevity we only present the results for nine interfaces with $N = 1$, 2 or 3 and maximal velocity deviations of 10%, 20% or 30%. These velocity profiles are shown in Figure 2.11. We do not show the results for negative velocity deviations as there is symmetry in the results for positive and negative velocity deviations at least for the cases we considered. We believe that the symmetry in the results for sinusoidal profiles is due to the symmetry in the top and bottom layers that is present.

Figure 2.12 presents contour plots for the most unstable growth rates for the nine different sinusoidal profiles we consider. We use the same contour intervals as we did in the linear case and in the hyperbolic tangent cases. Here the green lines again show the critical threshold for the necessary condition for inertial instability. Unlike the hyperbolic tangent interfaces, each of these fronts is potentially inertially unstable for some Froude numbers.

(a)

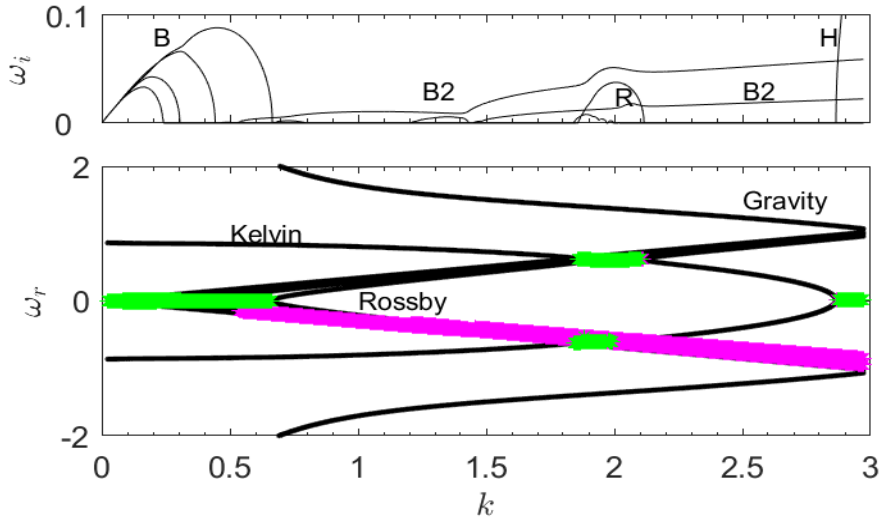

(b)

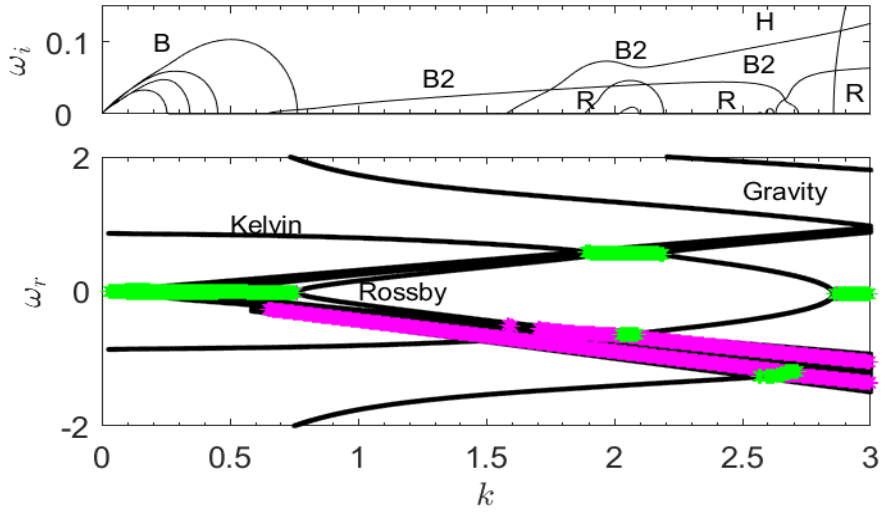

Figure 2.10: The dispersion curves and growth rates for the $\tilde{\eta}_T(y; -0.1, 10)$ interface (a), and the $\tilde{\eta}_T(y; 0.3, 10)$ interface (b). The data for these curves was taken along the line $F = k/3$. The top plots show the two largest growth rates with labels indicating the various types of instabilities, B for the baroclinic instability, R for Rossby-Kelvin instability, H for Kelvin-Helmholtz instability and B2 for the new baroclinic instability. The bottom plots show the phase speed. Here we label the types of modes and mark the phase speeds of growing modes with green asterisks for the B, R and H modes and magenta asterisks for the B2 modes.

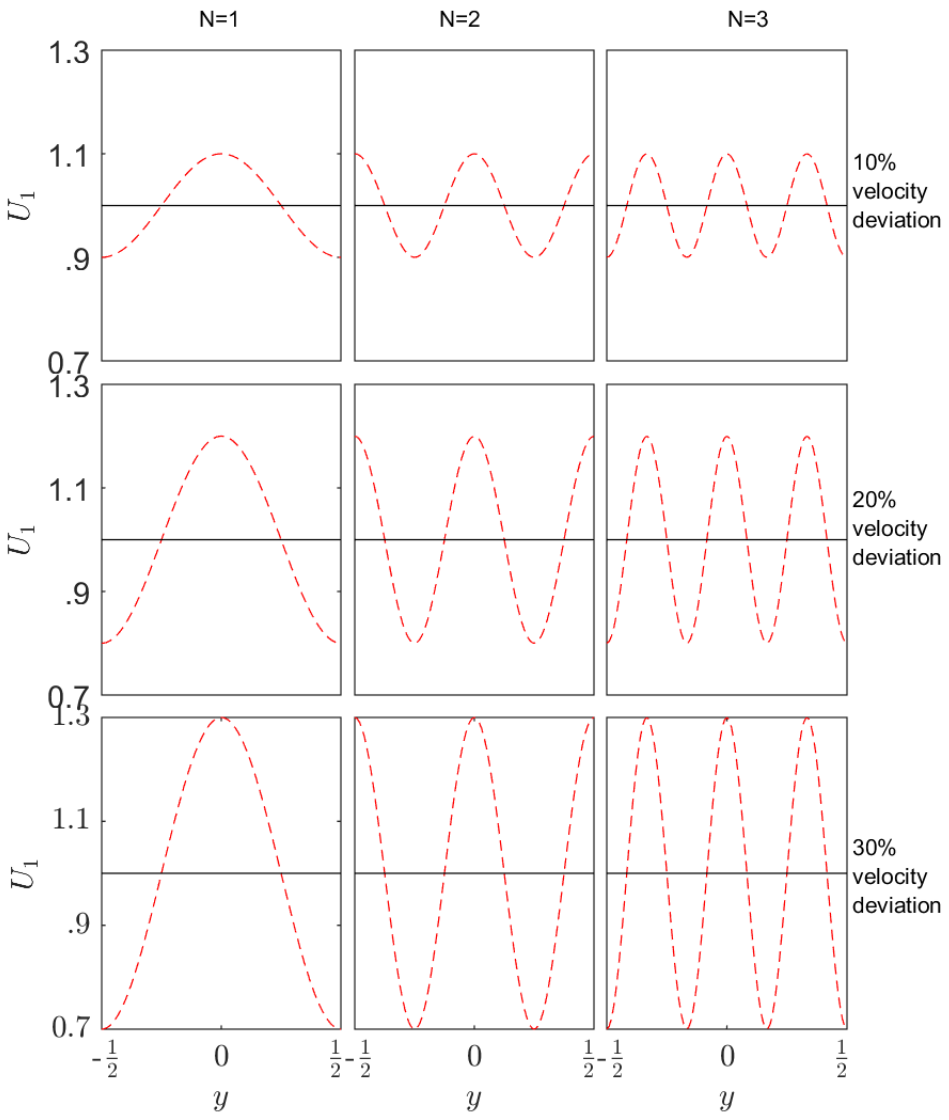

Figure 2.11: The background jets that to the sinusoidal interfaces we examine in Section 2.3.4. Here the parameters for the background jets are listed on the top and right of the figures.

The critical parameters for baroclinic instability, region (a), do not seem to be strongly affected by changes to the interface. Generally, as v increases and as N decreases, the maximal growth rate for baroclinic instability increases slightly.

The critical Froude number required for the Kelvin-Helmholtz instability increases with the maximum velocity. This change to the parameters for Kelvin-Helmholtz instability is caused by Doppler shifting of the Kelvin waves. As we saw before, the critical value seems to be independent of the wavenumber.

The Rossby-Kelvin instability, regions (c) and (d), are also affected by the presence of oscillations in the interface, however the new vertically curved-interface baroclinic instability tends to drown out the Rossby-Kelvin instabilities as we saw previously. Focusing on the (c) region, we see that as v increases the range of unstable Froude numbers increases and as the frequency increases the (c) region is overshadowed by the (e) region. Finally, the (d) region of Rossby-Kelvin instability intensifies as v or the frequency increases. In particular in the $N = 2$ and $N = 3$ plots for a 30% velocity deviation, the (d) region of Rossby-Kelvin instability approaches 0.6 which is larger than some of the Kelvin-Helmholtz instability growth rates.

We now examine the vertically curved-interface baroclinic instability region (e). As the wavelength of the interface perturbation decreases, the vertically curved-interface baroclinic instability exists for larger ranges of Froude numbers. It is notable that in the case of the mode 2 and 3 profiles, the vertically curved-interface baroclinic instability causes the front to be unstable for all values of F. Furthermore, decreasing the wavelength of the interface leads to an increase in the range of Froude numbers for which the new vertically curved-interface baroclinic instability exists.

Figures 2.13a and 2.13b show the growth rates and the frequencies for the $\tilde{\eta}_S(y; 0.2, 1)$ and $\tilde{\eta}_S(y; 0.1, 3)$ profiles respectively. In the top plots, we show the growth rate and label the types of modes by B, R, H and B2 for the baroclinic, Rossby-Kelvin, Kelvin-Helmholtz and the vertically curved-interface baroclinic instability respectively. As we saw previously in the hyperbolic tangent profile, the symmetry that was found in the case of a linear profile is no longer present. The analysis we applied for the hyperbolic profiles is still applicable, so to be concise we refer to our previous analysis. To this effect, the general behaviour of the baroclinic, Rossby-Kelvin and Kelvin-Helmholtz instabilities is unchanged from what we saw with the hyperbolic tangent profile and the vertically curved-interface baroclinic instability exists within regions where only vertically curved-interface Rossby waves can resonate. As one would expect, there are more Rossby waves that can resonate as the frequency of the sinusoidal profile increases. Unlike in the case of the hyperbolic tangent profiles, the fastest Rossby-Kelvin modes have growth rates larger than the vertically

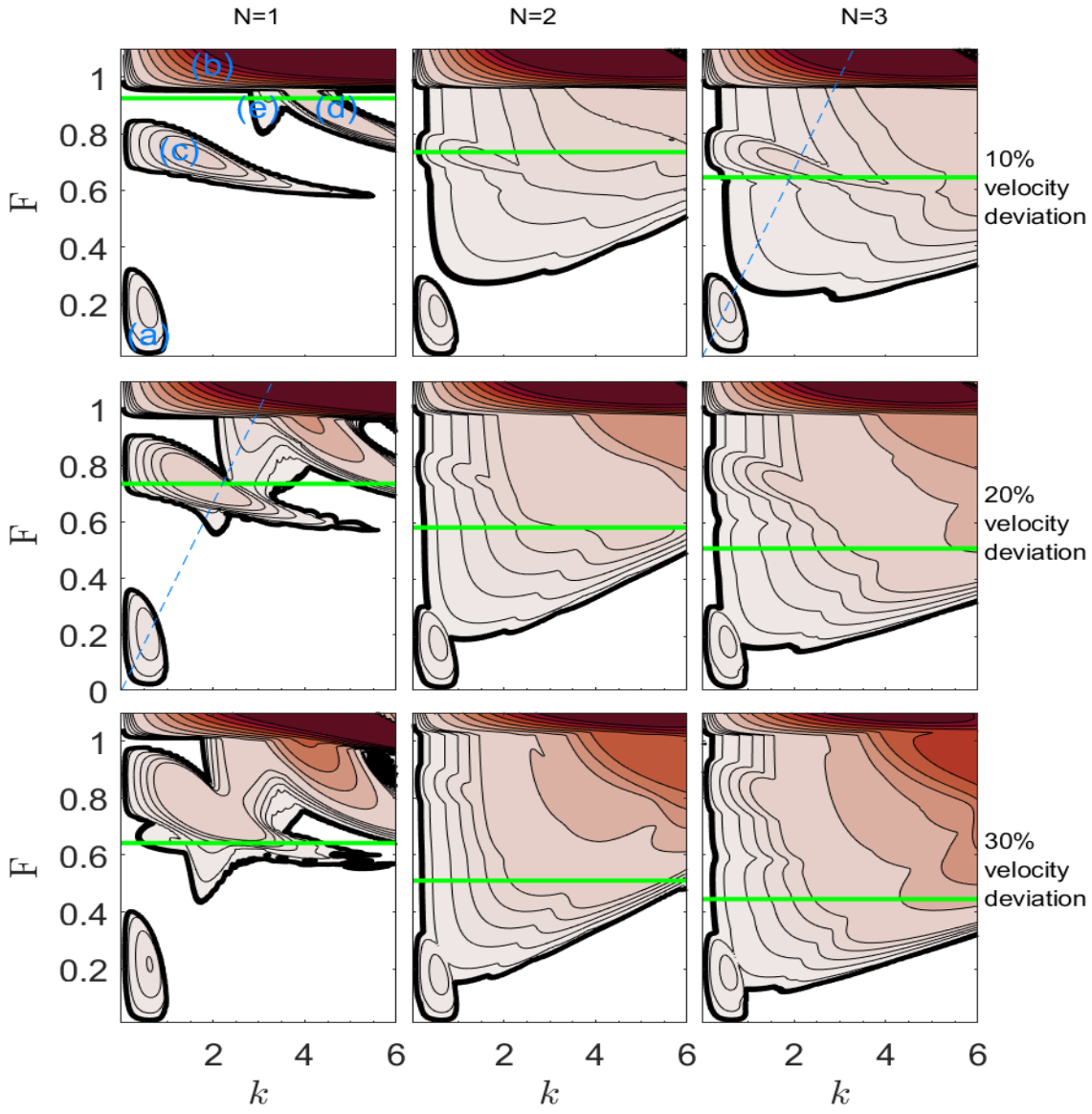

Figure 2.12: Contour plots for the growth rates for various sinusoidal profiles. From left to right the frequency increases from $N = 1$ to $N = 3$ and from top to bottom the v parameter is 10%, 20% and 30%. Here the contours and colorbars are the same as those in Figure 2.5. The growth rates along the blue lines are examined in detail later. The labels (a)-(d) correspond to the regions in Figure 2.5. The green lines show the minimum Froude numbers for which the fronts could potentially be unstable to inertial instabilities.

curved-interface baroclinic instability and can thus still be the dominant instability with curved interfaces.

Since the sinusoidal fronts are potentially unstable to II for a wide range of Froude numbers it is difficult to rule out the possibility that some of the instabilities in the (e) region are inertial modes. Nevertheless, for all of the fronts we considered there are unstable modes that do not satisfy the necessary condition for II and are thus not inertial modes. Furthermore, from the dispersion curves we can conclude that the new instability corresponds to resonating vertically curved-interface Rossby waves. There is also a continuous change in the growth rates and dispersion curves where the front becomes potentially inertially unstable. We thus do not expect any of the modes to be II but ruling out the possibility is beyond the scope of this thesis.

2.4 Conclusion

The linear stability of vertically curved fronts in channels has been examined via a two-layer SW model. We explored the effects of the choice of boundary conditions thereby partially addressing the open question left by GPZ about the applicability of the channel model to the open ocean. We then explored the effects of curvature on the stability properties of a front with closed boundaries and showed that curvature introduces a novel baroclinic instability we have named the vertically curved-interface baroclinic instability.

Comparing the previous models on linear fronts by Sakai [75], GPZ, Orlanski [58] and Iga [34], we found that when applying the methods of Sakai [75] and GPZ to the case of vanishing layer depths, the use of no-normal flow boundary conditions leads to the loss of a baroclinic mode that is present in fronts with radiation boundary conditions. Fortunately, the extra baroclinic mode that exists in the open boundary model tends to have smaller growth rates than other baroclinic modes that exist for larger wavenumbers. Despite this, the use of no-normal flow boundary conditions reduces the growth rates of all the modes and as a result the change from an open boundary model to a closed boundary model results in slower growing modes. Thus the open question left by GPZ about the applicability of the channel model to the open ocean has been partially addressed. In comparing the results of the model by GPZ with that of Iga [34] with no-normal flow boundary conditions, we see that with the exception of some differences in growth rates for small Froude numbers, the models produce very similar results. Thus, the models of GPZ and Iga [34] are comparable when applied to the same physical system.

We found the most significant difference between linear fronts to nonlinear fronts is the addition of a new vertically curved-interface baroclinic instability which is caused by the

(a)

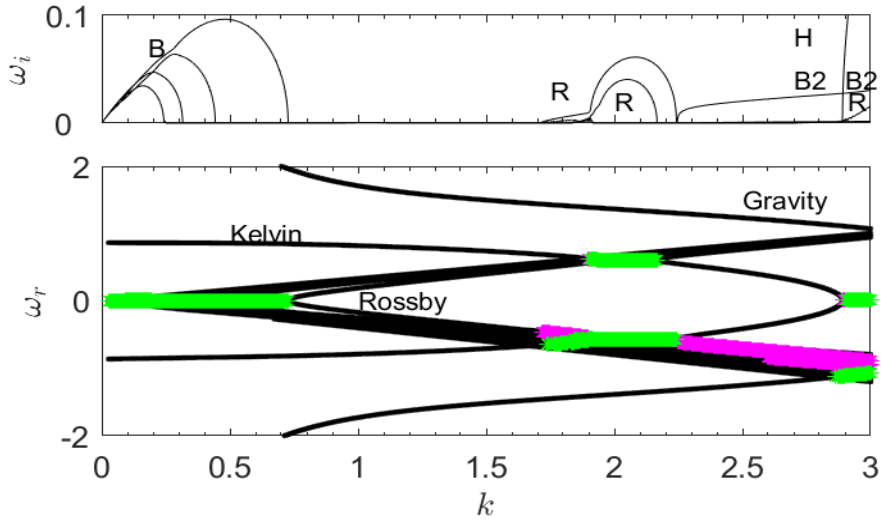

(b)

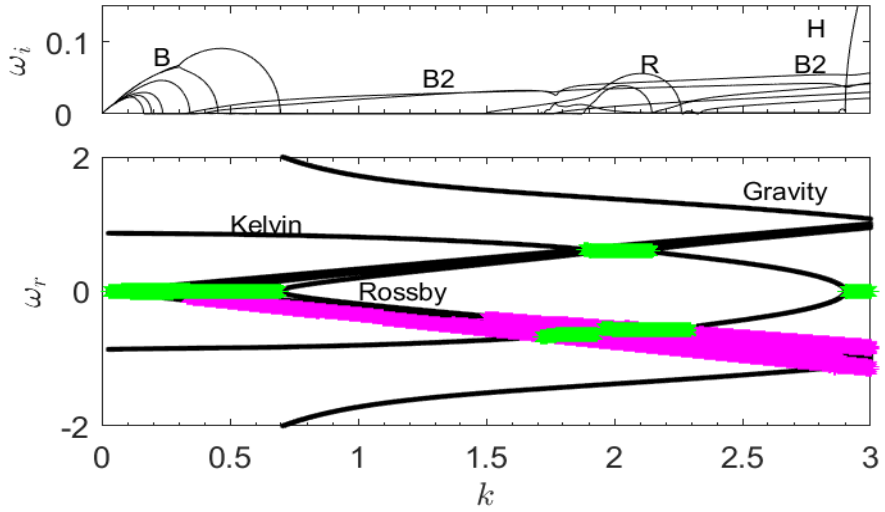

Figure 2.13: The dispersion curves and growth rates for the $\tilde{\eta}_S(y; 0.2, 1)$ interface (a), and the $\tilde{\eta}_S(y; 0.1, 3)$ interface (b). The data for these curves was taken along the line $F = k/3$. The top plots show the two largest growth rates with labels indicating the various types of instabilities, B for the standard baroclinic instability, R for Rossby-Kelvin instability, H for Kelvin-Helmholtz instability and B2 for the new baroclinic instability. The bottom plots show the phase speed. Here we label the types of modes and mark the phase speeds of growing modes with green asterisks for the B, R and H modes and magenta asterisks for the B2 modes.

resonance of vertically curved-interface Rossby waves. This new instability is important because it exists for a large range of Froude numbers and it can have relatively large growth rates. In fact, perturbing a linear front by mode two or three sinusoidal waves results in a front that is unstable for most Froude numbers. Thus the previous result that there are ranges of Froude numbers where the flow is stable may not hold even for moderate deviations from a linear front. One could expect 2-layer geophysical fronts to be unstable for most Froude numbers unlike what the theory for linear fronts predicts.

While the change to curved interfaces does not seem to modify the underlying cause of the Rossby-Kelvin, Kelvin-Helmholtz or baroclinic instabilities it does change the parameters for which the Rossby-Kelvin and Kelvin-Helmholtz instabilities exist. Generally, the baroclinic instabilities do not seem to be strongly affected by changes to the interface. The conclusion from Iga [34] that the most unstable mode is geostrophic if $F < 1$ and $k < 1$ (i.e. $Ri > 1$ in Iga's framework) and a Kelvin-Helmholtz type instability if $F > 1$ or $k > 1$ (i.e. $Ri < 1$ in Iga's framework) is not true for curved interfaces. The $\tilde{\eta}_T(y; -0.1, 10)$ interface provides an example where the cutoff is a larger Froude number and the $\tilde{\eta}_T(y; 0.3, 10)$ interface provides an example where the cutoff is a smaller Froude number. This means that in geophysical situations, there can be relevant Rossby-Kelvin type instabilities for larger Froude numbers than Iga's work predicts. Finally, our analysis of the hyperbolic tangent profiles showed that the Rossby-Kelvin instabilities can be replaced by a faster growing vertically curved-interface baroclinic instability.

Future expansions of this work include examining the effects of continuous stratification on the critical parameter cutoffs for various instabilities [79, 26, 86], examining how continuous stratification affects the spatial structures of the unstable modes [86, 79], adapting the model to allow for topography along with a curved interface [13], and formulating the appropriate interface perturbation boundary conditions to allow our more general model to use the radiating boundary conditions considered in Orlanski [58] and Iga [34]. Open questions include how the E mode that is present in models with an open boundary condition is affected by changes to the interface and how an open interface would modify the new baroclinic instability.

Chapter 3

Background for Inertial Instability

In Chapter 2 we focused on two-layer fronts that were potentially unstable to inertial instabilities for sufficiently large Froude numbers. We now focus on the inertial instabilities of barotropic Bickley jets and baroclinic Bickley jets that have a Gaussian structure in the vertical direction and a background linear stratification. We start by presenting some relevant background in Sections 3.1-3.4. This is followed by the derivation of eigenvalue problems for the linear stability analysis for both of the jets we consider in Section 3.5. Our eigenvalue problem for the barotropic jet differs from the eigenvalue problems studied by Carnevale et al. [9] and Ribstein et al. [73] due to our inclusion of a background linear stratification and our inclusion of viscous terms in the horizontal directions respectfully. The eigenvalue problem for our barotropic jet is much more computationally expensive to solve than the eigenvalue problem for the barotropic jet and to our knowledge has not been previously studied. In Chapter 4, we introduce the numerical methods we use. We start by introducing the methods we use to numerically solve each eigenvalue problem and then we introduce SPINS [83], the numerical model we use for 2D and 3D nonlinear simulations. In Chapter 5 we present the results of the linear stability analysis as well as numerical simulations for three particular parameter sets similar to those previously studied by Ribstein et al. [73], Dewar et al. [16] and Capet et al. [6]. This is followed by the results of a parameter study for most of the nondimensional parameters that appear in our governing equations.

3.1 Governing Equations and Background States

For linear stability theory to be applicable to our jets, we must consider exact solutions to the governing equations. While jet-like exact solutions to the inviscid Navier-Stokes equations are well known and have been considered extensively in the literature [7, 54, 55, 73, 98], without viscosity inertially unstable jets undergo an ultraviolet catastrophe [9, 43, 73]. On the other hand if we consider the viscous Navier-Stokes equations, exact jet like solutions are hard to come by. Previous studies have applied linear stability analysis to the viscous Navier-Stokes equations with a background jet that was a solution to the inviscid equations [7, 54, 55, 73, 98]. Instead of taking this approach, we first pick a steady state solution to the inviscid incompressible Navier-Stokes equations under the Boussinesq and f-plane approximations along with a thermodynamic equation of state [91]. We then compute the forcing terms that need to be added to the viscous equations so that our steady state solution also solves the forced viscous equations

$$\frac{D\vec{u}}{Dt} + \vec{f} \times \vec{u} = -\nabla\Phi + b\hat{z} + \nu\nabla^2\vec{u} - \nu\nabla^2\bar{\vec{u}}, \tag{3.1}$$

$$\nabla \cdot \vec{u} = 0, \tag{3.2}$$

$$\frac{Db}{Dt} = \kappa\nabla^2 b - \kappa\nabla^2\bar{b}. \tag{3.3}$$

Here $\vec{u} = \langle u, v, w\rangle$ is the velocity field in the two horizontal directions and vertical direction respectively, Φ is the pressure divided by reference density ρ_0, $b = -g\rho/\rho_0$ is the buoyancy where g is the gravitational constant and ρ is the density, $\vec{f} = f\hat{z}$ where f is the traditional Coriolis parameter and $\hat{z}$ is the vector that points in the upward direction, ν is the constant eddy viscosity, κ is the eddy diffusivity constant, $D/Dt = \partial_t + \vec{u}\cdot\nabla$ is the total (material) derivative, and $\bar{\vec{u}} = \langle \bar{u}, \bar{v}, \bar{w}\rangle$ and $\bar{b}$ are our aforementioned steady state solution to the inviscid equations. For boundary conditions, we apply free slip conditions.

If $\bar{\vec{u}}$ and $\bar{b}$ are solutions to the conservative version of equations (3.1)-(3.3) (i.e. equations (3.1)-(3.3) when ν and κ are both zero), then they are also solutions to equations (3.1)-(3.3). Thus we can use any exact solution to the conservative versions of equations (3.1)-(3.3) as a background state for our stability problems. We mention that at least for the cases we consider, the dynamical effects of the forcing terms in equations (3.1)-(3.3) are minor. Finally, we decompose the pressure and buoyancy fields as

$$\Phi = \Phi_0(z) + \hat{\Phi}(x, y, z, t) \qquad \text{and} \qquad b = b_0(z) + \hat{b}(x, y, z, t). \tag{3.4}$$

In this decomposition we are free to choose how to define $b_0(z)$ and $\Phi_0(z)$. For our background buoyancy field, $b_0(z)$, we assume a stable linear background stratification

$$-\frac{db_0(z)}{dz} = N^2 > 0 \tag{3.5}$$

where N is a constant known as the Brunt-Väisälä frequency. The background pressure field, $\Phi_0(z)$, is in hydrostatic balance with $b_0(z)$. Algebraically this relation is expressed by

$$\frac{d\Phi_0}{dz} = b_0(z). \tag{3.6}$$

We now can define the structure of the jets we consider by

$$\bar{u} = \bar{u}(y,z), \qquad \bar{v} = 0, \qquad \bar{w} = 0, \qquad \bar{b} = b_0(z) + \hat{b}(y,z), \qquad \bar{\Phi} = \Phi_0(z) + \hat{\Phi}(y,z), \tag{3.7}$$

where $\bar{u}(y,z)$ is the background velocity profile of some jet in the x direction, and $\hat{b}(y,z)$ and $\hat{\Phi}(y,z)$ are chosen to satisfy the geostrophic and hydrostatic relations

$$-f\bar{u} = \partial_y\hat{\Phi} \quad \text{and} \quad \partial_z\hat{\Phi} = \hat{b}$$

which together imply thermal wind balance

$$\partial_y\hat{b} = -f\partial_z\bar{u}.$$

With our assumptions on the buoyancy and pressure fields, equation (3.7) is a solution to the conservative version of system (3.1)-(3.3). This means that our background state given in equation (3.7) is an exact solution to system (3.1)-(3.3) as long as the forcing terms are given by the background state in equation (3.7).

If the background velocity $\bar{u}(y,z)$ is given, then geostrophic and hydrostatic balance along with the definitions of $b_0(z)$ and $\Phi_0(z)$ permit us to write equation (3.7) in the form

$$\bar{u} = \bar{u}(y,z), \qquad \bar{v} = \bar{w} = 0, \qquad \bar{b} = N^2 z - f\int \partial_z\bar{u}\, dy, \qquad \bar{\Phi} = \frac{N^2}{2}z^2 - f\int \bar{u}\, dy. \tag{3.8}$$

In this thesis we consider two classes of jets, barotropic and baroclinic jets. The barotropic jets we consider are Bickley jets of the form

$$\bar{u}_{BT}(y;U,L) = U\text{sech}^2\left(\frac{y}{L}\right), \tag{3.9}$$

where U is the maximum velocity of the jet and L is the characteristic horizontal length scale of the jet. We choose Bickley jets because they are a common idealization of geophysical jets [15, 73, 79]. A sample of this profile is given in Figure 3.1a.

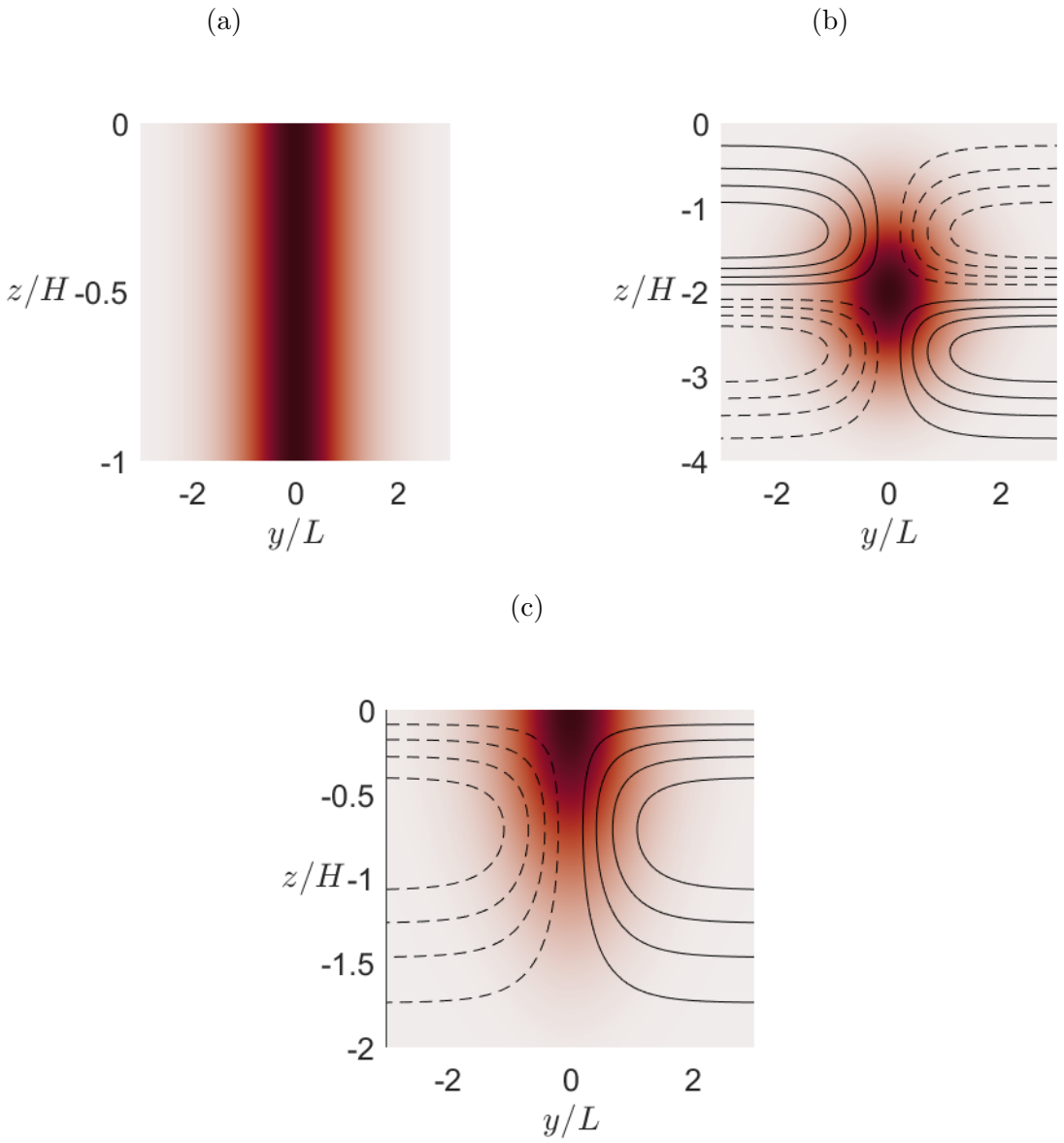

Figure 3.1: Sample plots for the velocity profiles u for the background jets we consider. Plot (a) is a sample barotropic Bickley jet, plots (b) and (c) are samples of interior and surface baroclinic jets respectively. The colorbar is chosen so that white represents no velocity while the darkest red is the maximum velocity. In the baroclinic cases, we plot isolines of the thermal wind part of the buoyancy field with solid contours for positive values and dashed contours for negative values respectfully.

For our study of baroclinic jets we use the velocity profile

$$\bar{u}_{BC}(y,z;U,L,H,D) = U\text{sech}^2\left(\frac{y}{L}\right)e^{\frac{-(z-D)^2}{H^2}} \tag{3.10}$$

where U is the maximum velocity of the jet, H and L are the characteristic vertical and horizontal length scales of the jet respectively, and D is the mid-depth of the jet. The choice of a vertical Gaussian profile for the jet is a common idealization of geophysical jets [52, 73, 79]. The inclusion of D allows the study of jets at any distance from the surface. Samples of an interior and surface baroclinic velocity profile along with contours of the corresponding thermal wind buoyancy profiles are given in Figures 3.1b and 3.1c respectively. In our work we restrict our analysis to the stability of the barotropic and interior baroclinic jet.

3.2 Nondimensional Formulation

In its current dimensional form the governing system of equations (3.1)-(3.3) depend on several dimensional quantities. We can nondimensionalize the system to decrease the number of parameters and significantly simplify our stability analysis. It is well known that the unforced version of equations (3.1)-(3.3) can be written in terms of five nondimensional parameters [48, 91]. The additional forcing terms will increase this number unless we use the same scalings for the velocity fields $\bar{u}$ and u and also the same scalings for the buoyancy fields $\bar{b}$ and b. For our current work, the initial state is given by the background state plus some small perturbation so we can use the same scalings with the linear regime.

To nondimensionalize the system (3.1)-(3.3), we use the scalings given in Table 3.1. Here, L is the characteristic width of the jet, H for barotropic jets is the total water depth and the characteristic height of the jet for the baroclinic jets, U is the maximum velocity of the jet, f is the Coriolis parameter, ν is the eddy viscosity and κ is the eddy diffusivity. We choose different scales for the horizontal and vertical lengths, an advective scale for time, and a geostrophic scaling for the pressure term. Different length scales for the vertical and horizontal directions are chosen because the horizontal and vertical scales in large scale flows typically differ. For our scaling for w, we choose not to use the traditional impressionable scaling UH/L but instead include the geostrophic scaling [63]. We now

Variable/Parameter	Scale
x and y	L
z	H
u, $\bar{u}$ and v	U
t	$\frac{L}{U}$
f	f
b and $\bar{b}$	$\frac{fUL}{H}$
w	$\frac{UH}{L}\left(\frac{fU^2}{N^2H}\right)$
Φ	fUL
ν	ν
κ	κ

Table 3.1: The scales we pick for the physical variables to nondimensionalize equations (3.1)-(3.3). The scales for b, $\bar{b}$, w and Φ are chosen based on the dynamics of equations (3.14), (3.13) and (3.11) respectively.

write the governing equations (3.1)-(3.3) in the form

$$\frac{D_h\vec{u}_h}{Dt} + w\partial_z\vec{u}_h + (\vec{f}\times\vec{u})_h = -\nabla_h\Phi + \nu\nabla_h^2(\vec{u}_h - \vec{\bar{u}}_h) + \nu\partial_{zz}(\vec{u}_h - \vec{\bar{u}}_h), \tag{3.11}$$

$$\frac{D_h\vec{w}}{Dt} + w\partial_z w = -\partial_z\Phi + b + \nu\nabla_h^2 w + \nu\partial_{zz}w, \tag{3.12}$$

$$\nabla_h\cdot\vec{u}_h + \partial_z w = 0, \tag{3.13}$$

$$\frac{D_h b}{Dt} + w\partial_z b = \kappa\nabla_h^2(b-\bar{b}) + \kappa\partial_{zz}(b-\bar{b}). \tag{3.14}$$

where $\vec{u}_h = \langle u, v\rangle$, $\vec{\bar{u}}_h = \langle\bar{u}, 0\rangle$, $\nabla_h = \langle\partial_x, \partial_y\rangle$, $\nabla_h^2 = \nabla_h\cdot\nabla_h$, and $D_h/Dt = \partial_t + \vec{u}_h\cdot\nabla_h$.

Under the scalings in Table 3.1, system (3.11)-(3.14) becomes

$$\frac{U^2}{L}\frac{D_h\vec{u}_h}{Dt}+\frac{fU^3}{N^2H^2}w\partial_z\vec{u}_h+fU(\hat{z}\times\vec{u})_h= \\ -fU\nabla_h\Phi+\frac{\nu U}{L^2}\nabla_h^2(\vec{u}_h-\bar{\vec{u}}_h)+\frac{\nu U}{H^2}\partial_{zz}(\vec{u}_h-\bar{\vec{u}}_h), \tag{3.15}$$

$$\frac{fU^3}{N^2HL}\frac{D_h\vec{w}}{Dt}+\frac{f^2U^4}{N^4H^5}w\partial_z w \\ =-\frac{fUL}{H}\partial_z\Phi+\frac{fUL}{H}b+\frac{\nu fU^2}{N^2L^2H}\nabla_h^2 w+\frac{\nu fU^2}{N^2H^3}\partial_{zz}w, \tag{3.16}$$

$$\frac{U}{L}\nabla_h\cdot\vec{u}_h+\frac{fU^2}{N^2H^2}\partial_z w=0, \tag{3.17}$$

$$\frac{fU^2}{H}\frac{D_hb}{Dt}+\frac{f^2U^3L}{N^2H^3}w\partial_z b=\frac{\kappa fU}{HL}\nabla_h^2(b-\bar{b})+\frac{\kappa fUL}{H^3}\partial_{zz}(b-\bar{b}), \tag{3.18}$$

where all variables are nondimensional and $\hat{z}$ is the unit vector in the vertical direction. We now divide equation (3.15) by fU, multiply equation (3.16) by $H/(fUL)$, multiply equation (3.17) by L/U and multiply equation (3.18) by $H/(fU^2)$ to obtain the nondimensional equations

$$\mathrm{Ro}\left(\frac{D_h\vec{u}_h}{Dt}+\mathrm{Bu}\ \mathrm{Ro}\ w\partial_z\vec{u}_h\right)+(\hat{z}\times\vec{u})_h \\ =-\nabla_h\Phi+\frac{\mathrm{Ro}}{\mathrm{Re}}\left(\nabla_h^2(\vec{u}_h-\bar{\vec{u}}_h)+\frac{1}{\delta^2}\partial_{zz}(\vec{u}_h-\bar{\vec{u}}_h)\right), \tag{3.19}$$

$$\left(\frac{\delta\mathrm{Ro}}{\mathrm{Bu}}\right)^2\left(\frac{D_h\vec{w}}{Dt}+\mathrm{Ro}\ w\partial_z w\right) \\ =-\partial_z\Phi+b+\frac{\mathrm{Ro}^2}{\mathrm{Re}\ \mathrm{Bu}}\left(\delta^2\nabla_h^2 w+\nu\partial_{zz}w\right), \tag{3.20}$$

$$\nabla_h\cdot\vec{u}_h+\frac{\mathrm{Ro}}{\mathrm{Bu}}\partial_z w=0, \tag{3.21}$$

$$\frac{D_hb}{Dt}+\frac{\mathrm{Ro}}{\mathrm{Bu}}w\partial_z b=\frac{1}{\mathrm{Pr}\ \mathrm{Re}}\left(\nabla_h^2(b-\bar{b})+\frac{1}{\delta}\partial_{zz}(b-\bar{b})\right), \tag{3.22}$$

where

$$\mathrm{Ro}=\frac{U}{fL},\qquad \mathrm{Re}=\frac{UL}{\nu},\qquad \mathrm{Bu}=\left(\frac{NH}{fL}\right)^2,\qquad \delta=\frac{H}{L},\qquad \text{and}\qquad \mathrm{Pr}=\frac{\nu}{\kappa}, \tag{3.23}$$

are the Rossby number, Reynolds number, Burger number, aspect ratio, and Prandtl number respectively [15, 91, 94]. In our later work we only consider the case with Pr$=\infty$.

The stability properties of our jets are a function of our choice of free slip boundary conditions, these parameters and the horizontal lengths and vertical height of the fluid domain, denoted L_x, L_y, and L_z respectfully. Our linear stability calculations do not depend on L_x but we must specify a length in our nonlinear simulations. We choose values of L_x that allow the most unstable modes as predicted by linear theory to fit in the domain of the various nonlinear simulations we consider. In the cross channel direction, we minimize the effect of the boundary conditions by letting L_y be sufficiently large so that the flow vanishes at the boundaries. Finally our choice for L_z depends on the jet we consider. For the barotropic jets, we use $L_z = H$ whereas for the interior baroclinic jets we choose L_z to be sufficiently large so that the flow at the vertical boundaries vanish.

The eigenvalue problems we derive in Section 3.5 depends on wavenumbers k and m and eigenvalues ω. When applicable, we nondimensionalize these as follows

$$\tilde{\omega} = \frac{\omega}{f}, \qquad \tilde{k} = \mathrm{Rd}\, k \qquad \text{and} \qquad \tilde{m} = Hm$$

where $\mathrm{Rd} = NH/f$ is the Rossby deformation radius.

Finally, instead of working with the nondimensional system directly, in our subsequent work we consider the dimensional equations (3.1)-(3.3) but use the nondimensional numbers in equation (3.23) along with some reference values for L and f, to define the needed dimensional parameters. We remind the reader that as long as the nondimensional parameters are the same, the choice of L and f have no effect on the dynamics of the system. With the nondimensional parameters given and values for L and f chosen, the rest of the dimensional parameters are computed via

$$U = f\mathrm{Ro}L, \qquad H = \delta L, \qquad N = \frac{f\sqrt{\mathrm{Bu}}}{\delta}, \qquad \nu = \frac{f\mathrm{Ro}L^2}{\mathrm{Re}}, \qquad \kappa = \frac{f\mathrm{Ro}L^2}{\mathrm{RePr}}. \tag{3.24}$$

3.3 Conditions for Instability

In our work, we wish to only examine flows that are both stable to Rayleigh Taylor instability and inertially unstable. To determine the nondimensional parameters that have this property, we apply well known criteria for Rayleigh Taylor (gravitational) instability and II to the jets we consider. Previous studies have shown that our jets can also be unstable to barotropic or baroclinic instabilities with growth rates that can be smaller, comparable or even larger than the growth rate of the fastest growing inertial mode [9, 69, 73]. We thus apply the necessary conditions for barotropic and baroclinic instability to determine if the jets are potentially unstable to these instabilities.

3.3.1 Rayleigh Taylor Instability (RTI)

RTI occurs when density decreases with fluid depth. For a flow with total buoyancy field b, a sufficient condition for a flow to be stable to RTI is that

$$\partial_z b \geq 0, \tag{3.25}$$

everywhere within the flow [48]. To determine the linear stability of the jets we consider, we find the nondimensional parameters such that condition (3.25) holds for our steady background buoyancy fields $\bar{b}$.

Barotropic jets: Since the buoyancy field for this case is the background linear stratification, N^2, the condition for a flow to be stable to RTI is $\partial_z \bar{b} = N^2 \geq 0$.

Baroclinic jets: Substituting equation (3.10) into equation (3.8), the condition for a flow to be stable to RTI is

$$\partial_z \bar{b} = N^2 - \frac{2ULf}{H^2}\left(\frac{2(z-D)^2}{H^2} - 1\right) e^{\frac{-(z-D)^2}{H^2}} \tanh\left(\frac{y}{L}\right) \geq 0.$$

As we only consider $N^2 \geq 0$, the above condition for stability holds when

$$N^2 \geq \frac{2ULf}{H^2} \max_{y,z}\left(\left(\frac{2(z-D)^2}{H^2} - 1\right) e^{\frac{-(z-D)^2}{H^2}} \tanh\left(\frac{y}{L}\right)\right),$$

where the maximum is taken over all values of y and z. This maximum is equal to one and occurs when $z = D + H\sqrt{6}/2$ and $y \to -\infty$. Thus, given that our domain is sufficiently wide, the baroclinic jets are stable to RTI whenever

$$N^2 \geq \frac{2ULf}{H^2}.$$

In terms of our nondimensional parameters the condition for stability becomes

$$\mathrm{Bu} \geq 2\,\mathrm{Ro}. \tag{3.26}$$

Thus for any Rossby number there is a minimum Burger number for the flow to be stable to RTI. This region is shown in Figure 3.2b.

3.3.2 Inertial Instability (II)

II occurs when the horizontal adiabatic transport of a fluid parcel leads to a situation where the Coriolis force acting on the parcel is greater than the restoring force provided by the pressure gradient of the surrounding fluid[15]. This imbalance then causes the parcel to be transported further from its initial position[15]. A well known necessary condition for II is that the product of the Coriolis parameter and the Ertel potential vorticity (EPV) of the flow is negative somewhere[15, 94]. Algebraically, this condition is that

$$(\vec{\omega} + \vec{f}) \cdot \nabla b < 0, \tag{3.27}$$

where $\vec{\omega} + \vec{f}$ is the total vorticity and $\vec{\omega} = \nabla \times \vec{u}$ is the relative vorticity, holds somewhere within the flow. For flows with the functional form given in equation (3.8), the necessary condition (3.27) simplifies to

$$(f - \partial_y \bar{u}) \left(N^2 - f \int \partial_{zz} \bar{u} \partial y \right) - f(\partial_z \bar{u})^2 < 0. \tag{3.28}$$

This condition agrees with the expressions found by Hoskins [31] and Hua et al. [33] when we simplify the β-plane to an f-plane.

Before examining the conditions for II for the particular jets we consider, we briefly mention that the nonlinear saturation of II mixes the EVP field of the fluid through non-conservative processes. The end result is a modified flow that is stable to II.

Barotropic jets: For the barotropic jet given in equation (3.9) we have $\partial_z \bar{u} = 0$ and thus condition (3.28) simplifies to the condition that $N^2(f - \partial_y \bar{u})$ is negative somewhere in the flow. As we only consider stably stratified flows, $N^2 > 0$ and the necessary condition for II simplifies to $f < \partial_y u$. Physically, this condition means that our barotropic jets are inertially stable whenever the relative vorticity is everywhere bounded by the Coriolis f parameter. Using the functional form of our barotropic background state, the condition for II is equivalent to

$$\begin{aligned} f &< \max_{y,z}(\partial_y(\bar{u})) \\ &= \frac{2U}{L} \max_{y,z} \left(\tanh\left(\frac{y}{L}\right) \operatorname{sech}^2\left(\frac{y}{L}\right) \right) \\ &= \frac{4\sqrt{3}U}{9L}. \end{aligned}$$

In terms of nondimensional parameters this condition is

$$\mathrm{Ro} > \frac{9}{4\sqrt{3}}. \tag{3.29}$$

Thus, there is a minimal Rossby number for the jet to be unstable to II. Yim et al. [98] found a similar result for barotropic anticyclones and anticyclones with a Gaussian profile in the vertical direction. A plot of the stability region for the barotropic jet is given in Figure 3.2a.

Baroclinic jets: We now simplify the necessary condition (3.28) for the baroclinic background state in equation (3.10). Using the nondimensional form of the baroclinic jet, equation (3.28) simplifies to

$$\left(1 + 2\mathrm{Ro}\tanh(y)\mathrm{sech}^2(y)e^{-z^2}\right)\left(\mathrm{Bu} - 2\mathrm{Ro}(2z^2-1)e^{-z^2}\tanh(y)\right) - 4\mathrm{Ro}^2 z^2 e^{-2z^2}\mathrm{sech}^4(y) < 0,$$

where y and z are now nondimensional. For the flow to be inertially unstable we thus need the minimum of the expression on the left to be less than zero somewhere within the flow. The above expression is quite complex but by using Maple [1] to minimize the left hand side of the inequality with the constraint that the flow is stable to RTI, we found that the necessary condition for instability is the same as the condition for the barotropic jet. More information on how we derived this condition is presented in Appendix B. In the case of a flow that is unstable to RTI, we have been unable to find an analytical condition for stability and hence computed the stability curve numerically. A diagram showing the various stability regions in Ro-Bu space for the baroclinic jets is shown in Figure 3.2b. We are interested in studying the white region where the flow is potentially unstable to II but stable to RTI.

3.3.3 Barotropic (BTI) and Baroclinic Instability (BCI)

As we have mentioned, previous studies have found that jets similar to the ones we consider can be unstable to barotropic instabilities (BTI) and baroclinic instabilities (BCI) [69]. We thus apply the Charney-Stern-Pedlosky necessary condition to test for the possibility that these instabilities are present for either of the jets we consider [91].

BTI condition for the barotropic jet: We begin by applying the Charney-Stern-Pedlosky necessary condition for barotropic instability to our barotropic jet. This is done by looking for changes in the sign of the y derivative of the EPV within the interior of the

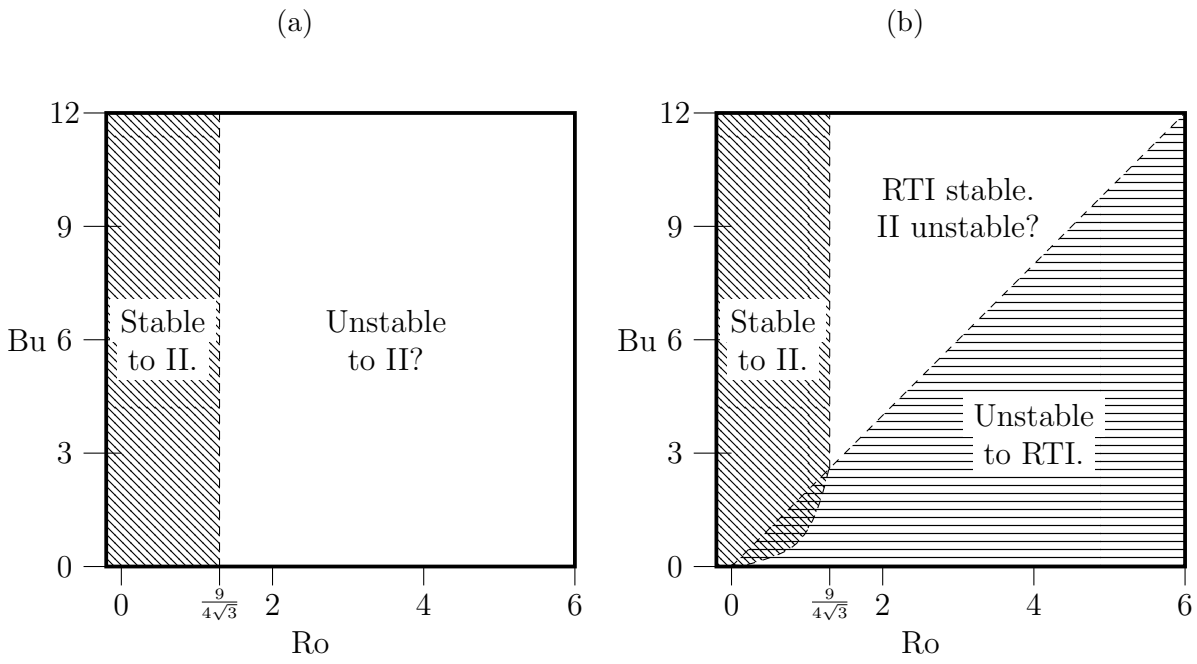

Figure 3.2: Diagrams showing the regions in Ro-Bu space that satisfy necessary conditions for II and RTI for both the barotropic jet, (a), and the baroclinic jets, (b), shown in Figure 3.1. In both diagrams, the white regions are the parameter regions that we are interested in examining. The regions shaded with diagonal lines are stable to II and the white region is stable to RTI and potentially inertially unstable.

fluid domain. For the barotropic jet, the EPV is simply the total vorticity scaled by the background linear stratification and a direct computation shows that

$$\partial_y(\text{EPV}) = N^2\partial_{yy}\bar{u}(y) = \frac{2UN^2}{L^2}\text{sech}^2\left(\frac{y}{L}\right)\left[2\tanh^2\left(\frac{y}{L}\right) - \text{sech}^2\left(\frac{y}{L}\right)\right].$$

Here, the term in square brackets changes signs at $y \approx \pm 0.6073L$ while the other terms are always positive. This means that there is a sign change in this quantity and thus the barotropic jet could be unstable to barotropic instabilities.

BTI condition for the baroclinic jet: Turning our attention to the baroclinic jet, the nontrivial stratification means that we now need to examine $\partial_y(\vec{\omega} + \vec{f})$. Evaluating this expression for the jet in equation (3.10) and simplifying yields the nondimensional expression

$$\partial_y(\text{EPV}) = \partial_y(\vec{\omega} + \vec{f}) = -4\text{Ro}^2 e^{-2z^2}\text{sech}^2(y)\left[\left(3\,\text{sech}^2(y) - 2\right)\left(2z^2 - 1\right) - \tanh(y)\right].$$

One can numerically see that the term in square brackets changes sign within our domain of interest while the other terms are positive definite. This means that our baroclinic jet is prone to barotropic instability.

BCI condition for the barotropic jet: We now apply the Charney-Stern-Pedlosky necessary condition for baroclinic instability to our barotropic jet and look for a change in the sign of $\partial_z(\text{EPV})$. Since the EPV field for the barotropic jet is constant in the vertical, it is stable to baroclinic instabilities.

BCI condition for the baroclinic jet: We finally turn our attention to the baroclinic jet and examine $\partial_z(\vec{\omega} + \vec{f})$ for the jet in equation (3.10). A direct computation yields

$$\partial_z(\text{EPV}) = -8\text{Ro}^2 e^{-2z^2}\text{sech}^2(y)\left[\tanh^2(y)(4z^4 - 6z) + \text{sech}^2(y)(-4z^3 + 2z)\right].$$

As with the previous case, the term in square brackets changes sign within our domain of interest while the other terms are positive. This means that our baroclinic current may be unstable to baroclinic instability.

The above analysis shows that our barotropic jet might be barotropically unstable and our baroclinic jet may be unstable to both barotropic and baroclinic instabilities. As we only consider jets that initially have negative EPV somewhere within the flow, we follow Wang et al. [93] and classify modes as II when the necessary condition that $f\cdot\text{EPV} < 0$ somewhere in the flow is satisfied.

3.4 Metric for Mixing Efficiency

As has been noted by Jiao and Dewar [37], II can efficiently mix the density field via a combination of local mixing during the growth phase of II and the subsequent generation of unbalanced flows due to the nonlinear saturation of II. Jiao and Dewar [37] estimate that II accounts for 10% of the loss of initial energy in a jet similar to the California undercurrent (CUC). We thus wish to examine a metric for mixing efficiency so that we can quantify it in our nonlinear simulations.

One metric for the mixing efficiency that has been used throughout the literature is the flux Richardson number [36, 37, 57, 61, 64, 96]

$$\mathrm{Ri}_f = \frac{B}{B+\epsilon}.$$

Here $B = -\overline{w'b'}$ is the turbulent buoyancy flux and $\epsilon = \overline{2\nu\left(e_{ij}e_{ij} - 1/3(e_{ii})^2\right)}$, where ν is the viscosity and $e_{ij} = 0.5(\partial_{x_j}u_i + \partial_{x_i}u_j)$ [48], is the dissipation rate due to viscous processes. The perturbation terms w' and b' are given by the Reynolds decomposition [61] and the overbar represents spatial averaging over the entire domain of the flow. Note that when computing the spatial averages we need not include the volume since they cancel when computing Ri_f. Also note that since we are using an incompressible model, the e_{ii} terms vanish in the above expression for ϵ. We choose to leave e_{ii} in the above equation as it is then applicable to a more general class of flows. The turbulent buoyancy flux is the irreversible transfer of available potential energy (APE) and kinetic energy (KE) to the background potential energy (BPE) [10, 37, 57, 64, 96]. In practice the quantities w' and b' have been approximated by perturbations with respect to the background state [37, 64] and we use this convention in our work. Finally, note that in the incompressible limit the dissipation rate is simply $\epsilon = 2\nu\overline{e_{ij}e_{ij}}$ [30, 37, 48].

We now discuss the theoretical range for Ri_f as well as typical values found in previous studies of various flows. Since the transfer of energy from APE and KE to BPE is non-reversible, $B \geq 0$. Furthermore, by definition $\epsilon \geq 0$. Thus, we have $0 \leq \mathrm{Ri}_f \leq 1$. Within this range, studies have found typical values for various instabilities. RTI is generally considered to have the largest mixing efficiency and thus provides an upper bound for the efficiencies we expect to see in our work [16, 49, 96]. In the classical example of RTI where the initial state consists of high density fluid above an equal mass of lower density fluid, the maximum the mixing efficiency is 0.5 [49]. Lawrie and Dalziel [49] and Wykes and Dalziel [96] showed that the mixing efficiency of RTI can theoretically be as large as 0.75 when one considers two layer fluids that are individually piecewise stable to RTI but unstable to RTI within some region of the middle of the fluid. This theoretical limit

for the mixing efficiency of RTI has been experimentally verified with Lawrie and Dalziel [49] finding mixing efficiencies as large as $\mathrm{Ri}_f \approx 0.56$ and Wykes and Dalziel [96] seeing mixing efficiencies of $\mathrm{Ri}_f = 0.75 \pm 0.02$. In comparison, Kelvin-Helmholtz (KH) instability, typically has a mixing efficiency between 0.2 and 0.3 with $\mathrm{Ri}_f = 0.2$ being classically used [16, 57, 61, 64]. Jiao and Dewar [37] found that the efficiency of II in a jet similar to the California Undercurrent (CUC) reached 0.35. Near the end of their simulation the efficiency continued to grow but Jiao and Dewar [37] stopped the simulation before the maximum efficiency was reached. Finally, we should mention that while Ri_f quantifies how efficiently the density field of a fluid is mixed, it does not directly quantify how efficiently the EPV field has mixed, which II does very effectively.

3.5 Linear Stability Problems

We now derive linear stability problems for the barotropic and baroclinic jets. Considering both jets allows for an examination of the differences between their stability properties which is not often considered in literature. We start by deriving eigenvalue problems for the baroclinic jet given in equation (3.7) where the Fourier decomposition of the perturbations is not made in either the y or z directions. We refer to these eigenvalue problems as the "2D eigenvalue problem". We then simplify the 2D eigenvalue problem for the barotropic jet by using a Fourier decomposition in the z direction. Physically, this additional Fourier decomposition implies that the modes are periodic in the vertical direction. We refer to this eigenvalue problem as the "1D eigenvalue problem". The 1D eigenvalue problem can be solved quickly and accurately via a direct numerical method, provides a good approximation for the results of the 2D eigenvalue problem for a barotropic jet and can be used to seed a Krylov subspace solver for the 2D eigenvalue problem for both jets.

3.5.1 2D Generalized Eigenvalue Problem

For our linear stability analysis problems, we consider system (3.1)-(3.3) under the hydrostatic approximation. By making the hydrostatic approximation, we eliminate the temporal derivatives in the z-momentum equation which simplifies the process of transforming the linear stability problems into eigenvalue problems. Physically the hydrostatic approximation is only valid when the aspect ratio is sufficiently small (*i.e.* $\delta \ll 1$). As our nonlinear simulations solve the system without the hydrostatic approximation, we expect some differences between the solutions of our eigenvalue problems and our numerical simulations for sufficiently large aspect ratios. To respect the hydrostatic approximation, we

limit our discussion of the aspect ratio to values less than 0.15. By taking the hydrostatic approximation and assuming our background state is of the form (3.7), system (3.1)-(3.3) simplifies to

$$\frac{Du}{Dt} - fv = -\partial_x \Phi + \nu \nabla^2 u - \nu \nabla^2 \bar{u}, \tag{3.30}$$

$$\frac{Dv}{Dt} + fu = -\partial_y \Phi + \nu \nabla^2 v, \tag{3.31}$$

$$\partial_z \Phi = b, \tag{3.32}$$

$$\frac{Db}{Dt} = \kappa \nabla^2 b - \kappa \nabla^2 \bar{b}. \tag{3.33}$$

$$\nabla \cdot \vec{u} = 0. \tag{3.34}$$

We now introduce perturbations to our background state via

$$u = \bar{u} + \hat{u}, \qquad v = \hat{v}, \qquad w = \hat{w}, \qquad b = \bar{b} + \hat{b}, \qquad \Phi = \bar{\Phi} + \hat{\Phi},$$

where the over-lined terms are the background state and the hatted terms are perturbations. Using the above decomposition in equations (3.30)-(3.34), dropping terms that are nonlinear with respect to the hatted terms (i.e. terms like $\hat{u}\partial_x \hat{u}$, $\hat{v}\partial_y \hat{u}$) and using the fact that the overlined terms solve the conservative equations, we obtain the linearized system

$$\partial_t \hat{u} + \bar{u}\partial_x \hat{u} + \hat{v}\partial_y \bar{u} + \hat{w}\partial_z \bar{u} - f\hat{v} = -\partial_x \hat{\Phi} + \nu \nabla^2 \hat{u}, \tag{3.35}$$

$$\partial_t \hat{v} + \bar{u}\partial_x \hat{v} + f\hat{u} = -\partial_y \hat{\Phi} + \nu \nabla^2 \hat{v}, \tag{3.36}$$

$$\partial_z \hat{\Phi} = \hat{b}, \tag{3.37}$$

$$\partial_t \hat{b} + \bar{u}\partial_x \hat{b} + \hat{v}\partial_y \bar{b} + \hat{w}\partial_z \bar{b} = \kappa \nabla^2 \hat{b}, \tag{3.38}$$

$$\nabla \cdot \vec{\hat{u}} = 0, \tag{3.39}$$

where the notation $\vec{\hat{u}}$ represents the vector of perturbation velocities. We now assume our flow is periodic in the x direction and make the Fourier decomposition

$$\langle \hat{u}, \hat{v}, \hat{w}, \hat{b}, \hat{\Phi} \rangle = e^{i(kx - \omega t)} \langle u'(y,z), v'(y,z), w'(y,z), b'(y,z), \Phi'(y,z) \rangle. \tag{3.40}$$

Under the above ansatz, the linearized system simplifies to

$$-i\omega u' + ik\bar{u}u' + v'\partial_y \bar{u} + w'\partial_z \bar{u} - fv' = -ik\Phi' + \nu(-k^2 u' + \partial_{yy} u' + \partial_{zz} u'), \tag{3.41}$$

$$-i\omega v' + ik\bar{u}v' + fu' = -\partial_y \Phi' + \nu(-k^2 v' + \partial_{yy} v' + \partial_{zz} v'), \tag{3.42}$$

$$\partial_z \Phi' = b', \tag{3.43}$$

$$-i\omega b' + ik\bar{u}b' + v'\partial_y \bar{b} + w'\partial_z \bar{b} = -\kappa(-k^2 b' + \partial_{yy} b' + \partial_{zz} b'), \tag{3.44}$$

$$iku' + \partial_y v' + \partial_z w' = 0. \tag{3.45}$$

The dependence of system (3.41)-(3.45) on z does not allow us to simplify to an eigenvalue problem in terms of Φ', u' and v' as was done by Ribstein et al. [73] when examining barotropic jets. We instead build a generalized eigenvalue problem for Φ', v' and w'. Our choice to eliminate the dependence of b' instead of Φ' was made because it results in a system with at most third derivatives as opposed to a one involving fourth derivatives. We now simplify system (3.41)-(3.45) by first solving the continuity equation (3.45) for u', substituting the solution into equations (3.41) and (3.42), and using equation (3.43) to eliminate the dependence of b' in equation (3.44). The end result is

$$\begin{aligned}
&\frac{\omega}{k}\left(\partial_y v' + \partial_z w'\right) - \bar{u}(\partial_y v' + \partial_z w') + v'\partial_y \bar{u} + w'\partial_z \bar{u} - fv' + ik\Phi' - \\
&\nu\left(\frac{k}{i}(\partial_y v' + \partial_z w') - \frac{1}{ik}(\partial_{yyy} v' + \partial_{yyz} w') - \frac{1}{ik}(\partial_{yzz} v' + \partial_{zzz} w')\right) = 0, \qquad (3.46)\\
&-i\omega v' + ik\bar{u}v' - \frac{f}{ik}(\partial_y v' + \partial_z w') + \partial_y \Phi' - \nu(-k^2 v' + \partial_{yy} v' + \partial_{zz} v') = 0, \qquad (3.47)\\
&(-i\omega + ik\bar{u} - \kappa(-k^2 + \partial_{yy} + \partial_{zz}))\partial_z \Phi' + v'\partial_{yz}^2 \bar{\Phi} + w'\partial_{zz}\bar{\Phi} = 0, \qquad (3.48)\\
&\partial_z \Phi' = b', \qquad (3.49)\\
&-\frac{1}{ik}(\partial_y v' + \partial_z w') = u'. \qquad (3.50)
\end{aligned}$$

This is a system of five equations with five unknowns, and the last two equations are decoupled from the first three. Equations (3.46)-(3.48) can be rewritten as the 2D generalized eigenvalue problem

$$\begin{aligned}
\omega\left(\partial_y v' + \partial_z w'\right) &= k\bar{u}(\partial_y v' + \partial_z w') - kv'\partial_y \bar{u} - kw'\partial_z \bar{u} + kfv' - ik^2\Phi' \\
&\quad + i\nu\left(-k^2(\partial_y v' + \partial_z w') + (\partial_{yyy} v' + \partial_{yyz} w') + (\partial_{yzz} v' + \partial_{zzz} w')\right), \qquad (3.51)\\
\omega v' &= k\bar{u}v' + \frac{f}{k}(\partial_y v' + \partial_z w') - i\partial_y \Phi' + i\nu(-k^2 v' + \partial_{yy} v' + \partial_{zz} v'), \qquad (3.52)\\
\omega\partial_z \Phi' &= (k\bar{u} + i\kappa(-k^2 + \partial_{yy} + \partial_{zz}))\partial_z \Phi' - iv'\partial_{yz}\bar{\Phi} - iw'\partial_{zz}\bar{\Phi}, \qquad (3.53)
\end{aligned}$$

which in matrix form is

$$\begin{aligned}
&\omega \begin{bmatrix} 0 & \partial_y & \partial_z \\ 0 & 1 & 0 \\ \partial_z & 0 & 0 \end{bmatrix} \begin{bmatrix} \Phi' \\ v' \\ w' \end{bmatrix} \qquad (3.54)\\
&= \begin{bmatrix} -ik^2 & k\bar{u}\partial_y - k\partial_y\bar{u} + kf + i\nu L\partial_y & k\bar{u}\partial_z - k\partial_z\bar{u} + i\nu L\partial_z \\ -i\partial_y & k\bar{u} + \frac{f}{k}\partial_y + i\nu L & \frac{f}{k}\partial_z \\ k\bar{u}\partial_z + i\kappa L\partial_z & -i\partial_{yz}\bar{\Phi} & -i\partial_{zz}\bar{\Phi} \end{bmatrix} \begin{bmatrix} \Phi' \\ v' \\ w' \end{bmatrix}.
\end{aligned}$$

In the matrix we have used $L(k,y,z) = (-k^2+\partial_{yy}+\partial_{zz})$ to represent the Laplacian in order to shorten the right hand side. By assuming that the background flow satisfies equation (3.8) where the velocity field is given by (3.9) or (3.10), the above system is a generalized eigenvalue problem for the barotropic and baroclinic jets we consider. We refer to equation (3.54) as the 2D eigenvalue problem because the perturbations we need to solve for are functions of y and z.

3.5.2 1D Eigenvalue Problem

For barotropic jets, the eigenvalue problem in equation (3.54) can be simplified to

$$\begin{aligned}\omega &\begin{bmatrix} 0 & \partial_y & \partial_z \\ 0 & 1 & 0 \\ \partial_z & 0 & 0 \end{bmatrix} \begin{bmatrix} \Phi' \\ v' \\ w' \end{bmatrix} \\ &= \begin{bmatrix} -ik^2 & k\bar{u}\partial_y - k\partial_y(\bar{u}) + kf + i\nu L\partial_y & k\bar{u}\partial_z + i\nu L\partial_z \\ -i\partial_y & k\bar{u} + \frac{f}{k}\partial_y + i\nu L & \frac{f}{k}\partial_z \\ k\bar{u}\partial_z + i\kappa L\partial_z & 0 & -iN^2 \end{bmatrix} \begin{bmatrix} \Phi' \\ v' \\ w' \end{bmatrix}. \end{aligned} \tag{3.55}$$

Here we dropped the z dependence of the background jet and assumed a background linear stratification. We now transform the two dimensional generalized eigenvalue problem in equation (3.55) into a one dimensional problem for $\phi'(y)$, $u'(y)$ and $v'(y)$ by assuming that the flow is periodic in the z direction and replacing the ansatz in equation (3.40) with the ansatz

$$\langle \hat{\Phi}, \hat{w}, \hat{v} \rangle = e^{i(kx+mz-\omega t)} \langle \Phi'(y), w'(y), v'(y) \rangle.$$

Under the above simplifications, system (3.55) reduces to

$$\begin{aligned}\omega &\begin{bmatrix} im & 0 & 0 \\ 0 & im & \partial_y \\ 0 & 0 & 1 \end{bmatrix} \begin{bmatrix} \Phi' \\ w' \\ v' \end{bmatrix} \\ &= \begin{bmatrix} ikm\bar{u} - m\kappa L_m & -iN^2 & 0 \\ -ik^2 & ikm\bar{u} - m\nu L_m & k\bar{u}\partial_y - k\partial_y(\bar{u}) + kf + i\nu L_m\partial_y \\ -i\partial_y & \frac{fm}{k}i & k\bar{u} + \frac{f}{k}\partial_y + i\nu L_m \end{bmatrix} \begin{bmatrix} \Phi' \\ w' \\ v' \end{bmatrix}, \end{aligned} \tag{3.56}$$

where $L_m(k,y,m) = -k^2 - m^2 + \partial_{yy}$ is used to represent the simplified Laplacian. Here we swapped the order of rows and changed the order of v' and w' to aid in simplifying the left hand matrix. Our new ansatz along with the continuity equation (3.50) allows us to

write $w' = m^{-1}(i\partial_y v' - ku')$. This expression permits us to replace the w' terms with u' and to write the above system in terms of Φ', u' and v'. Finally, we divide the first row by im, the second row by $-ik$ and multiply the last row by i to simplify system (3.56) to

$$\omega \begin{bmatrix} \Phi' \\ u' \\ iv' \end{bmatrix} = \begin{bmatrix} k\bar{u} + i\kappa L_m & \left(\frac{N}{m}\right)^2 k & -\left(\frac{N}{m}\right)^2 \partial_y \\ k & k\bar{u} + i\nu L_m & f - \partial_y(\bar{u}) \\ \partial_y & f & k\bar{u} + i\nu L_m \end{bmatrix} \begin{bmatrix} \Phi' \\ u' \\ iv' \end{bmatrix}. \tag{3.57}$$

The above system is a one dimensional eigenvalue problem for the barotropic stability problem that agrees with the system derived by Ribstein et al. [73] when we neglect the viscosity in the horizontal directions (i.e. when $L_m = -m^2$). The advantage of system (3.57) over system (3.55) is that our unknown functions now depend on only one continuous variable but this comes at the cost of having the additional wavenumber m for the vertical direction. Like in the works of Ribstein et al. [73] and Tort et al. [89], in the form above the barotropic $m = 0$ mode cannot be directly considered due to the obvious singularity at $m = 0$. The lack of dependence on the continuous variable z, obviously makes numerically solving system (3.57) faster than numerically solving system (3.55). Furthermore, direct numerical methods can be used to obtain the full spectrum of system (3.57). Generally, computing the full spectrum for system (3.55) with acceptable spatial resolutions is numerically infeasible and we need to rely on Krylov subspace methods to numerically solve system (3.55). We expand on these statements in Chapter 4 when we discuss the numerical methods we use to solve the eigenvalue problems.

Chapter 4

Numerical Methods for Inertial Instability

We now discuss the numerical methods used in our study of inertially unstable jets. First we discuss how to numerically solve both the 1D eigenvalue problem in equation (3.54) and the 2D generalized eigenvalue problem in equation (3.57). This is followed by a discussion of the Spectral Parallel Incompressible Navier-Stokes (SPINS) model, the numerical model we use to numerically simulate the nonlinear system [83].

4.1 1D Eigenvalue Problem

To numerically solve the 1D eigenvalue problem (3.57), we need to choose a numerical grid, build differentiation operators, define the background functions on the numerical grid and then apply an eigenvalue problem solver to the discretized system. With resolutions sufficient to capture the most unstable modes, the discretized matrices for the 1D eigenvalue problems are small enough for direct eigenvalue solvers to be applied. Such methods allow us to obtain the full spectrum and simplifies the process of finding the mode(s) with the largest growth rate.

4.1.1 Numerical Domain

When building the numerical domain for the 1D eigenvalue problem there are two things to consider, the type of grid and the length of the numerical domain.

Grid: We considered two types of grids, a linearly spaced staggered grid similar to the grid shown in Figure A.1 that we used in Chapter 2, and a Chebyshev grid. The advantages of using a linearly spaced staggered grid over a Chebyshev grid are the higher resolution in the middle of the domain and the ability to use sparse matrices for the differentiation operators. Unfortunately, these grids also produce a larger number of spurious modes. The Chebyshev grid by comparison has lower resolution in the middle of the domain but tends to produce fewer spurious modes. For more information on Chebyshev grids and how to build them numerically, we recommend the reader to see the excellent book by Trefethen [90]. We implemented both grid types and found that Chebyshev grids provided better results than linearly spaced staggered grids with second order finite differences used for the differential operators. We thus use Chebyshev grids for the 1D eigenvalue problem.

Numerical domain: We now need to pick the domain length for our numerical calculations. As we wish to study modes that do not interact with the lateral boundaries, the domain needs to be sufficiently large so that the modes not only fit within the domain but are also sufficiently small at the boundaries. An estimate for the width of the mode in the y direction is thus of interest. The work of Carnevale et al. [9] and Kloosterziel et al. [44] provide such an estimate for the case of an unstratified barotropic jet. They used the conservation of EPV to show that the spatial structure of II modes is not simply trapped within the region of negative EPV but also decays into the region of positive EPV. They estimate that the II modes are trapped within the interval $[y_l, y_h]$ that satisfies

$$\int_{y_l}^{y_h} \left(\bar{U}(y) - \frac{y}{\mathrm{Ro}} - m_c \right) dy = 0, \tag{4.1}$$

where m_c is an unknown constant, and y_l and y_h are the zeros of $\bar{U}(y) - \frac{y}{\mathrm{Ro}} - m_c$. Unfortunately, these results are only applicable for barotropic jets with no background linear stratification and a generalization of condition (4.1) that is applicable to barotropic jets with a background linear stratification has not yet been found. Even though we lack a condition for the stratified problem, previous studies on stratified jets suggest that II modes still tend to be largely trapped in the region of negative EPV and decay outside of this region [33, 45, 97]. These studies have found that given that the boundaries are sufficiently far away from the region of negative EPV, the influence of the boundaries on the mode is negligible. We experimentally found that for parameters we consider in this thesis, the interval $[-20L, 20L]$ where L is the horizontal length scale of the jet is sufficiently large. For the Rossby numbers we consider, this domain length is at least 4 times larger than what is prescribed by condition (4.1) but since we examine the stratified case we choose to err on the side of caution.

4.1.2 Differentiation Matrices

We now build discretizations for the first and second derivatives on a Chebyshev grid. Luckily for us, cheb(N) provides the first derivative matrix, D_y and the second derivative matrix, D_{yy}, is simply D_y^2 [90]. The differentiation matrices provided by cheb(N) do not apply any particular boundary conditions and we thus need to modify the operators appropriately. As we use free slip boundary conditions, we apply Dirichlet boundary conditions on v'. We do this by only considering the interior points of v' in system (3.57). Examining the equation for v' in (3.57), we see that Dirichlet conditions on v' imply that the u' and ϕ' fields satisfy $\partial_y \Phi' + f u' = 0$ at the boundaries. This means that our method could find solutions where u' is nontrivial at the boundary. Such solutions do not agree with our no-flow boundary conditions so we eliminate them from consideration.

4.1.3 Matrix for the Eigenvalue Problem

With the differentiation matrices and discretization for the spatial domain defined, we now discretize eigenvalue problem (3.57). The discretized analogue of equation (3.57) is

$$\omega \begin{bmatrix} \vec{\Phi}' \\ \vec{u}' \\ i\vec{v}' \end{bmatrix} = \begin{bmatrix} (k\bar{U} + i\kappa L_m) & \left(\frac{N}{m}\right)^2 kI & -\left(\frac{N}{m}\right)^2 D_y \\ kI & (k\bar{U} + i\nu L_m) & (fI - \bar{U}_y) \\ D_y & fI & (k\bar{U} + i\nu L_m) \end{bmatrix} \begin{bmatrix} \vec{\Phi}' \\ \vec{u}' \\ i\vec{v}' \end{bmatrix}$$

where $\vec{\Phi}'$, $\vec{u}'$, and v' are vectors located on the Chebyshev grid, D_y is the Chebyshev differentiation matrix, $L_m = (-k^2 I - m^2 I + D_y^2)$, I is the appropriately sized identity matrix and $\bar{U}$ and $\bar{U}_y$ are diagonal matrices whose entries are given by the background states $\bar{u}(y)$ and $\partial_y(\bar{u})$ evaluated on the Chebyshev grid. Recall here that we only consider the interior values of v' so the last row and column of the matrix above are not the full operators but are missing the boundary components of v'. For details on how to build this matrix, the interested reader is invited to look at lines 30-32 of the code in Appendix C or Trefethen [90].

4.1.4 Numerical Solution

To solve the discretized system, we simply use Matlab's direct eigenvalue problem solver eig(). This method produces the full spectrum of the discretized system but includes spurious modes that oscillate near the grid scale as well as modes that are not sufficiently

small at the lateral boundaries. These modes are deemed to be unphysical and therefore removed from the modes of interest.

To find spurious modes we have a few options. We could use the Fourier decomposition of each mode and examine the relative values of the coefficients or we could look for modes that oscillate on the grid scale by counting the number of grid points where a mode increases/decreases and then immediately decreases/increases *i.e.* count the points y_i such that $(u(y_{i+1}) - u(y_i))(u(y_{i+2}) - u(y_{i+1})) < 0$. We take this latter approach but to avoid filtering modes that oscillate in regions where they are nearly zero we add the restrictions that $|u(y_i) - u(y_{i+1})|$ and $|u(y_{i+2}) - u(y_{i+1})|$ are both greater than $0.001\,U$ where $U = \max_{y_i}(u(y_i))$. If the percentage of points satisfying this criterion is larger than 25%, we consider the mode to be spurious and eliminate it from consideration. We found that in cases where the most unstable mode has a relatively large growth rate, this filtering is often not needed in order to find the fastest growing mode.

To filter out modes that strongly interact with the boundary, we found that simply comparing the y values for which the mode obtains its maximum/minimum to the domain length was sufficient. We chose to eliminate modes that obtained their maximum/minimum outside the interval $[-19L, 19L]$.

For the interested reader, we provide an implementation of the method for the 1D eigenvalue problem with filtering in Appendix C.

4.2 2D Eigenvalue Problem

Similar to the 1D eigenvalue problem, to numerically solve the 2D eigenvalue problem in equation (3.54) we need to choose a numerical grid, build differentiation operators, define the background functions on the numerical grid and then apply an eigenvalue solver to the discretized system. The key difference between the previous problem and the 2D problem is that we now have two continuous variables to discretize instead of one. This means that for the same resolution in the y direction, the discretized system for the 2D generalized eigenvalue problem is significantly larger than that of the 1D eigenvalue problem and in practice Krylov subspace methods must be used. These methods are not guaranteed to find the most unstable modes and also tend to produce spurious modes that need to be eliminated [74].

4.2.1 Numerical Domain

Similar to the 1D eigenvalue problem, we need to decide what type of numerical grid to use and the appropriate length/height of the numerical domain. Since we have two spatial directions to discretize, our choice in the resolutions for each direction is more important than it was previously. We thus discuss how to pick appropriate resolutions. Finally, we mention how to turn the 2D grids into the vectorized analogue needed for standard eigenvalue problem solvers.

Grid: For the grid type, we again have two options: a Chebyshev grid or a linearly spaced grid. If we were to use a Chebyshev grid for this problem, the matrices in the 2D eigenvalue problem would be dense $(3 \cdot N_y \cdot N_z) \times (3 \cdot N_y \cdot N_z)$ matrices where N_y and N_z are the number of grid points in the y and z directions respectfully. For the resolutions needed to capture the most unstable modes, these matrices are far too large. We thus use a linearly spaced grid in both directions which allows us to use sparse matrices.

Numerical domain: We now need to choose the length and height of our numerical domain. Due to how the size of the discretized eigenvalue problem scales with respect to N_y and N_z, choosing the appropriate numerical domain length and width is quite important. The II modes must fit in the domain and decay at the boundaries but an excessively long domain causes the discretized eigenvalue problem to be larger than they need to be. This in turn increases the resources needed to find unstable modes and since we are using sparse solvers tends to cause more spurious modes to be produced.

As we can readily solve the 1D eigenvalue problem for a barotropic jet, finding an appropriate domain length is straight forward. Using our solution to the 1D eigenvalue problem, we first find the fastest growing mode for the barotropic jet and then find the smallest numbers y_- and y_+ for which the mode has decayed below $0.1\% \max(|u'|)$ on the intervals $[-20L, -y_-]$ and $[y_+, 20L]$ respectively. The horizontal domain for the 2D eigenvalue problem is then taken to be $[-y_-, y_+]$. While the II modes for the barotropic and baroclinic jets have different structures, this method has worked for all of the cases we have considered.

The appropriate domain height for the barotropic jet is trivial to find as the depth of the ocean in the physical problem is specified to be H. Choosing the domain height for the baroclinic jets is not as simple since we consider interior jets that do not interact with the vertical boundaries. Furthermore, we do not have an approximation for the expected vertical extent of the II modes for baroclinic jets. We know from previous studies that in the horizontal direction II modes tend to be centralized where the EPV is negative but decays into the region of positive EPV. This suggests that our domain height should

at a minimum contain the region where the EPV is negative. As the zeros of the EPV only provide an approximation for the appropriate domain height and are difficult to find analytically, we instead find the zeros of the total vorticity

$$f - \partial_y \bar{u} = f + \frac{2U}{L} e^{-\left(\frac{z-D}{H}\right)^2} \tanh\left(\frac{y}{L}\right) \operatorname{sech}^2\left(\frac{y}{L}\right).$$

The zeros of the above function lie on the curve

$$z = D \pm H\sqrt{\ln\left|2\mathrm{Ro}\tanh\left(\frac{y}{L}\right)\operatorname{sech}^2\left(\frac{y}{L}\right)\right|}$$

and the maximum and minimum z values are

$$z = D \pm H\sqrt{\ln\left(\frac{4Ro}{3^{3/2}}\right)}.$$

Thus for an interior baroclinic jet, our suggested minimum for the vertical domain length is $2H\sqrt{\ln\left(\frac{4Ro}{3^{3/2}}\right)}$ and for a surface jet the suggested minimum is $H\sqrt{\ln\left(\frac{4Ro}{3^{3/2}}\right)}$. In practice, we find that this choice for the vertical domain length is sufficient for cases when $\mathrm{Re} \gtrsim 10^7$ but at smaller Reynolds numbers, a larger domain is sometimes needed. Even though we did not encounter problems with changing the other parameters, we make no claim here that the Reynolds number is the only parameter that determines whether or not this choice in domain height is appropriate.

Minimum resolutions: We can use the 1D eigenvalue problem to impose a recommended minimum resolution in the vertical direction. For any given wavenumber k, solving the 1D eigenvalue problem gives us the most unstable mode for the barotropic eigenvalue problem in terms of a vertical wavenumber m. In the 2D problem we should at a minimum resolve this wavelength. We thus impose

$$N_z \geq \frac{L_z}{L_m/10}$$

where N_z is the number of grid points used in the vertical direction, $L_m = 2\pi/m$ and L_z is the domain height. This ensures that we use at least 10 points to resolve waves with wavenumber m. As far as the horizontal resolution is concerned, the most unstable mode seems to be non-oscillatory in the y direction and thus picking a sufficient resolution in this direction tends to be unproblematic.

Converting grids: Our 2D grids for y and z are elements of $\mathbb{R}^{N_y} \times \mathbb{R}^{N_z}$ of the form

$$Y = \begin{bmatrix} \vec{y} \\ \vdots \\ \vec{y} \end{bmatrix} \qquad \text{and} \qquad Z = \begin{bmatrix} \vec{z}_1 \\ \vdots \\ \vec{z}_{N_z} \end{bmatrix}$$

where $\vec{y} = \langle y_1, y_2, \ldots, y_{N_y} \rangle$, $\vec{z}_i = \langle z_i, z_i, \ldots z_i \rangle \in \mathbb{R}^{N_z}$. To build the vectorized grid we simply reshape the above to

$$\hat{Y} = \begin{bmatrix} \vec{y}^T \\ \vec{y}^T \\ \vdots \\ \vec{y}^T \end{bmatrix} \qquad \text{and} \qquad \hat{Z} = \begin{bmatrix} \vec{z}_1^T \\ \vec{z}_2^T \\ \vdots \\ \vec{z}_{N_z}^T \end{bmatrix} \tag{4.2}$$

where $\hat{Y}, \hat{Z} \in \mathbb{R}^{N_y \cdot N_z}$ are now one-dimensional.

4.2.2 Differentiation Matrices

To build differentiation matrices for the operators that appear in the 2D eigenvalue problem, it is sufficient to define discretizations for ∂_z, ∂_{zz}, ∂_{zzz}, ∂_y, ∂_{yy} and ∂_{yyy} with appropriate boundary conditions. Since we use free slip boundary conditions we need to impose

$$\begin{aligned} v'(y_\pm, z) &= 0, & \partial_y(w'(y,z))|_{y=\pm y} &= 0, & & \partial_y(\phi'(y,z))|_{y=\pm y} = 0, \\ \partial_z(v'(y,z))|_{z=\pm z} &= 0, & w'(y, z_\pm) &= 0, & \text{and} \quad & \partial_z(\phi'(y,z))|_{z=\pm z} = 0, \end{aligned}$$

where the boundaries are located at $y_\pm$ and $z_\pm$. With the above boundary conditions in mind, the comprehensive list of differential operators needed for the 2D eigenvalue problem is given in Table 4.1. For each operator in Table 4.1, we build a second order differentiation matrix that operates on either $\vec{y}$ or $\vec{z}_i$ by using standard second order central finite differences [21]. When these finite difference schemes depend on boundary points or on points outside of the domain, we either use the boundary conditions to simplify the central finite difference or use the boundary conditions to simplify an appropriate second order (or higher) one sided finite difference scheme. To avoid going into excessive detail here, the details of how we implemented the boundary conditions for each operator in Table 4.1 are presented in Appendix D.

With all the operators in Table 4.1 discretized, we now have operators for D_y^d, D_{yy}^d, D_{yyy}^d, D_z^d,D_{zzz}^d, D_y^n, D_{yy}^n, D_z^n, D_{zz}^n and D_{zzz}^n where we use d and n to denote Dirichlet and Neumann boundary conditions respectively. Each of these operators act on either $\vec{y}$ or $\vec{z}_i$ but we need operators that act on $\hat{Y}$ or $\hat{Z}$. These can be built by taking the appropriate Kronecker tensor products of a given operator with the identity matrix on the other grid. For example our discretized analogs of ∂_{yy} and ∂_{zzz} in the 2D eigenvalue problem are

$$\partial_{yy} \approx \text{kron}(D_{yy}^n, I_z) \qquad \text{and} \qquad \partial_{zzz} \approx \text{kron}(I_y, D_{zzz}^n),$$

Operators with Dirichlet BC	Operators with Neumann BC
$\partial_y, \partial_{yy}, \partial_{yyy}, \partial_z, \partial_{zzz}$	$\partial_y, \partial_{yy}, \partial_z, \partial_{zz}, \partial_{zzz}$

Table 4.1: A list of the operators we need to discretize to numerically solve the 2D eigenvalue problem in equation (3.54). The headers specify the type of boundary condition we need to apply for the given discretized operator.

where I_z is the $N_z \times N_z$ identity matrix, I_y is the $N_y \times N_y$ identity matrix and kron is the Kronecker tenser product.

4.2.3 Matrix for the Eigenvalue Problem

We now have all the operators needed to discretize the matrices in equation (3.54). If we let A be the matrix on the left hand side of equation (3.54) and B be the matrix on the right hand side of equation (3.54), then our discretizations of A and B are

$$A = \begin{bmatrix} 0 & D_y^d & D_y^d \\ 0 & I & 0 \\ D_z^n & 0 & 0 \end{bmatrix},$$

and

$$B = \begin{bmatrix} -ik^2 I & k\bar{U}D_y^n - k\partial_y\bar{U} + kfI + i\nu L_{v_y} & k\bar{U}D_z^d - k\partial_z\bar{U} + i\nu L_w \\ -iD_y^n & k\bar{U} + \frac{f}{k}D_y^n + i\nu L_v & \frac{f}{k}D_z^d \\ k\bar{u}D_z^n + i\kappa L_{\Phi_z} & -i\partial_{yz}\bar{\Phi} & -i\partial_{zz}\bar{\Phi} \end{bmatrix},$$

where $I = \text{kron}(I_y, I_z)$, all differential operators are taken to be their vectorized analogs (e.g. by D_{yy}^n we mean $\text{kron}(D_{yy}^n, I_z)$), the background terms are defined on the vectorized grid,

$$L_{\Phi_z} = -k^2 D_z^n + D_{yy}^n D_z^n + D_{zzz}^n, \qquad L_{v_y} = -k^2 D_y^d + D_{yyy}^d + D_{zz}^n D_y^d, \qquad L_v = -k^2 + D_{yy}^d + D_{zz}^n,$$

and

$$L_{w_z} = -k^2 D_z^d + D_{yy}^n D_z^d + D_{zzz}^d.$$

As we use uniform grids these matrices are sparse (see Figure 4.1).

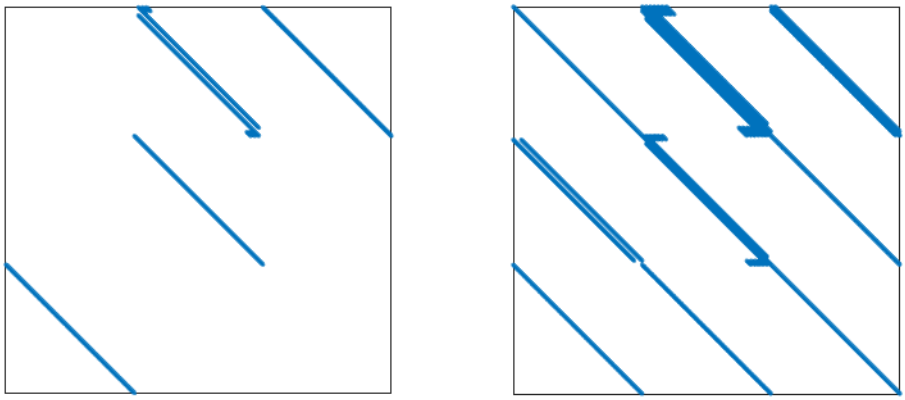

Figure 4.1: The sparseness pattern for the A matrix (left) and B matrix (right) for the 2D generalized eigenvalue problem in equation (3.54) for a resolution of $N_y = N_z = 32$.

4.2.4 Numerical Solution

As previously mentioned, for the resolutions needed to resolve the most unstable modes, the discretized system tends to be too large for direct methods to be applicable and we thus rely on Krylov subspace methods. Unfortunately, such methods do not find the full spectrum and thus are not guaranteed to find the fastest growing modes. Because of this, caution must be taken in order to ensure that the most unstable mode is found and that any non-physical modes are removed from consideration. In this section we explain how we apply a Krylov subspace method to the 2D generalized problem and then how we filter the results to eliminate nonphysical modes.

Matlab [2] provides a sparse solver "eigs" which is based on the ARnoldi PACKage (ARPACK) [2, 51]. The "eigs" function implements variants of the Arnoldi method to iteratively compute a specified number of modes and can be ran with different flags to control its convergence, accuracy, and runtime. We found that the standard configuration, "eigs(A,B)", and the configuration designed to find the eigenvalues with the largest imaginary components, "eigs(A,B,'largestimag')" were ineffective and inefficient at finding the fastest growing modes. We thus turned to the configuration "eigs(A,B,sigma)" where sigma is an approximation to the eigenvalue we wish to find. Under this configuration,

Matlab uses the Shift-and-Invert Arnoldi method which finds the eigenvalues that are closest in magnitude to the guess value sigma [2, 74]. We find that this method produces good results provided that we have an approximation for the eigenvalue of the fastest growing mode. One way to find such an approximation is use the eigenvalue computed by the 1D eigenvalue problem. Once we know the eigenvalue for the most unstable mode for one baroclinic jet, we can use this eigenvalue as a prediction for the most unstable eigenvalue for baroclinic jets with similar parameters.

The use of the Shift-and-Invert Arnoldi method along with the choice sigma begs the question "are we finding the most unstable mode or simply modes with eigenvalues near sigma". We address this potential issue, by using flags to find more modes and to increase the convergence of the method. By changing the number of modes found, we find eigenvalues further from the initial guess and are thus more likely to capture the mode with the largest growth rate. We find that computing 120 modes tends to cause "eigs" to find spurious modes with eigenvalues whose imaginary parts are close to zero. We believe that this is sufficient to capture the most unstable modes. To improve the convergence of the method, we specify the size of the Krylov space used, and increase the maximum number of iterations that can be used to find each mode [2, 81]. Explicitly, we increased the dimension of the Krylov space by roughly a factor of 5 over the default value and increased the maximum number of iterations from the default of 300 to 10^5. Interestingly, we found that increasing the maximum number of iterations tends to decrease the runtime of the method. This is likely because Matlab has two different criteria for the convergence, one for iterates below the maximum number of iterations and one for the final iteration [2, 81]. Thus by allowing Matlab to use more iterations to compute the first few eigenvectors they can be more accurately computed. Since these eigenvectors are then used to find the other requested eigenvectors, the total number of iterations required to compute the remaining eigenvectors may decrease which in turn can decrease the total run time of the method.

Now we turn our attention to filtering out spurious modes as well as modes that interact with the boundary. We eliminate spurious modes by modifying the method we used for finding oscillating modes in the 1D eigenvalue problem to check for grid scale oscillations in both the y and z directions. Likewise, modes that interact with the boundary are eliminated by finding where modes obtain their maximum values and comparing that location to the domain length and height. Sample code for the 2D eigenvalue problem solver is given in Appendix E.

4.3 Nonlinear Simulation

For our three-dimensional nonlinear simulations we choose to use the SPINS model, a three dimensional spectral method that solves the incompressible Navier Stokes equations [83]. To use SPINS to solve equations (3.1)-(3.3), we simply added the appropriate forcing terms.

Numerical stability: An attractive feature of spectral methods is the small amount of numerical dissipation they produce. Unfortunately, the lack of dissipation combined with the aliasing error of spectral methods allows energy to buildup at the smallest scales of our simulations [5]. Furthermore, even without the aliasing error there can be a cascade of energy to the grid scale due to nonlinear interactions. If this is not addressed it can result in numerically instability. To maintain stability, Subich et al. [83] added a spectral filter to remove energy at the smallest scales. In our simulations we set this filter to only remove energy from motions with wavelengths that correspond to four grid points [5]. In addition, we need to satisfy the CFL condition and we should ensure that gravity waves are well resolved. In the version of SPINS we use, the CFL condition is automatically applied and a maximal time step is forced to ensure that gravity waves are resolved with at least 10 time steps. In our work, the time step restriction imposed by resolving gravity waves is almost always more restrictive than the CFL condition.

Boundary conditions: For the barotropic and interior baroclinic jets we use uniform grids in all directions. Free slip boundary conditions are used in both the y and z directions and we use periodic boundary conditions in the x direction. Applying appropriate vertical boundary conditions for surface baroclinic jets is complicated by the sloping isopycnals at the top boundary. Out of the box, SPINS allows for such isopycnals only if one uses a Chebyshev grid and no-slip boundary conditions in the vertical direction. Unfortunately, in the viscous case no-slip conditions impose zero velocity at the surface which is obviously a problem for surface jets. One can circumnavigate this issue by using SPINS to solve a forced "inviscid" problem with no-slip conditions and a Chebyshev grid in the vertical direction where the viscous terms we need are treated as extra forcing terms. While we have done some preliminary nonlinear computations with an inviscid surface jet and examined the viscous linear stability problem for some surface jets, we choose to focus on the barotropic and interior baroclinic jets. An interesting future project would be to add the aforementioned viscous forcing to explore the dynamics of surface jets.

Initial conditions: While one could simply use the background states as the initial condition, the addition of an initial perturbation facilitates the growth of modes. We consider two types of initial perturbations: random perturbations and perturbations given by one

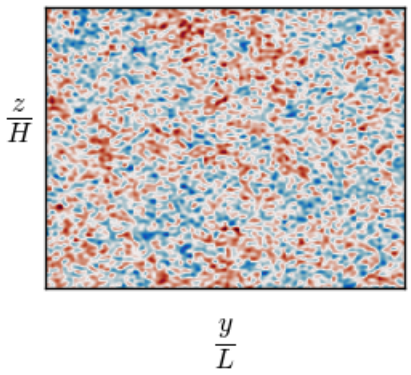

Figure 4.2: A sample of the random perturbations we use. Red indicates a positive perturbation, blue indicates a negative perturbation, and white is a perturbation of zero.

of the most unstable modes computed from linear theory. For the random perturbations, we simply perturb the buoyancy field with red/Brownian noise [99] with an amplitude between 4 and 7 orders of magnitude smaller than the maximum background buoyancy. We choose the exact amplitude to use based on the growth rate predicted by linear theory. Figure 4.2 provides an example of what a random initial perturbation looks like. In our work the random initial perturbations we use are a function of the resolution of the model and higher resolution models have smaller scale features. For the initial perturbations given by a particular unstable mode, we simply interpolate the high resolution results from our eigenvalue problem solver onto the grid used in the SPINS simulation. The maximum amplitude of the perturbation is chosen to be 4 or 5 orders of magnitude smaller than the maximum background buoyancy depending on the growth rate predicted by linear theory.

2D vs 3D simulations: In our work we consider both 2D and 3D simulations. For 2D simulations, SPINS forces us to use x and z as the main spatial coordinates. We therefore must change our background flow to be in the y direction and use v instead of u as our main velocity field. This results in a change to the sign of the buoyancy perturbation field due to the thermal wind balance of our background state. To stay consistent with our notation for the 3D simulations, we transform the results of the 2D simulation back into the notation we use in the 3D cases. That is to say we hide the fact that this transformation is happening in the background in order to be consistent with our notation.

Chapter 5

Numerical Results for Inertial Instability

In this chapter, we examine the stability characteristics of the barotropic jet (Figure 3.1a) and interior baroclinic jet (Figure 3.1b) for three sets of parameters shown in Table 5.1 and then perform a few parameter studies for the growth rates of II. The nondimensional parameters are Ro, Re, BU, δ and Pr as defined in equation (3.23) but we only consider cases where $Pr = \infty$. We no longer mention the Prandtl number. Parameter sets 1 and 2 are similar to parameters that have been used to study atmospheric jets [73]. Dimensionally, for these parameter sets the jets can be thought of as an atmospheric jet at a latitude of 30° N with a characteristic width of 100 km, a characteristic height of 3 km, a maximal velocity of 14.6 m/s and a background linear stratification corresponding to $N = 0.0103$ s^{-1}. The third set is similar to parameters used in studies of the California undercurrent [56]. We can think of parameter set 3 as an oceanic jet at a latitude of 38° N with characteristic width of 2 km, a characteristic height of 200 m, a maximal velocity of 0.036 m/s and a background linear stratification corresponding to $N = 0.0037$ s^{-1}.

For each set of parameters, we start by discussing the results of linear stability theory

	(Ro,Re,Bu,δ)
Parameter set 1	$(2, 1.1 \times 10^8, 17.26, 0.03)$
Parameter set 2	$(2, 2.2 \times 10^5, 17.26, 0.03)$
Parameter set 3	$(2, 2.2 \times 10^5, 17.26, 0.1)$

Table 5.1: The parameter sets we use to examine inertially unstable jets.

for the barotropic and baroclinic jets. For barotropic jets, we first examine the dependence of the growth rates on wavenumbers m and k and then present the structure of the most unstable mode. We then explore how the growth rates of the barotropic jet differ from those of the baroclinic jet by comparing the largest growth rates as a function of the vertical wavenumbers for both jets. We conclude by examining the structures of the unstable modes that are relevant to our nonlinear simulations for each jet.

Following each discussion of linear theory, we present the results of our nonlinear simulations. For each parameter set, the size of the simulation domain is chosen so that the fastest mode predicted by linear stability theory fits within the domain and the background state satisfies our free slip boundary conditions. For the first parameter set, we start by examining 3D simulations of a barotropic jet with a focus on the primary and secondary instabilities. We then examine the results of 2D and 3D simulations of a baroclinic jet. For the other two parameter sets, we focus on the results of 3D simulations of the baroclinic jets.

5.1 Parameter Set 1

We now examine the stability properties of jets with the nondimensional parameters (Ro,Re,Bu,δ)=$(2, 1.1 \times 10^8, 17.26, 0.03)$. These parameters are similar to those considered by Ribstein et al. [73] with two minor differences: they used a different definition for the Burger number and considered a different functional form for the same jet. Aside from these minor differences, Ribstein et al. [73] did not explicitly choose the viscous dissipation in their nonlinear simulations but instead relied on the numerical diffusion of the model they used (WRF). Furthermore, in their linear stability analysis they only considered viscosity in the vertical direction and restricted their investigation to barotropic jets. In our simulations, we use a spectral method to obtain the highest order of accuracy possible and also include viscosity explicitly which we refer to as an eddy viscosity. Even though Ribstein et al. [73] did not explicitly define a Reynolds number in their nonlinear simulations, by comparing their nonlinear simulations to their linear stability analysis they concluded that the Reynolds number of their simulation is greater than 5.6×10^6. Our Reynolds number was chosen to fit within this range. For this Reynolds number, the highest resolution model we consider is not sufficient to accurately capture the complete dynamics at the smallest scales. Nevertheless, by using a spectrally accurate method with a numerical filter, we improve upon these works by resolving the smaller scales more accurately than what can be done with the lower order methods they used.

We first examine the linear stability properties of the barotropic and baroclinic jets.

For the barotropic jets two linear instability problems are considered. One with periodic boundary conditions in the vertical direction (i.e. the 1D eigenvalue problem) and one with free slip conditions in the vertical direction (i.e. the 2D eigenvalue problem). We then compare the growth rates and the structures of the unstable modes for the barotropic and baroclinic jets and examine several nonlinear simulations for both jets. We start by examining 3D simulations of the more elementary barotropic jet. The dynamics of this jet are easier to analyze and allow for the detailed analysis of a secondary instability that follows the saturation of the primary inertial instability. We then examine 2D and 3D nonlinear simulations for the baroclinic jet. The 2D simulations allow us to examine the dynamics of the onset of II with greater resolution than is feasible in 3D simulations whereas the 3D simulations allow us to see the development of coherent vortices following the saturation of II. Our results qualitatively agree with the work of Ribstein et al. [73] and show that at least in this case, our numerical methods for solving the 1D and 2D eigenvalue problems produce the correct structures and growth rates for the most unstable modes.

5.1.1 Linear Stability Analysis: Barotropic Jet

We start our analysis on this parameter set with an examination of how the growth rates predicted by the 1D eigenvalue problem depend on the wave numbers in both the x and z directions and then we compare the structure and growth rates of the most unstable modes as predicted by the 1D and 2D eigenvalue problems.

1D eigenvalue problem: Figure 5.1 shows the growth rates predicted by our 1D eigenvalue problem solver. Unlike the work of Ribstein et al. [73] which only varied one wave number at a time, we present a 2D color plot of the growth rates. Our results agree quantitatively with the work of Ribstein et al. [73]. Most notably, for sufficiently large values of m (i.e. $mH \gtrsim 80$) the growth rates decrease and the ultraviolet catastrophe that is present in the inviscid case is adverted [9, 19, 25, 67, 73, 89]. As was noted by Ribstein et al. [73], the growth rates decrease for large wavenumbers k. Unlike in the work of Ribstein et al. [73], the fastest growing mode lies on the $m \cdot H$ axis and the vertical wavenumber of our most unstable mode differs from their work i.e. the SI mode is the most unstable inertial mode. Physically, this means that the fastest growing mode has no x dependence and is essentially two-dimensional. We also see a region of slow growing "barotropic" modes near the $m \cdot H = 0$ axis that was not previously examined in the work of Ribstein et al. [73] but is present in both the tanh and double jets examined by Wang et al. [93] in their study of vertical shear flows. The differences between our results and those presented in Ribstein et al. [73] are likely caused by our inclusion of viscosity in the horizontal directions.

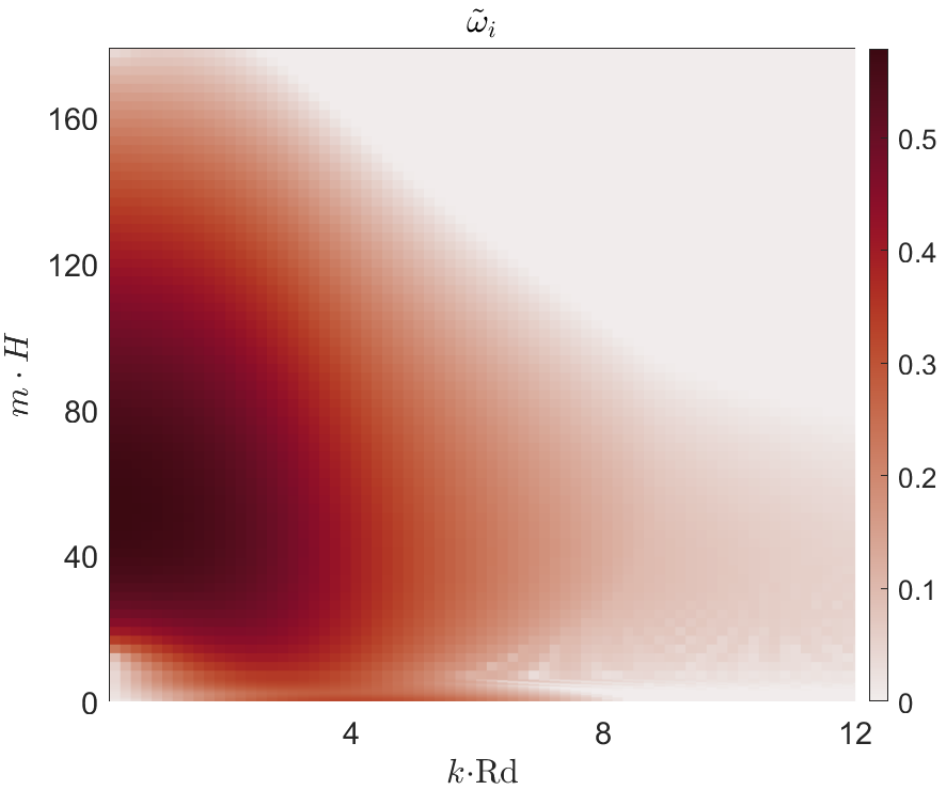

Figure 5.1: The largest normalized growth rates predicted by the 1D eigenvalue problem for the barotropic jet using parameter set 1 in Table 5.1.

Figure 5.2a shows the $y - z$ structure of the real part of the vertical velocity field as predicted by the 1D eigenvalue problem solver. Here the black lines represent the zero contour for the EPV field and the region between the two lines is where the EPV field is negative. To be consistent with our choice of water depth for the barotropic jets, we use a total water depth of H and show the structure of the mode over the whole water column. We only plot the real part of the mode because the real and imaginary parts of the perturbations are identical for SI modes ($k = 0$ modes). In the horizontal direction, the mode extends beyond the region where EPV is negative but decays as was previously noted by Carnevale et al. [9] and Kloosterziel et al. [44] in their studies of the unstratified problem. We see that the mode is indeed periodic in the vertical direction and has approximately twelve sinusoidal periods over the entire fluid depth. The general structure of this mode agrees with that predicted by Plougonven and Zeitlin [67] in their work on the SI of a barotropic Bickley jet with no background linear stratification.

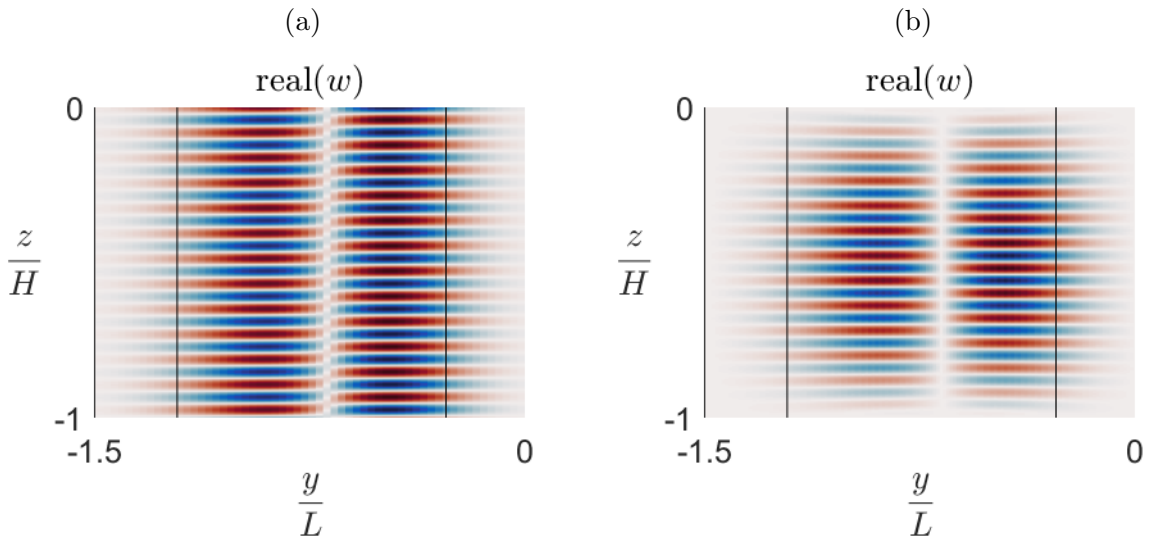

Figure 5.2: The real part of the fastest growing modes for the barotropic jet using parameter set 1 in Table 5.1 as predicted by the 1D eigenvalue problem with periodic boundary conditions, (a), and the 2D eigenvalue problem solver with free slip conditions, (b).

2D eigenvalue problem: The largest growth rate as predicted by the 2D eigenvalue problem has a wave number of the SI mode ($k = 0$) and matches the largest growth rate we found in the 1D eigenvalue problem. Figure 5.2b shows the structure of the most unstable mode as predicted by the 2D eigenvalue problem. Again, black contours mark where the EPV field vanishes and we only plot the real part of the mode. Similar to the mode predicted by the 1D eigenvalue problem, this mode extends into the region where EPV is negative but decays when the EPV is positive. Furthermore, like we previously saw with the mode predicted by the 1D eigenvalue problem, the 2D eigenvalue problem predicts that the most unstable mode has approximately twelve periods in the vertical direction. The most notable difference between the two cases is that the mode predicted by the 2D eigenvalue problem decays near the vertical boundaries in order to satisfy the no-flow boundary conditions. Thus the change of the boundary conditions caused the mode to be vertically trapped but does not have a significant effect on the mode away from the vertical boundaries.

5.1.2 Linear Stability Analysis: Baroclinic Jet

To validate the methodology of previous works that used the linear stability of barotropic jets with periodic boundary conditions in the vertical to discuss the stability of a baroclinic jet with the same nondimensional parameters, we first compare the growth rates for the baroclinic and barotropic jets for a range of wavenumbers k. This is followed by an examination of the structures of two unstable modes for the baroclinic jet. The results in this section are novel.

Growth rates: The 1D eigenvalue problem for the barotropic jet depends on the vertical wavenumber m while the 2D eigenvalue problem for the baroclinic jet does not. In order to compare the results of the two stability problems, we remove the dependence of m in the 1D eigenvalue problem by taking the maximum growth rate over m for any given wavenumber k. Figure 5.3 shows the largest nondimensional growth rates as a function of the x directional wave number as predicted by the 1D and 2D eigenvalue problems. We see that the barotropic and baroclinic jets have comparable growth rates over the range of wave numbers we consider. Furthermore, the most unstable mode for the barotropic jet has a slightly larger but comparable growth rate than the most unstable mode for the baroclinic jet. Thus, at least for this case, the linear stability analysis of the barotropic jet agrees rather well with that of the baroclinic jet. We would like to point out that when Ribstein et al. [73] compared the growth rates for the barotropic and baroclinic jets they used nonlinear simulations that did not explicitly specify an eddy viscosity to approximate the growth rates for the baroclinic case. Thus their comparison was limited to the fastest growing mode and they did not directly control the Reynolds number of the simulation making clean comparisons with their linear stability results virtually imposable.

Modal structures: We now examine the spatial structures of the most unstable modes for the SI mode ($k = 0$) and the nonsymmetric II mode with $k\mathrm{Rd} \approx 2.61$. We choose these wavelengths as they correspond to the fastest growing modes that fit in the domain we use in our 3D simulations ($\tilde{\omega}_i = 0.5753$ and $\tilde{\omega}_i = 0.4976$ respectively). Figure 5.4a shows the real part of the modal structure for the SI mode and Figures 5.4b and 5.4c show the real and imaginary parts of the most unstable nonsymmetric II mode ($kRd \approx 2.61$). In all plots we indicate the zero contour for the EPV field by a solid black line and mark the location of the middle of the jet with a red line. The imaginary component of the SI mode is not shown because it is the same as the real part of the mode but when examining the spatial structures for nonsymmetric II modes (i.e modes with $k \neq 0$) we need to consider both the real and imaginary part of the eigenfunction.

Unlike in the case of the barotropic jet, the modal structures for the baroclinic jet do not extend across the entire fluid depth. While this is not an unexpected result, the

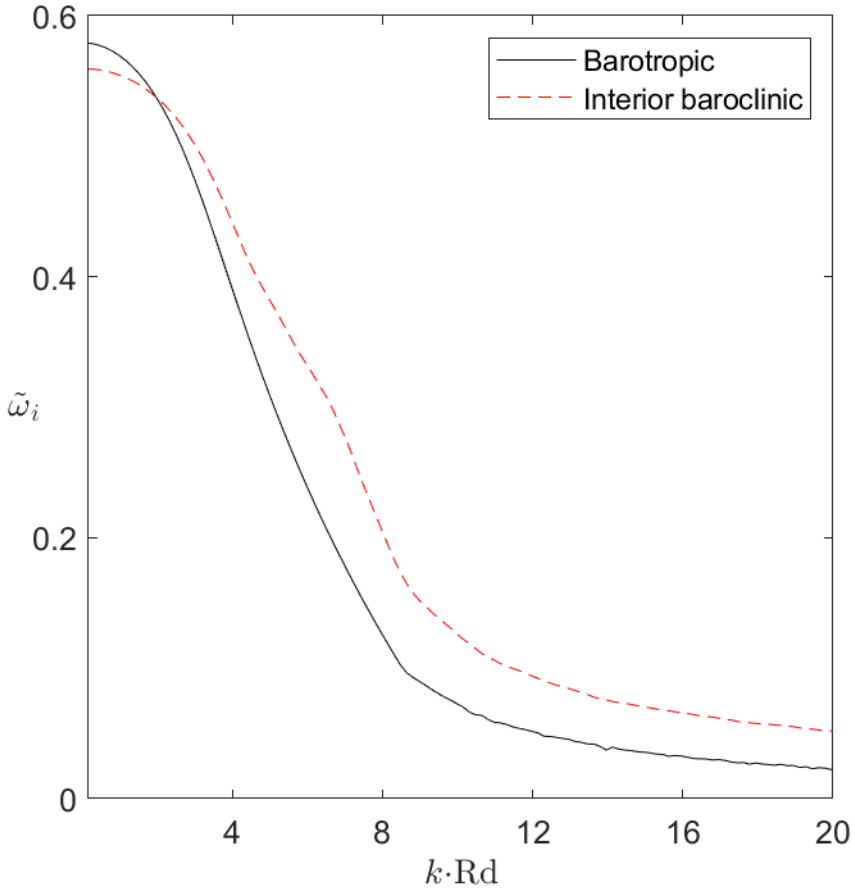

Figure 5.3: The largest normalized growth rates for the barotropic jet and the baroclinic jet using parameter set 1 in Table 5.1.

modes do not even span the entire vertical region where the EPV field is negative. Instead, they are localized to the middle of the domain where the EPV obtains its largest negative value. This result is consistent with the initial onset of the instability found in the previous work of Ribstein et al. [73]. Explicitly, even though Ribstein et al. [73] did not solve the baroclinic eigenvalue problem, they found that upon nonlinear saturation the initial change to the EPV field was concentrated in the interior region of the EPV field.

While the structures of the most unstable modes for the baroclinic jet are clearly different from those of the barotropic jet shown in Figure 5.2, there are still some noteworthy similarities. Firstly, in the horizontal direction the instabilities of both jets extend outside of the region where the EPV is negative and decay when the EPV is positive. Secondly, the vertical wavenumbers of the modes are quantitatively similar. That is to say, the vertical length scales of the instabilities of the baroclinic and barotropic jets are comparable. This is a feature we have seen in all cases we considered. Finally, all modes have the traditional "pancake" structure that is typical of II modes [97].

5.1.3 3D Nonlinear Simulations of a Barotropic Jet

In this section we consider three simulations each with a resolution of $256 \times 1024 \times 256$. The only difference in the simulations is their initial condition. In the first two simulations the initial condition is a perturbed inertially unstable barotropic jet. We either perturb the buoyancy field by a random field similar to that shown in Figure 4.2, or perturb all fields by the most unstable mode shown in Figure 5.2b. The initial condition for the third simulation is a inertially stable barotropic jet we extract from the first simulation. The details of how we extract this jet from the first simulation will be given after we discuss the results of the first two simulations. The first simulation demonstrates that the predicted modal structure forms from a random initial perturbation and grows at a rate similar to what linear theory predicts whereas the second simulation shows that the most unstable mode grows with the growth rate predicted by linear theory. The third simulation allows us to examine the details of the development of a secondary barotropic instability that occurs after the saturation of the primary inertial instability. Finally, we note that the work in this section is similar to the work of Plougonven and Zeitlin [67] on barotropic Bickley jets.

Growth rates: We start our examination of the first two nonlinear simulations by analyzing the temporal behaviour of the ℓ_2 norm of the buoyancy perturbation fields. Figures 5.5a and 5.5b show the ℓ_2 norm of the buoyancy perturbation fields for the simulation with the random initial perturbation and simulation where the initial perturbation is given

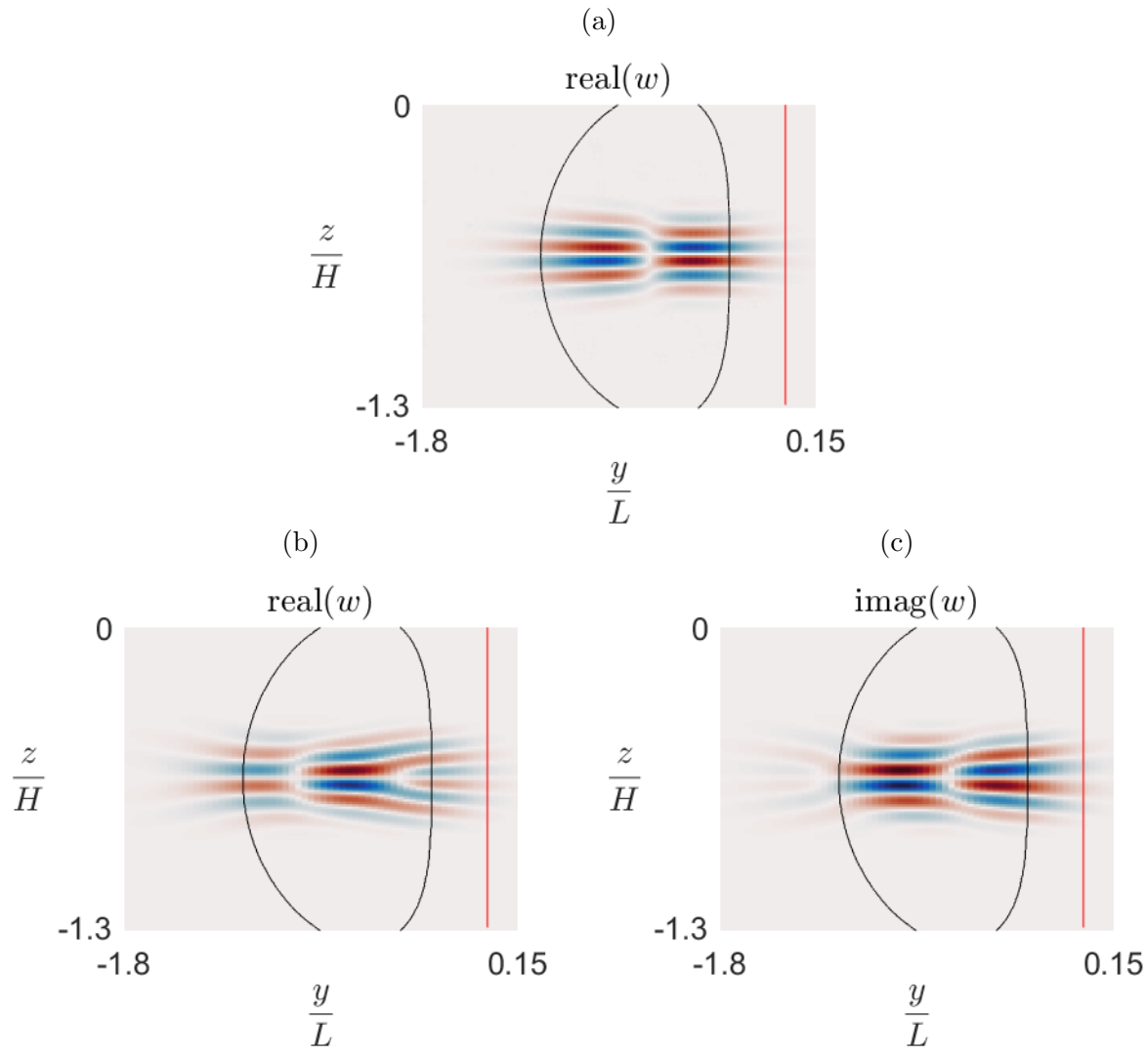

Figure 5.4: The structures for two unstable modes along with contours for zero EPV for the baroclinic jet using parameter set 1 in Table 5.1. In all plots we mark the location of the middle of the jet with a red line. Plot (a) shows the fastest growing SI mode ($k = 0$ mode) and plots (b) and (c) show the real and imaginary parts of the vertical velocity field for the most unstable nonsymmetric II mode ($kRd \approx 2.61$).

by the most unstable mode respectively. In each plot the red lines show the ℓ_2 norm of the buoyancy perturbation, the blue lines are predictions of the growth rates of the red curve, and the green lines represent the largest growth rate as predicted by the 2D eigenvalue problem solver. The blue curve is computed by using a fourth order finite difference method to approximate the log derivative of the ℓ_2 norm of the buoyancy perturbation. To minimize numerical artifacts, the ℓ_2 norm of the buoyancy perturbation is temporally averaged before computing the log derivative. The blue line provides a good approximation of the perturbation growth rate provided that the red line is growing exponentially. That is to say the blue line is not a good approximation of the growth rate unless the red curve is roughly log-linear.

In Figure 5.5a we see that the random perturbation initially has minimal change for $ft \lesssim 10$. This is followed by a region of exponential growth from $ft \approx 15$ to $ft \approx 28$, after which the predicted growth rate quickly decreases as the ℓ_2 norm of the buoyancy perturbation becomes comparable in magnitude to that of the ℓ_2 norm of the background buoyancy field itself. The ℓ_2 norm of the buoyancy perturbation then has a slower growing secondary adjustment from $ft \approx 40$ to $ft \approx 65$. As we will later show, this secondary adjustment is caused by a secondary baroclinic instability which in turn causes coherent vortices to form. This secondary instability is similar to secondary instabilities previously seen by Carnevale et al. [9] and Ribstein et al. [73]. We look at the details of this instability shortly. Focusing on the primary instability, it is immediately apparent that the growth rates predicted by the nonlinear model are smaller than what linear stability analysis predicts. Quantitatively, the largest nondimensional growth rate predicted by SPINS is 0.524 which corresponds to a relative error of 8.9% in the prediction of the growth rates. Further examining the time interval where the perturbation grows exponentially, we see that the computed growth rate increases until the assumptions of linear perturbation theory break down. This is not unexpected because a random initial condition will project onto several modes each with their own growth rate.

We now examine the simulation where the initial perturbation is given by the fastest growing mode as predicted by linear theory. In Figure 5.5b we see that the buoyancy perturbation immediately starts growing exponentially with a computed growth rate that visually agrees with the prediction from linear theory. Quantitatively, the maximal growth rate as predicted by SPINS is 0.573 which corresponds to a relative error of 0.39%. Furthermore, for this simulation the structure of the perturbation does not change over the region of exponential growth. The errors between linear theory and our nonlinear simulations are smaller than the errors that were found in the study by Plougonven and Zeitlin [67]. The low error in the prediction of the growth rate along with the spatial structure of the perturbation validates our 2D eigenvalue problem solver and is a testament to the

accuracy of SPINS.

Perturbation structure: Turning our attention back to the simulation with random initial condition, we examine how the structure of the perturbation evolves over time. Figures 5.6a-5.6c show the structure of the perturbation as predicted by SPINS for times $ft = 23$, $ft = 25$ and $ft = 28$ respectively. For each time, we choose to plot the buoyancy field, the vertical velocity field, and the EPV field. The buoyancy field is a good choice as it is our tracer field for the simulation, the vertical velocity field was chosen as it tends to be the field with the most noise and we examine the EPV field as it shows where inertial instability can form. For the buoyancy and velocity fields, each snapshot is fully saturated whereas for the EPV field each plot uses the colorbar to the right of 5.6a. In Figure 5.6a we also plot some black contours for the structure predicted by our 2D barotropic solver. Here we see that the structures are not identical to what linear theory predicts but have many of the basic features. In particular the number of oscillations in the vertical direction are similar and there is a clear region in the middle of the y direction where the perturbation vanishes. These differences in the structure are not unexpected as the growth rates predicted by SPINS differs by 8.9% from linear theory and by perturbing the buoyancy field with a random perturbation we have a mix of growing modes. Examining the two other times we present, we see that as the instability saturates the EPV field is advected in the horizontal direction and oscillations that correspond to the wavelength of the perturbation to the w field appear. This behavior of the convective cells upon nonlinear saturation was previously noted by Carnevale et al. [9] and Plougonven and Zeitlin [67] among others. We do not present plots of the structures after time $ft = 28$ because small scale features that are directly influenced by the numerical filter begin to appear.

EPV Hovmöller plot: We now examine a Hovmöller plot of the total EPV field over the spatial variable, y, and time, ft to show that the instability found above is indeed a inertial mode. Figure 5.7 is taken along the middle of x and mid-depth but slices at other locations are qualitatively similar. To highlight the regions of negative EPV, we define the colorbar so that the maximum/minimum values of the EPV field correspond to the darkest blue/red colors and zero EPV is highlighted by white. We see that for the first $ft \approx 30$ units of time there is no noticeable change to the EPV field. This is followed by an abrupt change where the EPV field develops small scale features as the instability saturates. The EPV field then becomes non-negative. We conclude that the instabilities previously found is indeed a inertial mode and the small scale features that appear are the result of II. Some of these small scale features are at the scales where the spectral filter removes the energy. Finally, around time $ft \approx 50$ a cyclonic and an anticyclonic vortex pair forms. As briefly mentioned in Ribstein et al. [73], these cyclones are caused by a secondary barotropic instability and we will shortly examine the details of this instability.

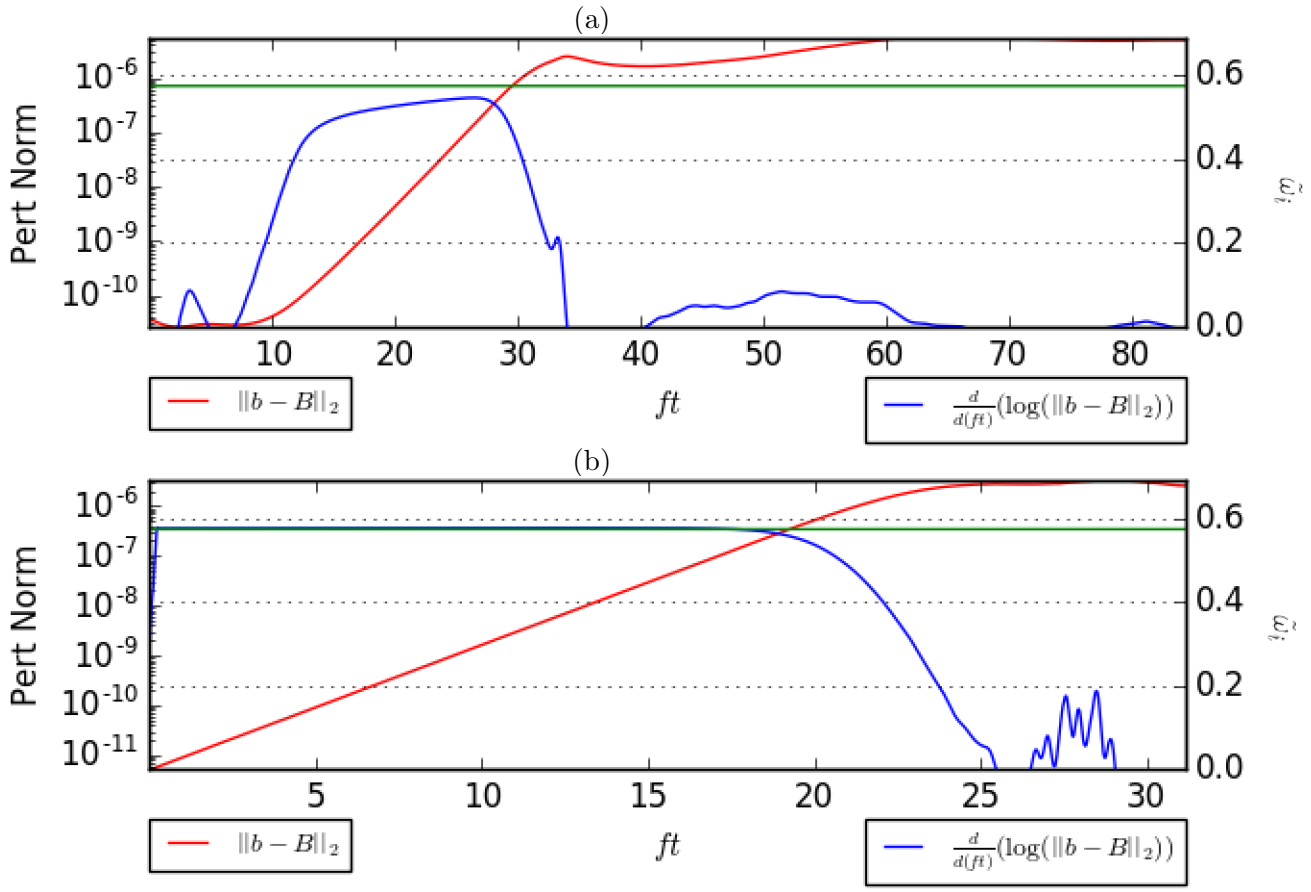

Figure 5.5: Plots of the ℓ^2 norm of the buoyancy perturbation field, approximations of the growth rate and the maximal growth rate from linear theory for two 3D simulations of the barotropic jet using parameter set 1 in Table 5.1. The red lines are plotted on the left axis while the blue and green curves are plotted on the right axis. Plot (a) shows a simulation with random initial buoyancy perturbation and plot (b) shows the simulation where initial perturbation given by the $\tilde{k} = 0$ mode which is the fastest growing mode predicted by linear theory. For both simulations a $256 \times 1024 \times 256$ resolution was used.

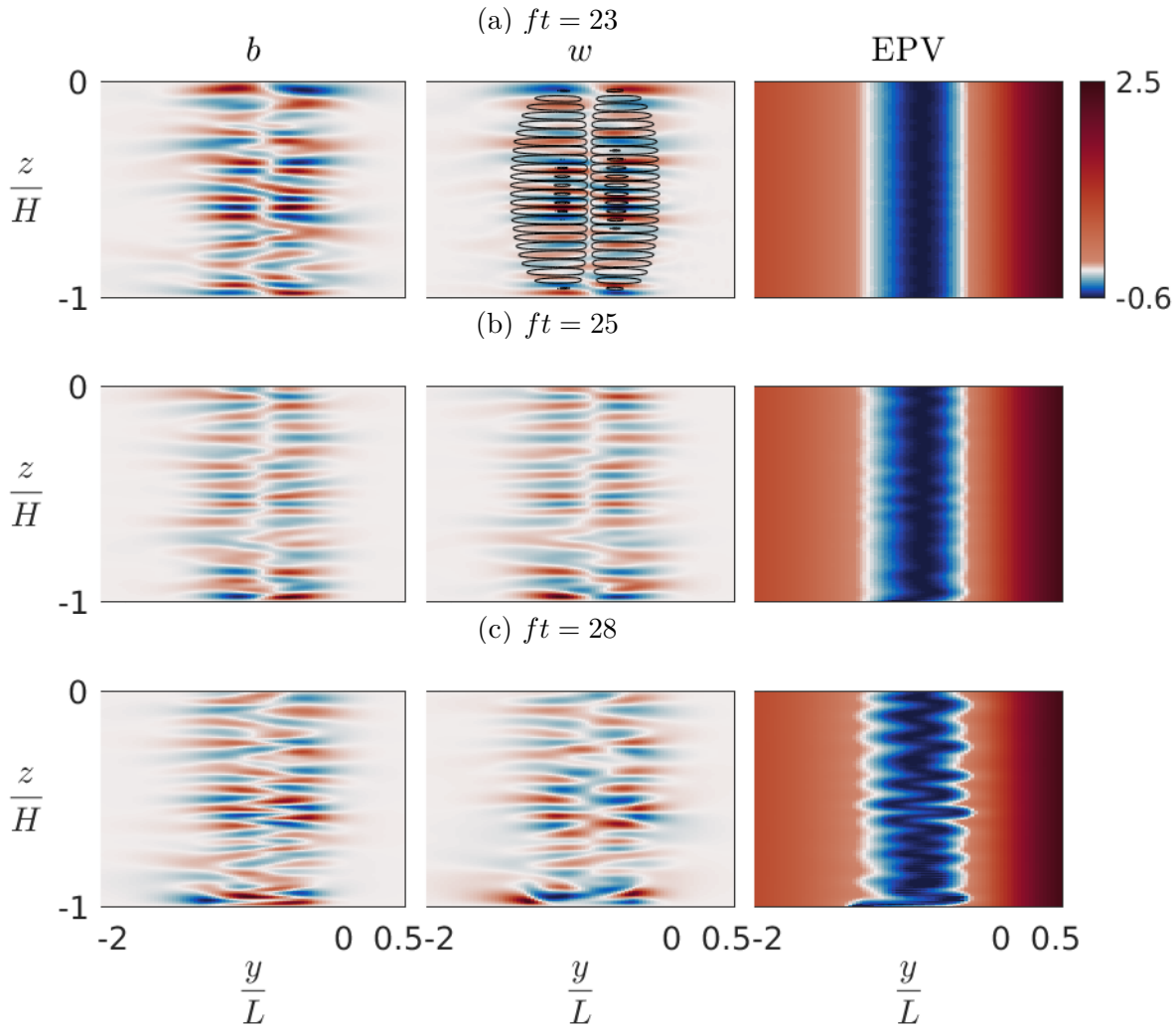

Figure 5.6: Slices of the buoyancy and vertical velocity perturbation fields along with the total EPV field for a $256 \times 1024 \times 256$ resolution simulation of a barotropic jet using parameter set 1 in Table 5.1. Here the buoyancy field of the jet was initially perturbed by a random field and the slices are taken in the middle of the x direction. The colormaps for the buoyancy and vertical velocity perturbation fields are fully saturated with zero being white. The EPV fields are fully saturated with zero being white and the same scale is used for all plots.

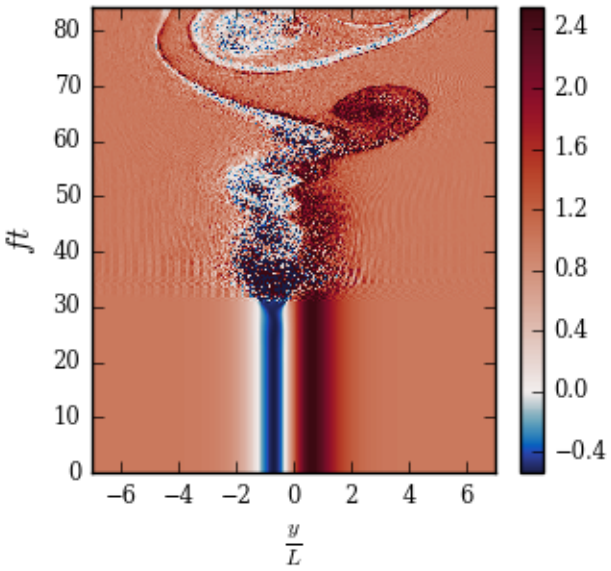

Figure 5.7: A Hovmöller plot of EPV for a 3D simulation of a barotropic jet using parameter set 1 in Table 5.1. We use a resolution of $256 \times 1024 \times 256$ and the slice is taken along the middle of the z and x planes.

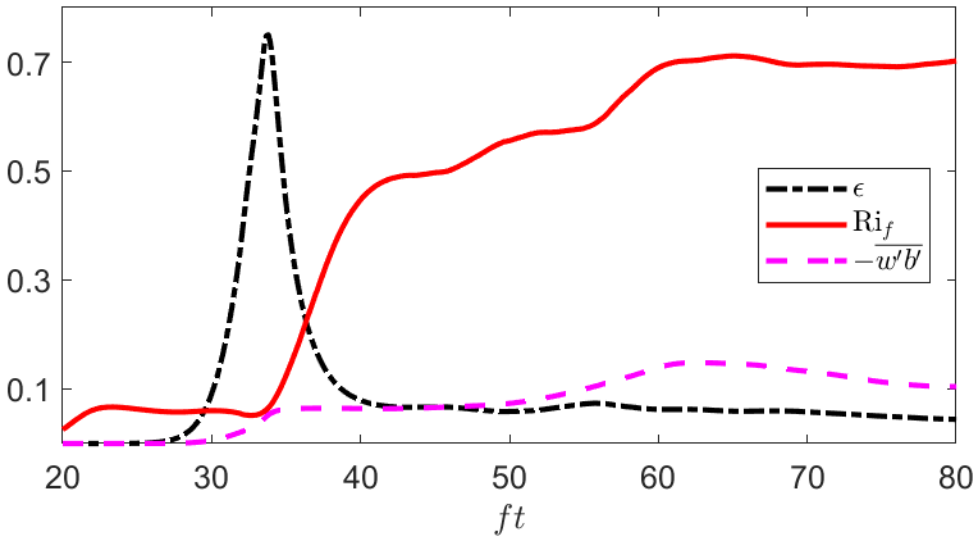

Figure 5.8: The flux Richardson number Ri_f for mixing efficiency for a 3D stimulation of the barotropic jet using parameter set 1 in Table 5.1. Here the black and magenta curves are the dissipation rate and turbulent buoyancy flux respectively. We normalized the dissipation rate to have a maximum of 0.75 and used the same normalization factor for the turbulent buoyancy flux.

Mixing efficiency: Before we discuss the details of the secondary instability, we examine the mixing efficiency of the simulation with a random initial condition. Recall that the flux Richardson number, Ri_f, defined in Section 3.4 is a number that is typically between 0 and 0.75 and represents how efficiently a flow is mixed over time. Figure 5.8 shows the mixing efficiency along with the dissipation rate and turbulent buoyancy flux for the barotropic simulation with random initial condition. Here we normalized the dissipation rate to have a maximum of 0.75 and used the same normalization factor for the turbulent buoyancy flux so that their relative values can be seen. Examining the flux Richardson number we see that during the initial onset of II the mixing efficiency is approximately 0.06 which is around a third of the efficiency typical of KH instability. Once the II begins to saturate the efficiency quickly reaches 0.5 and then saturates near 0.7. This is twice the efficiency that was found in the work of Jiao and Dewar [37] and is near the maximum efficiency of KHI (0.75). The large mixing efficiency could be an artifact of the large Reynolds number we used for this case.

5.1.3.1 Secondary Instability

We now examine the details of what is happening during the secondary adjustment in Figure 5.5a from time $ft \approx 40$ to $ft \approx 65$.

Initial condition: In order to use linear stability analysis to approximate the growth rate for this secondary adjustment, we need to extract a background state that is stable to II but still unstable to some secondary instability. We found that after the initial instability saturated, there was minimal structure in the vertical direction and we depth averaged the u velocity field to look for an initial condition to use for analyzing the secondary instability. Similar behaviour upon nonlinear saturation of the initial II mode has been noted by Plougonven and Zeitlin [67] and Carnevale et al. [9]. The first instance in time where the depth averaged EPV field is positive is $ft = 46$ so we used the velocity field at this time to compute a new background velocity field. Figure 5.9 shows the low-pass filtered depth averaged velocity field at time $ft = 46$ along with the initial condition used for the study of the primary instability. This plot is qualitatively similar to those found in the work of Carnevale et al. [9].

Growth rates: Our 2D eigenvalue solver predicts that the most unstable mode for the new jet has wavenumber $k\text{Rd}= 2.41$ and nondimensional growth rate 0.207. To check these results, we ran a 3D simulation for our new background current with an added random initial perturbation. The length of the numerical domain for this simulation was chosen so that one period of the most unstable mode fit within the domain. Figure 5.10 shows the ℓ_2 norm of the buoyancy perturbation for this simulation. Here we see that growth rate predicted by our simulation from $ft \approx 30$ to $ft \approx 80$ visually agrees with the growth rate predicted by our 2D eigenvalue problem solver.

Perturbation structure: Finally, the perturbation structure as predicted by SPINS at time $ft = 50$ along with contours of w as predicted by our 2D eigenvalue solver are shown in Figure 5.11. Since the EPV field is non-negative, the secondary instability is not II and based on the lack of structure in the vertical direction away from the boundaries it is likely a barotropic instability.

5.1.4 2D Nonlinear Simulations of a Baroclinic Jet

We now turn our attention to 2D nonlinear simulations of the baroclinic jet which allow us to use much higher resolutions and capture the smaller scale features of the saturation process. Since the linear stability analysis for the baroclinic jet under consideration shows that the most unstable mode is the SI mode ($k = 0$), these 2D simulations have the

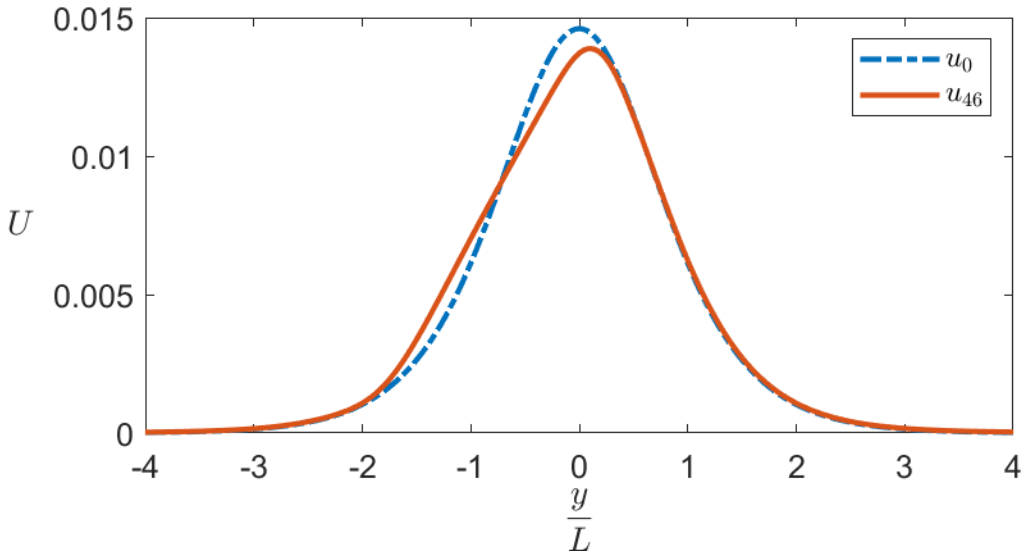

Figure 5.9: Depth and x directional averaged jets for the initial barotropic jet we study, shown in blue, and the jet as predicted by our nonlinear simulations at $ft = 46$, shown in red. The u_{46} jet is the initial condition we use to study the details of the secondary instability of a barotropic jet using parameter set 1 in Table 5.1.

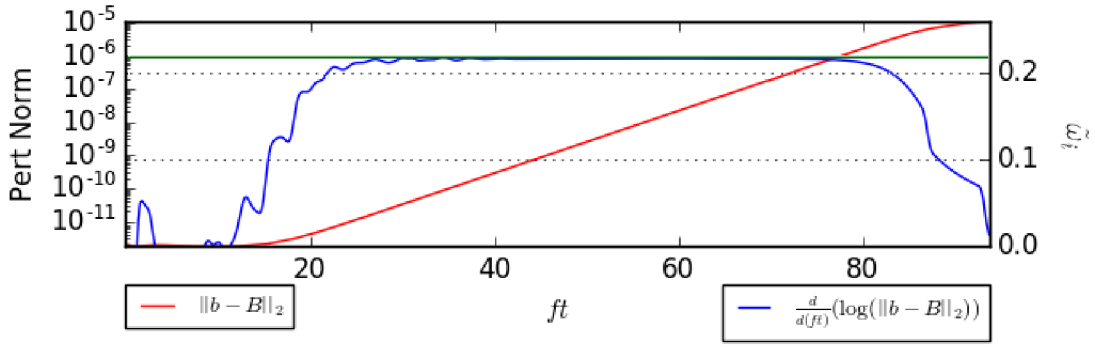

Figure 5.10: Plots of the ℓ^2 norm of the buoyancy perturbation field (red), approximations of the growth rate (blue) and the maximal growth rate from linear theory (green) for the secondary instability of a barotropic jet using parameter set 1 in Table 5.1. The initial condition for this simulation is given by u_{46} in Figure 5.9 plus a random perturbation. The red line is plotted on the left axis while the blue and green curves are plotted on the right axis.

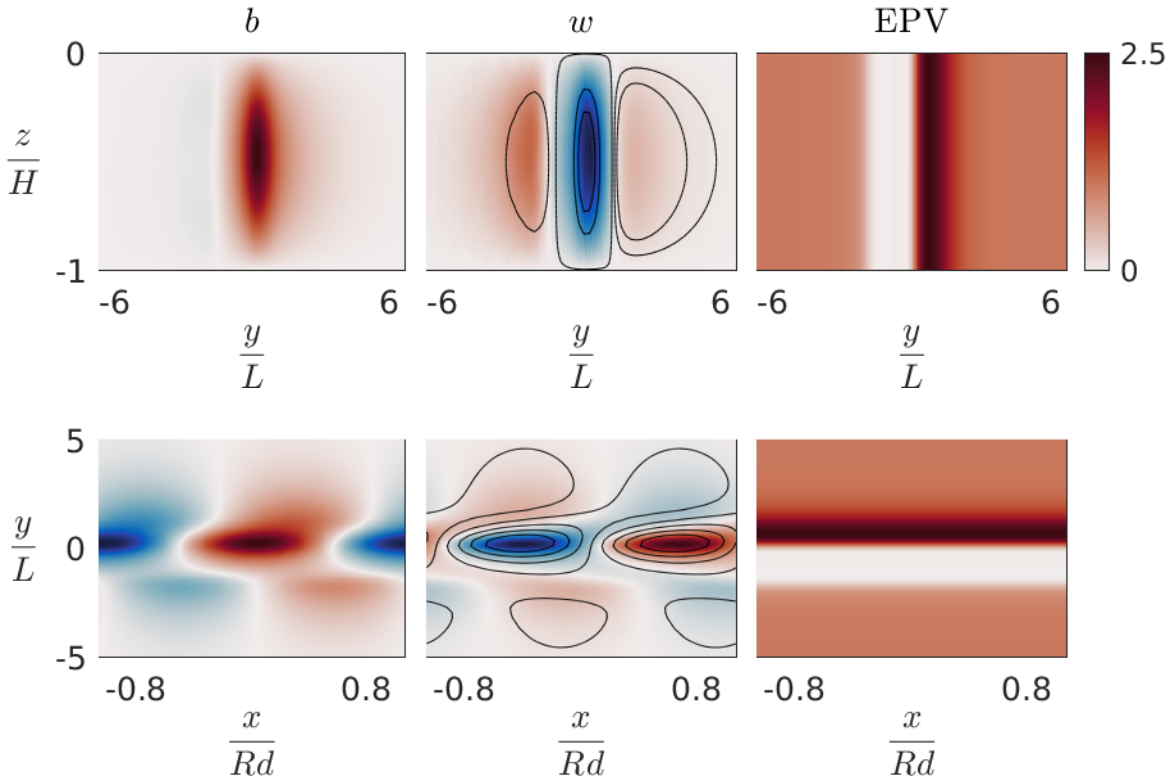

Figure 5.11: The buoyancy and vertical velocity perturbation fields along with the total EPV field for the $256 \times 1024 \times 256$ resolution simulation of a randomly perturbed barotropic jet with initial condition u_{46} shown in Figure 5.9. All plots are all taken at time $tf = 50$ and the slices are taken in the middle of the missing directions. For the w field, we plot contours for the perturbation as computed by linear theory. The colormaps for the buoyancy and vertical velocity perturbation fields are fully saturated with zero being white and the colormaps are the same for all three EPV fields shown.

potential to accurately capture the structure of the perturbations within the regime where linear theory is applicable. This said once the perturbations are sufficiently large, 2D simulations are unable to capture any three dimensional behaviors that could be present in 3D models (i.e. the secondary instabilities we previously saw for the barotropic jet). Three simulations are considered: 256×1024 and 32798×4096 resolution simulations where the initial perturbation is a random buoyancy field and a 256×1024 resolution simulation where the initial perturbation is given by the most unstable mode predicted by linear stability theory. The first two simulations allow us to explore the effects of resolution whereas the third case validates our linear stability analysis code for baroclinic jets.

Predicted growth rates: Figure 5.12 shows the ℓ_2 norm of the buoyancy perturbation field along with computed growth rates and the growth rate predicted by linear theory for each of our 2D simulations using the same the colouring convention that we used previously. Plots 5.12a and 5.12b show the 256×1024 and 32798×4096 resolution simulations with random initial buoyancy perturbation respectively, and plot 5.12c shows the 256×1024 case where the initial perturbation is given by the most unstable mode computed from linear stability theory.

In Figure 5.12a for the 256×1024 resolution 2D simulation with random initial buoyancy perturbation there is a region from $ft \approx 15$ to $ft \approx 40$ where the perturbation grows exponentially. The growth rate predicted by the nonlinear simulation is visually smaller than what linear theory predicts but monotonically increases over the region where the perturbation grows exponentially. This is not unlike what we previously saw in our 3D barotropic simulation with random initial buoyancy perturbation and again likely happens because our random buoyancy perturbation projects on several modes. Quantitatively, the nondimensional growth rate predicted by this simulation is 0.513, an 11% difference. While this is a nontrivial difference in the growth rate, this was also a low resolution simulation with a random buoyancy perturbation. Finally, after the perturbation saturates, there is no secondary instability. This is not unexpected as 2D simulations are unable to capture 3D structures and the secondary instability for the barotropic jet was fundamentally 3D in nature.

Turning to the higher resolution simulation (Figure 5.12b), we see an initial adjustment from $ft = 0$ to $ft \approx 5$ that was not present in the lower resolution simulation. We believe this initial adjustment is due to the fact that the two simulations have different initial random perturbation since the random perturbation we add is dependent on the simulation resolution. We verified this hypothesis by running high and low resolutions simulations where the initial perturbation was given by the same sinusoidal functions. With the perturbations fixed, the early behavior ($ft \lesssim 10$) of the buoyancy perturbation norms for the low and high resolution simulations are identical. After this initial adjustment, the

buoyancy perturbation norm is relatively constant until $ft \lesssim 18$ when it begins to grow exponentially with a growth rate that quickly approaches the growth rate predicted by linear theory. From $ft \approx 20$ to $ft \approx 38$ we see a clear region of exponential growth with a relatively constant growth rate that visually agrees with that of linear stability theory. Quantitatively, our nonlinear model predicts a nondimensional growth rate of 0.574 which has a relative error of 0.23%. While we cannot rule out the effects of using different initial buoyancy perturbation, at least in part this improvement should be due to the increase in resolution.

We now examine Figure 5.12c where the initial buoyancy perturbation is given by the most unstable SI mode. We see that there is some initial adjustment in the computed growth rate that was not present in the 3D barotropic case shown in Figure 5.5b. Examining the structure of the perturbation fields we see no visible adjustments to the initial perturbation. We are thus unsure what is causing the adjustment in the predicted growth rate for $ft \lesssim 3$. As we only see this behavior in this simulation and this is the only 2D simulation were we perturb by an unstable mode, we believe that the initial adjustment in the predicted growth rate is an artifact of the two dimensionality of the simulation. Nevertheless, after the initial adjustment to the predicted growth rate there is a region of exponential growth where the predicted growth rate visually agrees with linear theory. Quantitatively, the growth rate predicted by this simulation is 0.577 which corresponds to a relative error of 0.29%. This error is similar to that of the high resolution 2D simulation of the barotropic jet where the initial perturbation was given by the most unstable mode (Figure 5.12b). This relative error along with the fact that the spatial structure of the perturbation does not adjust over the period of exponential growth allows us to conclude that the results from linear stability theory are accurate and robust at least for the nondimensional parameters currently under consideration.

Perturbation structure: In order to explore the process of nonlinear saturation, we examine the spatial structure of the perturbation as predicted by the highest resolution 2D model we considered. As previously done for the 3D barotropic jet, we examine the structures of the buoyancy perturbations, vertical velocity perturbations and the total EPV field at a time while exponential growth occurs as well as two snapshots during the nonlinear saturation process.

Figures 5.13a-5.13c show the spatial structures for the b and w perturbations along with the total EPV fields for the nondimensional times $ft = 31$, $ft = 35$ and $ft = 37$ respectively. As in the case of the 3D barotropic jet, the colormaps for the buoyancy and velocity perturbation fields are fully saturated for each plot and do not show the fact that the perturbations are growing exponentially in time and the same colormap is used for all EPV fields. Figures 5.13a and 5.13b are taken while the perturbation norm is still growing

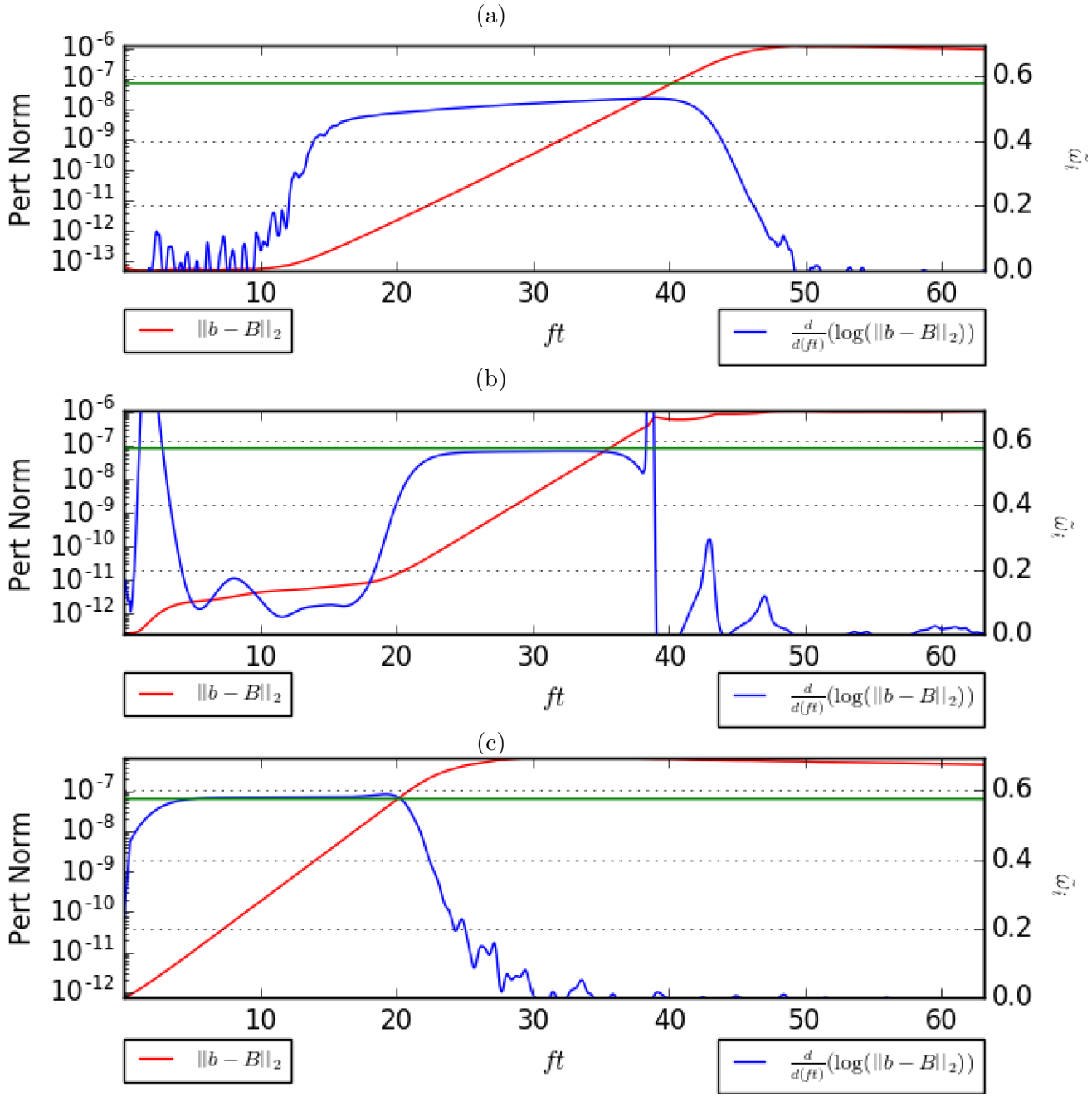

Figure 5.12: Plots of the ℓ^2 norm of the buoyancy perturbation field (red), approximations of the growth rate (blue) and the maximal growth rate from linear theory (green) for three 2D simulations of the baroclinic jet using parameter set 1 in Table 5.1. Plots (a) and (b) show the 256×1024 and 32798×4096 resolution simulations with random initial perturbations respectively, and plot (c) shows the 256×1024 resolution simulation with initial perturbation given by the SI mode.

exponentially whereas Figure 5.13c is taken when the perturbation has begun to saturate. The black contours shown in the w plot in Figure 5.13a are vertical velocity perturbation contours for the fastest growing mode as predicted by linear theory. The agreement between the w fields and the low relative error of 0.23% in the computed growth rate demonstrates that the results of this 2D simulation matches linear theory. In Figures 5.13b and 5.13c we see that as the perturbation saturates, the buoyancy perturbation, vertical velocity perturbation and the total EPV field are advected latterly. This horizontal advection of negative EPV coincides with mixing and stirring of the EPV field and is strongest where the initial EPV field is the most negative. The stirring is most obvious in Figure 5.13c where we can clearly see mushroom like regions of EPV being ejected into the region of positive EPV. The effects of mixing manifests as the desaturation of the blue regions of EPV due to the EPV being less negative than it was initially. The mushroom like clouds have been previously seen in the onset of the instability found in the previous study of barotropic vortices by Kloosterziel et al. [42]. Further, even though the resolutions used by Ribstein et al. [73] did not allow them to capture the mushroom like clouds, the general process of nonlinear saturation is consistent with their work on stratified baroclinic jets. The significantly higher resolution of our plots shows the formation process of the mushroom like regions more clearly than either of the aforementioned works. None of the previous studies we are aware of have examined the nonlinear saturation process at this high resolution.

The next time output from our high resolution simulation (not shown) develops small scale features that are not fully resolved. These features initially form on the shafts of the mushroom like regions and are filtered out by some combination of the numerical filter and implicit numerical diffusion of SPINS. We have ruled out the possibility that these grid scale features are due to RTI and thus believe that they are an unfortunate feature of the weak dissipation used in this case. Nevertheless, it was precisely the weak dissipation that makes the SI the most unstable II mode and allows us to utilize 2D nonlinear models to examine the details of the nonlinear saturation of the II at this high resolution.

EPV Hovmöller plot: Figure 5.14 shows a Hovmöller plot for the high resolution simulation with initial buoyancy perturbation given by a random field. We again fully saturated the colorbar to highlight the regions of positive and negative EPV. There are no noticeable changes to the EPV until $ft \approx 35$ where we see a region of positive EPV form in the middle of the region of negative EPV. This is followed by a fast adjustment that causes the EPV field to become nonnegative and is similar to what we saw in the barotropic case. The nonlinear saturation of II coincides with energy being rapidly transferred to the scales where the spectral filter in SPINS is active. This is seen by the pixelation in our Hovmöller plot shortly after $ft \approx 35$. It is unfortunate that this resolution is not sufficient

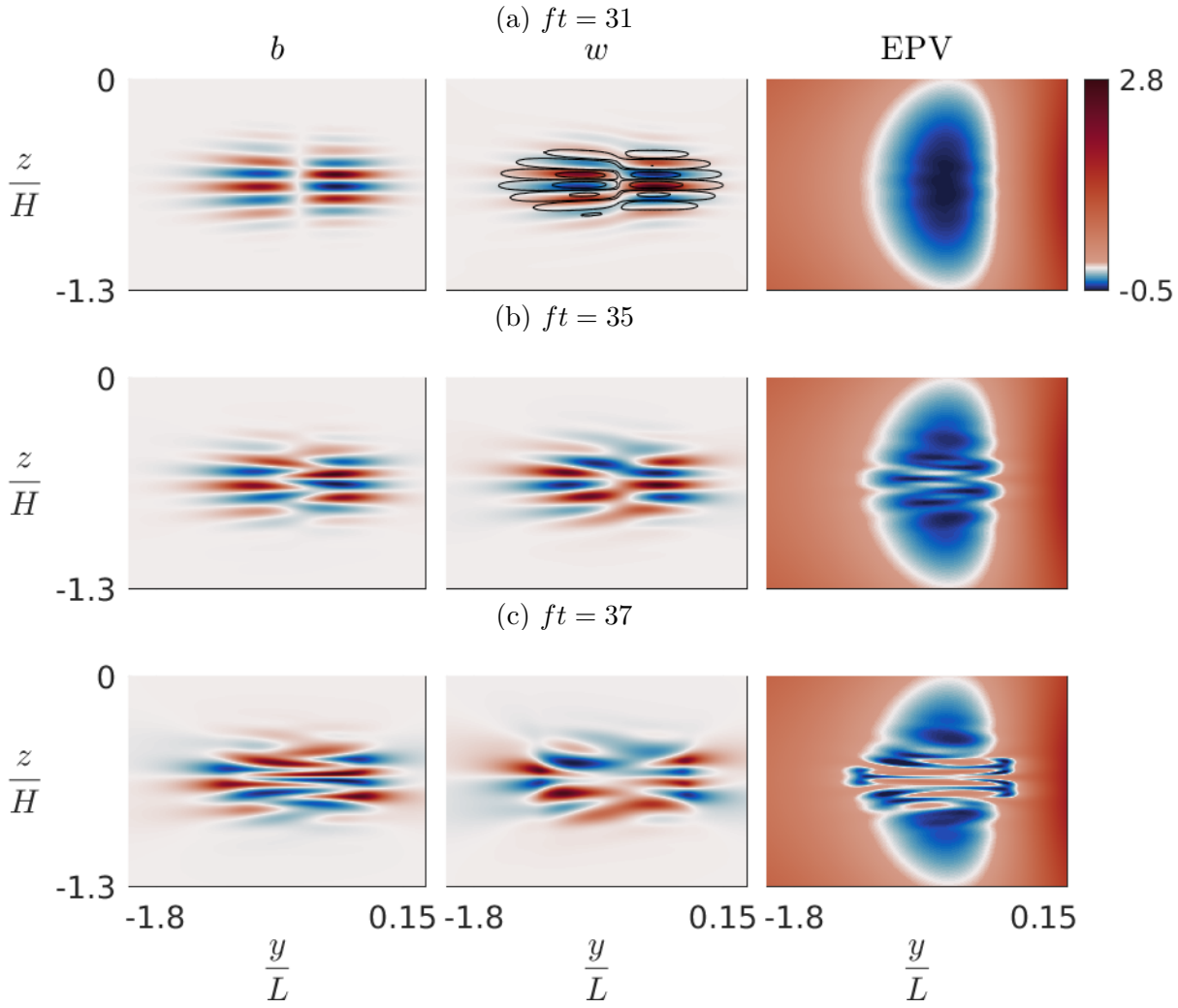

Figure 5.13: Slices of the buoyancy and vertical velocity perturbation fields along with the total EPV the field for the 32798×4096 resolution simulation of a randomly perturbed baroclinic jet using parameter set 1 in Table 5.1. All slices are taken in the middle of the x direction. In the w field for plot (a) we plot contours for the most unstable mode as computed by linear theory. The colormaps for the buoyancy and vertical velocity perturbation fields are fully saturated with zero being white and the colormaps are the same for all three EPV fields shown. The EPV field is fully saturated with zero being represented by white.

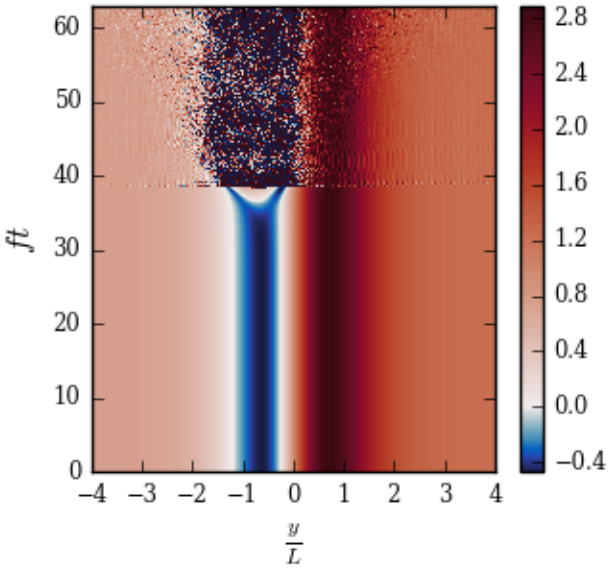

Figure 5.14: A slice of the total EPV field normalized by $N^2 f$ for a 2D simulation of the baroclinic jet using parameter set 1 in Table 5.1 and resolution 32798×4096. The slice is taken along the middle of the z plane where the EPV obtains its initial extrema.

to capture the transfer of energy to the small scales. Finally, even though we show the EPV Hovmöller plot for the 32798×4096 resolution case, the only real difference between the EPV field for this model and the other 2D simulations we ran is the resolution of the positive region of EPV that forms.

5.1.5 3D Nonlinear Simulations of a Baroclinic Jet

We now examine three 3D nonlinear simulations for the baroclinic jet: one where the initial buoyancy field is perturbed by a 3D random field, one where the initial perturbation is the fastest growing mode as computed from 2D baroclinic linear stability analysis (the SI mode), and one where the initial perturbation is the second fastest growing mode that fits within our domain (the nonsymmetric II mode - $k\text{Rd} \approx 2.61$). In all three cases, we use a resolution of $256 \times 512 \times 2048$. As the most unstable mode predicted by linear theory is the SI mode, the most unstable mode from linear theory always fits within the simulation

domain. Thus our choice of domain length only dictates which of the slower growing modes are present in our simulations. We choose to use a domain length that fits one period of a $k\text{Rd}= 2.61$ wavenumber mode. The primary differences between the simulations in this section and those presented by Ribstein et al. [73] is that we explicitly specify a Reynolds number and use a spectrally accurate numerical method. Our use of a spectral method can allow us to resolve the dynamics better than the more diffusive model used by Ribstein et al. [73].

Growth rates: Figure 5.15 shows the ℓ_2 norm of the buoyancy perturbation field along with an approximation of the growth rate and the relevant growth rates from the two-dimensional eigenvalue problem for the three aforementioned simulations.

In Figure 5.15a we show the results of the simulation where the initial buoyancy perturbation field is given by a random field. Here we see a distinct region of exponential growth that spans from time $ft \approx 20$ to time $ft \approx 40$. The computed maximal nondimensional growth rate over this time period is 0.538 which corresponds to a relative error of 6.4%. Similar to the 3D barotropic jet, there is a secondary region of growth which for this jet happens between times $ft = 60$ and $ft = 110$. As we will see when we examine the Hovmöller plot for the EPV for this simulation, the second adjustment in the norm of the buoyancy field corresponds to the development of coherent vortices.

Figures 5.15b and 5.15c show the simulations with initial perturbations given by the first and second most unstable modes respectively. As we use these simulations to validate that the results of the nonlinear model agree with linear theory for these nondimensional parameters, we only ran the model until shortly after the perturbations end their exponential growth phase. In both plots, the growth rate of the fastest and second fastest growing modes as predicted by 2D linear theory are marked by solid green and dashed green lines respectfully. In both figures, we see that the region of the exponential growth begins at the start of the simulation and continues until time $ft \approx 20$. Visually there is good agreement between the linear theory and our nonlinear calculations. Qualitatively, for Figures 5.15b and 5.15c the growth rates computed by our nonlinear model are 0.5795 and 0.4983 respectfully which correspond to relative errors of 0.78% and 0.15%. Finally, we note that in each simulation the structure of the perturbations visually did not change during the period of exponential growth. We thus conclude that our 2D baroclinic eigenvalue problem solver correctly predicts the growth rates and structures at least for the two fastest growing modes that fit in this domain.

Perturbation structure: We now examine the structure of the perturbations as predicted by the simulation with an initially random perturbation field. We chose to examine this simulation as it demonstrates that the structure predicted by linear theory can form

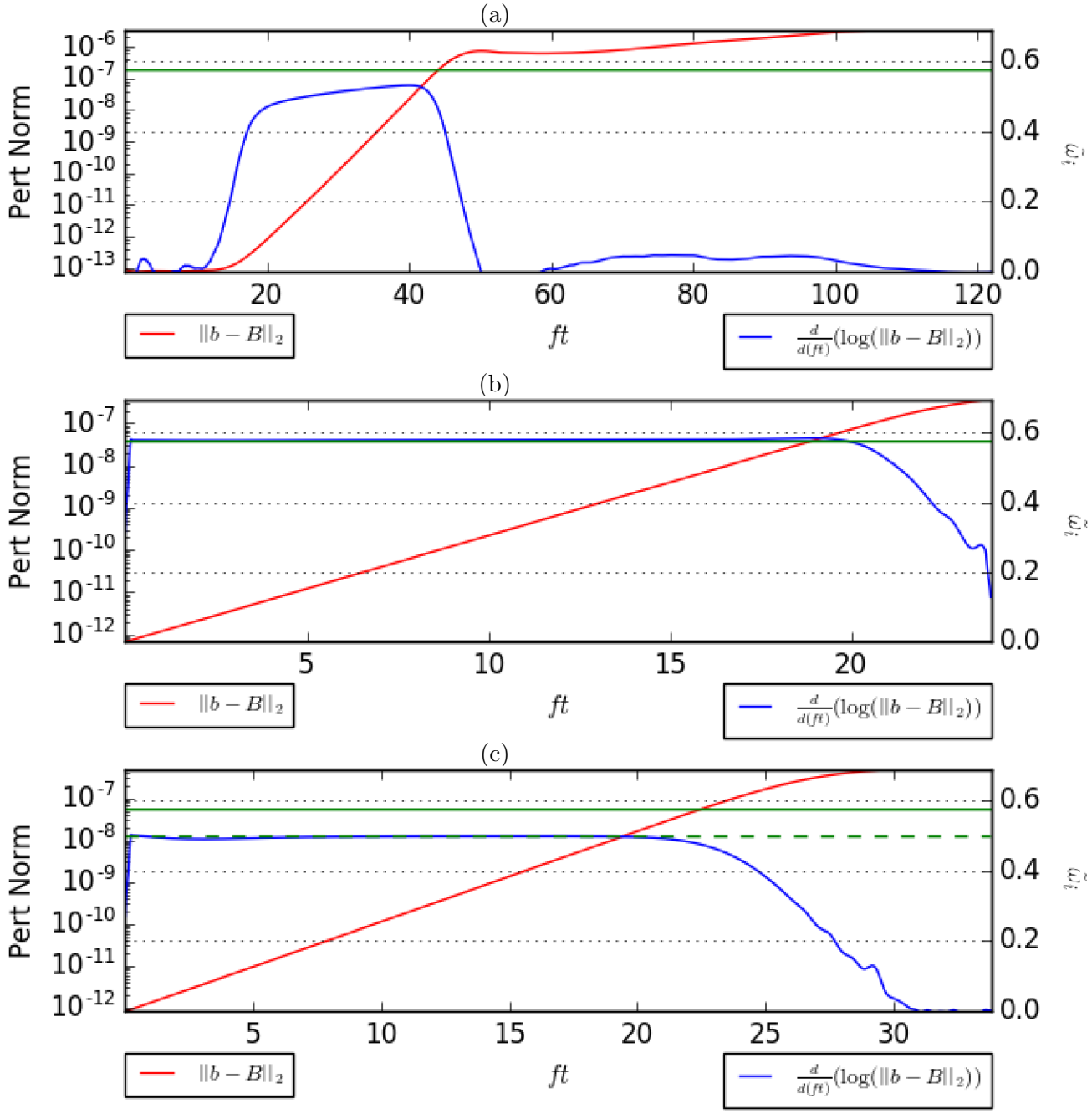

Figure 5.15: The ℓ^2 norm of the buoyancy perturbation field, approximations of the growth rate and the maximal growth rate from linear theory for three 3D simulations of a baroclinic jet using parameter set 1 in Table 5.1. The red lines are plotted on the left axis while the blue and green curves are plotted on the right axis. Plots (a)-(c) show the simulations where the initial buoyancy perturbation is given by a random field, the case where the initial perturbation is given by the fastest growing mode (SI mode), and the case where the initial perturbation is given by the second fastest growing mode that fits in the simulation domain respectively.

spontaneously. Figures 5.16a-5.16c show the $y-z$ structure of the buoyancy and vertical velocity perturbations along with the EPV field at times $ft = 34$, $ft = 42$ and $ft = 45$ respectively. The colormaps follow the same convention as the previously examined plots of this type.

Figure 5.16a is at a time where the perturbation is exponentially growing. Here we plot black contours for the isolines of the w field for the most unstable mode as predicted by linear stability theory. Visually one can see that the w velocity field agrees rather well with the predictions made by 2D linear theory.

Figures 5.16b and 5.16c show the spatial structures when the perturbation begins to saturate. By comparing these plots with Figure 5.13b, we see that the process of nonlinear saturation begins similarly in both the 2D and 3D simulations. Similar to the 2D simulation, the last structure we plot is the final output of our model before small scale features begin to appear. Due to the lower resolution of this simulation we are unable to capture the small scale mushroom cloud plumes of EPV that were previously seen in the high resolution 2D simulation. Nevertheless, the process of EPV stirring has began as seen by the formation of oscillations similar to those previously seen in our 2D simulation. As before, the number of oscillations correspond to the wavenumber of the vertical velocity perturbation field.

In the work by Ribstein et al. [73], the process of saturation of the EPV field was considerably more messy and while they saw that the initial onset of nonlinear saturation was concentrated in the middle of the region of negative EPV, they did not see the development of well-defined oscillations in the vertical direction. This is quite likely due to a combination of the lack of an explicit viscosity in their simulations, the ultraviolet catastrophe that is present in the inviscid problem, and the higher numerical diffusivity of WRF.

EPV Hovmöller plot: In Figure 5.17 we show the Hovmöller plot of the EPV at mid-depth and in the middle of the x direction for the 3D simulation with a random initial perturbation. Our choice for the value of z and x quantitatively changes the Hovmöller plot but does not qualitatively change the conclusions we draw. The EPV field for the 3D baroclinic jet initially has little variation in time but then there are small scale features that form and finally there is the development of coherent vortices due to a secondary instability. The secondary instability was previously noted in the work of Ribstein et al. [73]. Comparing Figure 5.17 to Figure 5.7 for the EPV Hovmöller plot for the 3D barotropic jet, we notice that the plots are qualitatively similar. On the other hand, comparing Figure 5.17 to the EPV Hovmöller plot for the 2D baroclinic jet shown in Figure 5.14 we see that the major difference is the lack of vortices in our 2D simulations. Notice that as we

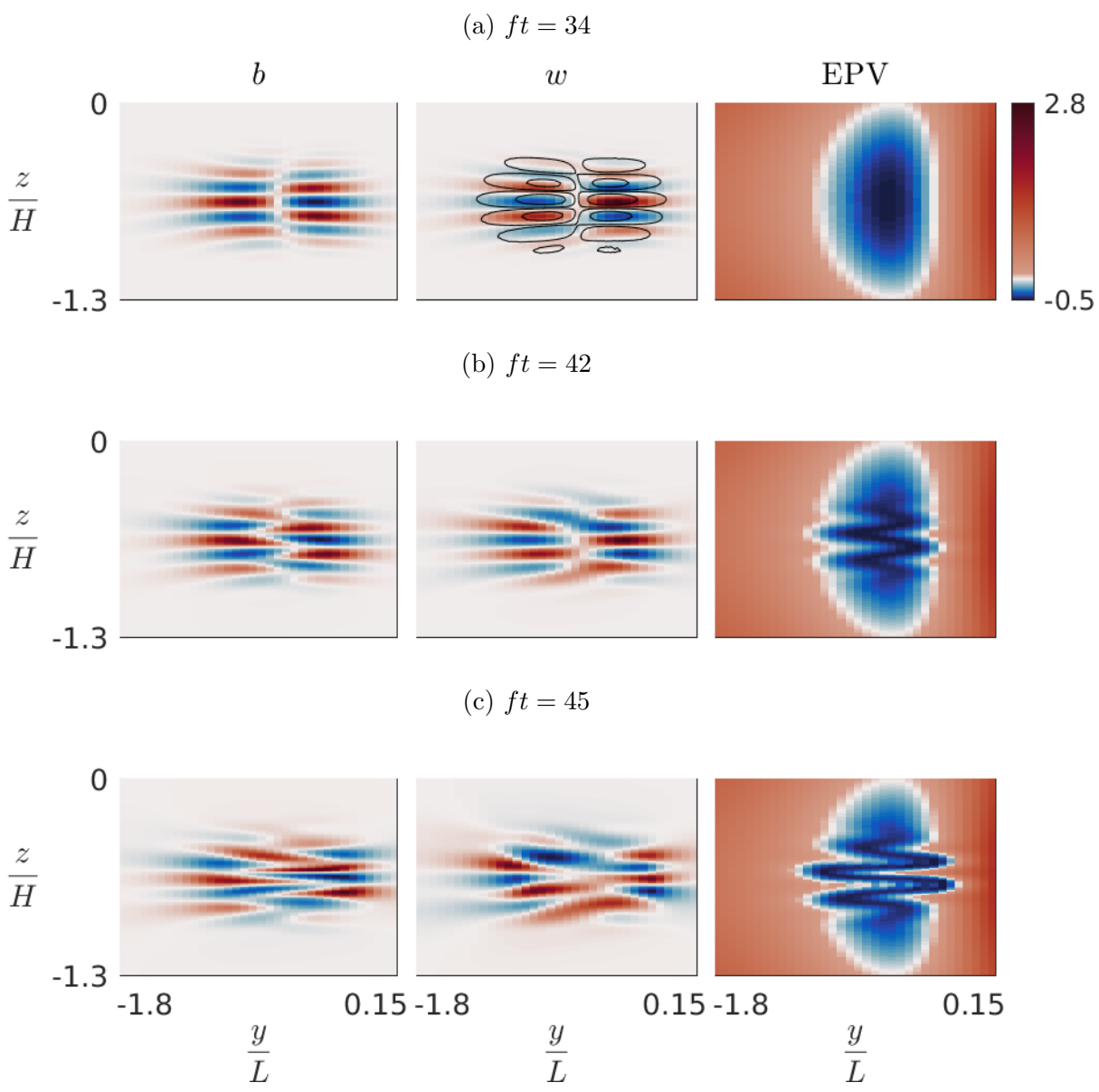

Figure 5.16: $y - z$ slices of the buoyancy and vertical velocity perturbation fields along with the total EPV the field for the $256 \times 512 \times 2048$ resolution simulation of a nonlinear model for a randomly perturbed baroclinic jet using parameter set 1 in Table 5.1. All slices are taken in the middle of the x direction. The colormaps for the buoyancy and vertical velocity perturbation fields are fully saturated with zero being white and the colormaps are the same for all EPV fields shown.

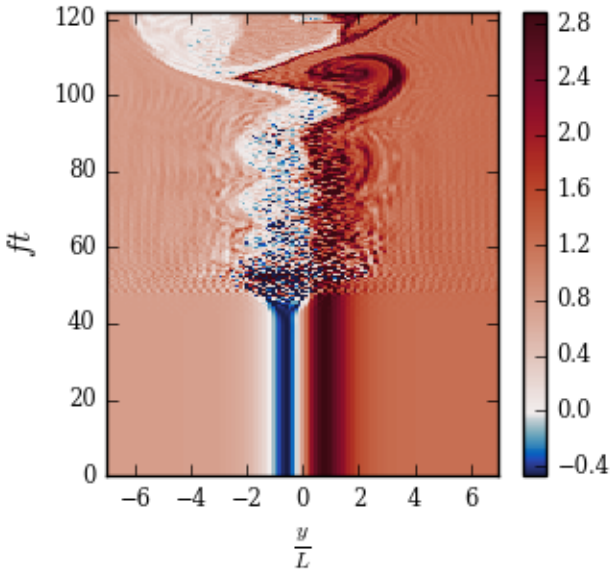

Figure 5.17: A slice of the total EPV field normalized by $N^2 f$ for a 3D simulation of the baroclinic jet using parameter set 1 in Table 5.1. The slice is taken along the middle of the z plane where the EPV obtains its initial extrema and at mid-length.

have previously seen, the development of small scale features coincide with the EPV field becoming non-negative. We conclude that the primary instability is II.

Mixing efficiency: Finally we examine the mixing efficiency of the instabilities via an examination of the flux Richardson number Ri_f defined in Section 3.4. Figure 5.18 shows the mixing efficiency along with the dissipation rate and turbulent buoyancy flux for the 3D baroclinic simulation with random initial perturbation. We normalized both the dissipation rate and turbulent buoyancy flux so that their relative values can be seen. Similar to the barotropic case, we see that during the initial onset of instability the flux Richardson number is small (0.09) which is around half the efficiency typical of KH instability. After the saturation of the instability, the mixing efficiency quickly increases to around 0.35 and once the secondary instabilities begin to grow, the mixing efficiency increases to 0.7 and continues to increase. Like in the barotropic case, large mixing efficiency could be a consequence of the large Reynolds number we used for this case.

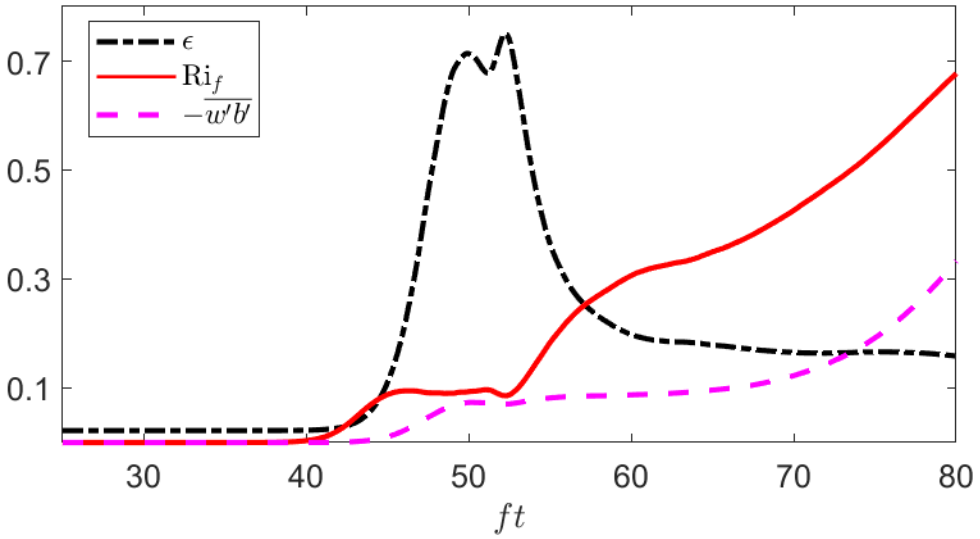

Figure 5.18: The flux Richardson number Ri_f for mixing efficiency for a 3D simulation of a randomly perturbed baroclinic jet using parameter set 1 in Table 5.1. Here the black and magenta curves are the dissipation rate and turbulent buoyancy flux respectively. We normalized the dissipation rate to have a maximum of 0.75 and use the same normalization factor for the turbulent buoyancy flux.

5.2 Parameter Set 2

Previously, we saw that the large Reynolds number we used led to the development of fast growing instabilities with grid scale features that we were unable to resolve in our nonlinear simulations. We expect that decreasing the Reynolds number will reduce the growth rates of the instability. We thus quantitatively and qualitatively study the effect of lowering the Reynolds number by almost three orders of magnitude and consider a simulation with a smaller Reynolds number of 2.2×10^5. All of the other nondimensional parameters are unchanged. This Reynolds number is similar to what Molemaker et al. [56] used to study the California undercurrent and is smaller than the Reynolds numbers considered by Ribstein et al. [73] and Plougonven and Zeitlin [67]. We start our analysis of barotropic and baroclinic jets with this parameter set by examining the linear stability analysis of both jets with the 1D and 2D eigenvalue problems respectfully. We then examine the details of two 3D nonlinear simulations of the baroclinic jet. To our knowledge, the results in this section are novel unless we specify otherwise.

5.2.1 Linear Stability Analysis: Barotropic Jet

Growth rates: The maximal growth rates for the barotropic jet as predicted by the 1D eigenvalue solver are shown in Figure 5.19. One immediately obvious difference between these growth rates and those found for parameter set 1 (Figure 5.1) is that the most unstable mode is now a nonsymmetric II and lies on the k-axis instead of the m-axis. By examining growth rate plots for jets with Reynolds numbers between these two cases, we have confirmed that the results vary continuously with the Reynolds number. In between these two parameter sets, the most unstable modes can occur for both $m \neq 0$ and $k \neq 0$. Generally speaking, the effect of lowering the Reynolds number is to decrease the vertical wave number of the most unstable mode while also increasing its horizontal wave number. Physically, this means that decreasing the Reynolds number moves the most unstable mode to larger scales in the vertical direction and shorter scales in the horizontal direction. This general behaviour has been previously noted by Wang et al. [93] among other. An example of this type of behaviour is shown Section 5.3 when we study the stability of jets with nondimensional parameters given by parameter set 3 and in Section 5.4 when we perform parameter studies. Finally, by comparing these growth rates to those presented in Figure 5.1 for parameter set 1 we see that the growth rates have decreased by nearly a factor of two. Thus the effect of lowering the Reynolds number is indeed to dampen the growth rates as expected and as has been previously reported throughout the literature [9, 67, 69, 73].

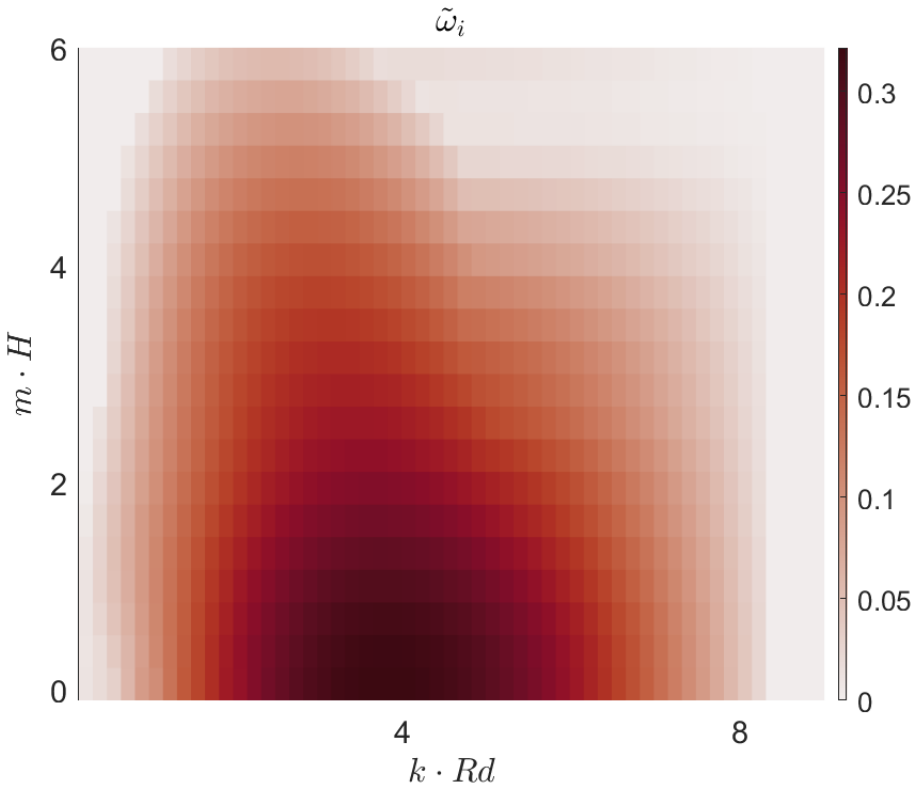

Figure 5.19: The largest normalized growth rates as predicted by the 1D eigenvalue problem for the barotropic jet using parameter set 2 in Table 5.1.

5.2.2 Linear Stability Analysis: Baroclinic Jet

Growth rates: Figure 5.20 shows growth rates for the baroclinic jet as predicted by the 2D eigenvalue problem alongside the growth rates for the barotropic jet as predicted by the 1D eigenvalue problem. Like we have previously done, the dependence of the growth rates of the barotropic jet on the vertical wavenumber m is removed by taking the maximum over m. It is apparent that while the qualitative behavior of the curves is quite similar, the growth rates of the baroclinic jet are significantly smaller than those for barotropic jet. Focusing on the fastest growing modes (kRd$\approx$ 3.9 mode) for both jets, we see that the fastest growing mode for the barotropic jet grows more than twice as rapidly as the fastest growing mode for the baroclinic jet. The significant difference between the growth rates of the barotropic jet and the baroclinic jet in this case means that despite what some previous studies have done, one cannot always use the stability properties of barotropic jets to quantify the stability of their baroclinic counterparts.

Modal structures: We now examine the structure of the SI mode and the II mode with k Rd$=$ 3.9 as predicted by the 2D baroclinic eigenvalue problem solver. Recall that the SI mode was the most unstable mode for parameter set 1 and that kRd$\approx$ 3.9 is the most unstable mode for the parameter set currently under consideration. Figure 5.21a shows the real part for the vertical velocity of the most unstable symmetric mode which nondimensional growth rate $\tilde{\omega}_i = 0.0059$ and Figures 5.21b-5.21c show the real and imaginary parts for the vertical velocity of the most unstable mode with nondimensional growth rate $\tilde{\omega}_i = 0.140$. Like we did when examining the modes for parameter set 1, we mark the 0 contour for the EPV field by a black curve. The spatial structures are completely different to those we previously saw. The vertical and horizontal extent of these modes is significantly larger than the region where the EPV of the background current is negative. This is an unexpected but intriguing result. Furthermore, the vertical velocity for the fastest growing mode ($kRd = 3.9$) has a $m = 1$ structure in the vertical direction instead of the more typical "pancake" like structure of II modes. Based on this structure, we predict that during the nonlinear saturation process, the EPV field will also develop a $m = 1$ structure in the vertical. Turning our attention to the symmetric inertial mode, we see a barotropic like $m = 0$ structure in the vertical. Generally speaking, we do not expect this mode to be relevant in our nonlinear simulations as its growth rate is much smaller than the growth rate of the most unstable mode.

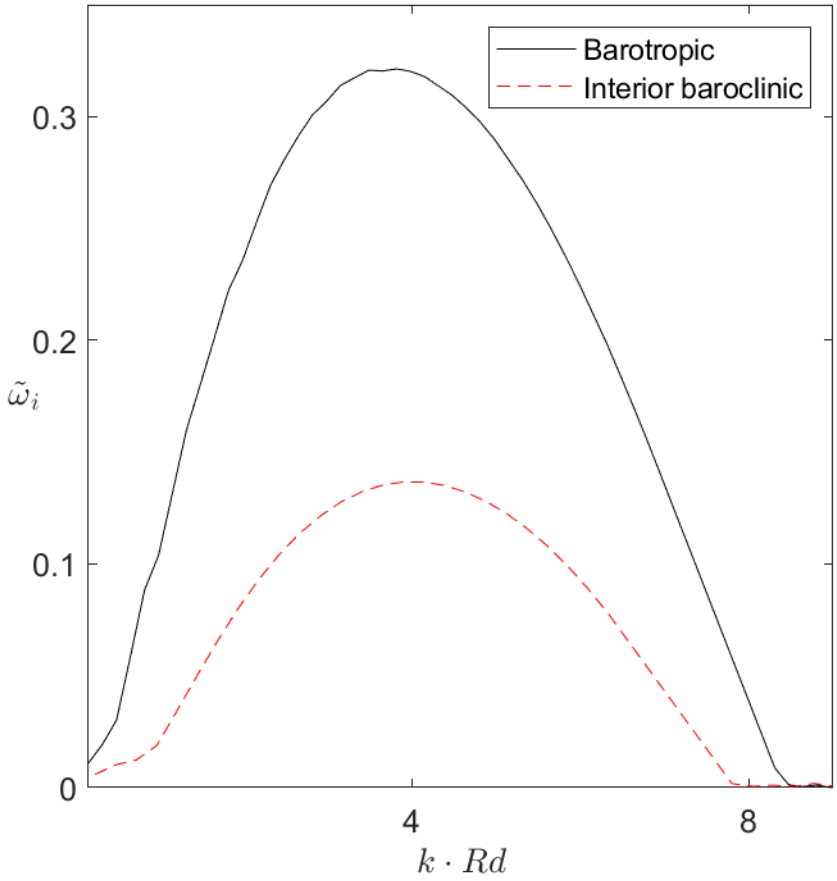

Figure 5.20: The largest normalized growth rates over all vertical wave numbers, m, for the barotropic jet as computed by the 1D eigenvalue solver (solid black) and for the baroclinic jet as computed by the 2D eigenvalue solver (dashed red) using parameter set 2 in Table 5.1.

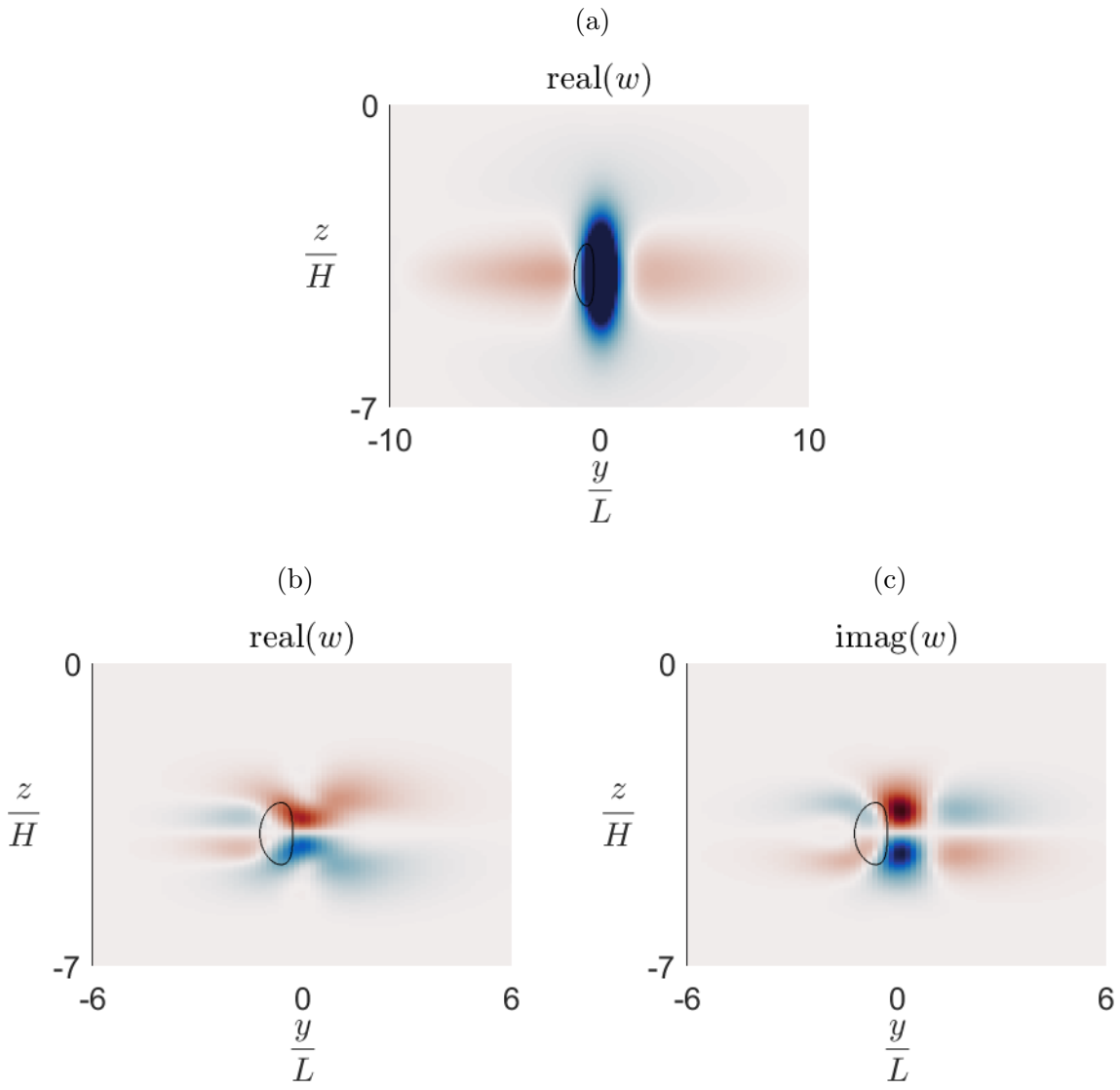

Figure 5.21: The structures for two different unstable modes along with contours for zero EPV for the baroclinic jet using parameter set 2 in Table 5.1. Plot (a) shows the slow growing $k = 0$ mode and plots (b) and (c) show the real and imaginary parts of the vertical velocity field for the most unstable mode with $k\mathrm{Rd} \approx 3.9$.

5.2.3 3D Nonlinear Simulations of a Baroclinic Jet

We now examine the results of the two 3D nonlinear simulations - one with a random initial perturbation to the buoyancy field and one where the perturbation is given by the most unstable mode which for this parameter set is a nonsymmetric inertial mode. In both simulations, we use a resolution of $256 \times 256 \times 1024$ and a domain length that fits one wavelength of the most unstable mode as predicted from 2D linear theory ($k\text{Rd}= 3.9$ mode).

Growth rates: Figure 5.22 shows the evolution of the ℓ_2 norm of the buoyancy perturbation, approximated growth rate, and the largest growth rate predicted by 2D linear theory.

We start by examining the results for the simulation with a random initial buoyancy perturbation shown in Figure 5.22a. Here the growth rate predicted by the simulation is approximately constant from $ft \approx 50$ to $ft \approx 150$. Over this time period, the perturbation has a computed growth rate of 0.138 which differs from linear theory by 1.4%. The agreement between linear theory and this nonlinear simulation is both significantly better than what we saw for 3D simulations with random initial buoyancy perturbations for parameter set 1 and significantly better than what we have seen in previous studies of SI. The better agreement compared to what we saw in parameter set 1 could be because the most unstable mode for parameter set 2 has larger scale features than the mode in parameter set 1 and is thus better resolved while the better agreement as compared to previous works is likely because of our use of a spectral model. Unlike in our higher Reynolds number case, there is no secondary adjustment to the buoyancy norm after the perturbation nonlinearly saturates and thus there might not be a secondary instability. A similar behavior has been previously seen in the work of Radko and Lorfeld [69] when studying the relative growth rates of inertial and baroclinic instabilities in jets unstable to both types of instability. More evidence of this claim is provided when we examine the spatial structures of the instability.

In Figure 5.22b for the seeded simulation, we see the buoyancy norm has the expected behaviour. Due to the smaller growth rate for the instability, we increased the size of the initial perturbation by three orders of magnitude. The computed growth rate of the nonlinear model is 0.140 which is the same as linear theory. These results show that our 2D barotropic eigenvalue problem solver accurately computes the most unstable mode for this parameter set. We have thus extended the range of parameters for which we have validated our 2D eigenvalue solver.

Perturbation structure: In order to understand how the perturbation saturates, we now examine the spatial structures as predicted by the simulation with a random initial

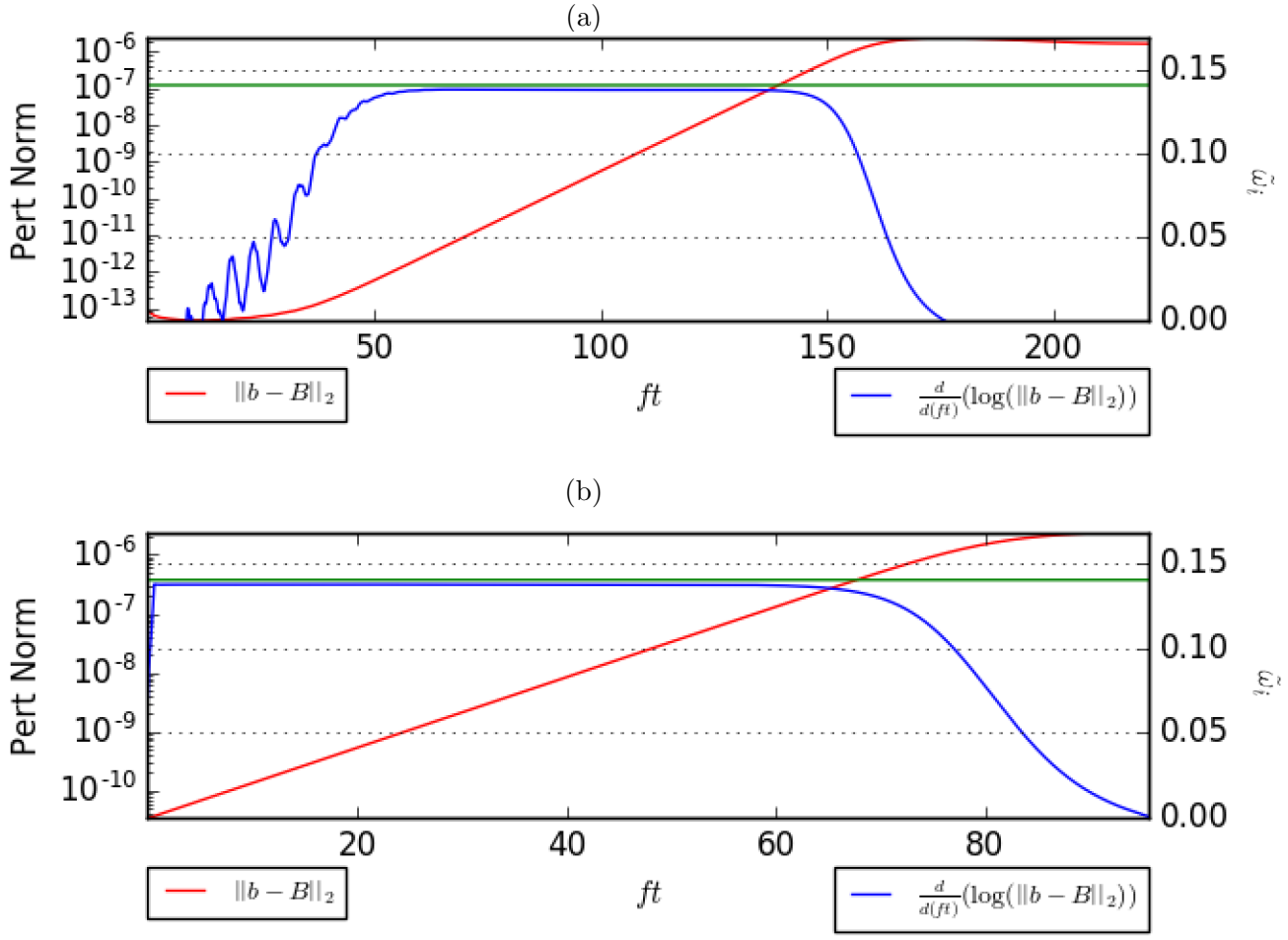

Figure 5.22: Plots of the ℓ^2 norm of the buoyancy perturbation field, approximations of the growth rate and the maximal growth rate from linear theory for two 3D simulations of the baroclinic jet using parameter set 2 in Table 5.1. The red lines are plotted on the left axis while the blue and green curves are plotted on the right axis. All plots have a resolution of $256 \times 256 \times 1024$. In plot (a) we show the 3D case where the initial buoyancy perturbation is given by a random field and in plot (b) we show the 3D case where the initial perturbation is given by the fastest growing mode as predicted by our 2D eigenvalue problem.

perturbation. Figure 5.23 shows the $y-z$ structure of the buoyancy perturbation, the vertical velocity perturbation, and the total EPV field while Figure 5.24 shows the $x-y$ structures for the same fields. We choose to fix $x=0$ for the plots in Figure 5.23 and to take z to be mid-depth for the plots in Figure 5.24. This means that as time evolves so does the phase of the perturbation. For consistency with our plots for parameter set 1, we use the same coloring scheme.

Figures 5.23a and 5.24a show the perturbation structure at time $ft = 102$ during the middle of the exponential growth phase. We chose this specific value of ft because the spatial structures at this time agree with the imaginary part of the fastest growing mode as predicted by linear theory. To this point, the black contours is Figure 5.23a are isolines of the imaginary part of the mode shown in Figure 5.21c and the wavelength of the perturbation in Figure 5.24a matches our prediction from linear theory.

Figures 5.23b and 5.24b are taken at time $ft = 148$. We chose this time because it shows good agreement with the real part of the fastest growing mode as predicted by linear theory. The black curves in Figure 5.23b are contours of the real part of the predicted w field shown in Figure 5.21b. Similar to before, the perturbation in Figure 5.24b has the wavenumber that linear theory predicts.

The process of nonlinear saturation at times $ft = 159$ and $ft = 168$ is shown in Figures 5.23c-5.23d and 5.24c-5.24d. Here we see that the EPV field oscillates in the y direction, has a $m = 1$ like structure in the z direction, and has a wavelength in the x direction that matches the most unstable mode. Furthermore as we have previously predicted, near grid scale features no longer develop. Instead, we can clearly see the process by which the EPV becomes positive. As the perturbation saturates, the EPV is advected laterally and mixing of the EPV field occurs. This mixing coincides with the formation of a cyclonic-anticyclonic pair of vortices. Figures 5.24c and 5.24d show that the EPV in the core of the anticyclonic vortex becomes non-negative as the vortices form. Since the vortex pairs form at the same time as the II mode saturates, there is no secondary instability and II is directly responsible for the formation of a cyclonic-anticyclonic vortex pair that is centrifugally stable.

Mixing efficiency: Figure 5.25 shows the mixing efficiency along with the dissipation rate and turbulent buoyancy flux for the 3D baroclinic simulation with random initial perturbation. Here we normalized both the dissipation rate and turbulent buoyancy flux so that their relative values can be seen. In this simulation the mixing efficiency of II is very close to zero for early times and obtains a maximum of around 0.08 when nonlinear saturation occurs. Thus at least for this case II has a relatively low mixing efficiency. This is likely due to the large vertical length scale of the most unstable mode.

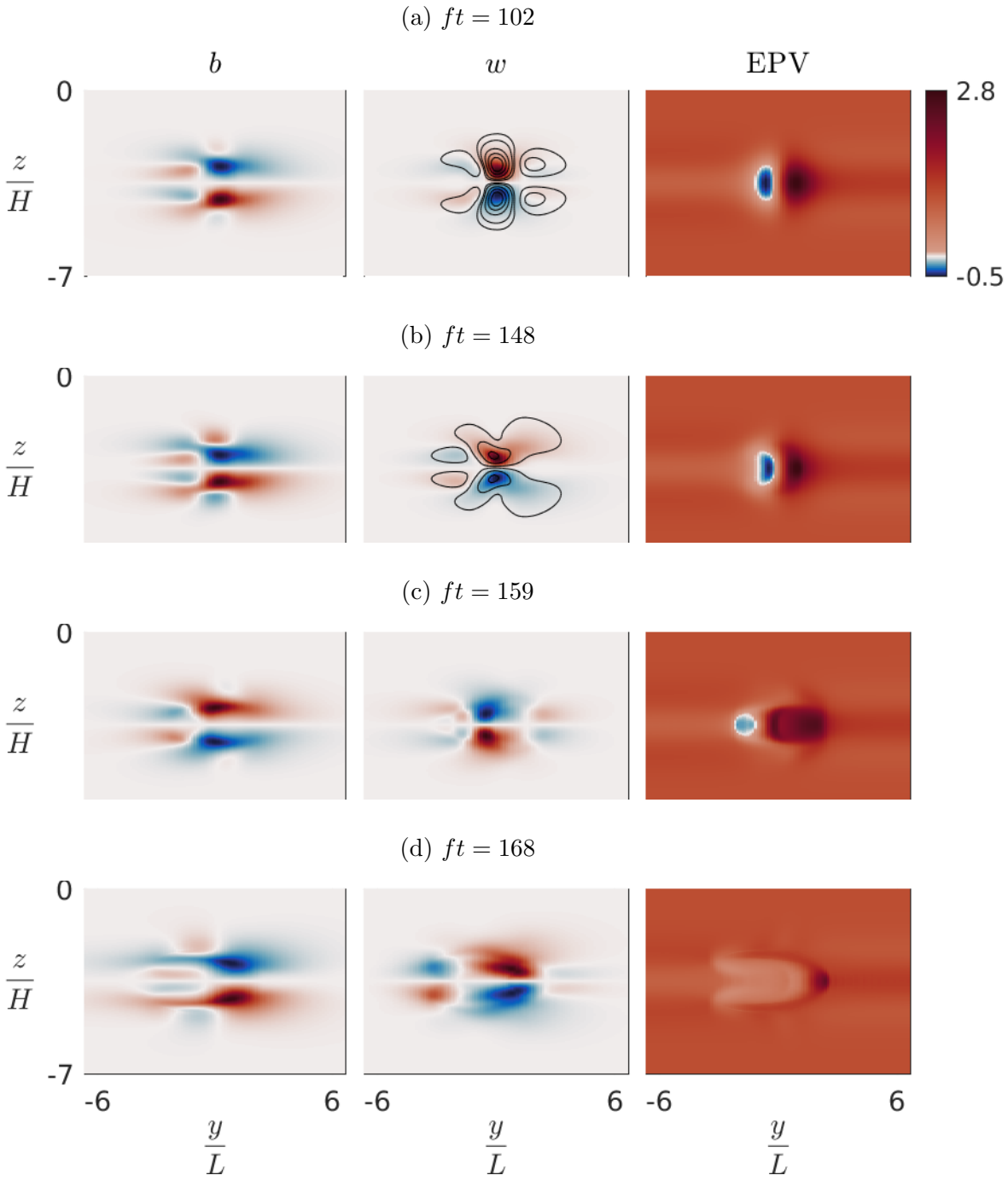

Figure 5.23: $y-z$ slices of the buoyancy and vertical velocity perturbation fields along with the EPV field for the $256\times256\times1024$ resolution nonlinear model for a randomly perturbed baroclinic jet using parameter set 2 in Table 5.1. Here the slices are taken in the middle of the x direction. The colormaps for the buoyancy and vertical velocity perturbation fields are fully saturated with zero being white and the colormaps are the same for all EPV plots.

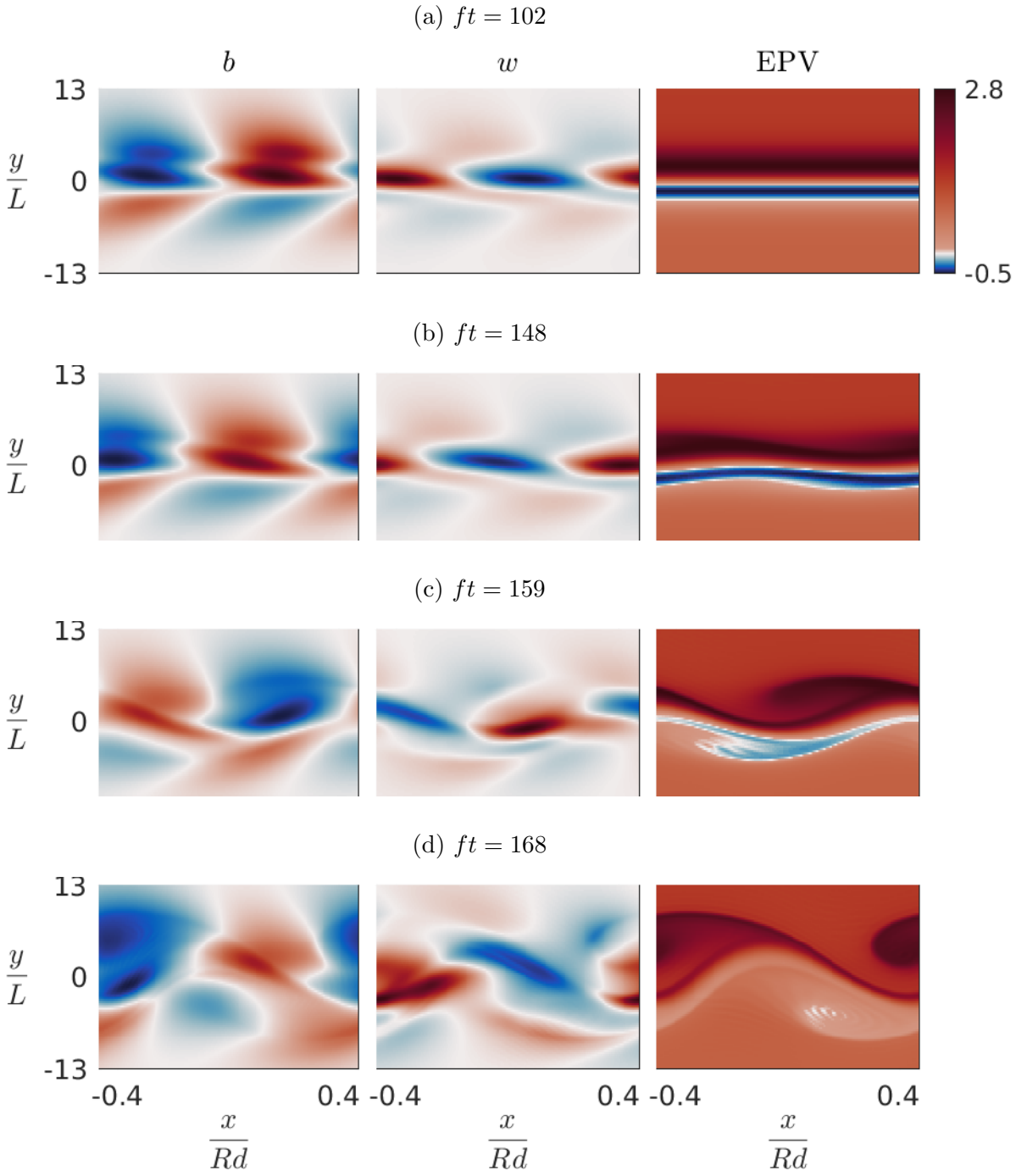

Figure 5.24: Mid-depth $x - y$ slices of the buoyancy and vertical velocity perturbation fields along with the EPV field for the $256 \times 256 \times 1024$ resolution nonlinear simulation for a randomly perturbed baroclinic jet using parameter set 2 in Table 5.1. The colormaps for the buoyancy and vertical velocity perturbation fields are fully saturated with zero being white and the colormaps are the same for all EPV plots.

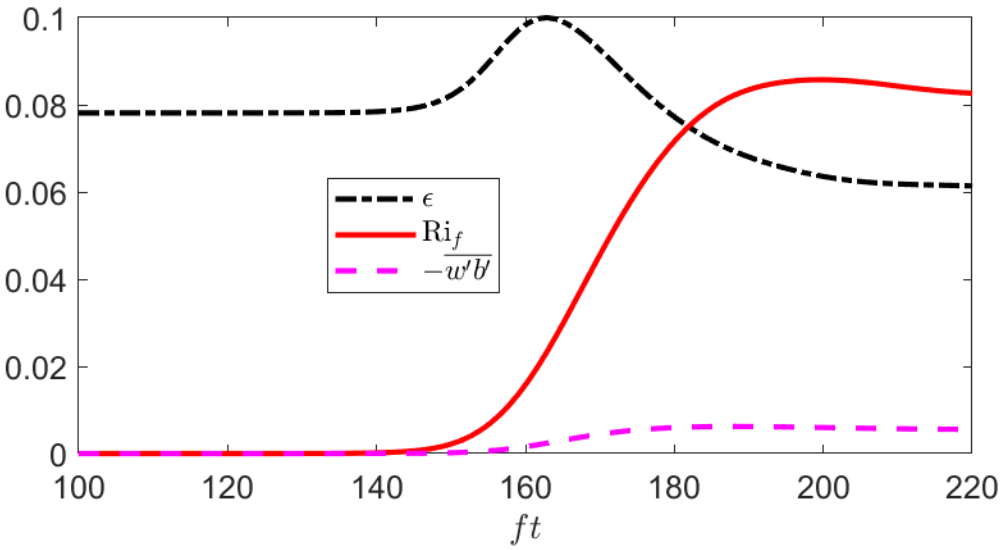

Figure 5.25: The flux Richardson number Ri_f for mixing efficiency for a 3D stimulation of a randomly perturbed baroclinic jet using parameter set 2 in Table 5.1. Here the black and magenta curves are the dissipation rate and turbulent buoyancy flux respectively. We normalized the dissipation rate to have a maximum of 0.1 and use the same normalization factor for the turbulent buoyancy flux.

5.3 Parameter Set 3

The final set of parameters we consider are identical to parameter set 2 except that the aspect ratio is larger, $\delta = 0.1$. Physically this means that ratio of the height to the length of this jet is approximately three times larger than in the previous section and as a result there is a larger region where the EPV is negative. For this parameter set, if we were to choose a characteristic length scale of $L = 4$ km and an f value of $0.864 \times 10^{-4} s^{-1}$ then our jet is similar to the jet used by Molemaker et al. [56] in their study of the California undercurrent. One of the unstratified barotropic jets studied by Carnevale et al. [9] had similar nondimensional parameters but a smaller Reynolds number of 1.25×10^4. We first examine the stability analysis of the barotropic and baroclinic jets and then we examine two 3D simulations of the baroclinic jet. To our knowledge, the results in this section are novel unless we specify otherwise.

5.3.1 Linear Stability Analysis: Barotropic Jet

Growth rates: Figure 5.26 shows the largest growth rate as predicted by the 1D eigenvalue problem for the barotropic jet. While the largest growth rates are comparable to what we saw when examining parameter set 2, the general behaviour of the growth rates as a function of the wavenumbers for this parameter set are different. Most notably, there are now three distinct regions of instabilities: one with $k \approx 0$ and $mH \gtrsim 10$, one with nontrivial vertical and horizontal wave numbers, and one with $m \approx 0$. Note that there is a region of small growth rates that separates the symmetric inertial modes from the nonsymmetric inertial modes with large wavenumbers k.

Modal structures: In order to differentiate the three regions in Figure 5.26, we examine the y structure of a representative mode within each region. Explicitly, we choose the fastest growing modes for $m = 0$ and $mH = 8$ as well as the $(k, mH) = (0, 18)$ mode. Figure 5.27 shows the cross channel structure for each of the three modes we consider. As each mode has a complex valued free parameter for its phase, to be consistent we choose the phase that maximizes real(w). The main distinction between these modes is their vertical structures but there are also differences in the cross-channel structures. The $(k, mH) = (0, 18)$ mode is entirely real as we have seen for the other symmetric inertial modes. Examining the structures of the $mH = 8$ and $mH = 0$ modes, we see that they have some differences in their cross channel structures. Finally the cross channel structures of both the SI mode with $mH = 18$ and the most unstable nonsymmetric II modes for $mH = 8$ and $mH = 0$ are comparable to the structures of the respective modes found by

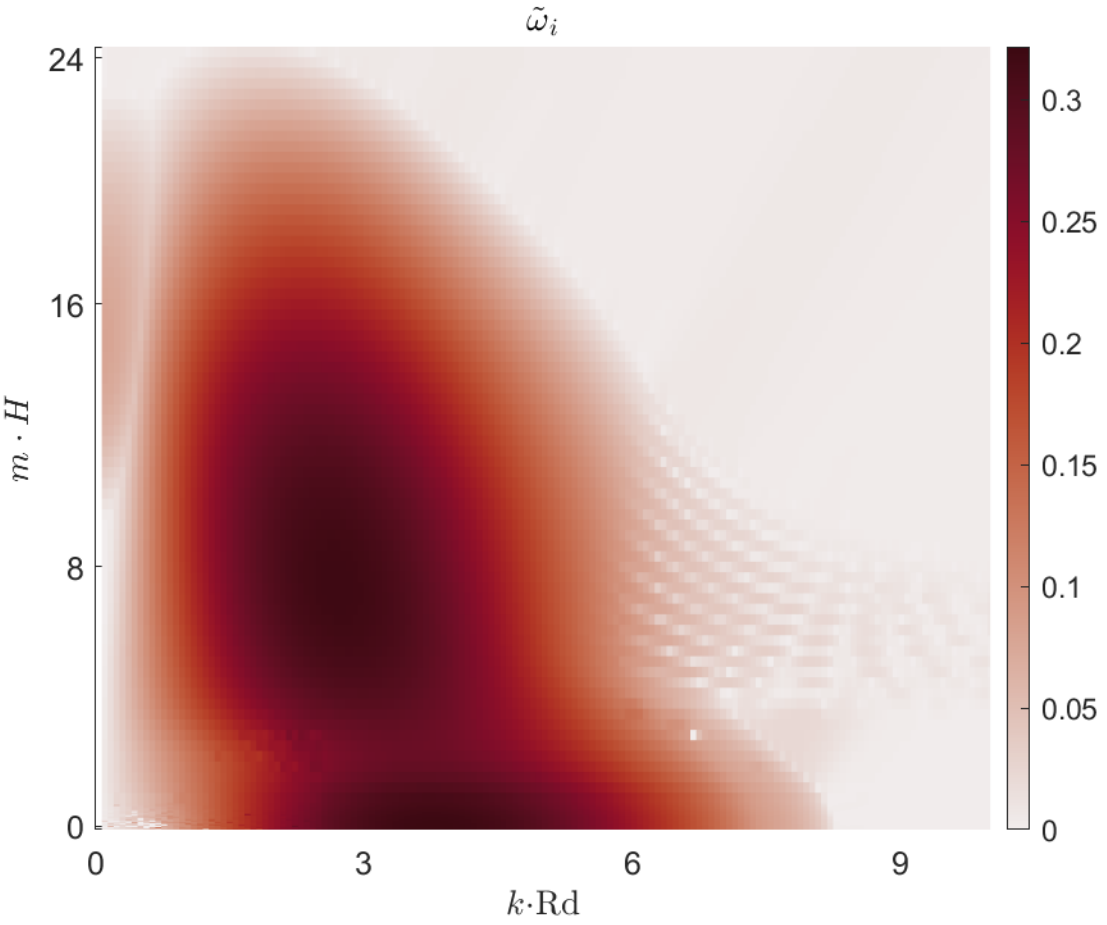

Figure 5.26: The largest normalized growth rates as predicted by the 1D eigenvalue problem for the barotropic jet using parameter set 3 in Table 5.1. These nondimensional parameters correspond to some flows that have been observed in the California undercurrent.

Tort et al. [89] when they considered their reference configuration ($\delta = 0.1$ and Ro$= 2.7$) under an inviscid 2-layer SW model.

5.3.2 Linear Stability Analysis: Baroclinic Jet

Growth rates: Figure 5.28 plots the maximal growth rates of the baroclinic jet alongside the growth rates of the $mH = 0$, $mH = 8$, and $mH = 18$ modes for the barotropic jet. Focusing on the fastest growing modes, we see that the fastest growing inertial mode for the baroclinic jet has a wavenumber of $k \cdot Rd \approx 2.46$ and its nondimensional growth rate of $\tilde{\omega}_i = 0.2752$ is slightly smaller than the fastest growing mode for the barotropic jet. Compared to the most unstable mode for the baroclinic jet with parameter set 2, the most unstable mode for this baroclinic jet grows twice as fast.

Qualitatively, the growth rates for both the baroclinic jet and the $mH = 8$ and $mH = 18$ modes for the barotropic jet increase as the wavenumber k decreases for small wavenumbers. This hints that for small k, the most unstable modes for the baroclinic jet might have a more oscillatory structure in the vertical direction. This is confirmed shortly when we examine the spatial structure of the SI mode. While the above is an interesting observation, due to the relatively small growth rates we do not expect the SI modes to be geophysically relevant. Finally, with the exception of the oscillatory behaviour of the $mH = 8$ mode for $k\text{Rd} \gtrsim 6$, the behaviour of the baroclinic growth rate curves agrees with the behaviours of the barotropic curves for $k\text{Rd} \gtrsim 0.5$. We believe the oscillatory behaviour of the $mH = 8$ curve for large values of k is a numerical artifact.

Modal structures: We now examine the spatial structure of the most unstable ($k\text{Rd} \approx 2.46$) mode for the baroclinic jet as well as the structure for the $k = 0$ mode. Figure 5.29a shows the real part of the $k = 0$ mode and Figures 5.29b and 5.29c show the real and imaginary parts for the most unstable mode respectively. Both modes are vertically bounded by the zeros of the EPV field similar to what we saw in parameter set 1 but unlike what we saw in parameter set 2. In the horizontal direction the structures tend to decay away of the region of negative EPV but obtain their maxima outside of the zero EPV contour. Focusing on the $k = 0$ mode shown in Figure 5.29a we see the oscillatory behaviour we previously predicted and the "pancake" like structures typical of II. In comparison, the most unstable mode shown in Figures 5.29b-5.29c has a less "pancake" like structure but instead looks like an $m = 2$ mode.

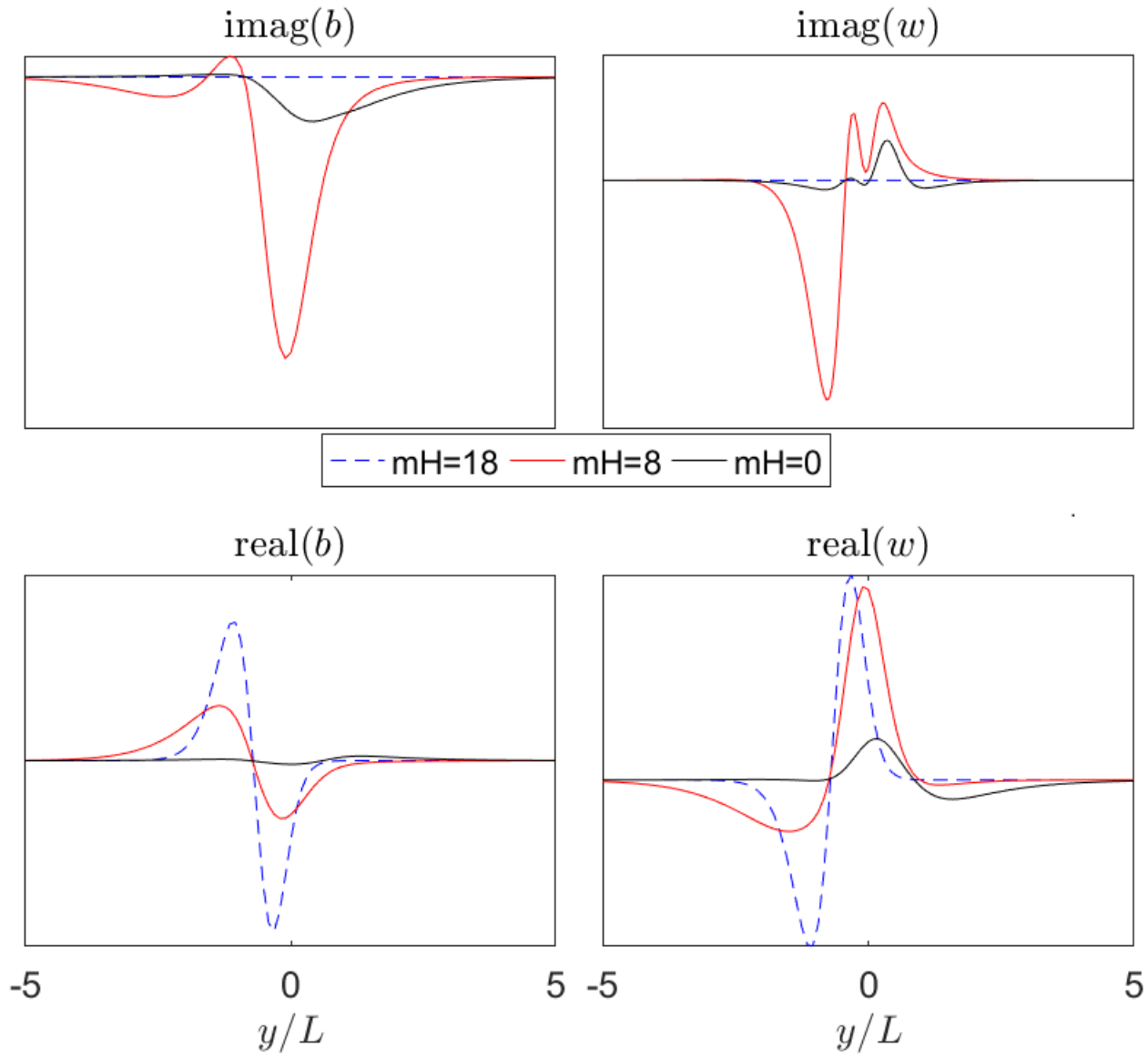

Figure 5.27: The lateral structure of the most unstable mode for $m = 0$, $mH = 8$ as well as the $(k, mH) = (0, 18)$ mode for the barotropic jet using parameter set 3 in Table 5.1.

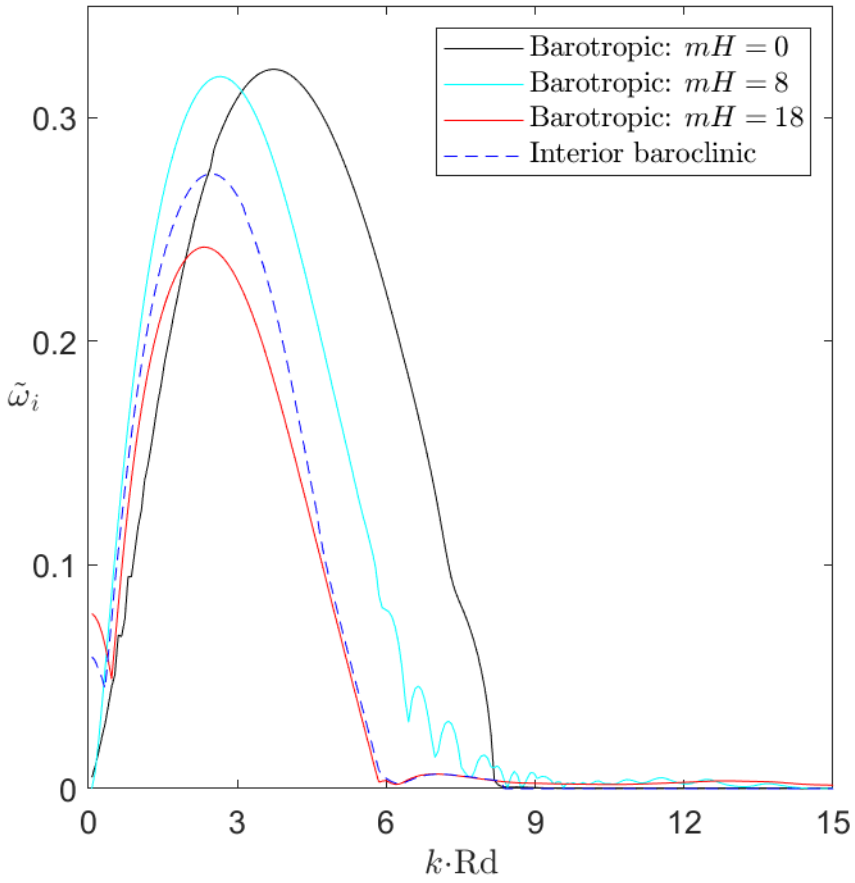

Figure 5.28: The largest normalized growth rates as predicted by the 1D eigenvalue problem for the barotropic jet for various wavenumbers m (solid black, teal and red) and the largest normalized growth rates as predicted by the 2D eigenvalue problem for the baroclinic jet (dashed blue). For both jets, we use the nondimensional numbers given by parameter set 3 in Table 5.1.

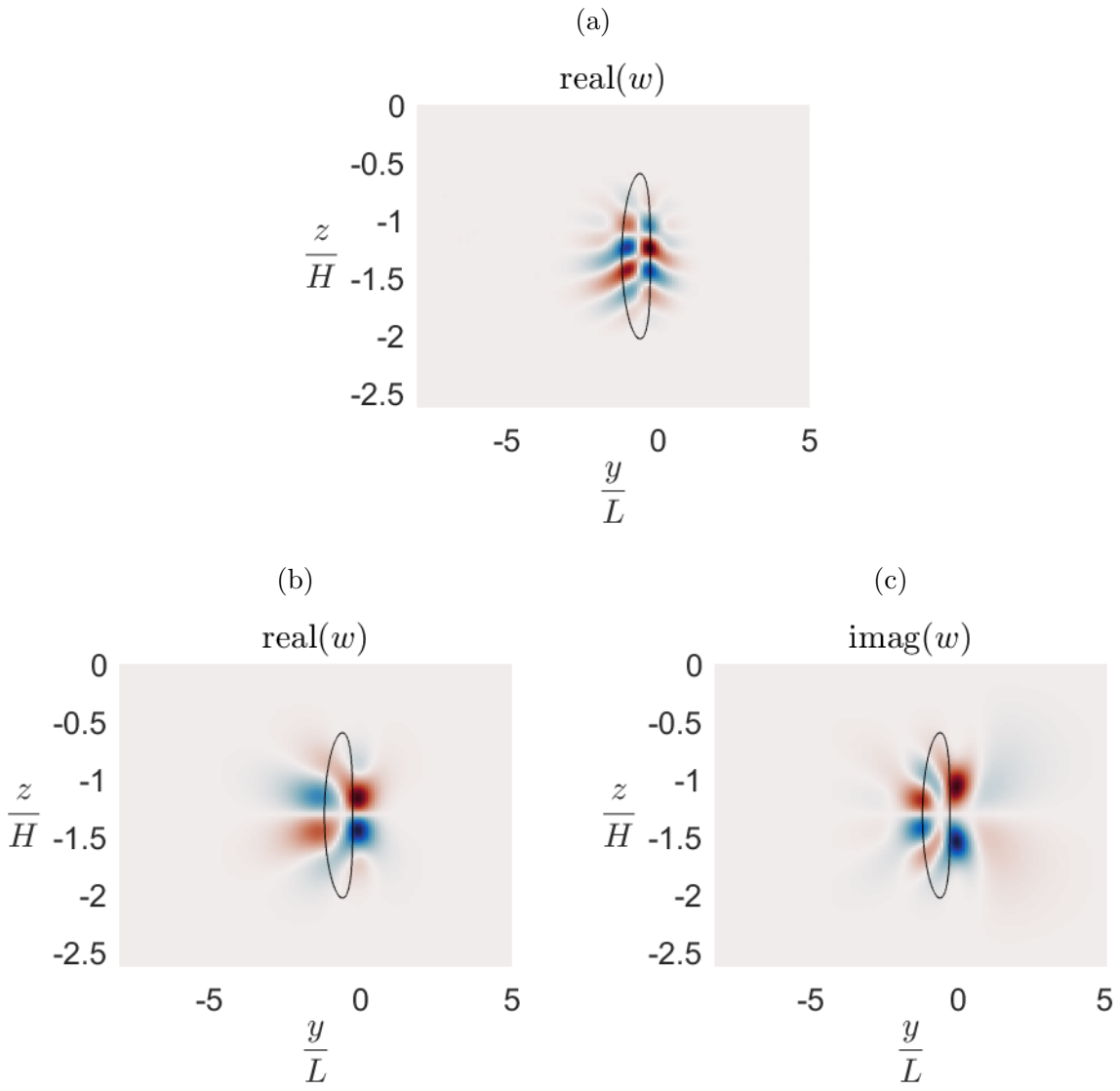

Figure 5.29: The structures for two unstable mode along with contours for zero EPV for the baroclinic jet using parameter set 3 in Table 5.1. Plot (a) shows the real part of the $k = 0$ mode and plots (b)-(c) are the real and imaginary parts of the vertical velocity field for the most unstable mode $k \cdot Rd \approx 2.46$.

5.3.3 3D Nonlinear Simulations of a Baroclinic Jet

We now examine two simulations for this parameter set: one where the buoyancy perturbation is initially random and one where the perturbation is given by the fastest growing mode predicted from linear theory ($k\text{Rd}\approx 2.46$). Both simulations use a resolution of $256 \times 256 \times 1024$. Unlike the previous cases where we use a domain length in the x direction that fit only one wavelength of the most unstable mode, we choose the domain length that contains four wavelengths of the most unstable mode.

Growth rates: Figure 5.30 plots the change in the ℓ_2 norm of the buoyancy perturbations for each simulation.

From time $ft \approx 20$ to $ft \approx 60$ in Figure 5.30a we see a region of exponential growth with a relatively constant predicted growth rate that visually agrees with what linear theory predicted. The predicted growth rate in Figure 5.30b likewise agrees with linear theory from $ft = 0$ to $ft \approx 40$. Quantitatively, the computed growth rate for the random initial perturbation is 0.273 (0.80% relative error) and the computed growth rate for the seeded simulation 0.277 (0.65% relative error). Like in parameter set 2, this level of relative error is smaller than what we have seen in previous literature. In terms of spatial structure, the seeded simulation did not experience any visual adjustments to the structure of the perturbation during the time of exponential growth. Thus our 2D eigenvalue problem solver correctly predicted the structure and growth rate for this parameter set.

In both plots, after the nonlinear saturation of the primary instability occurs, there is a secondary bump in the predicted growth rates. As we will see when examining the structures of the perturbation and the EPV field, the secondary bump in the first growth rate plot is caused by centrifugally unstable anticyclonic vortices that form during the nonlinear saturation of the initial instance of inertial instability.

Perturbation structure: We now examine the spatial structure of the perturbations as predicted by the simulation with random initial perturbation. Figure 5.31 shows the $y-z$ structures taken at the middle of the x domain whereas Figure 5.32 shows $x-y$ structures at mid-depth. For both of these figures, subplots (a)-(d) show the buoyancy and vertical velocity perturbations fields as well as the total EPV field at the times $ft = 35,\ 54,\ 59$ and 74 respectively.

As with the previous parameter sets we examined, the structure of the perturbation inside the regime of exponential growth agrees with the structure predicted by our 2D baroclinic eigenvalue problem solver. In Figure 5.31a we see that the w velocity field qualitatively matches the black contours for the real part of the w velocity field as predicted by 2D linear theory. Likewise in Figure 5.32a there are approximately four periods of

(a)

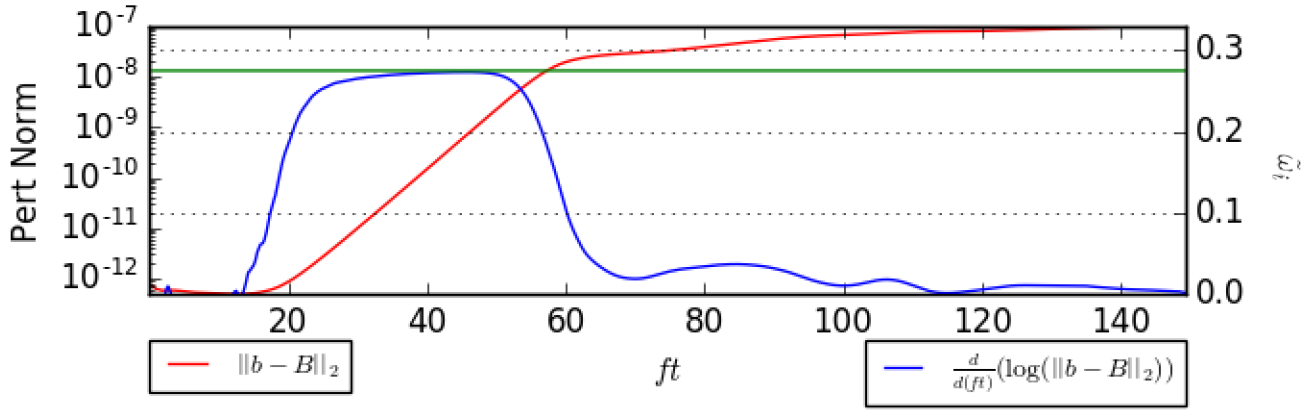

(b)

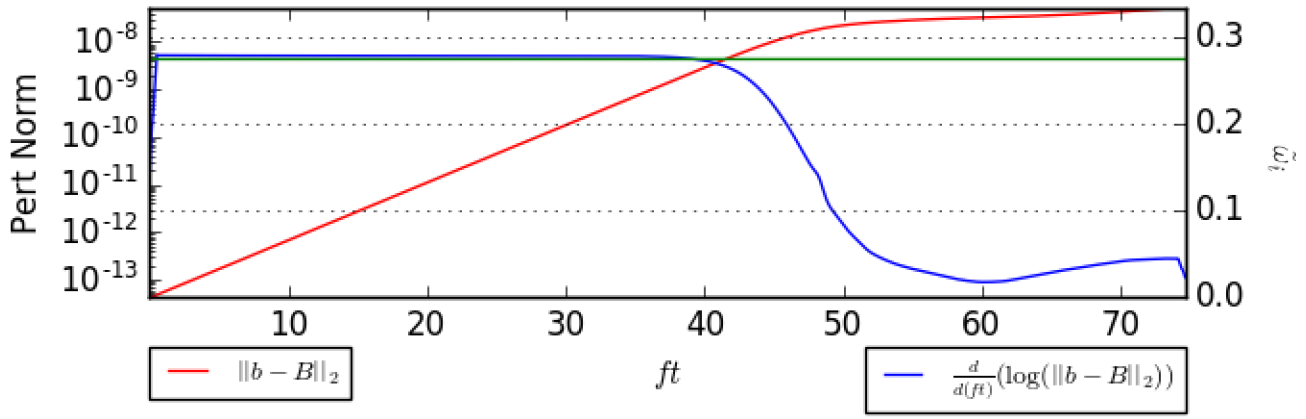

Figure 5.30: Plots of the ℓ^2 norm of the buoyancy perturbation field, approximations of the growth rate and the maximal growth rate from linear theory for two 3D simulation of the baroclinic jet using parameter set 3 in Table 5.1. The red lines are plotted on the left axis while the blue and green curves are plotted on the right axis. All plots have a resolution of $256 \times 256 \times 1024$. In plot (a) we show the results of the simulation with random initial condition and in plot (b) we show the results for the simulation where the initial perturbation is given by the fastest growing mode.

oscillation in the x direction for the buoyancy and vertical velocity perturbations. Here we see that the structure in the x direction is not perfectly periodic. This is likely due to a combination of the fact that we started with a random initial perturbation and that the most unstable modes come in leftward-rightward propagating pairs.

The next time we present, $ft = 54$, coincides with the start of the saturation process. In Figure 5.31b we clearly see a $m = 2$ structure appear in the $y - z$ direction of the EPV field and in Figure 5.32b we see the development of four periods of oscillation in the x direction. In the EPV field, we also see the beginnings of the development of four vortices.

At $ft = 59$, Figure 5.31c shows that the $m = 2$ structure continues to develop in the vertical direction while the minimal value of the EPV field has clearly become less negative. Examining Figure 5.32c for the $x - y$ EPV field, we clearly see that four anticyclonic vortices have formed. Each of these anticyclones has a core of negative EPV and there are some striations in the EPV in the middle of the vortices. An examination of the w fields indicates that gravity waves are likely being emitted. This could be the underlying cause of the striations seen in the EPV field. Finally, we point out that the choice to fully saturate the colorbar for the EPV field based on the initial extrema hides the fact that for each anticyclone there is a corresponding cyclone.

Finally, we examine Figures 5.31d and 5.32d for the flow at time $ft = 74$. Focusing on the w fields, we see that as the flow evolves, gravity waves continue to be radiated by the anticyclonic vortices. The EPV field itself shows that the region of negative EPV in the anticyclonic vortices has substantially decreased and the flow is becoming centrifugally stable. To this effect, two of the four vortices have completely lost their negative EPV core while the other two vortices still have cores of slightly negative EPV. Over time these cores further mix until the EPV field becomes non-negative everywhere.

Centrifugally unstable vortices: This discussion leaves an open question: Why do we have anticyclonic vortices with cores of negative EPV in this case but not the previous cases? The obvious explanation for the existence of the centrifugally unstable vortices is that for this parameter set the larger aspect ratio means that the region where the EPV is negative is thicker than it was in the previous cases. The thicker region of negative EPV could keep the initial instability from stirring the EPV field in a way that facilitates the mixing of the EPV field as the initial inertial mode saturates.

Finally, once the anticyclones with negative EPV cores form, they are unstable to centrifugal instabilities. While fully examining the stability properties of these anticyclones could be an entire thesis in and of itself, the w fields from this simulation hint that at least in this case the centrifugally unstable anticyclones could become stable by radiating gravity wave [42].

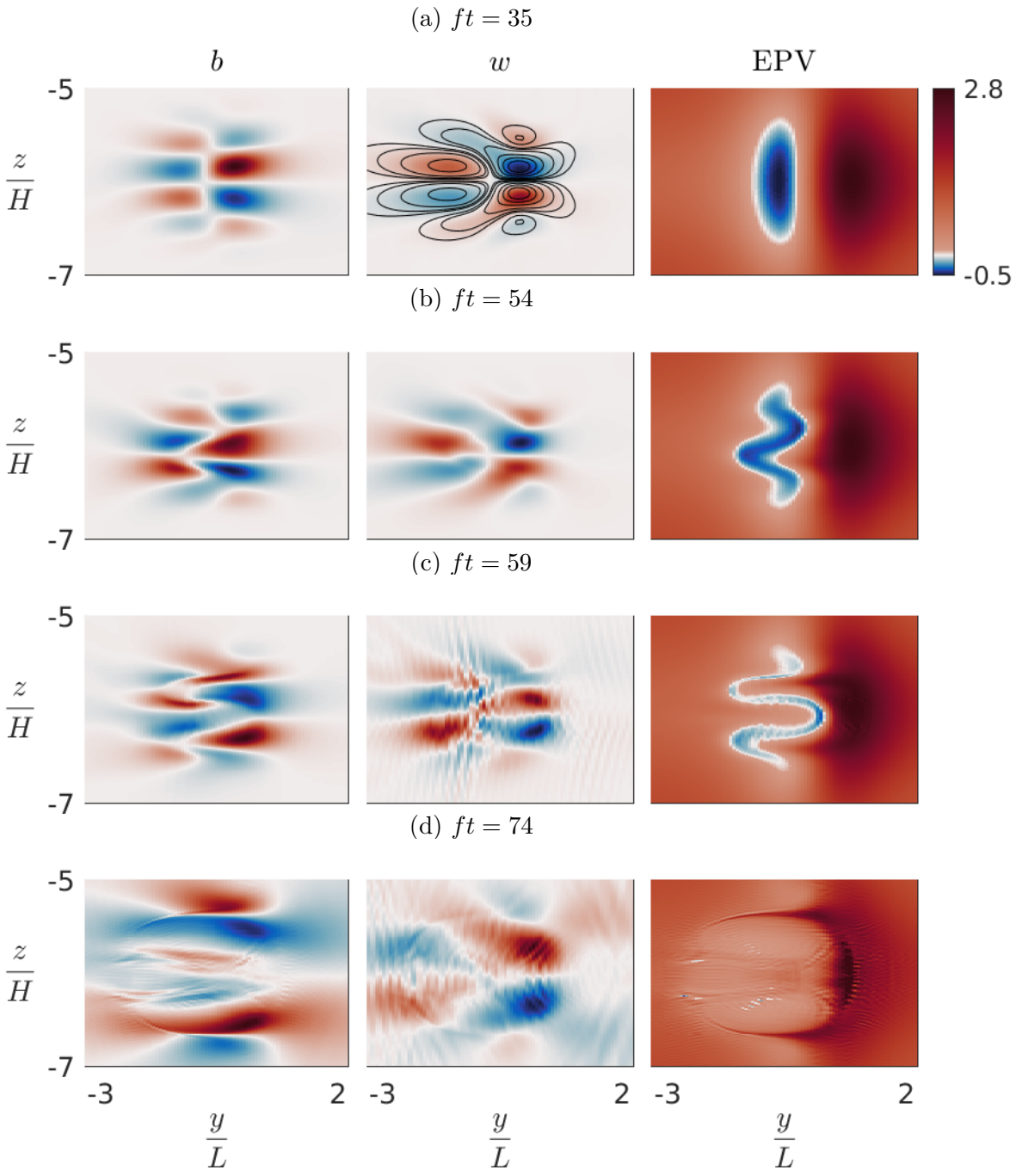

Figure 5.31: $y-z$ slices of the buoyancy and vertical velocity perturbation fields along with the EPV field for the $256 \times 256 \times 1024$ resolution nonlinear model of a randomly perturbed baroclinic jet using parameter set 3 in Table 5.1. All slices are taken in the middle of the x direction. The colormaps for the buoyancy and vertical velocity perturbation fields are fully saturated with zero being white and the colormaps are the same for all EPV plots.

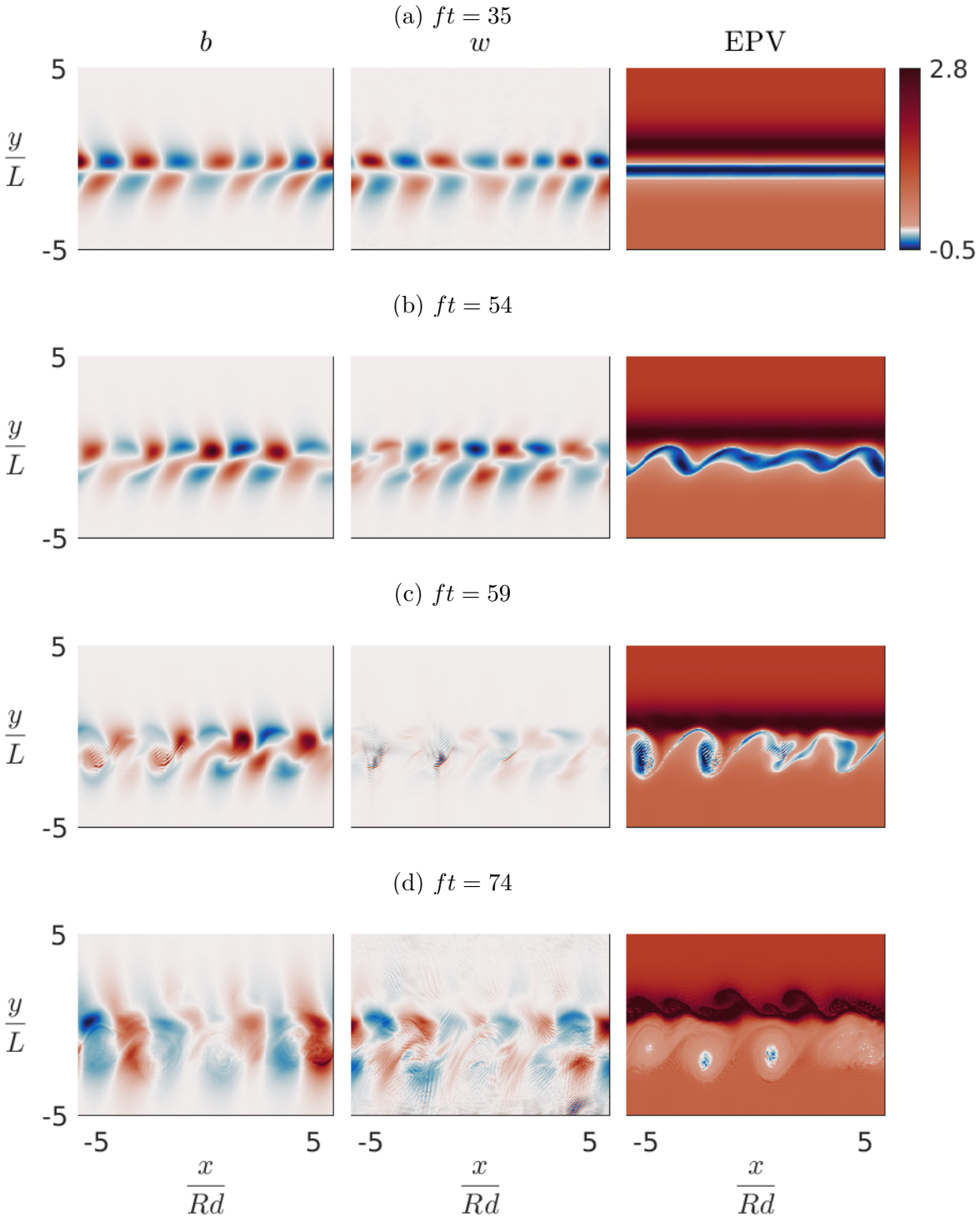

Figure 5.32: Mid-depth $x - y$ slices of the buoyancy and vertical velocity perturbation fields along with the EPV field for the $256 \times 256 \times 1024$ resolution nonlinear model of a randomly perturbed baroclinic jet using parameter set 3 in Table 5.1. The colormaps for the buoyancy and vertical velocity perturbation fields are fully saturated with zero being white and the colormaps are the same for all EPV plots.

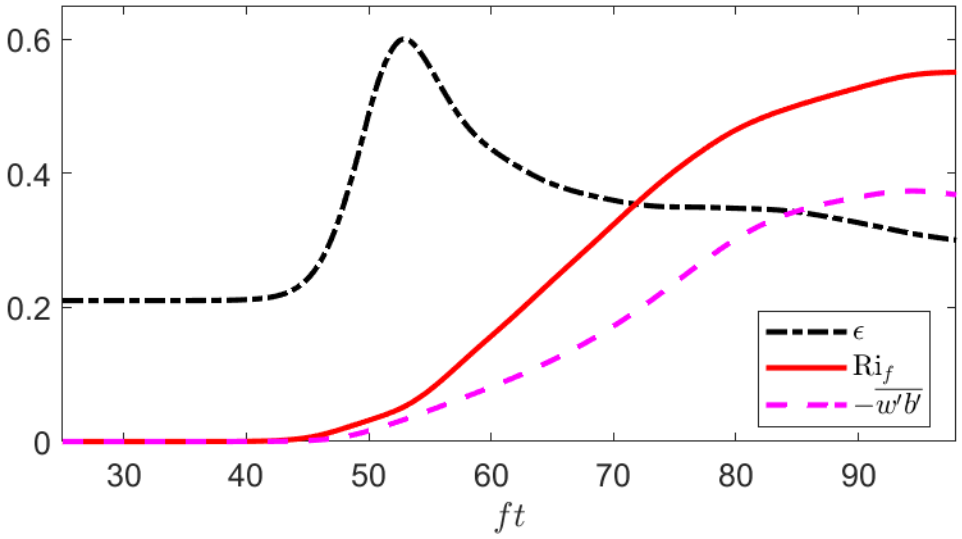

Figure 5.33: The flux Richardson number Ri_f for mixing efficiency for a 3D simulation of a randomly perturbed baroclinic jet using parameter set 3 in Table 5.1. Here the black and magenta curves are the dissipation rate and turbulent buoyancy flux respectively. We normalized the dissipation rate to have a maximum of 0.6 and use the same normalization factor for the turbulent buoyancy flux.

Mixing efficiency: Figure 5.33 shows the mixing efficiency along with the dissipation rate and turbulent buoyancy flux for the 3D baroclinic simulation with random initial perturbation. As we have previously done, we normalize the dissipation rate and turbulent buoyancy flux so that their relative values can be seen. In this simulation the mixing efficiency of II is nearly zero for early times, grows as the initial instability grows and then saturates to a maximum of around 0.55 as the EPV cores of the anticyclones become nonnegative. This mixing efficiency is much larger than what we previously saw with the lower aspect ratio jet. At $ft \approx 60$ where the initial instability has saturated and the anticyclones have formed, the mixing efficiency is only approximately 0.15. This shows that for this case the high mixing efficiency is due to the mixing caused by the secondary instabilities of the anticyclones.

5.4 A Parameter Study of Inertial Instability

Now that we have demonstrated the accuracy of our numerical methods for solving the 1D and 2D eigenvalue problems for the linear stability of the barotropic and baroclinic jets, we perform some parameter studies. Our starting nondimensional parameters for this analysis is parameter set 1 in Table 5.1. We independently vary the Rossby number, the Reynolds number, the Burger number, and the aspect ratio and then we conduct a two parameter study by varying both the Rossby and Burger number simultaneously. For each parameter study, we compare the results for both the barotropic and baroclinic jets shown in Figures 3.1a and 3.1b respectively. By examining the growth rates for both jets, we gain a better understanding of when one can apply the stability results of the barotropic jet to the baroclinic jet. Due to the number of eigenvalue problems we must solve to capture the fastest growing mode for any given parameter set, we are computationally limited in the number of parameters we can consider.

Before we present the results of our parameter studies, we briefly remind the reader about some parameter studies that have been previously conducted. Table (5.2) summarizes what parameters were examined by the various studies we have discussed throughout this thesis. In addition to the studies in Table (5.2), Tort et al. [89] examined the effects of changing the dimensional viscosity/dissipation, Brunt-Väisälä frequency and a type of aspect ratio on the growth rates of a barotropic Bickley jet within a continuously stratified Boussinesq model. They also explored the effects of adding in the non-traditional terms in the Coriolis parameter. While there is a wide range of jet-like background states considered both within Boussinesq models and 2-layer SW models, notice that none of the aforementioned studies examined a 2-dimensional background state. Furthermore, the range of parameters we consider is generally larger than what has been considered in previous studies and we tend to use higher resolutions.

5.4.1 Varying Ro

From equation (3.23) we have Ro$= U/(fL)$. Thus the Rossby number can be increased by increasing U or by decreasing f or L.

Figure 5.34 shows the result of our Rossby number parameter study. Here we normalize the largest nondimensional growth rate by the Rossby number. Our choice to normalize the nondimensional growth rates is to more clearly illustrate the dependency of the relative growth rate on the Rossby number.

Parameter	Authors	Model	Jet
Ro	Griffiths [25]	Inviscid hydrostatic Boussinesq on a β-plane	Barotropic Bickley jet w/ linear stratification
	Carnevale et al. [9]	Inviscid hydrostatic Boussinesq on a f-plane	Unstratified Gaussian barotropic jet
	Ribstein et al. [73]	Viscous hydrostatic Boussinesq on a f-plane	Barotropic Bickley jet w/ linear stratification
	Wang et al. [93]	Inviscid hydrostatic Boussinesq model on a f-plane	Three different vertical shear flows
	Bouchut et al. [4]	2-layer SW on f-plane	Barotropic Bickley jet
	Tort et al. [89]	2-Layer SW on f-plane and NT f-plane	Barotropic Bickley jet
δ_{NH}	Tort et al. [89]	2-Layer SW on f-plane and NT f-plane	Barotropic Bickley jet
Bu	Ribstein et al. [73]	Viscous hydrostatic Boussinesq on a f-plane	Stratified barotropic Bickley jet
	Bouchut et al. [4]	2-layer SW on f-plane	Barotropic Bickley jet
	Tort et al. [89]	2-Layer SW on f-plane and NT f-plane	Barotropic Bickley jet
Re	Carnevale et al. [9]	Inviscid hydrostatic Boussinesq on a f-plane	Unstratified Gaussian barotropic jet
	Ribstein et al. [73]	Viscous hydrostatic Boussinesq on a f-plane	Stratified barotropic Bickley jet

Table 5.2: A summary of the various models and background studies that have been conducted for each of the parameters we consider in our work. The Burger number for the SW models is the SW Burger number and δ_{NT} is our aspect ratio scaled by the ratio of the non-traditional Coriolis parameter to the f Coriolis parameter.

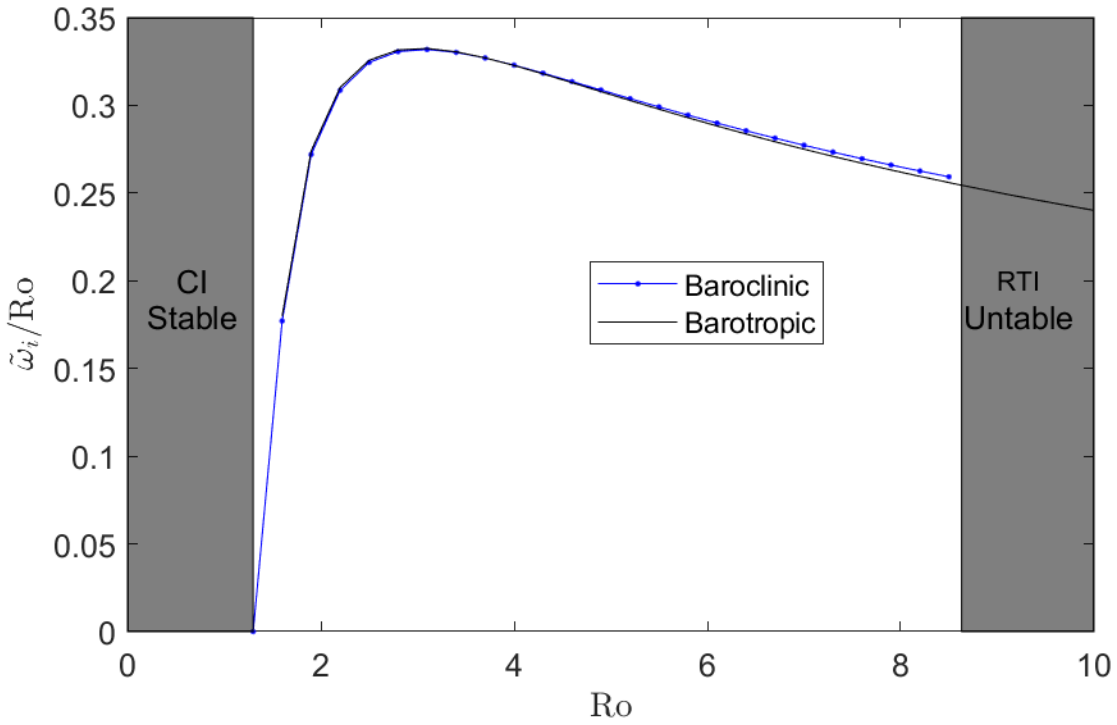

Figure 5.34: The largest nondimensional growth rates normalized by Ro for the barotropic and baroclinic jets with the nondimensional parameters (Re, Bu, δ) = (1.168×10^8, 17.26, 0.03). Here the gray region on the left represents jets that are stable to inertial instability whereas the gray region on the right represents baroclinic jets that are unstable to RTI.

For all Rossby numbers where both growth rates were computed, the barotropic and baroclinic growth rates are virtually identical. The only notable difference in the growth rates is that the baroclinic jet has negligibly larger growth rates for Ro$\approx$ 8. It is interesting that there are peaks in the Rossby number normalized nondimensional growth rates for both jets around Ro= 3. This behavior was previously seen in the studies listed under Ro in Table 5.2. As the Rossby number approaches the critical number for II, the growth rates of both jets approach zero. Finally, the barotropic jets are not susceptible to RTI and we thus compute the growth rates for a few jets in the region where the baroclinic jet is unstable to RTI.

5.4.2 Varying δ

An increase in δ can be caused by either a decrease in the horizontal length scale of the jet L or an increase in the vertical length scale of the jet H.

Figure 5.35 shows the largest nondimensional growth rate for both the barotropic and baroclinic jets for various aspect ratios. Notice that outside of the two smallest aspect ratios considered, the growth rates for the inertial modes of the baroclinic jets again agree rather well. We see that a decrease in the aspect ratio leads to a decrease in the nondimensional growth rates for both jets. To understand why this might be, we fix the horizontal length scale, L, and vary the aspect ratio by changing the vertical length scale, H. Here a decrease in the aspect ratio is equivalent to a decrease in H and jets with smaller aspect ratios have smaller regions of negative EPV. This limits the vertical extent where II can exist. In the extreme limit where $\delta \to 0$, H vanishes and jets become stable to II. The continuity of the eigenvalue problem with respect to the δ parameter implies that at some point a decrease in the aspect ratio must cause a decrease in the growth rate of II. The study of δ_{NH} by Tort et al. [89] found that the growth rates have a similar dependence on their aspect ratio even though their aspect ratio is scaled by the ratio of the non-traditional Coriolis parameter to the traditional Coriolis parameter and thus has a different physical interpretation.

Finally, we remind the reader that in the governing equations (3.30)-(3.34) for the stability problem we made the hydrostatic approximation. This approximation is only valid when $\delta \ll 1$ and thus our model might begin to breakdown at the larger values of δ we consider.

5.4.3 Varying Bu

We now examine the effect that the Burger number has on the largest growth rates for both jets. From Bu$= (NH)^2/(fL)^2$, it follows that an increase to the Burger number is physically caused by either an increase in N or H or by a decrease in f or L. Figure 5.36 shows the computed growth rates for both jets as a function of Burger number. After examining the relationship between $\tilde{\omega}$ and Bu, we decided to plot the largest nondimensional growth rate as a function of $\sqrt[4]{\text{Bu}}$ to more clearly show the dependence of the nondimensional growth rates on the Burger number.

As with the previous parameter studies, we do not see a significant difference between the growth rates of the instabilities of the two jets. By inspection, we see that the growth rates for the baroclinic jet are almost always slightly smaller than those of the barotropic jet. Further, both curves monotonically decrease with respect to the Burger number. The

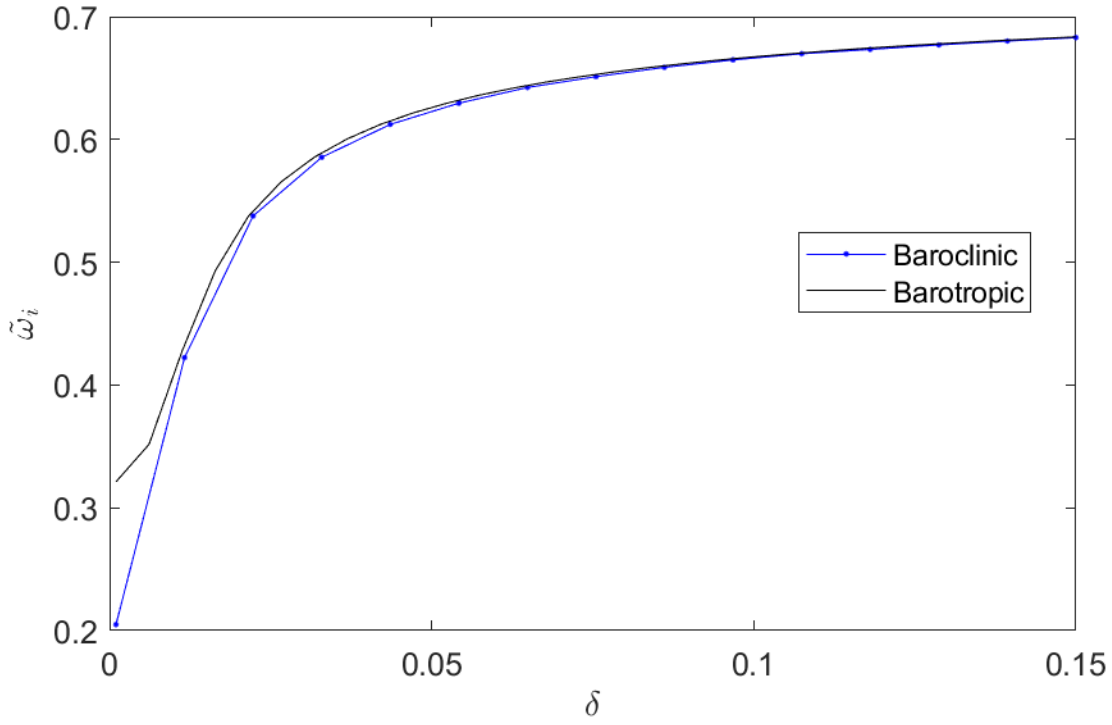

Figure 5.35: The largest nondimensional growth rate for the barotropic and baroclinic jets with the nondimensional parameters (Ro, Re, Bu) = (2, 1.168×10^8, 17.26).

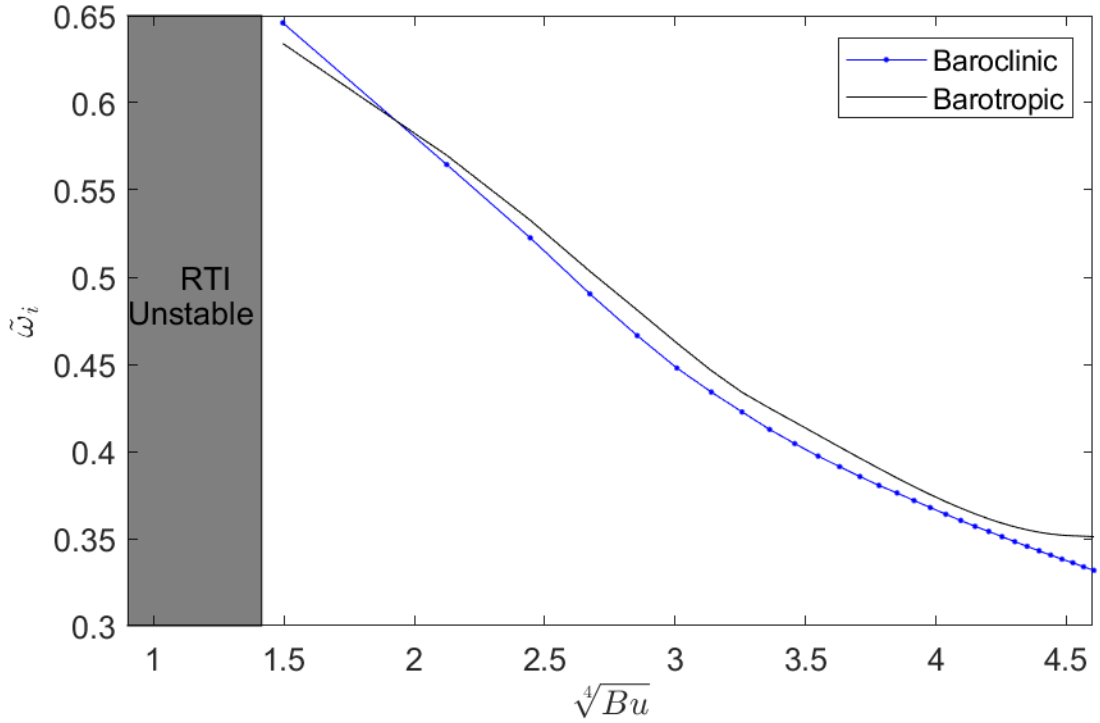

Figure 5.36: The largest nondimensional growth rate for the barotropic and baroclinic jets with the nondimensional parameters (Ro,Re,δ)=$(2, 1.168 \times 10^8, 0.03)$. Here the gray box represents the region where the baroclinic jet is unstable to RTI.

dependence of the growth rate on the Burger number can be explained by fixing H, f and L and thinking of the Burger number as a function of only N. In this situation, as the Burger number increases so does the stratification. Since a more strongly stratified fluid resists vertical movement more than a weakly stratified fluid, it is not unexpected that the growth rate will tend to decrease as the Burger number increases. For large values the curve for the barotropic jet appears to flatten out. Qualitatively, the monotonic dependence on the Burger number agrees with the various studies listed under Bu in Table 5.2. For larger Burger numbers than we considered here (i.e. $\sqrt[4]{\text{Bu}} \approx 9$), the previous studies predict that the front should become stable to II.

5.4.4 Varying Re

We now examine how the growth rates depend on the Reynolds number. In our examination of parameter sets 1, 2 and 3, we saw that for smaller Reynolds numbers the largest growth rates for the barotropic jet and baroclinic jet can differ. We explore this process in greater detail here.

Figure 5.37 shows the nondimensional growth rates as a function of Re. Here we plot one curve for the baroclinic jet and four curves for the barotropic jet: one for the maximum over all modes, one for the SI mode, one for the $\tilde{m} = 10^{-6}$ mode and one for the $\tilde{m} = 75$ mode. Plotting multiple curves for the barotropic jet highlights the differences between the growth rates for the various modes.

We start by discussing the curve for the most unstable mode for the barotropic jet. For sufficiently small Reynolds numbers (i.e. $\mathrm{Re} \lesssim 10$) the barotropic jet is stable. This is followed by a range of Reynolds numbers ($10 \lesssim \mathrm{Re} \lesssim 10^2$) where the growth rate rapidly increases with the Reynolds number. The largest growth rate is then essentially constant until $\mathrm{Re} \approx 10^6$ when there is a second parameter region where the growth rate rapidly increases with the Reynolds number. Finally for sufficiently large Reynolds numbers ($\mathrm{Re} \gtrsim 10^9$), the growth rates saturate towards some supremum as the jet presumably undergoes an ultraviolet catastrophe. To understand what is happening to the wavenumbers of the most unstable modes in each of these parameter regions, we examine the various growth curves for the barotropic jet along with Figures 5.1, 5.19, and 5.26 for the largest growth rates as a function of the wavenumbers for parameter set 1, 2 and 3 respectively. The $\tilde{m} = 10^{-6}$ mode is dominate for $\mathrm{Re} \lesssim 10^6$ and does not seem to depend on the Reynolds number for $\mathrm{Re} \gtrsim 10^3$. In Figures 5.1, 5.19, and 5.26 we see that for $\tilde{m} \approx 0$ there is a region of unstable modes that does not seem to depend strongly on the nondimensional parameters. The most unstable mode in this region has horizontal wavenumber $\tilde{k} \approx 3.9$ and a maximum nondimensional growth rate around 0.33. Thus the most unstable mode for $\mathrm{Re} \lesssim 10^6$ is the $(\tilde{k}, \tilde{m}) \approx (3.9, 0)$ mode. The red curve for the symmetric inertial mode matches the curve for the fastest growing mode for the barotropic jet at $\mathrm{Re} \approx 2 \times 10^7$. Thus from $Re \approx 10^6$ to $Re \approx 2 \times 10^7$, the most unstable wavenumber rapidly changes from $(3.9, 0)$ to $(0, \tilde{m})$. Finally, the magenta curve for the most unstable $\tilde{m} = 75$ mode shows that for $\mathrm{Re} \gtrsim 2 \times 10^7$ the vertical wavenumber of the most unstable mode increases with the Reynolds number. That is to say the jet experiences the ultraviolet catastrophe as has been well documented throughout literature. We note here that the works in Table 5.2 focused on larger Reynolds numbers, did not show that the flow becomes stable for sufficiently small Reynolds numbers but agree with our result that the growth rate increases with the Reynolds number.

We now examine the growth rates for the II modes of the baroclinic jet. First note that the general behaviour of the curve for the growth rates of the baroclinic jet mirrors what we saw in the barotropic case. For Re$\lesssim 10^4$ the baroclinic jet is stable to II, for $10^4 \lesssim$Re$\lesssim 10^5$ the growth rate rapidly increases with the Reynolds number, for $10^5 \lesssim$Re$\lesssim 5\times10^6$ the growth rates have little dependence on the Reynolds number, from Re$\approx 5\times10^6$ to 10^9 the growth rate rapidly increases with the Reynolds number and finally we see an ultraviolet catastrophe for sufficiently large Reynolds numbers. We now discuss the horizontal wavenumbers and vertical structure of the most unstable modes. The most unstable modes of the baroclinic jet for Re$\lesssim 5\times10^6$ have a wavenumber of kRd≈ 3.9 and spatial structures similar to that shown in Figures 5.21b and 5.21c. These modes are the baroclinic analogues of the $(k\text{Rd}, m) \approx (3.9, 0)$ modes of the barotropic jet. Like we saw for the barotropic jet, as the Reynolds number increases modes with more oscillatory behaviours in the vertical direction (e.g. ones like the modes in Figures 5.4 and 5.29) are no longer suppressed and become more unstable than the kRd≈ 3.9 mode. Presumably, there is an ultraviolet catastrophe in the Re$\to\infty$ limit like we saw for the barotropic jet.

Finally, we compare the growth rates for the baroclinic and barotropic jets. For $10 \lesssim$Re$\lesssim 10^4$ the barotropic jet is unstable to II but the baroclinic jet is stable. For small Reynolds numbers between 10^4 and 5×10^6, the growth rates differ by at least a factor of 2 and the growth rates agree for sufficiently large Reynolds numbers. This means that at a minimum when considering low Reynolds numbers, caution should be taken when applying the results of instability analysis of barotropic jets to baroclinic jets.

5.4.5 Varying Bu and Ro

Finally, we examine the effects of changing both the Burger number and the Rossby number at the same time. Figure 5.38 shows the inverse Rossby number normalized nondimensional growth rates for both the barotropic and baroclinic jets. Both plots use the same colorbar and contours. The white region shown in the baroclinic jet plot corresponds to the parameters where the baroclinic jet becomes unstable to RTI.

Focusing on the barotropic jet, we see that for any given Rossby number, the growth rate decreases as the Burger number increases. This was previously seen in the Ro$=2$ case we examined earlier. It is also apparent that for each Burger number the inverse Rossby number normalized nondimensional growth rate still obtains its maximum near the line Ro≈ 3. Examining the baroclinic jet we see similar behaviors with the only notable difference being the cutoff for RTI. By comparing the contours for the two jets, we see that the largest growth rate over all Burger numbers for any given Rossby number is roughly

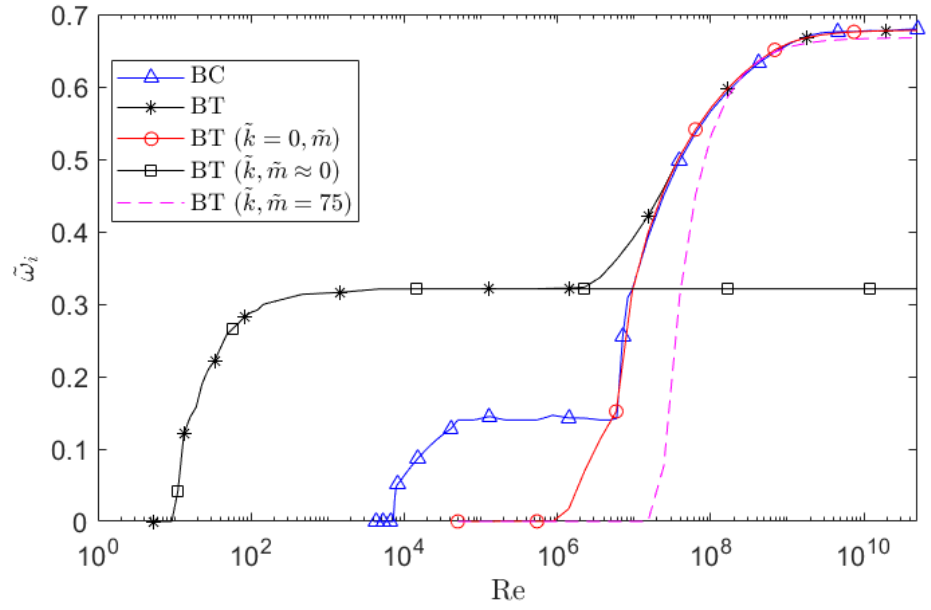

Figure 5.37: The largest nondimensional growth rate for the barotropic and baroclinic jets with the nondimensional parameters (Ro,Bu,δ)=$(2, 17.26, 0.03)$. We split the barotropic modes into the SI mode, the $\tilde{m} \approx 0$ mode, the $\tilde{m} = 75$ mode and the maximum over all other values of m.

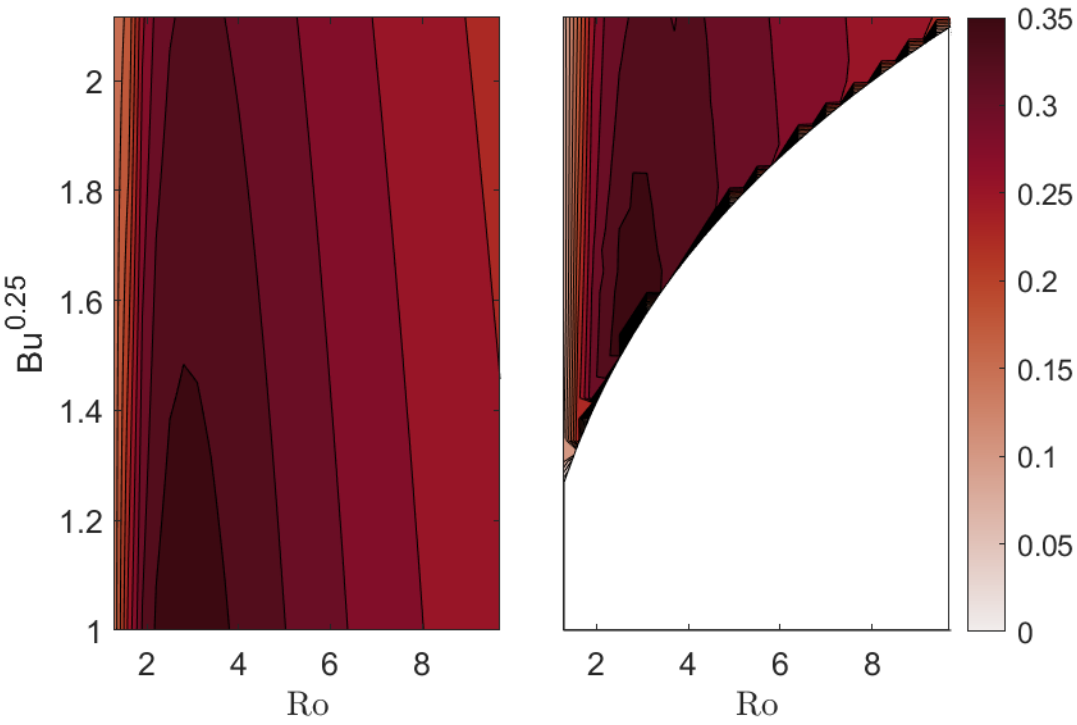

Figure 5.38: The largest nondimensional growth rates normalized by Ro for the barotropic jet (left) and baroclinic jet (right) with the nondimensional parameters (Re,δ)=($1.168 \times 10^8, 0.03$). Here the white region on the plot for the baroclinic jet corresponds to RTI unstable jets and the leftmost axis is the limit where the flow becomes stable to II.

the same. None of these results were unexpected from our previous work examining the effects of Bu and Ro independently and these results qualitatively agree with the works in Table 5.2.

5.5 Conclusion

Inertially unstable barotropic and baroclinic jets have been examined within a forced version of the viscous Navier-Stokes equations under the hydrostatic, Boussinesq, and f-plane approximations. We presented detailed results for the linear stability of both jets for three sets of nondimensional parameters, nonlinear simulations of both jets for one set of nondi-

mensional parameters, nonlinear simulations of the baroclinic jet for the two other sets of nondimensional parameters and the results of five parameter linear stability analysis studies for both jets.

To determine the linear stability properties of the jets, we derived a novel 2D eigenvalue problem. While this eigenvalue problem allows us to explore the linear stability of jets with both horizontal and vertical structures, it is more difficult and computationally intensive to numerically solve compared to the 1D eigenvalue problems previously considered by Ribstein et al. [73] and others. By utilizing the results of the 1D eigenvalue problem for barotropic jets and a Krylov subspace method, we developed an algorithm to numerically solve our novel 2D eigenvalue problem. In our nonlinear simulations, we made two improvements to the works of Molemaker et al. [56] and Ribstein et al. [73]. Firstly, we add forcing terms to the governing equations so that our background state is an exact solution of the viscous equations we numerically solve. Secondly, the nonlinear simulations we conduct are spectrally accurate and we explicitly define an eddy viscosity to more accurately simulate various Reynolds numbers. Previous studies used more dissipative numerical schemes and some studies, such as the work by Ribstein et al. [73], did not explicitly define a viscosity but instead relied entirely on the dissipation of the numerical scheme to extract energy from the smallest scales in their simulations.

Our numerical simulations and linear stability results for three particular nondimensional parameters show that the details of how the jet becomes stable to II depends strongly on the nondimensional parameters. For our first parameter set, the jet became stable to II upon the saturation of the initial instability. The resulting jet was unstable to secondary barotropic instabilities that in turn produced vortices. By lowering the Reynolds number in the second parameter set, the jet still becomes stable to II upon the saturation of the initial instability but the saturation of II coincided with the development of vortices. Finally, by increasing the aspect ratio of the jet for our third parameter set, the saturation of the initial II mode resulted in the generation of vortices with cores of negative EPV. Since the cores of the vortices have negative EPV, they are centrifugally unstable. This instability resolves itself by generating what appears to be gravity waves. For all three parameter sets we considered, our 2D eigenvalue problem accurately predicted the growth rate and structure of the most unstable mode and was thus validated.

By comparing the growth rates of the II modes for the barotropic and baroclinic jets, we found that the largest growth rates for both jets were comparable for the first parameter set but the barotropic jet has larger growth rates for the other two parameter sets. We examined the details of the differences by conducting five parameter studies using our numerical method for the 2D eigenvalue problem. At least for the parameter set (Ro, Re, Bu, δ, Pr) = (2, 1.1×10^8, 17.26, 0.03, ∞) there is not a significant difference between the

growth rates for the two jets when changing Ro, Bu, or δ and the dependence of the growth rate on Ro and Bu agrees with previous studies. There is however a nontrivial difference between the growth rates when changing the Reynolds number. For $10 \lesssim \mathrm{Re} \lesssim 10^4$ the barotropic jet is unstable to II while the baroclinic jet inertially stable. For slightly larger Reynolds numbers ($10^4 \lesssim \mathrm{Re} \lesssim 5 \times 10^6$) the largest growth rate for the barotropic jet is larger than that of the baroclinic jet by at least a factor of 2. Interestingly, for sufficiently small Reynolds numbers, the most unstable modes for both jets have a wavenumber of $k\mathrm{Rd} \approx 3.9$ and have similar cross channel structures. Thus, this particular mode does not seem to be affected by changes of the Reynolds numbers until the Reynolds number is sufficiently small so that it begins to suppress the mode. For $3 \times 10^7 \lesssim \mathrm{Re}$, we found that the growth rates of the II modes for the two jets tended to agree. Since the growth rates for the barotropic and baroclinic jets can differ as a function of the Reynolds number, caution should be taken when applying the stability results of the barotropic jet to those of the baroclinic jet at least for small Reynolds numbers.

5.5.1 Future Work

There are a few ways our work can be expanded. Firstly, we examined a limited number of nondimensional parameters. Increasing the number of base parameters examined in our sections of the linear stability of the jets is low hanging fruit for expanding our work and would increase the robustness of our results. Secondly, in our work we use a background linear stratification. Examining more realistic non-constant stratification profiles would be an interesting expansion to the presented work. Thirdly, we restricted our examination of baroclinic jets to interior jets. Examining how the dynamics change for surface jets is an interesting extension to our work. Preliminarily, we have examined one surface jet and found that at least for the parameter set we considered the structure of the mode changes while the growth rate was left unchanged. Fourthly, we only considered the dynamics on a f-plane but the work of Tort et al. [89] shows that for weaker stratifications the NT terms can be important to the dynamics of II. While the particular jets we examined had a strong background stratifications, exploring the effects of relaxing the f-plane approximation is an interesting expansion of our work. Finally, we have pointed out that the dynamics of how the flows become stable to II in the three cases we considered greatly differ. A study classifying what nondimensional parameters lead to what type of behaviour would be quite interesting.

Chapter 6

Conclusions

We have examined the stability of two layer fronts with vertically curved interfaces as well as the stability of inertially unstable continuously stratified baroclinic and barotropic jets.

In Chapter 2 we studied the stability of two layer fronts with vertically curved interfaces. We began by closing the gap between previous studies on linear fronts by exploring how the choice of the boundary condition changes their stability properties. It was shown that changing the boundaries from radiation conditions to no-normal flow conditions results in the loss of a slow growing baroclinic mode that is present with radiation boundary conditions. This addresses an open question posed by Gula et al. [26] on whether or not the stability results of channel fronts are applicable to fronts in the open ocean. We then examined the effects that the curvature of the interface has on the stability of the front. While we did not see any strong evidence of II for the parameters we considered, the addition of vertical curvature causes the PV field to be non-constant. This can make the front inertially unstable for sufficiently large Rossby numbers as noted by Bouchut et al. [4] and others. We showed that at least for the 18 vertically curved fronts we considered, there is an additional novel baroclinic instability that does not exist for linear fronts. This new instability is caused by the interactions of a pair of Rossby waves that propagate within each fluid layer. We named the new Rossby waves "vertically curved-interface Rossby waves" since their existence is due to the addition of curvature to the interface. While this new instability tends to have relatively small growth rates, it nevertheless destabilizes the front for many Froude numbers and can sometimes be the most dominant instability. In addition, we found that curvature can modify the parameters for which the Rossby-Kelvin and Kelvin-Helmholtz instabilities exist. In particular we find that the conclusion of [34] that for linear fronts the most unstable mode is geostrophic if $F < 1$ and $k < 1$ and is a

Kelvin-Helmholtz type instability if $F > 1$ or $k > 1$ no longer holds for many vertically curved fronts.

In Chapters 3-5 we expanded on several works that examined continuously stratified inertially unstable baroclinic and barotropic jets. We started by building 1D and 2D eigenvalue problems for the linear stability for the barotropic and baroclinic jets respectively. Our 2D eigenvalue problem for the baroclinic jet is novel and allows us to compare and contrast the differences in the stability properties of baroclinic and barotropic jets. We then examined nonlinear simulations for three different parameter sets and found that while linear stability theory accurately predicted the structure of the initial instability it told us little about what happens after the nonlinear saturation of the mode. For the first parameter set we considered, we found that the jet that results from the saturation of II is unstable to a secondary barotropic instability. The jet in the second parameter set we examined has no such secondary instability but instead the saturation of II caused coherent centrifugally stable vortices to form. The saturation of II for the third parameter set we considered caused coherent centrifugally unstable vortices to form. Our study of the nonlinear saturation of II was followed by a study of how the growth rates depend on the various parameters. We found that at least for the values of Ro, Bu, δ, and Pr we considered, the largest growth rates for the barotropic and baroclinic jets agree for sufficiently large Reynolds numbers. For smaller Reynolds numbers, the growth rates for the barotropic jet are larger than those of the baroclinic jet and when the Reynolds number is less than 10, the both jets are stable to II.

While our work in this thesis has expanded on previous research on instabilities and examined the robustness of previous studies, there is still much more work that can be done on both topics. One could examine the instabilities for larger Rossby numbers to explore inertial instabilities, examine the effects of continuous stratification on the growth rates and structure of the new baroclinic instability, examine the effects of topography, and further analyze the effects of the choice of boundary conditions. On the other hand, our work on the II of baroclinic and barotropic jets can be expanded by increasing the range of nondimensional parameters considered, considering non-constant stratification and explicitly quantifying when there is a secondary barotropic instability, a secondary centrifugal instability or no secondary instability at all. The quantification of when these secondary instabilities form will aid in understanding when II efficiently mixes the fluid. Finally, one could expand our analysis of the baroclinic jet by considering surface trapped baroclinic jets.

References

[1] *Maple (17)*. 2013.

[2] *MATLAB version 9.4.0.813654 (R2018a)*. Natick, Massachusetts, 2018.

[3] M. Abramowitz and I. Stegun. Handbook of mathematical functions, 1964.

[4] F. Bouchut, B. Ribstein, and V. Zeitlin. Inertial, barotropic, and baroclinic instabilities of the bickley jet in two-layer rotating shallow water model. *Physics of Fluids*, 23 (12):126601, 2011.

[5] J. P. Boyd. *Cheyshev and Fourier spectral methods*. Dover publications, 2001.

[6] X. Capet, J. C. McWilliams, M. J. Molemaker, and A. F. Shchepetkin. Mesoscale to submesoscale transition in the california current system. part I: Flow structure, eddy flux, and observational tests. *Journal of Physical Oceanography*, 38(1):29–43, 2008. doi: 10.1175/2007JPO3671.1.

[7] X. Capet, J. C. McWilliams, M. J. Molemaker, and A. F. Shchepetkin. Mesoscale to submesoscale transition in the california current system. part II: Frontal processes. *Journal of Physical Oceanography*, 38(1):44–64, 2008. doi: 10.1175/2007JPO3672.1.

[8] X. Capet, J. C. McWilliams, M. J. Molemaker, and A. F. Shchepetkin. Mesoscale to submesoscale transition in the california current system. part III: Energy balance and flux. *Journal of Physical Oceanography*, 38(10):2256–2269, 2008. doi: 10.1175/2008JPO3810.1.

[9] G. F. Carnevale, R. C. Kloosterziel, and P. Orlandi. Inertial and barotropic instabilities of a free current in three-dimensional rotating flow. *Journal of Fluid Mechanics*, 725:117–151, 2013.

[10] C. P. Caulfield and W. R. Peltier. The anatomy of the mixing transition in homogeneous and stratified free shear layers. *Journal of Fluid Mechanics*, 413:1–47, 2000.

[11] M. Chanona, F. J. Poulin, and J. Yawney. The stability of oceanic fronts in a shallow water model. *Journal of Fluid Mechanics*, 785:462–485, 2015.

[12] J. G. Charney and M. E. Stern. On the stability of internal baroclinic jets in a rotating atmosphere. *Journal of the Atmospheric Sciences*, 19(2):159–172, 1962.

[13] C. Chen and I. Kamenkovich. Effects of topography on baroclinic instability. *Journal of Physical Oceanography*, 43(4):790–804, 2013. doi: 10.1175/JPO-D-12-0145.1.

[14] H. R. Cho, T. G. Shepherd, and V. A. Vladimirov. Application of the direct liapunov method to the problem of symmetric stability in the atmosphere. *Journal of the atmospheric sciences*, 50(6):822–836, 1993.

[15] B. Cushman-Roisin and M. Beckers. *Introduction to Geophysical Fluid Dynamics Physical and Numerical Aspects*. McGraw-Hill, 2010.

[16] W. K. Dewar, J. C. McWilliams, and M. J. Molemaker. Centrifugal instability and mixing in the california undercurrent. *Journal of Physical Oceanography*, 45(5):1224–1241, 2015.

[17] P. G. Drazin and W. H. Reid. *Hydrodynamic Stability*. Cambridge Mathematical Library. Cambridge University Press, 2 edition, 2004. doi: 10.1017/CBO9780511616938.

[18] T. J. Dunkerton. On the inertial stability f the equatorial middle atmosphere. *Journal of the Atmospheric Sciences*, 38(11):2354–2364, 1981.

[19] T. J. Dunkerton. A Nonsymmetric Equatorial Inertial Instability. *Journal of the Atmospheric Sciences*, 40(3):807–813, 03 1983. ISSN 0022-4928. doi: 10.1175/1520-0469(1983)040⟨0807:ANEII⟩2.0.CO;2.

[20] T. Eldevik and K. B. Dysthe. Spiral eddies. *Journal of Physical Oceanography*, 32(3): 851–869, 2002.

[21] B. Fornberg. Generation of finite difference formulas on arbitrarily spaced grids. *Mathematics of Computation*, 51(184):699–706, 1988.

[22] R. Griffiths, P. Killworth, and M. Stern. Ageostrophic instability of ocean currents. *Journal of Fluid Mechanics*, 117:343 – 377, 04 1982. doi: 10.1017/S0022112082001669.

[23] R. W. Griffiths and P. F. Linden. Laboratory experiments on fronts. *Geophysical & Astrophysical Fluid Dynamics*, 19(3-4):159–187, 1982. doi: 10.1080/03091928208208954. URL https://doi.org/10.1080/03091928208208954.

[24] S. D. Griffiths. Nonlinear vertical scale selection in equatorial inertial instability. *Journal of the atmospheric sciences*, 60(7):977–990, 2003.

[25] S. D. Griffiths. The limiting form of inertial instability in geophysical flows. *Journal of Fluid Mechanics*, 605:115–144, 2008.

[26] J. Gula, R. Plougonven, and V. Zeitlin. Ageostrophic instabilities of fronts in a channel in a stratified rotating fluid. *Journal of Fluid Mechanics*, 627:485–507, 2009.

[27] J. Gula, M. J. Molemaker, and J. C McWilliams. Topographic generation of submesoscale centrifugal instability and energy dissipation. *Nature Communications*, 7: 12811, 2016.

[28] T. W. N. Haine and J. Marshall. Gravitational, symmetric, and baroclinic instability of the ocean mixed layer. *Journal of physical oceanography*, 28(4):634–658, 1998.

[29] B. Haurwitz and H. Panofsky. Stability and meandering of the Gulf Stream. *Trans. Amer. Geophysics. Union*, 31:723–731, 1950.

[30] D. Henningson and M. Berggren. *Fluid Dynamics. Theory and Computation.* 2005.

[31] B. J. Hoskins. The role of potential vorticity in symmetric stability and instability. *Quarterly Journal of the Royal Meteorological Society*, 100(425):480–482, 1974.

[32] B. J. Hoskins. The mathematical theory of frontogenesis. *Annual Review of Fluid Mechanics*, 14(1):131–151, 1982.

[33] B. L. Hua, D. W. Moore, and S. Le Gentil. Inertial nonlinear equilibration of equatorial flows. *Journal of Fluid Mechanics*, 331:345–371, 1997.

[34] K. Iga. Reconsideration of Orlanski's instability theory of frontal waves. *J. Fluid Mech.*, 255:213–236, 1993.

[35] K. Iga. Shear instability as a resonance between neutral waves hidden in a shear flow. *Journal of Fluid Mechanics*, 715:452, 2013.

[36] G. N. Ivey and J. Imberger. On the nature of turbulence in a stratified fluid. part I: The energetics of mixing. *Journal of Physical Oceanography*, 21(5):650–658, 1991.

[37] Y. Jiao and W. K. Dewar. The energetics of centrifugal instability. *Journal of Physical Oceanography*, 45(6):1554–1573, 2015.

[38] S. Jones. Rossby wave interactions and instabilities in a rotating, two-layer fluid on a beta-plane. part I: Resonant interactions. *Geophysical and Astrophysical Fluid Dynamics*, 11(1):289–322, 1978. doi: 10.1080/03091927808242671. URL https://doi.org/10.1080/03091927808242671.

[39] S. Jones. Rossby wave interactions and instabilities in a rotating, two-layer fluid on a beta-plane. part II: Stability. *Geophysical & Astrophysical Fluid Dynamics*, 12 (1):1–33, 1979. doi: 10.1080/03091927908242674. URL https://doi.org/10.1080/03091927908242674.

[40] H. Kaneko, I. Yasuda, K. Komatsu, and S. Itoh. Observations of the structure of turbulent mixing across the kuroshio. *Geophysical Research Letters*, 39(15), 2012.

[41] W. Kelvin. Hydrokinetic solutions and observations. *Phil. Magazine*, 42:362–377, 1871.

[42] R. Kloosterziel, G. Carnevale, and P. Orlandi. Inertial instability in rotating and stratified fluids: Barotropic vortices. *Journal of Fluid Mechanics*, 583:379 – 412, 07 2007. doi: 10.1017/S0022112007006325.

[43] R. C. Kloosterziel and G. F. Carnevale. Vertical scale selection in inertial instability. *Journal of Fluid Mechanics*, 594:249–269, 2008.

[44] R. C. Kloosterziel, P. Orlandi, and G. F. Carnevale. Saturation of inertial instability in rotating planar shear flows. *Journal of Fluid Mechanics*, 583:413, 2007.

[45] R. C. Kloosterziel, G. F. Carnevale, and P. Orlandi. Equatorial inertial instability with full Coriolis force. *Journal of Fluid Mechanics*, 825:69–108, 2017.

[46] J. A. Knox and V. L. Harvey. Global climatology of inertial instability and rossby wave breaking in the stratosphere. *Journal of Geophysical Research: Atmospheres*, 110(D6), 2005.

[47] N. Kotschin. Über die stabilität von margulesschen diskontinuitätsflächen. *Beitr. Phys. Atmos.*, 18:129–164, 1932. URL https://ci.nii.ac.jp/naid/10003555666/en/.

[48] P. K. Kundu. Fluid mechanics. *Academic Press, INC*, 1990.

[49] A. G. Lawrie and S. B. Dalziel. Rayleigh–taylor mixing in an otherwise stable stratification. *Journal of fluid mechanics*, 688:507–527, 2011.

[50] P. H. LeBlond and L. A. Mysak. *Waves in the Ocean*. Elsevier, New York, 1978.

[51] R. B. Lehoucq, D. C. Sorensen, and C. Yang. *ARPACK users' guide: solution of large-scale eigenvalue problems with implicitly restarted Arnoldi methods*, volume 6. Siam, 1998.

[52] M. S. Lozier and M. S. C. Reed. The influence of topography on the stability of shelfbreak fronts. *Journal of physical oceanography*, 35(6):1023–1036, 2005.

[53] J. C. McWilliams, I. Yavneh, M. J. P. Cullen, and P. R. Gent. The breakdown of large-scale flows in rotating, stratified fluids. *Physics of Fluids*, 10(12):3178–3184, 1998.

[54] M. Molemaker, J. McWilliams, and Y. Yavneh. Baroclinic instability and loss of balance. *Journal of Physical Oceanography*, 35, 2005.

[55] M. Molemaker, J. McWilliams, and X. Capet. Balanced and unbalanced routes to dissipation in an equilibrated eady flow. *Journal of Fluid Mechanics*, 654:3563, 2010. doi: 10.1017/S0022112009993272.

[56] M. J. Molemaker, J. C. McWilliams, and W. K. Dewar. Submesoscale instability and generation of mesoscale anticyclones near a separation of the california undercurrent. *Journal of Physical Oceanography*, 45(3):613–629, 2015.

[57] S. G. Monismith, J. R. Koseff, and B. L. White. Mixing efficiency in the presence of stratification: when is it constant? *Geophysical Research Letters*, 45(11):5627–5634, 2018.

[58] I. Orlanski. Instability of frontal waves. *J. Atmos. Sci.*, 25:178–200, 1968.

[59] W. M. F. Orr. The stability or instability of the steady motions of a perfect liquid and of a viscous liquid. part i: A perfect liquid. In *Proceedings of the Royal Irish Academy. Section A: Mathematical and Physical Sciences*, volume 27, pages 9–68, 1907.

[60] W. M. F. Orr. The stability or instability of the steady motions of a perfect liquid and of a viscous liquid. part II: A viscous liquid. In *Proceedings of the Royal Irish Academy. Section A: Mathematical and Physical Sciences*, volume 27, pages 69–138, 1907.

[61] T. R. Osborn. Estimates of the local rate of vertical diffusion from dissipation measurements. *Journal of physical oceanography*, 10(1):83–89, 1980.

[62] J. Pedlosky. The stability of currents in the atmosphere and the ocean: Part I. *Journal of the Atmospheric Sciences*, 21(2):201–219, 1964.

[63] J. Pedlosky. Geophysical fluid dynamics , 2nd edn. *Springer*, 1987.

[64] W. R. Peltier and C. P. Caulfield. Mixing efficiency in stratified shear flows. *Annual review of fluid mechanics*, 35(1):135–167, 2003.

[65] G. Perret, T. Dubos, and A. Stegner. How large-scale and cyclogeostrophic barotropic instabilities favor the formation of anticyclonic vortices in the ocean. *Journal of Physical Oceanography*, 41(2):303–328, 2011.

[66] N. Phillips. Energy transformations and meridional circulations associated with simple baroclinic waves in a two-level, quasi-geostrophic model. *Tellus*, 6(3):274–286, 1954.

[67] R. Plougonven and V. Zeitlin. Nonlinear development of inertial instability in a barotropic shear. *Physics of fluids*, 21(10):106601, 2009.

[68] F. J. Poulin and G. R. Flierl. The nonlinear evolution of barotropically unstable jets. *Journal of Physical Oceanography*, 33(10):2173–2192, 2003. doi: 10.1175/1520-0485(2003)033⟨2173:TNEOBU⟩2.0.CO;2. URL https://doi.org/10.1175/1520-0485(2003)033<2173:TNEOBU>2.0.CO;2.

[69] T. Radko and D. Lorfeld. Effects of weak planetary rotation on the stability and dynamics of internal stratified jets. *Physics of Fluids*, 30(9):096602, 2018.

[70] L. Rayleigh. On convection currents in a horizontal layer of fluid, when the higher temperature is on the under side. *Phil. Mag.*, 32(192):529–546, 1916.

[71] L. Rayleigh. On the dynamics of revolving fluids. *Proc. Roy. Soc. Lond. A*, 93:148–154, 1916.

[72] L. Rayleigh and J. W. Strutt. Investigation of the Character of the Equilibrium of an Incompressible Heavy Fluid of Variable Density, 1883.

[73] B. Ribstein, R. Plougonven, and V. Zeitlin. Inertial versus baroclinic instability of the bickley jet in continuously stratified rotating fluid. *Journal of Fluid Mechanics*, 743, 2014. doi: 10.1017/jfm.2014.26.

[74] Y. Saad. *Numerical Methods For Large Eigenvalue Problems*. The Society for Industrial and Applied Mathematics, 2011.

[75] S. Sakai. Rossby-Kelvin instability : a new type of ageostrophic instability caused by a resonance between rossby waves and gravity waves. *J. Fluid Mech.*, 202:149–176, 1989.

[76] R. M. Samelson and E. D. Skyllingstad. Frontogenesis and turbulence: A numerical simulation. *Journal of the Atmospheric Sciences*, 73, 09 2016.

[77] C. Y. Shen and T. E. Evans. Inertial instability and sea spirals. *Geophysical research letters*, 29(23):39–1, 2002.

[78] W. C. Skamarock, J. B. Klemp, J. Dudhia, D. O. Gill, D. M. Barker, X.-Y. Huang M. G Duda, W. Wang, and J. G. Powers. A description of the advanced research WRF Version 3. *NCAR Tech*, page 113, 2008. doi: 10.5065/D68S4MVH.

[79] W. Smyth and J. Moum. Waves and instability in an asymmetrically stratified jet. 35:265–294, 01 2002.

[80] A. Sommerfield. Ein beitrag zur hydrodynamischen erklarung der turbulenten flüssigkeisbewegung. *Atti Congr. Int. Math. 4th Rome*, 1908.

[81] G. W. Stewart. A Krylov–Schur algorithm for large eigenproblems. *SIAM Journal on Matrix Analysis and Applications*, 23(3):601–614, 2002.

[82] P. H. Stone. On non-geostrophic baroclinic stability. *Journal of the Atmospheric Sciences*, 23(4):390–400, 1966.

[83] C. J. Subich, K. G. Lamb, and M. Stastna. Simulation of the Navier–Stokes equations in three dimensions with a spectral collocation method. *International Journal for Numerical Methods in Fluids*, 73(2):103–129, 2013.

[84] H. Taniguchi and M. Ishiwatari. Physical interpretation of unstable modes of a linear shear flow in shallow water on an equatorial beta-plane. *Journal of Fluid Mechanics*, 567:1, 2006.

[85] G. I. Taylor. Stability of a viscous liquid contained between two rotating cylinders. *Philosophical Transactions of the Royal Society of London. Series A, Containing Papers of a Mathematical or Physical Character*, 223(605-615):289–343, 1923.

[86] L. N. Thomas. On the effects of frontogenetic strain on symmetric instability and inertia-gravity waves. *Journal of Fluid Mechanics*, 711:620–640, November 2012. doi: 10.1017/jfm.2012.416.

[87] L. N. Thomas, J. R. Taylor, R. Ferrari, and T. M. Joyce. Symmetric instability in the gulf stream. *Deep Sea Research Part II: Topical Studies in Oceanography*, 91:96–110, 2013.

[88] K. M. Thyng, C. A. Greene, R. D. Hetland, H. M. Zimmerle, and S. F. DiMarco. True colors of oceanography: Guidelines for effective and accurate colormap selection. *Oceanography*, 29, 2016. URL https://doi.org/10.5670/oceanog.2016.66.

[89] M. Tort, B. Ribstein, and V. Zeitlin. Symmetric and asymmetric inertial instability of zonal jets on the f-plane with complete coriolis force. *Journal of Fluid Mechanics*, 788:274–302, 2016.

[90] L. N. Trefethen. *Spectral Methods in MATLAB*. SIAM, Philadelphia, 2000.

[91] G. K. Vallis. *Atmospheric and Oceanic Fluid Dynamics: Fundamentals and Large-Scale Circulation*. Cambridge University Press, 2006. doi: 10.1017/9781107588417.

[92] P. Wang, J. C. McWilliams, and Z. Kizner. Ageostrophic instability in rotating shallow water. *Journal of Fluid Mechanics*, 712:327, 2012.

[93] P. Wang, J. C. McWilliams, and C. Ménesguen. Ageostrophic instability in rotating, stratified interior vertical shear flows. *Journal of fluid mechanics*, 755:397–428, 2014.

[94] F. White. *Fluid Mechanics 7th ed.* Academic Press, 2011.

[95] D. G. Wright. Baroclinic Instability in Drake Passage. *Journal of Physical Oceanography*, 11(2):231–246, 02 1981. doi: 10.1175/1520-0485(1981)011⟨0231:BIIDP⟩2.0.CO;2.

[96] M. S. Davies Wykes and S. B. Dalziel. Efficient mixing in stratified flows: experimental study of a rayleigh–taylor unstable interface within an otherwise stable stratification. *Journal of Fluid Mechanics*, 756:1027–1057, 2014.

[97] E. Yim, P. Billant, and C. Ménesguen. Stability of an isolated pancake vortex in continuously stratified-rotating fluids. *Journal of Fluid Mechanics*, 801:508–553, 2016.

[98] E. Yim, A. Stegner, and P. Billant. Stability criterion for the centrifugal instability of surface intensified anticyclones, 05 2018.

[99] H. Zhivomirov. A method for colored noise generation. *Romanian Journal of Acoustics and Vibration*, 15(1):14–19, 2018.

APPENDICES

Appendix A

Numerical computations

Here we present our numerical algorithm to compute the growth rates and the y structures of $u_1,\ u_2,\ v_1,\ v_2,$ and η in equations (2.10)-(2.13). The algorithm presented here is based on the work of Iga [34] with minor changes due to our more general framework and our use of different averaging operators.

In order to solve the instability problem given an arbitrary interface function $\eta_I(y) = y + 2y_m\tilde{\eta}_I(y/(2y_m)) + S$, we must find an appropriate interface $\tilde{\eta}_I(y)$ such that $\overline{H_2} = 1$ and $\lambda = F\max\{|\eta_I(y)\}$. By definition we have that

$$\overline{H_2} = \frac{1}{2y_m}\int_{-y_m}^{y_m} 1 + F(y + 2y_m\tilde{\eta}_I(y/(2y_m)) + S)dy.$$

Setting $\overline{H_2} = 1$ and solving for S as a function of y_m gives $S = -\int_{-y_m}^{y_m}\tilde{\eta}_I(y/(2y_m))dy$. To enforce the λ condition we simply numerically solve

$$0 = \lambda - F\max_{[-y_m,y_m]}\left\{y + 2y_m\tilde{\eta}_I(y/(2y_m)) - \int_{-y_m}^{y_m}\eta_I(y)dy\right\}$$

for y_m. Note that unlike in the work of GPZ, because the interface function need not be monotonic there is not necessarily a unique solution to the above equation for y_m. Thus when considering non-monotonic non-antisymmetric profiles one must ensure that the smallest root is being used.

To solve the eigenvalue problem we follow Iga [34], and define $u_j,\ v_j,\ \eta$ and η_I, on the grid shown in Figure A.1. We define the following averaging and difference operators that

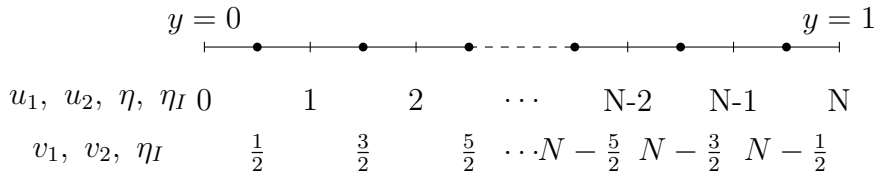

Figure A.1: Grid used in our numerical algorithm. Note that the x-directional velocities as well as the wave height are on the edges of the domain while the y-directional velocities are on a staggered grid.

compute derivatives and values from one grid to the other

$$D_{u\to v}(f_l) \equiv \frac{f_l - f_{l-1}}{\Delta y}, \qquad D_{v\to u}(f_l) \equiv \frac{f_{l+\frac{1}{2}} - f_{l-\frac{1}{2}}}{\Delta y},$$
$$A_{u\to v}(f_l) \equiv \frac{f_l + f_{l-1}}{2}, \quad \text{and} \quad A_{v\to u}(f_l) \equiv \frac{f_{l+\frac{1}{2}} + f_{l-\frac{1}{2}}}{2},$$

where $\Delta y \equiv 1/N$ where N is the number of gird points. Each of the above operators is only defined for $l \in [1, N-1]$. Each of these operators is a first order approximation. With these operators, we discretize equations (2.15) on the staggered grid and all other equations on the unstaggered grid. The result is a $(5N-2)\times(5N-2)$ eigenvalue problem that we solve via a direct method.

The implementation of our wall boundary condition is straightforward. One simply expands the definition of the differencing operators and averaging operators, adds ghost points on either edge of our computational domain, and then eliminates the ghost points via the wall condition.

Appendix B

Derivation of the II condition for a RTI stable baroclinic jet

For fixed values of Ro and Bu a baroclinic jet is unstable to II if

$$\underbrace{\left(1+2\mathrm{Ro}\tanh(y)\mathrm{sech}^2(y)e^{-z^2}\right)}_{A}\underbrace{\left(\mathrm{Bu}-2\mathrm{Ro}(2z^2-1)e^{-z^2}\tanh(y)\right)}_{G}-\underbrace{4\mathrm{Ro}^2z^2e^{-2z^2}\mathrm{sech}^4(y)}_{C^2}<0$$

holds for some $y,\ z\in\mathbb{R}$. Since $Ro\geq 0$, $C^2\geq 0$ for all $y\ , z\in\mathbb{R}$ and that $G>0$ for flows that are stable to RTI. We consider two cases:

- If $\frac{9}{4\sqrt{3}}<Ro$ then $A<0$ from our work on the case of a barotropic jet. It then follows that $AG<0$. Thus $AG-C^2<0$ and the flow is unstable to inertial instability.
- If $\frac{9}{4\sqrt{3}}\geq Ro$, we have that $0\leq Ro\leq\frac{9}{4\sqrt{3}}$. Since the flow is stable to RTI, it follows that $2Ro\leq Bu<\infty$. To check for II, we now need to determine if $AG-C^2<0$ holds for any $y,\ z\in\mathbb{R}$ within the parameter points in shaded region in Figure B.1. Using maple [1], we minimized the EPV over this domain of parameters for $y,z\in\mathbb{R}$ and found that the minimum value of 0 was obtained at the point $(Ro,Bu)=(0,0)$ and along the line $(Ro,Bu)=(9/(4\sqrt{3}),Bu)$. Thus the flow is stable to II within this region.

Putting the above work together, we see that at least when the flow is stable to RTI, the conditions for inertial instability for a baroclinic jet and a barotropic jet are the same. Direct numerical computations shows that this is not the case when the baroclinic jet is unstable to RTI.

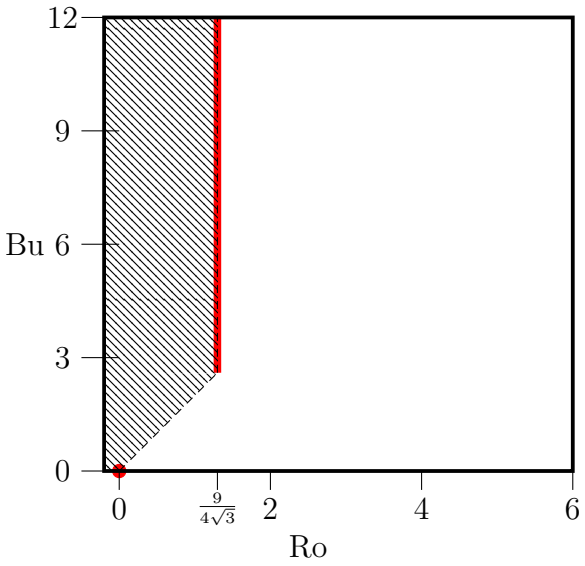

Figure B.1: The region of parameters to minimize the EPV over to determine weather or not the flow is stable to II. The red regions are the locations where the Ertel obtains its minimum value of 0.

Appendix C

Code for the 1D eigenvalue problem

Code for numerically solving eigenvalue problem (3.57) for the 1d barotropic problem. Here the cheb(N) function is provided in [90].

```
function [omega,y,Fy]=LSA_1d(k,m,Ro,Bu,delta,Re,Pr)
%% Compute the largest growth rate and structure for the fastest growing
%% mode for the given paramaters

%% Define L, and f
L = 100;f = 0.73e-4;
%% Compute the rest of the paramaters
U0 = Ro*f*L;
H  = delta *L;
N  = f*sqrt(Bu)/delta;
nu = f*Ro*L^2/Re;
kappa=f*Ro*L^2/(Re*Pr);
%% Define the domain paramaters
Ny   = 512;Ldom = 20*L;
%% define y, Dy, Dyy and I
[Dy,y] = cheb(Ny);
y   = y*Ldom;
Dy  = Dy*(1/Ldom);
Dyy = Dy*Dy;
I = eye(Ny+1);
% Define Basic State
U  =   U0./(cosh((y/L )).^2)';
Up = -(2*U0/L )*tanh(y/L ).*(1./cosh(y/L ).^2);
% Define useful matrices
Umat  = k*diag(U,0) - 1j*nu*((k^2+m^2)*I-Dyy);
Umatv  = k*diag(U,0) +(1/1j)*nu*((k^2+m^2)*I-Dyy);
Umatz = k*diag(U,0) - 1j*kappa*((k^2+m^2)*I-Dyy);
Qmat = diag(f-Up);
%% Build matrix
A = [[      Umatz    , (N^2/m^2)*k*I  ,  - (N^2/m^2)*Dy(:,2:end-1)];...
     [        k*I    ,      Umat      ,         Qmat(:,2:end-1)   ];...
```

```
      [  Dy(2:end-1,:),  f*I(2:end-1,:),     Umatv(2:end-1,2:end-1)]];
% Solve Eigenvalue Problem Directly
[eigVecs,eigVals] = eig(A); eigVals=diag(eigVals);
%% Apply filtering
checkcnt=1;
while checkcnt<=length(eigVals)
    % find when modes are decreasing and increasing
    vec1=eigVecs(1:Ny+1,checkcnt);cutoff=1e-3*max(real(abs(vec1)));
    diff1=real(diff(vec1));p1=diff1>cutoff;n1=diff1<cutoff;
    %remove the endpoints so we can find points where the mode increases and then decreases
    p1(1)=[];n1(end)=[];alt1=p1+n1;sum1=sum(alt1==2);
    %find location of the max of the abs of the mode
    [~,ind]=max(abs(vec1));
    %filter if needed
    if ((sum1>=length(vec1)/4))||abs(abs(y(ind))-Ldom)<L
        eigVals(checkcnt)=0*eigVals(checkcnt);
        eigVecs(:,checkcnt)=0*eigVecs(:,checkcnt);
        checkcnt=checkcnt+1;
    else
        checkcnt=checkcnt+1;
    end
end
% Sort eigenvalues and eigenvectors by imag part
[~,ind] = sort(-imag(eigVals));eigVals = eigVals(ind);
eigVecs = eigVecs(:,ind);
% Take the eigenpair with the largest real part
omega=eigVals(1);
Fy=eigVecs(:,1);
end
```

Appendix D

Discretizations of the boundary conditions for the operators in Table 4.1

To simplify the construction of the discretizations of the differential operators listed in Table 4.1, we build matrices that act on a dummy spatial variable x which is assumed to be discretized on some linearly spaced grid $\{x_1, \ldots, x_N\}$.

For the operators with Dirichlet boundary conditions, we have the following:

∂_x: The second order central differences for this derivative evaluated at the points x_1, x_2, x_{N-1}, and x_N rely on either the boundary points or on points outside the domain and thus must be appropriately modified. For the boundary points x_1 and x_N, we apply third order one sided finite differences and use the boundary conditions $f(x_1) = 0 = f(x_N)$. For x_1 the finite difference scheme we use is

$$\partial_x(f)|_{x=x_1} \approx \frac{3f(x_2) - 3/2f(x_3) + 1/3f(x_4)}{\Delta x}$$

and we use a similar scheme for x_N. For the points x_2 and x_{N-1} we simply use the boundary conditions directly in the second order central differences. Our boundary conditions at x_2 is

$$\partial_x(f)|_{x=x_2} \approx \frac{-f(x_3)}{2\Delta x}$$

and a similar condition is used for x_{N-1}.

∂_{xx}: This operator requires modifications at the same grid points as the previous one. Like before, we use one sided differences for the endpoints x_1 and x_N but we use fourth order finite differences instead of second order ones. For x_2 and x_{N-1} we simply use the boundary conditions to simplify the second order central differences. Our boundary conditions at x_1 and x_2 are

$$\partial_{xx}(f)|_{x=x_1} \approx \frac{-77/6f(x_2) + 107/6f(x_2) - 13f(x_4) + 61/12f(x_5) - 5/6f(x_6)}{(\Delta x)^2} \quad \text{and}$$

$$\partial_{xx}(f)|_{x=x_2} \approx \frac{-2f(x_2) + f(x_3)}{(\Delta x)^2}$$

with similar conditions for x_{N-1}, x_N

∂_{xxx}: For this operator we need to apply the boundary conditions at the points x_1, x_2, x_3 x_{N-2}, x_{N-1}, and x_N. We use higher order one sided differences for x_1, x_2, x_{N-1} and x_N and simplify the centered difference for x_3 and x_{N-2} by using the boundary conditions. Because of the lengths of the schemes and because it does not add anything interesting to show long finite difference formulas, we omit these differences here. The formulas for these differences along with many others are computed in [21].

For the Neumann boundary conditions, we have the following for each of the operators:

∂_x: For this operator, we need to apply boundary conditions at x_1 and x_N. As the boundary condition is a Neumann condition, we simply set the coefficients in the finite difference to zero at the ends of the domain.

∂_{xx}: For this case we again only need to use our boundary condition at x_1 and x_N. A second order approximation for the boundary condition at x_1 is

$$0 = \partial_x(f)|_{x=x_1} \approx \frac{f(x_0) - f(x_2)}{2\Delta x}$$

and thus we have $f(x_0) = f(x_2)$ to second order accuracy. Using this condition to eliminate the ghost point in the second order finite difference for ∂_{xx} yields the finite difference

$$\partial_{xx}(f)|_{x=x_1} \approx \frac{2f(x_1) + 2f(x_2)}{(\Delta x)^2}.$$

A similar condition is readily found for x_N.

∂_{xxx}: For this operator we need to modify the discretized operator at the boundary points $x_1,\ x_2, x_{N-1}$, and x_N. At the endpoints x_1 and x_N we use the one sided third order finite differences readily available in the work of Fornberg [21]. For the points x_2 and x_{N-1} we use second order central finite differences where we eliminate the ghost points at x_0 and x_{N+1} by using second order central difference approximation for the boundary conditions. For the endpoint x_2 we use $f(x_0) = f(x_2)$ to approximate the boundary condition and the resulting finite different approximation is

$$\partial_{xxx}(f)|_{x=x_2} \approx \frac{f(x_1) - 1/2 f(x_2) - f(x_3) + 1/2 f(x_4)}{(\Delta x)^3}.$$

A similar condition for the other boundary at x_{N-1} is similarly found.

Appendix E

Code for the 2D eigenvalue problem

Code for numerically solving eigenvalue problem (3.54) for the 2d barotropic problem. Here we apply the methods described in Section 4.2 to build the numerical domain, the needed operators, compute the solution to the 2d eigenvalue solver and to filter the results.

```
%% nondimentional paramaters
Ro    = 2;
Bu    = 17.2608;
delta     = 3/100;
Re    = 1.168e8;
Pr    = inf;

%% Horizontal wave number
k = 0.00005;

%% Define Ny and a floor for Nz
Ny = 128;Nz = 256;

%% Number of modes we wish to find
Num_modes = 3;

%% Define various bools
Barotropic_problem = false;
Interior_jet = true;

%% Define L and f
L = 100;f = 0.73e-4;

%% compute the rest of the patamaters
U0 = Ro*f*L;  H  = delta*L; N  = f*sqrt(Bu)/delta;
nu = f*Ro*L^2/Re; kappa = f*Ro*L^2/(Re*Pr);

%% Check for the existance of instabilities for the barotropic case
if (Ro<9/(4*sqrt(3)))
```

```
30      disp('THERE IS NO II!!!!!!');return
31  end
32      if (Bu<=2*Ro)
33      disp('WE HAVE RTI!!!!!!');return
34  end
35
36  %% RUN 1D code  for several vertical wave numbers to compute the domain size
37  disp('Solving 1d Barotropic problem')
38  mv = 0.05:0.5:20;  Bt_Growth_rate = 0;
39  for i=1:length(mv)
40      [omega,y_bt,Fy]=LSA_1d2(k,mv(i),Ro,Bu,delta,Re,Pr);
41      % if this mode is faster than the previously found ones, save it
42      if imag(Bt_Growth_rate) < imag(omega)
43          Bt_Growth_rate = omega; mmax=mv(i);
44          Bt_mode = Fy(1:length(y_bt)+1);
45      end
46  end
47  % Find horizontal length for the mode to be under tol% of the maximum
48  Tol = 1e-3; subzerovals = y_bt(abs(Bt_mode)>Tol*max(abs(Bt_mode)));
49  y = linspace(min(subzerovals),max(subzerovals),Ny);
50
51  %% Find the vertical length by looking at the 0's of the total vorticity
52  if Interior_jet
53      Lz = H*sqrt(log(4*Ro/3^(3/2)));
54  else
55      Lz = 2*H*sqrt(log(4*Ro/3^(3/2)));
56  end
57  % Extra restrictions to resolve the bt m wave number
58  Lz = max(Lz,min(1,2*pi/mmax)); Nz = max(Nz,floor(Lz/((2*pi/mmax)/10)));
59  z = linspace(-Lz,0,Nz);
60
61  %% Build the 2d grid
62  [Y,Z] = meshgrid(y,z);
63
64  %% Define differentation matrices for z. Dd is a Dirichlet boundary,
65  %% Dn is a Neumann boundry
66  e_z = ones(Nz,1);
67  dz  = z(2)-z(1);
68
69  Dd_z = spdiags([-e_z 0*e_z e_z]/(2*dz),-1:1,Nz,Nz);
70  Dd_z(1,1:4)=[0 3 -3/2 1/3]/(dz);
71  Dd_z(2,1:3)=[0 0 1]/(2*dz);
72  Dd_z(end-1,end-2:end)=[-1 0 0]/(2*dz);
73  Dd_z(end,end-3:end)=[-1/3 3/2 -3 0]/(dz);
74
75  Dn_z = spdiags([-e_z 0*e_z e_z]/(2*dz),-1:1,Nz,Nz);
76  Dn_z(1,1:3)=[0 0 0]/dz;
77  Dn_z(end,end-2:end)=[0 0 0]/dz;
78
79  Dd_zz = spdiags([e_z -2*e_z e_z]/(dz^2),-1:1,Nz,Nz);
80  Dd_zz(1,1:6)=[0 -77/6 107/6 -13 61/12 -5/6]/dz^2;
81  Dd_zz(2,1)=0;
82  Dd_zz(end-1,end)=0;
83  Dd_zz(end,end-5:end)=[-5/6 61/12 -13 107/6 -77/6 0]/dz^2;
```

```
84
85  Dn_zz = spdiags([e_z -2*e_z e_z]/(dz^2),-1:1,Nz,Nz);
86  Dn_zz(1,1:2)=[-2 2]/dz^2;
87  Dn_zz(end,end-1:end)=[2 -2]/dz^2;
88
89  Dd_zzz = spdiags([-1/2*e_z e_z 0*e_z -e_z  1/2*e_z]/(dz^3),-2:2,Nz,Nz);
90  Dd_zzz(1,1:7)=[0 29 -461/8 62 -307/8 13 -15/8]/dz^3;
91  Dd_zzz(2,2:8)=[-49/8 29 -461/8 62 -307/8 13 -15/8]/dz^3;
92  Dd_zzz(3,1:5)=[0 1 0  -1 1/2]/dz^3;
93  Dd_zzz(end-2,end-4:end)=[-1/2 1 0 -1 0]/dz^3;
94  Dd_zzz(end-1,end-7:end-1)=[15/8 -13 307/8 -62 461/8 -29 49/8]/dz^3;
95  Dd_zzz(end,end-6:end)=[15/8 -13 307/8 -62 461/8 -29 0]/dz^3;
96
97  Dn_zzz = spdiags([-1/2*e_z e_z 0*e_z -e_z  1/2*e_z]/(dz^3),-2:2,Nz,Nz);
98  Dn_zzz(1,1:5)=[-5/2 9 -12 7 -3/2]/dz^3;
99  Dn_zzz(2,1:4)=[1 -1/2 -1 1/2]/dz^3;
100 Dn_zzz(end-1,end-3:end)=[-1/2 1 1/2 -1]/dz^3;
101 Dn_zzz(end,end-4:end)=[3/2 -7 12 -9 5/2]/dz^3;
102
103 %% Define differentation matrices for y. Dd is a Dirichlet boundary,
104 %% Dn is a Neumann boundry
105 e_y = ones(Ny,1);
106 dy  = y(2)-y(1);
107
108 Dd_y = spdiags([-e_y 0*e_y e_y]/(2*dy),-1:1,Ny,Ny);
109 Dd_y(1,1:4)=[0 3 -3/2 1/3]/(dy);
110 Dd_y(2,1:3)=[0 0 1]/(2*dy);
111 Dd_y(end-1,end-2:end)=[-1 0 0]/(2*dy);
112 Dd_y(end,end-3:end)=[-1/3 3/2 -3 0]/(dy);
113
114 Dn_y = spdiags([-e_y 0*e_y e_y]/(2*dy),-1:1,Ny,Ny);
115 Dn_y(1,1:3)=[0 0 0]/dy;
116 Dn_y(end,end-2:end)=[0 0 0]/dy;
117
118 Dd_yy = spdiags([e_y -2*e_y e_y]/(dy^2),-1:1,Ny,Ny);
119 Dd_yy(1,1:6)=[0 -77/6 107/6 -13 61/12 -5/6]/dy^2;
120 Dd_yy(2,1)=0;
121 Dd_yy(end-1,end)=0;
122 Dd_yy(end,end-5:end)=-[5/6 -61/12 13 -107/6 77/6 0]/dy^2;
123
124 Dn_yy = spdiags([e_y -2*e_y e_y]/(dy^2),-1:1,Ny,Ny);
125 Dn_yy(1,1:2)=[-2 2]/dy^2;
126 Dn_yy(end,end-1:end)=[2 -2]/dy^2;
127
128 Dd_yyy = spdiags([-1/2*e_y e_y 0*e_y -e_y  1/2*e_y]/(dy^3),-2:2,Ny,Ny);
129 Dd_yyy(1,1:7)=[0 29 -461/8 62 -307/8 13 -15/8]/dy^3;
130 Dd_yyy(2,2:8)=[-49/8 29 -461/8 62 -307/8 13 -15/8]/dy^3;
131 Dd_yyy(3,1:5)=[0 1 0  -1 1/2]/dy^3;
132 Dd_yyy(end-2,end-4:end)=[-1/2 1 0 -1 0]/dy^3;
133 Dd_yyy(end-1,end-7:end-1)=[15/8 -13 307/8 -62 461/8 -29 49/8]/dy^3;
134 Dd_yyy(end,end-6:end)=[15/8 -13 307/8 -62 461/8 -29 0]/dy^3;
135
136 Dn_yyy = spdiags([-1/2*e_y e_y 0*e_y -e_y  1/2*e_y]/(dy^3),-2:2,Ny,Ny);
137 Dn_yyy(1,1:5)=[-5/2 9 -12 7 -3/2]/dy^3;
```

```
Dn_yyy(2,1:4)=[1 -1/2 -1 1/2]/dy^3;
Dn_yyy(end-1,end-3:end)=[-1/2 1 1/2 -1]/dy^3;
Dn_yyy(end,end-4:end)=[3/2 -7 12 -9 5/2]/dy^3;

%% Build identity matrix
I_y = sparse(eye(Ny,Ny));
I_z = sparse(eye(Nz,Nz));

%% Define the basic state
if Barotropic_problem
    U      = U0*sech(Y/L).^2;
    UY     = -(2*U0/L)*tanh(Y/L).*sech(Y/L).^2;
    UZ     = 0*Z;UZZ = 0*Z;UZZZ = 0*Z;
    Theta  = N^2*Z;
    Phi    = -f*U0*L*tanh(Y/L)+(N^2/2)*Z.^2;
    Phi_zy = 0*Z;
    Phi_zz = N^2+0*Z;
else
    if Interior_jet
        D = 0;
    else
        D = Lz/2;
    end
    U      = U0*exp(-((Z+D)./H).^2).*sech(Y/L).^2;
    UZ     = U0*(-(2*(Z+D)./H.^2)).*exp(-((Z+D)./H).^2).*sech(Y/L).^2;
    UZZ    = U0*(-(2*(Z+D)./H.^2).^2.*exp(-((Z+D)./H).^2)+(-2/H^2)...
             .*exp(-((Z+D)./H).^2)).*sech(y/L).^2;
    UZZZ   = U0*(-4*((Z+D)./H).*(2*((Z+D)./H).^2-3)...
             .*exp(-((Z+D)./H).^2)).*sech(y/L).^2;
    UY     = U0*exp(-((Z+D)./H).^2).*(-2*tanh(Y/L).*sech(Y/L).^2/L);
    Theta  = N^2*Z - U0*L*f*(2*Z+Lz)/(H^2).*exp(-((Z+D)./H).^2).*tanh(Y/L);
    Phi    = -f*U0*L*tanh(Y/L).*exp(-((Z+D)./H).^2)+N^2/2*Z.^2;
    Phi_zy = 2*f*L*U0/(H^2*L)*exp(-((Z+D).^2)/H^2).*(Z+D).*sech(Y/L).^2;
    Phi_zz = N^2+2*f*L*U0/H^2*exp(-(Z+D).^2/H^2).*tanh(Y/L)...
             -4*f*L*U0/H^4*exp(-(Z+D).^2/H^2).*(Z+D).^2.*tanh(Y/L);
end

%% Build 1D operators out of the 2D operators
% Backgound state and identity
U1      = spdiags(U(:),0,sparse(Ny*Nz,Ny*Nz));
U1_y    = spdiags(UY(:),0,sparse(Ny*Nz,Ny*Nz));
U1_z    = spdiags(UZ(:),0,sparse(Ny*Nz,Ny*Nz));
Phi1_zy = spdiags(Phi_zy(:),0,sparse(Ny*Nz,Ny*Nz));
Phi1_zz = spdiags(Phi_zz(:),0,sparse(Ny*Nz,Ny*Nz));
I = kron(I_y,I_z);

% Derative operators for Phi'
D1phi_y   = kron(Dn_y,I_z); D1phi_yy  = kron(Dn_yy,I_z);
D1phi_z   = kron(I_y,Dn_z); D1phi_zzz = kron(I_y,Dn_zzz);

% Derative operators for v'
D1v_y   = kron(Dd_y,I_z); D1v_yy  = kron(Dd_yy,I_z);
D1v_yyy = kron(Dd_yyy,I_z); D1v_z   = kron(I_y,Dn_z);
D1v_zz  = kron(I_y,Dn_zz); D1v_zzz = kron(I_y,Dn_zzz);
```

```
192
193 % Derative operators for w'
194 D1w_y   = kron(Dn_y,I_z); D1w_yy  = kron(Dn_yy,I_z);
195 D1w_z   = kron(I_y,Dd_z); D1w_zz  = kron(I_y,Dd_zz);
196 D1w_zzz = kron(I_y,Dd_zzz);
197
198 %% Build the matrices
199 A=[[ 0*I , D1v_y, D1w_z];...
200    [ 0*I ,     I,  0*I];...
201    [D1phi_z,   0*I,  0*I];];
202 % define viscous terms for the B matrix
203 L_Phi_z = -k^2*D1phi_z+Vis_in_y*D1phi_yy*D1phi_z+D1phi_zzz;
204 L_v     = -k^2*I+D1v_yy+D1v_zz;
205 L_v_y   = -1i*k^2*D1v_y+1i*D1v_yyy+1i*(D1v_y*D1v_zz);
206 L_w_z   = -1i*k^2*D1w_z+1i*D1w_yy*D1w_z+1i*D1w_zzz;
207 B = [[-1i*k^2*I , k*(U1*D1v_y)-k*U1_y+k*f*I+nu*L_v_y , k*(U1*D1w_z)+nu*L_w_z ];...
208      [-1i*D1phi_y , k*U1+f/k*D1v_y+1i*nu*L_v , f/k*D1w_z ];...
209      [ k*(U1*D1phi_z)+1i*kappa*L_Phi_z , -1i*Phi1_zy , -1i*Phi1_zz ];];
210
211
212 %% Solve the eigenvalue problem
213 % Set the solver paramaters
214 ne = 120; % number of eigenvalues to find
215 opts.maxit=1e5; % max iterations
216 opts.p=10*ne+20; % increase the number of basis vectors in the Krylov space
217 % the default is max(2*ne,20)
218 % Use the Shift-and-Invert Arnoldi method with the barotropic eigenvalue
219 % as the seed
220 [eigVecs,eigVals] = eigs(B,A,ne,Bt_Growth_rate,opts);
221 % get rid of any nan eigenvalues and diagonalise
222 eigVals(isnan(eigVals))=0;
223 eigVals=diag(eigVals);
224
225
226 %% Remove spurious modes
227 % Method 1 occilations - if more than 1/2 of the grid is grid scale
228 % oscillation then get rid of that mode
229
230 for Counter=1:length(eigVals)
231     diffvec=reshape(eigVecs(Nz*Ny*2+1:end,Counter ),Nz,Ny);
232     vec1=diffvec(:,floor(Ny/2));diff1=real(diff(vec1));p1=diff1>0;n1=diff1<0;
233     vec2=diffvec(floor(Nz/2),:)';diff2=real(diff(vec2));p2=diff2>0;n2=diff2<0;
234     p1(1)=[];n1(end)=[];p2(1)=[];n2(end)=[];
235     alt1=p1+n1;alt2=p2+n2;
236     sum1=sum(alt1==2); sum2=sum(alt2==2);
237     if ((sum1>=Nz/2)||(sum2>=Ny/2)) %if it occilates on the grid
238         eigVals(Counter )=0*eigVals(Counter );
239         eigVecs(:,Counter )=0*eigVecs(:,Counter );
240         disp(['removed mode: ', num2str(Counter )])
241     end
242 end
243 % Post filter sort
244 [~,ind] = sort(imag(eigVals),'descend');
245 eigVals = eigVals(ind);eigVecs = eigVecs(:,ind);
```

```
246
247
248
249 % Filter 2 rerun the solver and look for convergance
250 mode = 1;
251 modes_found = 0;
252 while (modes_found < Num_modes)||(mode > length(eigVals))
253     [~,val] = eigs(B,A,1,eigVals(mode),opts);
254     [~,val2] = eigs(B,A,1,val,opts);
255     if abs(val-val2)/(abs(val)+abs(val2))<10^-6
256         modes_found = modes_found+1;
257         mode = mode + 1;
258     else
259         eigVals(mode)=0;
260         eigVecs(:,mode)=0*eigVecs(:,mode);
261         disp(['Filter 2 removed mode: ', num2str(mode)])
262         mode=mode+1;
263     end
264 end
265 % Wipe the rest of the modes;
266 for i=mode:length(eigVals)
267     eigVals(mode)=0;
268     eigVecs(:,mode)=0*eigVecs(:,mode);
269 end
270
271 % Post filter sort
272 [~,ind] = sort(imag(eigVals),'descend');
273 eigVals = eigVals(ind); eigVecs = eigVecs(:,ind);
```